INAUGURAL - DISSERTATION

zur

Erlangung der Doktorwürde

der

Naturwissenschaftlich-Mathematischen

Gesamtfakultät

der

Ruprechts-Karls-Universität

Heidelberg

vorgelegt von

Diplom-Mathematiker Kai Harold Kopfer

aus Siegen

Tag der mündlichen Prüfung: _____

A MECHANOCHEMICAL MODEL FOR NEUTROPHIL POLARIZATION

Gutachter: Prof. Dr. Dr. h.c. mult. Willi Jäger

Acknowledgements

I would like to express my gratitude to

- my advisor, Prof. Dr. Dr. h.c. mult. Willi Jäger and my group leader Prof. Dr. Franziska Matthäus, for encouraging me to step into the investigation of this topic, for providing support and advice whenever necessary, for their scientific input, and for their patience,
- the *Interdisciplinary Center for Scientific Computing Heidelberg* (IWR) and the *Center for Modelling and Simulation in the Biosciences* (BIOMS) for providing financial support,
- the staff of the *Faculty of Mathematics and Computer Science* and in particular of the *Institute of Applied Mathematics at the Heidelberg University* for the organizational support,
- my research group *AMJ* and my junior research group *CBS* for fruitful discussions and scientific input, in particular Dr. Jan Fuhrmann, Dr. Moritz Mercker and Stefano Belloni, and
- Katia Herberger, Mareike Bereswill, Dr. Johannes Schmidt, and my parents, Annette and Prof. Dr. Herbert Kopfer, for their support in every respect and for their patience.

Abstract

Directed migration of eukaryotic cells is caused by a polarization of the actomyosin cytoskeleton (ACM). Throughout many cell types the polar alignment of the AMC is i.a. initiated by the activation of the Rho GTPases Rac and RhoA. In response to an external chemical gradient active Rac accumulates and determines the cell front, while active RhoA predominantly accumulates at the rear of the cell. Current experimental evidence indicates that in neutrophils mechanical tension of the plasma membrane confines Rac activity patterns to the leading front.

The patterning mechanism behind the Rho-based polarization process of eukaryotic cells has interested mathematical modellers over the last decades. While elaborated concepts for purely biochemical and purely mechanical patterning processes are available, the basics of mechanochemical patterning with respect to cell polarization are not well understood yet. In accordance to the aforementioned experimental findings, we suggest a mechanochemical model for cell polarization, including Rho GTPase mediated AMC dynamics and changes in membrane tension as upstream controller of Rho GTP, in which active Rac patterns are locally confined to the cell front by membrane tension. Rho proteins can become activated or inactivated due to complex formation with specific effector proteins. In the model active Rac and active RhoA mediate actin polymerization and the generation of myosin-dependent contractile force, respectively. The model cell is considered as a two dimensional layer adhering to a flat substrate, wherein the embedded AMC is modelled as a viscous active gel. Morphological changes of the AMC induce changes in membrane tension. Rho based chemical signalling is modelled by reaction-diffusion equations. Chemical signalling induces a mechanical response of the AMC. Actomyosin mechanics are modelled by a Stokes-related equation. The spatial change of the domain is determined by a free-boundary problem. We numerically demonstrate that the model exhibits key features of neutrophil polarization and shape generation and we explain the underlying patterning mechanism. The model accounts for a minimal mechanochemical circuit capable of generating robust polarity patterns and demonstrates how cell mechanics could serve as a long range signal transmitter in Rho based cell polarization.

Zusammenfassung

Die gerichtete Migration eukaryotischer Zellen bedingt eine Polarisation des Actomyosin-Zytoskeletts (AMC). Die polare Anordnung des AMC wird in vielen Zelltypen u.a. durch die Aktivierung der Rho GTPasen Rac und RhoA eingeleitet. Aktiviertes Rac akkumuliert an der Zellfront, während aktiviertes RhoA im hinteren Teil der Zelle konzentriert wird. Experimentelle Befunde über Neutrophile legen nahe, dass Rac-Aktivierung durch die Generierung von Membranspannung auf die Zellfront beschränkt wird.
Während eine Fülle aussagekräftiger Modelle zur Beschreibung von sowohl rein biochemischer als auch rein mechanischer Musterbildungsprozesse aufgestellt wurden, sind mechanisch-chemische Musterbildungsprozesse, die bei der Polarisation von Zellen auftreten, in großen Teilen unerforscht. In dieser Arbeit wird ein mechanisch-chemisches Zellpolarisationsmodell vorgeschlagen, in dem die Rho GTPasen Rac und RhoA die Mechanik des AMC und damit indirekt die Plasmamembranspannung beeinflussen. Andererseits reguliert in dem Modell die Änderung der Membranspannung die Aktivierung von Rho GTP, sodass Rac-Aktivierung lokal auf die Zellfront beschränkt bleibt.
Rho GTPasen können entweder aktiv oder inaktiv auftreten, indem sie an spezielle Effektorproteine binden. Aktives Rac und RhoA steuern sowohl die Polymerisation von Actin als auch Myosin-Kontraktionen, die auf das Aktin-Netzwerk wirken. Die zugrunde gelegte Geometrie des Modells wird durch eine zweidimensionale Schicht beschrieben, welche den Verbund von Plasmamembran und AMC reprs̈entiert und die auf einem flachen Substrat liegt.
Das Modell behandelt chemische Signaltransduktion per Reaktions-Diffusionsgleichungen, welche die Mechanik des AMC beeinflusst. Im Modell wird die Mechanik des AMC wird durch eine Viskositätsgleichung beschrieben, die der Stokes'schen Gleichung ähnelt. Die geometrische Änderung der Zelle wird durch die Lösung eines freien Randwertproblems bestimmt. Die Membranspannung im Modell wird durch eine Integralgleichung beschrieben, die abhängig von der Zellmorphologie ist.
Wir weisen numerisch nach, dass das Model in der Lage ist, grundlegende Eigenschaften der Polarisationscharakteristika von Neutrophilen reproduzieren zu können, und wir erklären den zugrunde liegenden Musterbildungsprozess. Das Modell stell ein Minimalsystem dar, das in der Lage ist robuste Muster zu produzieren und dabei mechanische Spannung als Langstreckensignalleiter mit einbezieht.

Contents

List of Figures

Abbreviations

AMC	**A**ctin-**m**yosin **c**ytoskeleton
G-actin	Monomeric actin
F-actin	Filamentous actin
GTP	**G**uanine-**t**ri-**p**hosphate
GDP	**G**uanine-**d**i-**p**hosphate
GEF	**G**uanine **e**xchange **f**actor
GAP	**G**TPase **a**ctivating **p**rotein
GDI	**G**DP **d**issociation **i**nhibitors

Symbols

u	Concentration of active Rac	μmol/dm^2
w	Concentration of active RhoA	μmol/dm^2
a	F-actin concentration	μmol/dm^2
b	G-actin concentration	μmol/dm^2
τ	Apparent membrane tension	Pa
v	Convection velocity of F-actin	μm/s
V	Outward normal boundary velocity	μm/s
p	Polarity field	-
Π	Pressure	Pa
σ^{tot}	Total stress tensor	Pa
σ^{act}	Actively generated stress	Pa
σ^{pas}	Viscous stress	Pa
Ω_t	Cell domain at time t	-
Ω_t^{L}	Domain of the lamellipodium at time t	-
Ω_t^{B}	Domain of the cell body	-
Γ_t	Boundary of the cell domain at time t	-
Γ_t^{L}	Boundary of the lamellipodium at time t	-
Γ_t^{B}	Boundary of the cell body at time t	-

Chapter 1

Introduction

1.1 What is cell polarity?

Polarization, a fundamental attribute of eukaryotic cells, means the spatial reorganization of certain lipids and proteins in response to a chemical external stimulus. This symmetry break activates a whole cascade of downstream effectors initializing the directional alignment of the cytoskeleton. In particular, in motile cells like neutrophils polarization of Rho proteins is regarded as the initial step of locomotion
The cellular key processes involved in polarization and their respective interactions have been studied in great detail - both through theoretical investigation [1–8] and experimental research [9–11]. For many cell types it is assumed that biochemical signalling alone is responsible for the establishment and maintenance of polarity patterns and precedes mechanical responses involving cytoskeletal activity [12, 13]. In other cell structures like keratocyte fragments solely the mechanical properties of the actin cytoskeletal network appear sufficient for polarization of the cytoskeleton [14, 15]. However, in neutrophils it has been shown that both, biochemical and mechanical signalling, are necessary to generate and to maintain polarity patterns [11] in response to external chemical stimuli. Key players in the biochemical signalling pathway of neutrophils include the Rho GTPases family, whose members Rac, RhoA and Cdc42 cycle between an active form and an inactive form [16, 17].
Rac activity is highly polarized at the leading front in response to external chemical gradients like cAMP as well as in the presence of uniformly distributed chemoattractants [18, 19] and recruits downstream effectors like Arp2/3 and the Scar/WAVE complex that promote actin polymerization [20, 21]. The so caused actin-driven membrane protrusion at spots of high Rac activity induce an increase of the cell surface and thus induce a global increase in membrane tension [11, 22].
Membrane tension, in turn, confines Rac activation to the leading front: Houk et al. [11] demonstrate that increased tension, generated by stretching neutrophils using micropipette aspiration, inhibits both, the formation of protrusions and Rac activation

aside from the leading front. In response to chemoattractants and in addition to increased Rac activity at the leading front, active RhoA increases predominately at the back of the cell where it targets its downstream myosin II [9].
Myosin II proteins form small aggregates via binding to each others tail region and crosslink actin filaments. Conformational changes due to energy consumption provided by ATP hydrolysis exerts a contractile force to the network [23]. The contractile force at the rear of the cell induces the trailing of the dorsal cell, which reduces the cell surface area and thus may decrease membrane tension. This balancing mechanism could serve as a regulator in the maintenance of Rac signals at the front: Tension increases due to front protrusion confines active Rac to the leading while tension decreases due to trailing of the dorsal cell prevents the Rac signal at the front to expire.

1.1.1 State of research: Models for cell polarity

The mechanism behind Rho GTPase based cell polarity has interested modellers over the last four decades and has led to various concepts to explain cell polarization mathematically. The most prominent model approaches can be subdivided into three qualitatively different classes:

1) *Turing based models*,
2) *LEGI mechanisms*
3) wave based models.

In the following paragraphs we will briefly account to the first two classes. The third class will be explained more in detail, since it shares some features with the presented model in this thesis. For a more detailed discussion we refer to [7].

1) Turing based models Some diffusion-reaction systems expose the ability of a symmetry break due the appearance of bifurcation branches in the linearized system. In mathematical biology these types of pattern mechanisms are commonly called Turing mechanisms.
Due to the capability to explain pattern formation processes in general, Turing mechanisms provide a wide application in the theoretical investigation of cell polarity. From a biological point of view these systems are based in their core on the following assumptions: There is a slow diffusing activator, a fast diffusing inhibitor, and nonlinear reaction functions that couple activator and inhibitor. [1, 2, 24, 25]. In the simplest conceivable case, Turing patterns can occur in systems of the form

$$\begin{aligned} \partial_t a &= D_a \partial_x^2 a + f(a,b) \quad \text{on } \mathbb{R}_+ \times (0,1), \\ \partial_t b &= D_b \partial_x^2 b + g(a,b) \quad \text{on } \mathbb{R}_+ \times (0,1), \end{aligned}$$

together with homogenous Neumann boundary conditions, where $a(t,x)$ and $b(t,x)$ are the concentration of the activator and the inhibitor, respectively. D_a and D_b are the diffusion coefficients of the activator ant the inhibitor, respectively. Necessary conditions for Turing pattern formation are that the system above is linearly unstable at steady state and that the spatially homogenous system

$$\begin{aligned}\partial_t a &= f(a,b),\\ \partial_t b &= g(a,b),\end{aligned}$$

is linearly stable at steady state. If the steady state is perturbed, patterns can evolve due to occurring bifurcations.
Turing models are well-suited for modelling polarity in eukaryotic cell types lacking of the ability to repolarize, like e.g. budding yeast. This is due to the fact that Turing processes tend to *freeze* after the pattern is formed [7].

2) LEGI mechanisms Another approach to explain how cell polarity is provided by local-excitation-global-inhibition (LEGI) models [26–28]. Therein a spatially static activator is coupled to a fast diffusing inhibitor, both activated in direct proportion to the external stimulus, which together regulate a downstream response element. The simplest conceivable LEGI-mechanism is represented by the set of equations

$$\begin{aligned}\partial_t a &= k_a S(t,x) - k_{-a} a && \text{on } \mathbb{R}_+ \times (0,1),\\ \partial_t b &= D\ \partial_x^2 b + k_b S(t,x) - k_{-b} b && \text{on } \mathbb{R}_+ \times (0,1),\\ \partial_t r &= k_r A(r_T - r) - k_{-r} b r && \text{on } \mathbb{R}_+ \times (0,1),\end{aligned}$$

with homogenous Neumann boundary conditions for $a(t,x)$ and initial conditions representing the steady state. Here $a(t,x)$ denotes the concentration of the activator, $b(t,x)$ denotes the concentration of the inhibitor, $r(t,x)$ is the concentration of the response element, and $S(t,x)$ is concentration profile for the external stimulus. D is the diffusion coefficient of the inhibitor, r_T is a constant that denotes the total amount of the response element, and the letters k denote kinetic rates.
For appropriate choices of the constants and assumptions on $S(t,x)$, this system is capable of generating patterns with respect to the response element r, see [28]. In particular, LEGI accounts to certain features experimentally observed in some cell types like e.g. in Dictyostelium discoideum: LEGI captures an increasing response to stronger gradients, and the reversal of polarity if the gradient is reversed [7].

3) Wave-based models A relatively new approach to model cell polarity is to consider polarization as a consequence of a wave-based process. Wave-based models are designed to overcome a crucial issue of the formerly described model types: Both, Turing based polarity models and LEGI models require an inhibitor, but in cell types having

a Rho GTPase driven polarization process a chemical inhibitor has not been experimentally verified yet [7].

Various wave-based concepts have been suggested [29–32]. A prominent representative of this class are reaction-diffusion systems that exhibit a phenomena commonly referred to as *wave-pinning* [8, 33]. In these models a travelling wave is initiated at one end of a finite, homogenous 1D domain. The triggered wave travels across the domain while its speed simultaneously decreases. The wave-speed decelerates and the wave-front is eventually stopped inside the domain. The initially homogenous concentration profile (representative of a resting cell) develops into a an asymmetric stationary front profile (typical of a polarized cell).

The key characteristics of the wave-pinning mechanism can be highlighted by a special *shadow system*, which consists of a reaction-diffusion equation on $\mathbb{R}_+ \times [0,1]$ coupled to an integral equation having the form

$$\begin{aligned} \varepsilon \partial_t u - \varepsilon^2 \Delta u &= f(u,v), \\ v &= K - \int_0^1 u \, dx, \end{aligned} \tag{1.1}$$

with boundary conditions

$$\partial_x u = 0, \quad x = 0, 1. \tag{1.2}$$

K is a positive constant. The scaling-parameter ε is thought to be very small ($\varepsilon << 1$), and the right-hand side $f(u,v)$ satisfies the following properties:

1) *Bistability.* The dynamical system $\mathrm{d}_t u = f(u,v)$ has to be bistable for fixed v in some parameter range $v_{\min} \leq v \leq v_{\max}$. The stable points are $u_-(v) < u_+(v)$.
2) *Spatial stability.* The homogenous states $(u_\pm(v), v)$, $v_{\min} \leq v \leq v_{\max}$, are stable states of system (1.1).
3) *Maxwell condition.* There is a value $v_c \in [v_{\min}, v_{\max}]$ for which the integral

$$I(v) = \int_{u_-(v)}^{u_+(v)} f(u,v) \, du$$

vanishes.

We briefly explain the model's ability of wave-pattern generation. For a slightly different access to wave-pinning, but an almost identical and a more detailed asymptotic analysis, we refer to [33].

Consider the case where (1.1) is perturbed by the initial condition

$$u^0(x) = \begin{cases} u_+(v), & 0 \leq x < \phi^0, \\ u_-(v), & \phi^0 < x \leq 1, \end{cases}$$

where ϕ^0 is an element of $(0,1)$.
By using matched asymptotic analysis can be explained that the a wavefront-like solution is generated and the location of the front is pinned within finite time. Let $\phi(t)$ a position in the interval (0,1) at time $t > 0$ such that $\phi(0) = \phi^0$. Assume that the solution of (1.1) is analytical with respect to ε in each subdomain $(0, \phi(t) - \varepsilon)$, $(\phi(t) - \varepsilon, \phi(t) + \varepsilon)$, $(\phi(t) + \varepsilon, 1)$ of $(0,1)$.
Expanding $u = u_0 + \varepsilon u_1 + ...$ and likewise for v, substituting the expansions into (1.1), (1.2), and retaining leading order terms yield the outer solution:

$$u_0(t,x) = \begin{cases} u_+(v_0), & 0 \le x < \phi(t) - \varepsilon, \\ u_-(v_0), & \phi(t) + \varepsilon < x \le 1. \end{cases}$$

For the condsideration of the inner on $(\phi(t) - \varepsilon, \phi(t) + \varepsilon)$, a stretched coordinate $\zeta = (x - \phi(t))/\varepsilon$ is introduced. The inner solution is denoted by U, where

$$U(\zeta, t) = u(t, (x - \phi(t))/\varepsilon)$$

and $\zeta \in (-\infty, \infty)$. Expansion of $U = U_0 + \varepsilon U_1 + ...$ and likewise for ϕ, and substitution into (1.1) leads in the leading order to the equation

$$\partial_\zeta^2 U_0 - d_t\phi_0 \partial_\zeta U_0 + f(U_0, v_0) = 0, \tag{1.3}$$

Inner and outer solution of u_0 match, if the solution of (5.27) adopts the limits

$$\lim_{\zeta \to -\infty} U_0(\zeta) = u_+(v_0), \quad \lim_{\zeta \to \infty} U_0(\zeta) = u_-(v_0).$$

Since v_0 is spatially constant, can be shown that a heteroclinic solution $U_0^\phi(\zeta, v_0)$, unique up to translation, exists. The profile of the solution is a travelling wave-front, having the wave speed

$$c(v_0) = \left(\int_{-\infty}^{\infty} (\partial_\zeta U_0^\phi(\zeta, v_0))^2 \, d\zeta \right)^{-1} \int_{u_-(v_0)}^{u_+(v_0)} f(s, v_0) \, ds.$$

It can be shown that the speed $c(v_0)$ and the rate of change $d_t v_0$ have opposite signs. As long as $c(v_0)$ is positive depletes v_0, until requirement 3) engages and the wave pins. To the leading order, the result is a pattern with a plateau near $u_+(v_0)$ in the front of $[0,1]$ and a flat part near $u_-(v_0)$ in the rear, mutually segregated by a sharp transition zone.
Mathematical models for cell polarization relying on wave-pinning are commonly build on the experimental observation that Rho proteins cycle between an active and an inactive state, and that Rho is not resynthesized during the polarization process [8]. In

a one dimensional domain Rho activation is modelled by the system

$$\partial_t u - D_u \Delta u = f(u, v),$$
$$\partial_t v - D_v \Delta v = -f(u, v),$$

with zero flux boundary conditions, where u (resp. v) is the concentration of active Rho (resp. inactive Rho).
In these models is supposed that the diffusion of inactive Rho is very fast. In the limit $D_v \to \infty$, the system above formally reduces to (1.1). Thus, the concentration of inactive Rho becomes effectively a global variable, enabling the cell to communicate with its back while changes of Rho activity occur at the front.

Model issues The presented models consider Rho based polarization as a purely bio-chemical phenomenon. More in particular, Turing-based-, LEGI- and wave-pinning-models are based on the assumption that chemical polarization *precedes* the mechanical response of the cell and that mechanical cell responses have no upstream effect on the biochemical polarization process.
However, recent experimental findings of the group of Weiner suggest that polarity due to Rac activation in neutrophils is affected by mechanical effects [11]. There is evidence that membrane tension confines active Rac proteins to the leading , and that a sufficient decrease in membrane tension leads to an expiration of the activated Rac pattern.
Moreover, it has been shown theoretically and experimentally that in highly elongated but still polarized neutrophils biochemical signalling cannot be responsible for polarity patterns exclusively, since diffusive processes are too slow to serve as viable long-range signal transmitters. Consequently, the demanded diffusion in the models is unrealistically high [11].

1.2 A mechanochemical model for cell polarization

In this thesis a model is presented that gives an account how biochemical and mechanical signalling could interact as a self-stabilizing process in order to generate robust polarization in neutrophils. Although other proteins and lipids are involved in the polarization of neutrophils [34] and several mutual crosstalk circuits have been identified [35], we assume that only two types of Rho GTPases, namely Rac and RhoA, are decisive for the control of downstream effectors for actomyosin dynamics.
Based on previous studies [8, 33], we model the Rho GTPase dynamics via reaction-diffusion equations which include certain characteristics, that give them the ability of *wave-pinning*. Wave-pinning systems are well suited to explain the mechanism of Rho GTPase patterning in neutrophil polarization. As mentioned above, their mode of action relies on a unrealistically fast diffusing inactive form and a slow diffusing active form of the considered Rho GTPases. A possible aspirant to replace the fast diffusion form and

to serve as a long-range signal transmitter for Rac is membrane tension, since tethering experiments on neutrophils revealed that an an increase in membrane tension confines Rac activity [11].
To take these phenomena into consideration, we incorporate membrane tension and its generation due to dynamics of the actomyosin cortex (AMC) in our model to the Rho GTPase circuit. The modelled kinetics of each considered Rho GTPase loosely relates to [8]. Therein, GTPase activation relies on exchange of GDP by GTP, inactivation on hydrolysis and dephosphorylation of GTP to GDP. Both processes are intrinsically very slow and need the catalyzation by a GEF (guanine exchange factor) and GAP protein (GTPase activating protein), respectively. As in [36] we assume that the effect of GEF activity leads to an autocatalytic feedback of Rho activation while the GAP controlled inactivation rate is assumed to be constant, provided both, GAP and GEF, are present in sufficiently high amounts. Moreover, we hypothesize that increases in membrane tension globally lower the Rac activation rate and promote RhoA activation. A mutual inhibitive feedback-loop between Rac and RhoA has been identified [35]. Taking this into consideration, we explicitly model that Rac inhibits RhoA activation by affecting the RhoA deactivation rate.
In order to describe AMC mechanics as simply as possible, we resort to an extension of former models [37, 38] describing the cortex as a mechanochemical sol-gel complex: Eliding the role of myosin filaments, filamentous actin (F-actin) is treated as an active gel with viscous properties, while globular actin (G-actin) is regarded as a solute. Active Rac mediates downstream effectors promoting G-actin to polymerize to F-actin. F-actin treadmilling occurs at the front if a critical F-actin concentration is exceeded. We act on the simplifying assumption that RhoA mediates myosin II cross linking and conformational changes directly. Thus, in the model, myosin II induced AMC contraction is directly controlled by active RhoA. Both in combination, F-actin treadmilling and myosin II contraction, exert mechanical force that increases membrane tension. This increase, in turn, suppresses Rac activation and promotes RhoA activation. In addition to forces emanating from AMC dynamics, we assume that both, tension and curvature related force act on the cell periphery. See Figure 1.1 for the model outline.

1.2.1 Goals of this thesis

The goal of this thesis is to present a minimal model explaining polarization as the result of the interplay of the functional key units Rho GTPase activity, membrane tension, and AMC mechanics capturing the following qualitative key features of neutrophil polarization [7]:

1) *Spatial amplification.* Neutrophils are able to sense both, steep and shallow external gradients (where the difference between front and back receptor concentration is as small as 1%-2%) within a vast range of concentrations. Polarization leads to an amplification of this asymmetry to some macroscopic level.

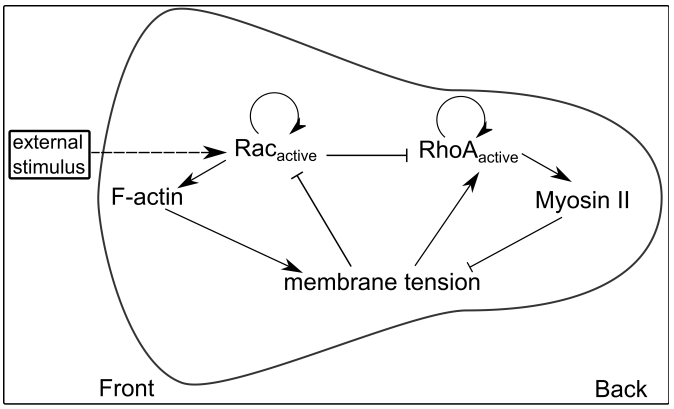

FIGURE 1.1: Model outline. An external stimulus triggers Rac activation. Rac activation promotes F-actin polymerization via downstream effectors. F-actin treadmilling globally increases membrane tension. Membrane tension inhibits Rac activation and promotes RhoA activation. RhoA a induces myosin contractions reducing membrane tension. Rac activation is affected by external stimuli. Accumulation of active Rac determines the cell front. Active RhoA is located in the dorsal cell, since Rac is supposed to suppress RhoA.

2) *Maintenance.* In neutrophils, polarity is maintained after the triggering stimulus is removed.

3) *Re-excitability.* Polarized neutrophils remain sensitive to new stimuli, and can reorient when the stimulus gradient is changed [17] .

4) *Resolving conflicts.* In response to multiple stimuli (such as two sources of chemoattractant), neutrophils form multiple "fronts" in certain situations, and rapidly resolve the conflict with a *unique axis of polarity.*

5) *Noise sensitiveness.* Neutrophils can spontaneously polarize, that is, they establish an axis of asymmetry in the absence of spatial cues.

In the model morphological changes of the AMC and Rho pattern formation affect each other. With respect to this, the goal is to validate if the model is capable of a realistic rendering of the cell shape and the location of Rho patterns under various circumstances. As biological reasonable, we consider the following features:

6) In response to a single chemical stimulus neutrophils develop a region of increased Rac activity that defines the front of the cell. Directional cell movement is generated along the front-back axis with constant speed [39].

7) Migrating neutrophils develop a "V"-shape with a broad front and a tapered rear [40].

8) Neutrophils adopt a dumbell-like shape if two spatially opposite stimuli are applied [11].

9) If the cell depolarizes, a spherical resting state is adopted [40].

The proposed mechanism is designed to provide the characteristics of formerly introduced wave-pinning mechanisms without relying on an unrealistically fast diffusive control substance, but on biologically reasonable mechanical long-range signal transmission. Similar to other pattern mechanisms, a rigorous representation of the underlying pattering mechanism of the model is due to its complexity difficult to achieve. However, one goal of this thesis is to provide at least an heuristic account for the model-based generation of Rho patterns.

1.2.2 Results

We demonstrate numerically that the model captures item 1) quite well within an accurate range between steep and shallow gradients; 2) very well: due to the bistable behavior, the polarized cell does not change the axis of polarity in response to weak, new applied stimuli, but changes its polarity as soon as the stimulus is sufficiently strong. The model exhibits feature 3) in response to a broad variety of different stimuli. In particular, repolarization in response to spatially fixed stimuli is captured well by the model. However, the model does not exhibit reorientation properly, when the applied stimulus varies in space. The model captures feature 4) only to a certain extent. If the distance of the multiple fronts is sufficiently high, the model is capable to erase all but one fronts. If the multiple fronts are closely neighboured, the model is not capable to generate a single polarity front. 5) A minor limitation of the model is that it is not noise sensitive. We numerically validate: 6) The polarized model cell adopts a constant migration speed and evolves in a morphological steady state. 7) The interplay of the considered units in the model generates a morphology that is similar to the "V"-shape of migrating neutrophils. 8) If two spatially opposite stimuli are applied, the cell adopts a dumbell-like shape. Thereby two possible scenarios occur. Either one Rac activity front erases while the other persists and the cell develops one single axis of polarity and adopts a V"-shape or both Rac activity fronts erase and the cell readopts a spherical resting state (9). The model cell has the ability to depolarize and to readopt a spherical resting state if membrane tension is artificially increased. This is in accordance to suction experiments where neutrophils with a polarized front depolarize if the cell body is highly elongated [11].

Apart from the aforementioned goals the model exhibits a further feature: Some cell types exhibit adaptation in a uniform stimulus, that is, the cells generate a persistent response to a gradient of chemoattractant, but transient response to a temporal change in a uniform stimulus [7]. To a certain extent the model captures this feature: The model cell swells in response to a uniform stimulus and shrinks if the stimulus is removed.

Finally, the provided explanation of the patterning mechanism does not serve as a rigorous proof. However, the explanation conveys insights of the necessary characteristics that endow to model to capability to generate patterns. We consider the explanation as a suitable starting point for a more sophisticated analysis of the patterning mechanism.

Scientific contribution of the model In general, the interplay between cell mechanics and chemical signalling in the cell polarization process is a current state of research and of great scientific interest, experimentally as well as theoretically [22, 41–43]. The presented approach in this thesis contributes to the rising demand of models that provide a coupling of mechanical and chemical signal transduction [22].
The presented model exhibits novelties that differ form the aforementioned biochemical models and is capable to generate patterns that do not rely on long-range diffusion. The model considers the mechanochemical interplay of the functional units regarded as necessary for cell polarization and cell movement in a two dimensional spacial setting. Therefore the model does not only provide an account for Rho-based cell polarization, but gives also an account how cell mechanics may affect polarity characteristics.
The model is not restricted to particular choices of the functions chosen in this thesis, but rather consists of basic units whose modelling requires certain qualitative characteristics. Thus, our approach provides a suitable framework for more complex models aiming at mechanochemical cell polarization.

1.3 Thesis outline

In **Chapter** 2 a brief survey of the biological background of cell polarity and motility is displayed. We confine ourself to describe the basal composition of the actomyosin cytoskeleton, its role in cell motility, Rho GTPase signalling and its effect on the actomyosin cytoskeleton.
In **Chapter** 3 the mathematical model is derived. As a starting point, we consider in **Section** 3.2 a three-dimensional spacial setting for the model geometry that consist of a bulk region and two subjacent thin layers. The bulk region refers to the cytosol, the two layers refer to the AMC and the plasma membrane, respectively. Under the assumption that the model equations exhibit certain scaling properties, it is shown that the spatially three-dimensional model can be approximated by an essentially spatially two-dimensional model. In **Section** 3.4 a characterization of the domain is presented if the domain has do be determined by a free boundary problem. **Section** 3.4 is devoted to model the biochemistry of Rho GTPase activation and actin dynamics. The mechanical features of the model are derived in **Section** 3.5. Mechanical modelling of the AMC is loosely based on active gel theory. A brief survey about the theory is presented in **Appendix** B. In **Section** 3.6 the obtained model equations are listed. **Section** 3.7 is devoted to a brief assessment of the model assumptions with respect to biological relevance.
In **Chapter** 4 the simulation results of the model are presented. The considered parameters are presented and briefly discussed in **Section** 4.2. The response of the model cell to both, transient and persistent stimuli is simulated. Moreover, we test whether the model cell exhibits certain qualitative features as the ability to repolarize if the stimulus relocates and the behavior of the model cell in response to different stimuli, as well as

the ability to form multiple fronts. In **Section** 4.5 we demonstrate how the simulation results are affected by parameter variations. In **Section** 4.6 the most important simulation results are summarized and are compared to biological data. Finally we draw a conclusion to what extent the model is capable to exhibit the demanded features listed in Section 1.2.1. In **Appendix** C.1 a brief survey of the numerical implementation of the model system is presented.

In **Chapter** 5 a phenomenological explanation of the patterning mechanism is presented. A one-dimensional toy-model related to the original model is suggested for which we formulate necessary conditions that may endow the model with the ability of wave-pinning. The explanation is based on arguments provided by matched asymptotic analysis. It is a priori not evident if the one-dimensional possesses a solution. In **Appendix** D we proof that under certain conditions a solution for sufficiently small times exists.

In **Chapter** 6 we summarize the model and the obtained main results. We assess in how far the model accounts to a reasonable approach for neutrophil polarization and point out the most considerable limitations of the model. In the outlook, we briefly discuss experimental tests that can be used to verify the model predictions and highlight possible extension of the model.

Chapter 2

Biological Background

The ability to migrate in response to external signals is an important feature of many eukaryotic cells. Cell motility is necessary for foraging of single celled organisms and is needed for immune response, wound healing and carcinogenesis in multi-celled organisms. The social amoeba *Dictyostelium discoideum* migrates under starvation conditions, relaying signals to one another to form aggregates. Immune system cells, such as neutrophils and macrophages chase after peptide gradients produced by bacteria. In wound healing, Fibroblasts migrate in response to epidermal growth factors to the wound side to remodel connective tissues. Cancerous cells develop the ability to scatter in response to growth factors and invade surrounding tissue. Understanding the mechanisms that enable the cell to sense external signals and directional migrate towards them is of a great interest in cell biology. In this chapter a brief summary of the cellular actors that contribute to cell motility is presented.

2.1 Actin-based cell motility

Under laboratory conditions, cell motility is usually studied on a flat substratum. Due to the spatial assembly of the actomyosin cytoskeleton (AMC), migrating cells on a flat substrate build a bulge. The bulge is called *pseudopod* ('false foot'). Movement is generated by alternating extensions of the pseudopod and retraction of the cell body. Consequently, pseudopodia are usually located at the front of the cell.
Pseudopodia are classified into several varieties (*lobopodia, filopodia, lamellipodia, reticulopodia, and axopodia*), according to their optical appearance [44]. Neutrophils, in particular, build a *lamellipodium* [45], a broad membrane protrusion, filled with a dense, branched network of actin filaments. In migrating cells, the lamellipodium is propelled forward due to *treadmilling*, i.e. a constant turnover of actin filament in which new filament polymerizes at the leading front. This endows the lamellipodium with a polarity, since in the mean the actin filaments align towards the direction of movement. The

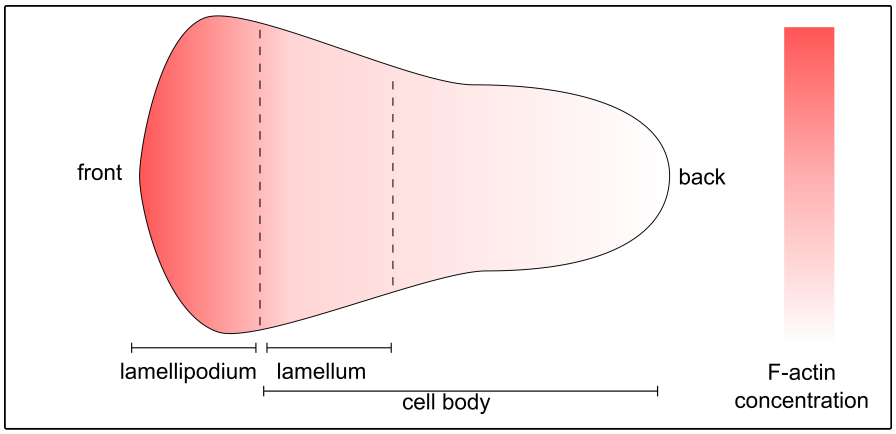

FIGURE 2.1: Typical shape of a migrating neutrophil on a flat substrate from the top view. The cell migrates to the left. The lamellipodium is located at the left hand side. The concentration of actin filament (F-actin) decreases from the left to the right.

lamellipodium is flat (on the order of $10^{-1}\mu$m) compared to the diameter of the cell (on the order of $10^{0} - 10^{1}\mu$m) [46].

A further functional unit of the AMC is the *lamellum*. The lamellum is located in the cell body and is attached to the posterior of the lamellipodium via actin filament. The lamellum also consists of actin filaments, but lacks of a significant polarity of filament alignment since the filament network is more interlaced arranged. Actin filaments in the lamellum do not treadmill. However, in the lamellum *myosin motor proteins* bind to the filament network and exert under energy consumption provided by ATP a contractile force. The contractile force induces the tailing of the posterior cell edge.

In the presence of adhesion sites between the cell and the substrate, the interplay of the continuous extension of the lamellipodium and the retraction of the cell body due to myosin activity generates directional movement. The reorganization of the AMC that generates movement also induces a morphological change of the cell shape. Resting neutrophils have a spherical resting state. In the initiation of movement the shape changes to a broad flat arc at the leading front and tapered cell body [47]. See Figure 2.1 for an illustrated top view on a migrating neutrophil.

In the next sections we will discuss the molecular structures and processes of the AMC more in detail and highlight to role of Rho GTPases activity in the orchestration cell motility.

2.1.1 The actomyosin cytoskeleton

Eukaryotic cells contain a cytoskeleton. The cytoskeleton can be subdivided into different structures. In eukaryotic cells the cytoskeleton consists mainly of three different types of filaments: *microtubules*, *intermediate filaments*, and *actin filaments*. Each of these types carries different functions. Microtubules primary serve as a transport medium of organelles. Intermediate filaments act as scaffold in order to stabilize the cell shape and to connect multiple cells among each other. The network consisting primary

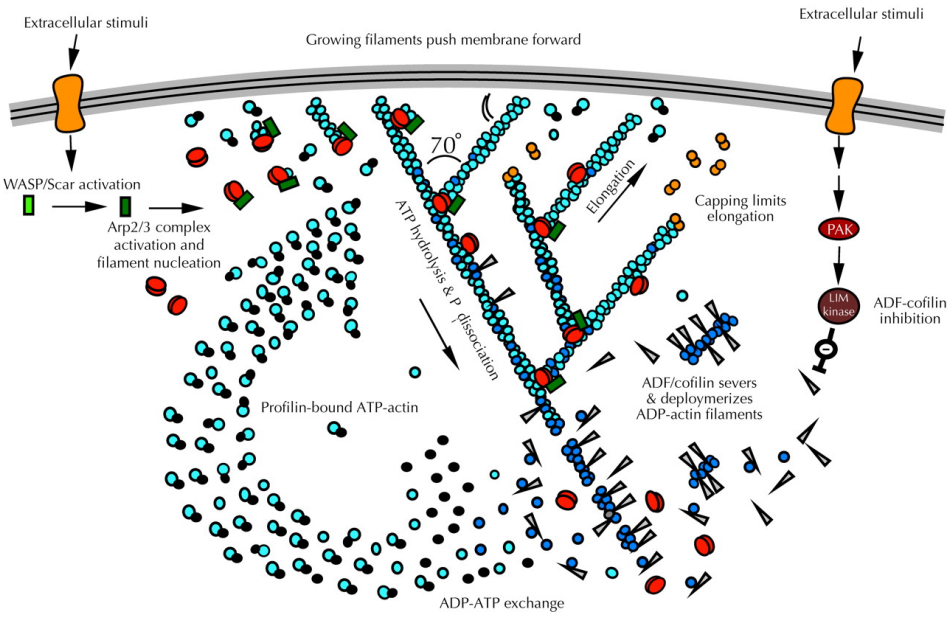

FIGURE 2.2: Standard model for F-actin assembly and disassembly in the lamellipodium. Due to an external stimulus, activated Rho (not shown) recruits downstream effectors like the WASP/Scar and the Arp2/3 complex that promote under ATP consumption actin polymerization and branching. The scheme is taken from [48].

of actin filaments is called actomyosin cytoskeleton (AMC). The AMC is a highly dynamic structure that is involved in the determination of the cell morphology and is one of the key players in the locomotion machinery [49]. Thus, an analysis of the interplay between cell polarity and cell migration requires a deeper understanding of the AMC.
On a molecular level, the AMC predominantly consists of actin monomers (G-actin), actin filaments (F-actin) and myosin proteins. G-actin is a globular protein with the ability to polymerize to F-actin. F-actin builds a chain with a length of approximatively 375 amino acids and a weight of approximatively 42 kDa. Each filament consists of two proto-filaments winding around each other in a right-handed helical arrangement. Controlled by the activation of the protein families WASP/Scar/WAVE and PAK G-actin assembles to F-actin over three sequent phases: 1) *nucleation*, 2) *elongation*, and 3) *treadmilling* [48] (see figure 2.2).
1) In the *nucletation* phase G-actin forms actin nuclei. The nuclei are complexes of three G-actin monomers. The nuclei predefine a polar structure of the filament. One end is called '(+)-end' and the other is the '(−)-end'. 2) The *elongation* phase is characterized through a rapid bonding of G-actin at the '(+)-end'. In order to maintain the polymerization process with a steady pool of actin filaments, G-actin dissociates from the '(−)-end'. Dissociation is mediated by cofilin, a protein which binds to F-actin at the (−)-end, unwinds the helical proto-filaments of F-actin and dissociates in a complex with G-actin from the filament. 3) The dissociation rate at the (−)-end is slower the binding rate at the (+)-end [50]. The result is a steady state of actin assembly, where a constant net flux of actin subunits throughout filament is conserved, even if the length of the filament is kept constant. This steady state is called *treadmilling*.

In motile cells extending a lamellipodium, the actin cytoskeleton assembles at the front with the (+)-ends pointing towards the plasma membrane at the leading front and the (−)-ends facing the cell body behind [50]. The force generated by the treadmilling process of F-actin is transmitted to the substrate (in vitro) or to the extracellular matrix (in vivo) via focal adhesions, respectively. Focal adhesions are linkings of F-actin and membrane based integrins, that are interconnected by forming complexes with vinculin, talin, and smaller proteins. Integrins are heterodimeric cell surface receptors. Moreover, integrins mediate adhesion of cells to the substrate, the extracellular matrix as well as to other cells. The cytosolic domain of an integrin is linked to the actin filaments of the AMC [51].
A further characteristic of the AMC dynamic is filament *branching*. The Arp2/3 complex, a protein family consisting of Arp2, Arp3 and five smaller proteins is a downstream effector of Scar/WAVE that binds to sides of F-actin and nucleates to an assembly of new filament branches [20]. Subsequent elongation of the branches forms a Y-shaped structure with an angle of approximately 70°. The physical advantage of this Y-shaped structure is the increased bending rigidity of a branched interconnected network in comparison to a parallel alignment of the filaments [52]. This characteristic is also supported by the proteins α-actinin and filamin. These proteins crosslink neighboring actin filaments and thus organize actin filaments into networks.
Aside from actin, myosin is the principal component of the AMC. Myosin is a subclass of an enzyme family that catalyze hydrolysis of ATP, the so called ATPases. Myosin has a F-actin binding affinity and the ability to move along the filaments. In particular, myosin II, a member of the myosin family predominantly found in the cytoskeleton, consists of a head domain (also called *heavy chain*) and a tail region (also called *light chain*). Myosin II proteins form small aggregates (*mini filaments*) by binding to each others tail region. The head domain of myosin II binds to F-actin. Thus a mini filament can crosslink several actin filaments [53]. The head domain performs conformational changes due to energy consumption provided by ATP hydrolysis. Thereby, the head domain folds around approximately 40° relative to the tail region. In this way myosin II aggregates bound to the filament exert a contractile force to the network [23].
Myosin II induced ACM contractions take predominately place at lamellum. Compared to the AMC located in the lamellipodium, the lamellum does not have the structure of a branched network, but rather forms arc-like bundles oriented parallel to cell edge. These bundles and focal adhesions form aggregates. When myosin II binds to F-actin and undergo a change in conformation, contractile force is exerted to the underlying substrate [45].

2.1.2 Ameobid motion

Cell migration on a flat substrate is commonly explained by the *contraction-protrusion* model. Therein, the cooperation of F-actin treadmilling, myosin motor activity, and the

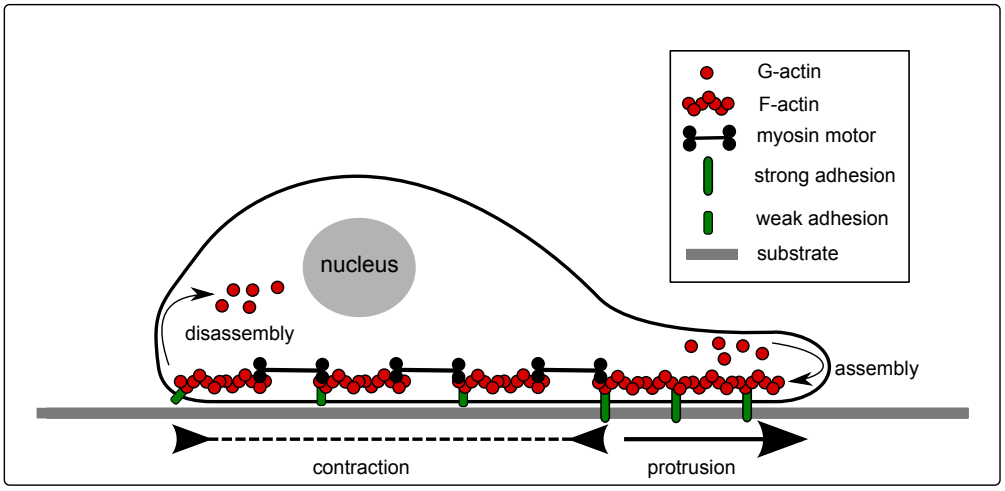

FIGURE 2.3: Schematic representation of the mechanism generating cell locomotion. Due to the strong adhesion at the cell front, F-actin treadmilling generates a protrusive force that propels the leading cell edge forward. Myosin II motor aggregates, predominantly located at rear end of the lamellipodium, exert contractile stress to the filamentous network. Since the adhesion to the substrate at the back of the cell is low compared to the front, the contractile force induces the retraction of the posterior.

linkage of adhesion sites to the network are responsible to generate an ameboid motion of the cell [45, 54].

At the lamellipodium, where the F-actin concentration of a moving cell is high compared to the rest of the cell also the adhesion to the substrate is strong. The F-actin network is anchored to the substrate via adhesions sites. In consequence, the fixation of filament at the front enables the treadmilling process to generate a protrusive force propelling the leading cell edge forward. In addition to the protrusion mechanism at the front, a contractile stress is exerted along the filaments due to myosin motor activity. The posterior of the cell does not resist the emanating contractile stress since the adhesion sites are predominantly located at cell front and myosin motors mostly aggregate at the rear end of the lamellipodium. Thus, the exerted contractile stress promotes the retraction of the posterior. In combination, protrusion at the leading edge and retraction at the back results in directional movement of the cell (see Figure 2.3) [45].

Although the strong adhesion at the leading front prevents the retraction of the cell front, the anterior of the F-actin network is not completely unaffected by myosin mediated contraction: A retrograde flow of F-actin induced by myosin contractions has been observed in experimental studies [55]. The net flux of the AMC is oppositely directed to the direction of motion of the cell. A possible role of this retrograde material flow is that it clears the space between the network and the cell membrane and thus facilitate the binding of G-actin at the tip of the filament located at the leading front. This would promote the maintenance of filament treadmilling [55, 56].

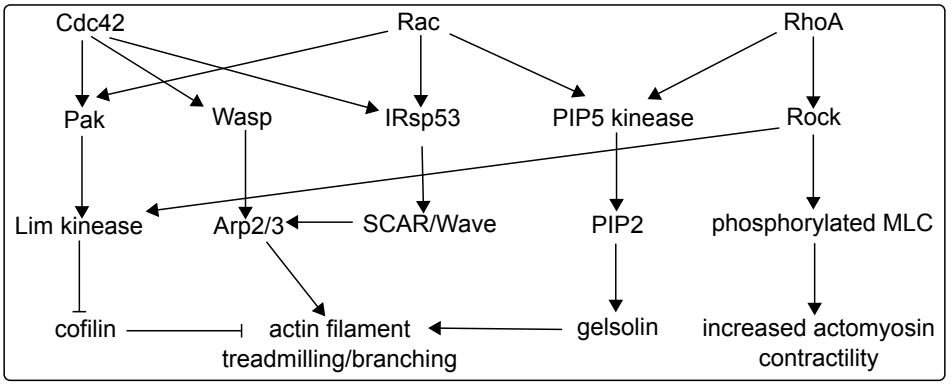

FIGURE 2.4: Downstream effectors of Cdc42, Rac, and Rho. Effectors that have functions unrelated to the cytoskeleton are not shown. The scheme is a modified version of the scheme presented in [57].

2.2 Regulation of cell motility: Rho GTPases

Rho GTPases are members of the GTP-binding proteins (G-proteins) superfamily, which are conserved across a broad range of eukaryotic cells [16, 17]. G-proteins are an important class of cell messengers containing a GTP-binding domain that function as molecular switches. Rho GTPases have a molar mass of 20-40kDa.

Rho GTPases relay external stimuli to the AMC and thus provide a coupling link between external stimuli and the interior of the cell. Rho proteins do not directly interact with the AMC, but bind to downstream effectors, which regulate the AMC [58, 59]. Common to the diverse families of GTPase is the cycling between an *active state* and an *inactive state*. Rho GTPases must be bound to GTP in order to become activated: GTP-bound Rho proteins undergo a conformational change such that they can interact with downstream effectors.

Besides the activation-inactivation cycle there is also a spatial cycle: in the cytosol almost all Rho GTPase is inactive whereas the active state is only present at the membrane.

The most prominent and best studied subclasses of Rho GTPases are Cdc42, Rac, and RhoA [13]. In motile cells Rac and Cdc42 affect F-actin polarization and F-actin alignment in the AMC: Active forms of Rac and Cdc42 stimulate via the Scar/WAVE complex Arp2/3 activation [13]. Arp2/3, in turn, stimulates actin polymerization. Moreover, the active forms of Rac and Cdc42 trigger PAK and LIM to interact with the AMC [13]. These proteins contribute to the branching of the actin network [48].

Active RhoA targets at the myosin-filament interaction. Active RhoA induces the phosphorylation of the light chain of myosin (MLC) via its downstream target ROCK. Phosphorylated MLC promotes myosin motor linkage to the actin network and so produces contractile actomyosin bundles [60]. See Figure 2.4 for details of the Rho GTPase mediated regulation of the cytoskeleton. However, it should be mentioned that the signal transduction is even more complex than displayed. The listed activation and inhibition

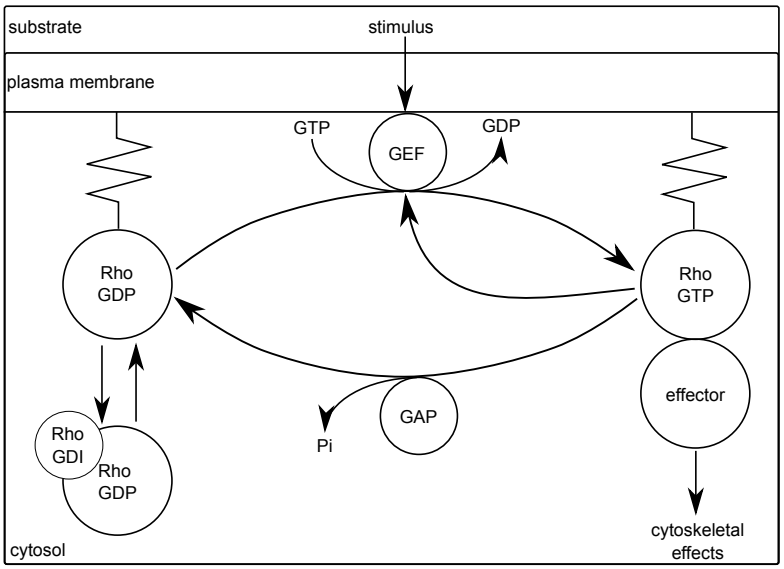

FIGURE 2.5: A schematic diagram of the activation and membrane translocation cycles of a Rho family GTPase. Active Rho is bound to GTP-bound. Inactive Rho is bound to GDP. Translocation of Rho from the membrane into the cytosol is induced by the binding of Rho to GDI. Dephosphorylation from the GDP-bound to the GDP-bound form is facilitated by GEF. Phosphorylation of GTP to GDP is facilitated by GAP. Rho-GDP forms a complex with Rho GDI and detaches from the membrane.

pathways can change their role under certain circumstances and mechanical upstreams of the AMC have been observed [43, 61].

Rho activation. Throughout the Rho GTPase subclasses Rac, Cdc42, and RhoA several key-properties are shared.

Rho GTPases can form complexes with GTP (Guanine-tri-phosphate) and GDP (Guanine-di-phosphate). Rho GTPases act as cell internal messengers. Their cycling between a GTP- bound and a GDP-bound state has the role of a *molecular switch*: GTP-bound Rho is the active and GDP-bound Rho is the inactive state.

Each Rho GTPase cycles between a GTP- and a GDP-bound state. Interconversion between these states is due to hydrolysis followed by dephosphorylation of GTP to GDP or the exchange of GDP by GTP, respectively. Being intrinsically slow processes, GDP-to-GTP-exchange is catalyzed by GEF (guanine exchange factor) and dephosphorylation is catalyzed by GAP (GTPase activating protein) [62, 63]. GTP-bound Rho is known to recruit GEF-effector complexes [64].

Moreover, GEF is regulated by an upstream signal. In response to chemical stimulation of integrins and receptor tryosine kineases located at the plasma membrane, GEF accumulates at the leading front of a motile cell [65]. In eukaryotic cells GEF outnumbers Rho protein by a threefold, such that multiple GEFs are capable to activate one single Rho protein [66].

The second regulator of Rho activity, GAP, affects the rate of phosphorylation of GTP to GDP. Phosphorylation of GTP to GDP leads to a conformational change of the Rho

protein, such that the protein GDI (GDP dissociation inhibitors) can bind to Rho-GDP complexes.
While GTP-bound Rho proteins are predominantly located at the cell membrane, GDP-bound can detach from the membrane: Membrane attached, GDP-bound Rho binds to GDI. GDI dissociates the complex from the membrane and prevents re-association [67]. Although it is less clear how Rho GTPase is decoupled from the complex with GDI and how it associates to the membrane again, mediation by a GDI displacement factor (GDF) as a possible mechanism has been proposed [68].
It is assumed that RHO proteins need to be both, membrane-based and bounded to GTP in order to interact with downstream effectors that affect the cytoskeleton. In the following we refer to membrane based, GTP-bound Rho-GTP as the *active* and to GDP-bound Rho as the *inactive* form.

Rho GTPase pattern formation. Eukaryotic cells have spatial gradient sensing (unlike bacteria, which use a temporal mechanism), that is, they can detect chemical concentration gradients [7]. In response to external chemical gradients (e.g. a ligand like cAMP) transmembrane receptors like integrins activate Rho GTPases. In motile cells Rac and Cdc42 are predominantly activated where the ligand concentration is the highest [69, 70]. In this way Rac and Cdc42 predefine the location and alignment of the lamellipodium. Active RhoA predominantly accumulates at the posterior, where it triggers myosin induced contractions promote the tailing of the back [71, 72].
From a general point of view is the directional redistribution of Rho proteins due to external signals a *symmetry break*: Formerly homogeneously distributed substances become more concentrated (or activated) in what will become the front of the cell, and others become more concentrated in what will become the back of the cell. With respect to Rho GTPases this symmetry break is called *cell polarization*. The interplay of the processes that generate the symmetry break is experimentally not easy to determine, although many contributors of the activation process are known. On a macroscopic level, various features of polarization are shared by many cell types [7]:

1) Cells are able to sense both steep and shallow external gradients (where the difference between front and back receptor concentration is as small as 1%–2%) within a vast range of concentrations. Polarization leads to an amplification of this asymmetry to some macroscopic level.

2) Polarized chemotactic cells remain sensitive to new stimuli, and can reorient when the stimulus gradient is changed.

3) In many types of cells, polarity is maintained after the triggering stimulus is removed (maintenance).

4) Some cells spontaneously polarize, that is, they establish an axis of asymmetry in the absence of spatial cues.

5) Some cell types exhibit adaptation in a uniform stimulus, that is, the cells generate a persistent response to a gradient of chemoattractant, but transient response to a temporal change in a uniform stimulus.

6) In response to multiple stimuli (such as two sources of chemoattractant), some cells form multiple fronts in certain situations, whereas others rapidly resolve the conflict with a unique axis of polarity.

7) In some cells, pseudopods are continually extended and retracted. Some of these types of cells reorient by splitting one pseudopod into two, one of which becomes dominant.

Budding yeast, *Saccharomyces cerevisiae*, exhibits features 3),4),6). The social amoeba *D. discoideum* exhibits features 1)-5), and 7). Mammalian neutrophils polarize and directionally migrate in response to N-formylated peptide gradients produced by bacteria. These cells exhibit features 1)– 4), 6). Some evidence suggests that in neutrophils feature 3) requires an intact AMC and plasma membrane. We will highlight this requirement in the next section. Successful mathematical modelling that provides possible qualitative characteristics of interacting contributors has to reflect some of these features.

2.3 The plasma membrane and membrane tension

In eukaryotic cells the plasma membrane confines the interior of the cell from the external environment. Although it prevents the cytosol from deliquescence into the external environment, the plasma membrane is far from being a passive participant. The plasma membrane regulates processes as endo- and exocytosis, and serves as a signalling link between the external and the internal of cell. As already displayed in Section 2.2 messenger proteins, lipids, integrins, and Rho GTPases are associated at the membrane.

Signal transduction via mechanical changes of the plasma membrane In recent years it has come clear that the plasma membrane does not solely communicate via biochemical pathways with the interior cell and the external environment. Also communication via mechanical signal transduction and, moreover, via mechanochemical interactions of the plasma membrane is crucial for the organization of eukaryotic cells [73]. Some evidence suggests that in neutrophils and fibroblasts changes of membrane tension contribute to cell motility and Rac signalling [11, 74].
For neutrophils in particular, it has been experimentally validated that membrane tension serves as a long-range deactivator for Rac [11]. The authors of [11] found that membrane tension doubles during leading-edge protrusion, and that this increase in tension is sufficient for long-range inhibition of actin assembly and Rac activation. Moreover, they reported that a decrease of membrane tension causes uniform actin assembly. In

consequence the authors suggest that tension, rather than diffusible molecules generated or sequestered at the leading front, is the dominant source of long-range Rac deactivation.
However, the molecular mechanisms by which cells sense and respond to mechanical signals are not fully understood yet. Several concepts of membrane tension induced chemical response have been proposed. Mechanosensitive channels in the plasma membrane, curvature sensing proteins, and actomyosin cortex associated proteins are possible aspirants for the missing link (see [43] for a review). We will reconsider these concepts more in detail in the discussion of this thesis.

Mechanical features of the plasma membrane From a theoretical viewpoint the plasma membrane is commonly described as a lipid bilayer in which proteins are thought to diffuse freely [75]. This lipid bilayer has low shear modulus of the magnitude 10^{-3}–$10^{-2}\mathrm{N/m}^2$, and a high elastic modulus of the magnitude $10^3\mathrm{N/m}^2$. The viscosity and the bending stiffness of the lipid bilayer vary in dependance of the membrane composition. The viscosity of membranes in vesicles has the magnitude 10^2–10^3Pa s, while the bending stiffness is of the order of 10^{-19} Nm (see [43] for a review).
In the literature membrane tension is not uniformly equal defined. However, most definitions have in common that the notion *membrane tension* is related to the required force in order to deform the membrane. A definition of membrane tension which is frequently used aims at the elastic properties of the membrane. This approach was initially used for the measurement of tension of lipid vesicles [76]. Presuming the membrane is an isotropic, two dimensional, flat medium with a linear elasticity, the membrane tension τ^* is defined to be proportional to the deviation of the cell surface area $A + \Delta A$ area from its value A at rest:

$$\tau^* = E\frac{A + \Delta A}{A},$$

where E is the elastic area stretch modulus and A is the surface area of the vesicle.
In eukaryotic cells the structure of the plasma membrane is more complex than in lipid vesicles. Eukaryotic cells contain an actomyosin cortex beneath the membrane. The cortex is a layer of actomyosin that runs parallel to the membrane at the cytosolic side. The cortex is attached to the plasma membrane via actomyosin adhesions [43]. Similar to the ACM, the actomyosin cortex is in constant turnover and influences the configuration of the membrane: The actomyosin cortex activity causes membrane ruffling and wrinkling. It has been argued that large changes in plasma membrane tension primarily reflect changes in actomyosin activity [77]. In experiments it is hard to distinct between the elastic portion of the plasma membrane and the force impact of the cortex [43]. Therefore in experimental settings the *apparent tension* τ is often measured. The apparent tension is based on the assumption that the membrane-cortex-complex behaves like an elastic material, such that τ can still be written to the linear order as

$$\tau = E_m\frac{A + \Delta A}{A},$$

where E_m is the apparent elastic area stretch modulus. The apparent elastic area stretch modulus varies from cell to cell and also depends on the properties of the cortex. The apparent stretch modulus is usually lower than the elastic modulus of the membrane itself since the cortex provides the membrane with wrinkles that unfold if the membrane is stretched.

Chapter 3

Mathematical Formulation of the Model

3.1 Cell geometry

Consider a cell adhering to a flat substrate. The AMC spreads along the horizontal plane, parallel to the substrate, like a thin sheet. The intermediate layer between the actin area and the substrate is the plasma membrane. The cross section of the superposed layers consist of the substrate itself, the plasma membrane, the AMC, and the cytosol, see Figure 3.1. We assume that these layers comprise the functional units of the cell that are sufficient for robust cell polarization.
The average diameter of a neutrophil on a surface is about $\sim 10\mu$m. The height of the cell is about $\sim 0.1 - 0.2\mu$m [46, 53]. We aim at a description of the AMC-cytosol-plasma-membrane compound as a two dimensional sheet embedded in the x_1-x_2-plane. Both, the AMC and the plasma membrane are highly heterogenous structures. We will assume that considered proteins may diffuse without restriction in the tangential direction of each layer, while the diffusion in the normal direction is constrained due to the heterogeneity of the plasma membrane and the AMC. In the cytosol, however, we

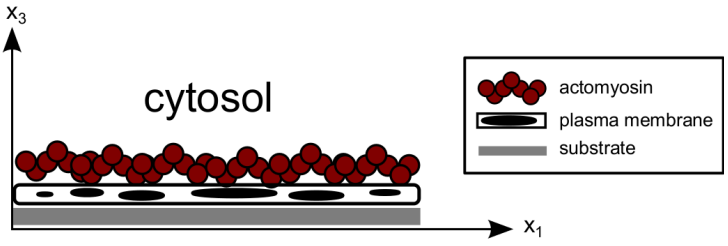

FIGURE 3.1: Schematic cross section of the contact layers between substrate and cell from a sideview. The top layer is the AMC. The intermediate layer represents the plasma membrane, where active form of Rho is located. The bottom layer stands for the substrate.

assume that the substance may diffuse freely in every direction. In each compartment chemical reactions may occur.
In the next section we will give an account for the assumptions that enable us to consider the plasma membrane and the AMC as effectively two dimensional sheets.

3.2 A boundary-layer approximation for a parabolic-elliptic system

In this section, we argue that we may reduce a spacial three dimensional problem on two thin heterogenous layers to an effectively two dimensional problem in space. Our model problem consists of a semi-linear reaction diffusion system defined in each layer with transmission conditions on the interfaces and a diffusion equation in a bulk domain. The heterogeneity of the layers induces a fast diffusion in the tangential direction but a slow diffusion in the normal direction of the interfaces. We assume that the thickness of each layer is of order ε and the diffusion in the normal direction towards the interfaces is of order ε^{1+2l}, $l > 1/2$.

3.2.1 Scaling properties of the system

For the lower-dimensional approximation we assume that the considered substances in the plasma membrane and in the AMC possess certain scaling properties whose biological reasonability will be discussed below.
In biochemistry, concentration is the abundance of a constituent with respect to the unit volume. As approximation, we seek a scaling property of the concentrations, such that the amounts of the substances are conserved if the height of the layer ε changes. Let n_U be the amount of a substance U contained in the unit volume $[0,1]^3$. The concentration of U is

$$u = \frac{n_U}{|[0,1]^3|}.$$

Let $[0,1]^2 \times [0,\varepsilon]$ be a reference volume of a layer having the height ε. If the amount of a substance is conserved, the concentration is

$$\overline{u} = \frac{n_U}{|[0,1]^2 \times [0,\varepsilon]|} = \frac{1}{\varepsilon}\frac{n_U}{|[0,1]^3|} = \frac{1}{\varepsilon}u.$$

In the following section we will consider concentrations having this scaling property. We model the actin and Rho-protein kinetics as reaction-diffusion systems.The considered reaction functions are of the form

$$f(u) \propto k_+(u_1)u_2 - k_-(u_3)u_4,$$

where $k_\pm(\cdot)$ are either Michaelis-Menten-type-functions of order two or constants. In the first case we have with respect to the unit volume

$$k_\pm(u_1) = \frac{u_1^2}{K^2 + u_1^2},$$

where the apparent dissociation constant K is derived from the law of mass action (the equilibrium constant for dissociation). Let u_1, w, and z be the concentrations of the protein U, the ligand L, and the product Z at homogenous steady state, respectively. From the law of mass action, the apparent dissociation constant K is an equilibrium constant, having the form:

$$K(u_1, w, z) = \frac{u_1 w^2}{z}.$$

Since we assumed that the amounts of the substances are conserved in $[0,1]^2 \times [0,\varepsilon]$, we obtain the scaling property

$$K(\overline{u}_1, \overline{w}, \overline{z}) = \frac{1}{\varepsilon} K(u_1, w, z),$$

where the bar $\bar{\cdot}$ denotes the concentration of the substance in $[0,1]^2 \times [0,\varepsilon]$. Consequently, the reaction functions have the scaling property

$$f(\overline{u}) = f\left(\frac{1}{\varepsilon}u\right) = \frac{1}{\varepsilon} f(u).$$

Both, the plasma membrane and the AMC are highly structured media. Rho proteins bind to the plasma membrane and the Rho-receptor-complex diffuses tangentially to the membrane. Since Rho proteins are relatively big, diffusion in the normal direction to the membrane is highly attenuated due to the composition of the membrane [78]. We assume that, depending on the height of the layer ε, the diffusion normally to the membrane is of the order ε^{l_1}, $l_1 > 0$, while the diffusion tangentially to the membrane remains independent of ε.

The AMC consists of a dense polymer network that aligns parallel to the plasma membrane. Diffusion in the normal direction may be constrained due to the density of the network. As in the plasma membrane, we assume that, depending on the height of the layer ε, the diffusion normally to the AMC is of the order ε^{l_2}, $l_2 > 0$. However, we assume that diffusion parallel to the network is unaffected by the thickness of the layer. In the following section, we present a reaction-diffusion system defined on three compartments with variable height on each domain and transmission conditions. The presented reaction-diffusion system has the assumed scaling properties. We will determine the scaling-powers l_1 and l_2, such that in the limit $\varepsilon \to 0$ fluxes between the compartments vanish and the occurring reaction-diffusion equations in the AMC and in the plasma membrane reduce to spatially two dimensional systems. The dimension of the solutions of the limit equations in the layer transforms from volume density to area density.

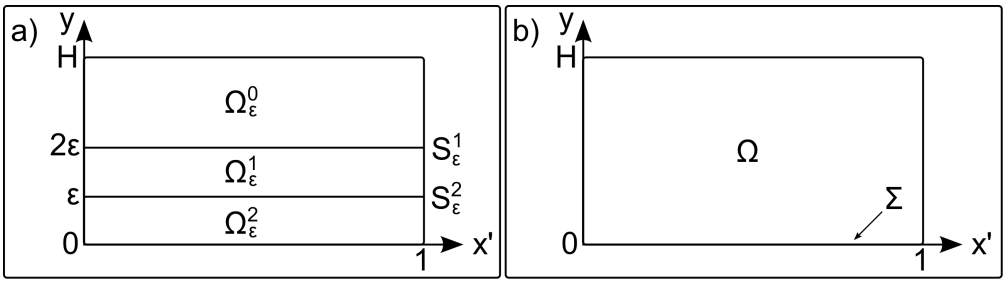

FIGURE 3.2: a) The domain Ω for $\varepsilon > 0$ including the thin layers Ω_ε^1 and Ω_ε^2. The bulk domain Ω_ε^0 represents the cytosol, the layer Ω_ε^1 represents the AMC, the layer Ω_ε^2 represents the cell membrane. b) The structure of the domain Ω in the limit $\varepsilon = 0$.

3.2.2 Setting of the problem

Let $\varepsilon > 0$ be a sequence of strictly positive numbers tending to zero, with the property $\frac{1}{\varepsilon} \in \mathbb{N}$. Let H be a fixed real number.

For each $\varepsilon > 0$, we consider the domain $\Omega = (0,1)^{n-1} \times (0,H) \subset \mathbb{R}^n$, $n \geq 2$, consisting of three subdomains: The *bulk region* Ω_ε^0 and the *thin heterogeneous layers* Ω_ε^1, Ω_ε^2. Ω_ε^0 and Ω_ε^1 are separated by the interface S_ε^1; Ω_ε^1 and Ω_ε^2 are separated by the interface S_ε^2; see Figure 3.2 **a**.

More precisely, we consider

$$\Omega = \Omega_\varepsilon^0 \cup \Omega_\varepsilon^1 \cup \Omega_\varepsilon^2 \cup S_\varepsilon^1 \cup S_\varepsilon^2,$$

where $\Omega_\varepsilon^0 = (0,1)^{n-1} \times (2\varepsilon, H)$, $\Omega_\varepsilon^1 = (0,1)^{n-1} \times (\varepsilon, 2\varepsilon)$, $\Omega_\varepsilon^2 = (0,1)^{n-1} \times (0,\varepsilon)$, $S_\varepsilon^1 = (0,1)^{n-1} \times \{2\varepsilon\}$, $S_\varepsilon^1 = (0,1)^{n-1} \times \{\varepsilon\}$. We denote

$$\Sigma = (0,1)^{n-1} \times \{0\}.$$

The outer unit normals at the boundaries of the domains Ω and Ω_ε^1 are denoted by ν and ν_1, respectively. If there is no likelihood of confusion, we will simply write ν instead of ν_1. For $x \in \Omega$, we set $x = (x', y)$, where $x' \in (0,1)^{n-1}$, $y \in (0,H)$, and we write for $u : \mathbb{R} \to \mathbb{R}$, $w : \mathbb{R}^n \to \mathbb{R}$

$$\nabla_{x'} u := (\partial_1 u, ..., \partial_{n-1} u, 0)^T, \quad \nabla_y u := (0, ..., 0, \partial_n u)^T,$$
$$\Delta_{x'} u := \sum_{i=1}^{n-1} \partial_i^2 u, \quad \Delta_y u := \partial_n^2 u,$$
$$\mathrm{div}_{x'} w := \sum_{i=1}^{n-1} \partial_i w_i, \quad \mathrm{div}_y w := \partial_{x_n} w_{x_n}.$$

Let $l > 1/2$ and let $I = (0,T)$, $T > 0$, be a time interval. We consider the following reaction-diffusion system for the unknown vector $u_\varepsilon = (u_{1\varepsilon}, ..., u_{m\varepsilon}) : I \times \Omega \to \mathbb{R}^m$:

$$\begin{aligned}
\partial_t u^0_{j\varepsilon} - \operatorname{div}\left(D^0_j \nabla u^0_{j\varepsilon}\right) &= f^0_j(u^0_\varepsilon) && \text{in } I \times \Omega^0_\varepsilon,\\
\frac{1}{\varepsilon}\partial_t u^1_{j\varepsilon} - \frac{1}{\varepsilon}\operatorname{div}_{x'}\left(D^1_j \nabla_{x'} u^1_{j\varepsilon}\right) + \varepsilon^{1+2l}\operatorname{div}_y\left(\overline{D}^1_j \nabla_y u^1_{j\varepsilon}\right) &= \frac{1}{\varepsilon} f^1_j\left(u^1_\varepsilon\right) && \text{in } I \times \Omega^1_\varepsilon,\\
\frac{1}{\varepsilon}\partial_t u^2_{j\varepsilon} - \frac{1}{\varepsilon}\operatorname{div}_{x'}\left(D^2_j \nabla_{x'} u^2_{j\varepsilon}\right) + \varepsilon^{1+2l}\operatorname{div}_y\left(\overline{D}^2_j \nabla_y u^2_{j\varepsilon}\right) &= \frac{1}{\varepsilon} f^2_j\left(u^2_\varepsilon\right) && \text{in } I \times \Omega^2_\varepsilon,
\end{aligned} \tag{3.1}$$

with the boundary conditions

$$\nabla u_{j\varepsilon} \cdot \nu = 0 \quad \text{on } \partial\Omega, \tag{3.2}$$

and the initial condition

$$u_\varepsilon(0,x) = U_\varepsilon(x) \quad x \in \Omega. \tag{3.3}$$

On the interfaces S^1_ε and S^2_ε we impose natural transmission conditions for u_ε, i.e the continuity of the solution and of the transversal fluxes:

$$\begin{aligned}
u^0_\varepsilon &= u^1_\varepsilon && \text{on } S^1_\varepsilon,\\
D^0_j \nabla u^0_{j\varepsilon} \cdot \nu &= \varepsilon^{1+2l} \nabla u^1_{j\varepsilon} \cdot \nu && \text{on } S^1_\varepsilon,\\
u^1_\varepsilon &= u^2_\varepsilon && \text{on } S^2_\varepsilon,\\
\nabla u^1_{j\varepsilon} \cdot \nu &= \nabla u^2_{j\varepsilon} \cdot \nu && \text{on } S^2_\varepsilon.
\end{aligned} \tag{3.4}$$

3.2.3 Variational formulation of the problem

The variational formulation of problem (3.1)–(3.4) is given as follows: Find

$$u_\varepsilon : I \times \Omega \to \mathbb{R}^m,$$

such that $u_\varepsilon \in L^2(I, L^2(\Omega, \mathbb{R}^m))$, $\partial_t u_\varepsilon \in L^2(I, L^2(\Omega, \mathbb{R}^m))$, and for almost every $t \in I$ and for all $\varphi \in L^2(I, H^1(\Omega, \mathbb{R}^m))$ holds

$$\begin{aligned}
&\int_{\Omega^0_\varepsilon} \partial_t u^0_{j\varepsilon}\varphi_j \, dx + \int_{\Omega^0_\varepsilon} D^0_j \nabla u^0_{j\varepsilon} \nabla \varphi_j \, dx + \Sigma^2_{k=1}\left(\frac{1}{\varepsilon}\int_{\Omega^k_\varepsilon} \partial_t u^k_{j\varepsilon}\varphi_j \, dx\right)\\
+\Sigma^2_{k=1}&\left(\frac{1}{\varepsilon}\int_{\Omega^k_\varepsilon} D^k_j \nabla_{x'} u^k_{j\varepsilon} \nabla_{x'}\varphi_j \, dx\right) + \Sigma^2_{k=1}\left(\int_{\Omega^k_\varepsilon} \varepsilon^{1+2l}\overline{D}^k_j \nabla_y u^k_{j\varepsilon} \nabla_y \varphi_j \, dx\right)\\
&= \Sigma^2_{k=1}\left(\frac{1}{\varepsilon}\int_{\Omega^k_\varepsilon} f_j\left(u^k_\varepsilon\right)\varphi_j \, dx\right) + \int_{\Omega^0_\varepsilon} f_j(u^0_\varepsilon)\varphi_j \, dx.
\end{aligned} \tag{3.5}$$

Moreover, the initial conditions

$$u_\varepsilon(0,x) = U_\varepsilon(x) \quad \text{for a.e. } x \in \Omega \tag{3.6}$$

need to be satisfied.

3.2.4 Assumptions on the data.

We assume that the diffusion coefficients

$$D_j^0(x),\ D_j^i(x'),\ \overline{D}_j^i(x', y/\varepsilon) \geq c > 0 \quad \text{for a.e. } x = (x', y)$$

are essentially bounded functions on Ω_ε^0, and Ω_ε^i $(i = 1, 2)$, respectively. For the initial function U_ε we assume that

$$U_{j\varepsilon}^i \in H^2(\Omega_\varepsilon^i) \cap L^\infty(\Omega_\varepsilon^i),\ i = 0, 1, 2,$$

satisfy the boundary conditions (3.2) and the compatibility conditions (3.4), and that the following estimates hold:

$$\frac{1}{\sqrt{\varepsilon}}\|U_{j\varepsilon}^i\|_{L^2(\Omega_\varepsilon^i)} + \frac{1}{\sqrt{\varepsilon}}\|\nabla U_{j\varepsilon}^i\|_{L^2(\Omega_\varepsilon^i)} \leq C \quad (i = 1, 2), \tag{3.7}$$

We assume the reaction terms $f_j^i : \mathbb{R}^n \to$ are Lipschitz continuous. Moreover, we assume that $c > 0$, $C > 0$, $l > 1/2$, and $M > 0$ exist such that

$$f_j^i(z) < cz_j \quad \text{for } z_j > M,$$

and

$$\sum_{j=1}^m f_j^i(z)(z_j)_- \leq C \sum_{j=1}^m |(z_j)_-|^2,$$

where $(z_j)_- := \min(z_j, 0)$.
Then, for each $\varepsilon > 0$ a unique solution $(u_\varepsilon, u_\varepsilon)$ exists, where

$$\begin{aligned} u_{j\varepsilon} &\in L^2(I, H^1(\Omega)) \cap L^\infty(I \times \Omega), \\ \partial_t u_{j\varepsilon} &\in L^2(I, L^2(\Omega)), \\ v_{j\varepsilon} &\in L^2(I, H^1(\Omega_\varepsilon^1)) \cap L^\infty(I \times \Omega_\varepsilon^1), \end{aligned} \tag{3.8}$$

If the initial conditions for u_ε are a.e. non-negative, the solution u_ε is a.e. non-negative. The assertions can be achieved by usage of standard techniques and the a priori estimates provided in the proof of the following result.

3.2.5 Statements

The main result of Section 3.2 is, roughly spoken, that the solutions of the system above converge to solution of a reaction-diffusion system defined in the bulk region and

and to solutions of a parabolic-elliptic system in defined the limit-layer for ε, and the subsystems do not interact with each other. More precisely it holds

Theorem 3.1. *For $\varepsilon \to 0$ a sequence u_ε of solutions of (3.5), (3.6) and a limit function u_0 exists which is a weak solution of the problem*

$$\partial_t u_{j0}^0 - \operatorname{div}\left(D_j^0 \nabla u_{j0}^0\right) = f_j^0(u_0^0) \quad \text{in } I \times \Omega, \tag{3.9}$$

$$\partial_t u_{j0}^1 - \operatorname{div}\left(D_j^1 \nabla u_{j0}^1\right) = f_j^1(u_0^1) \quad \text{in } I \times \Sigma', \tag{3.10}$$

$$\partial_t u_{j0}^2 - \operatorname{div}\left(D_j^2 \nabla u_{j0}^2\right) = f_j^2(u_0^2) \quad \text{in } I \times \Sigma', \tag{3.11}$$

with the initial conditions

$$u_0^0(0,\cdot) = U_0^0 \quad \text{in } \Omega, \tag{3.12}$$

$$u_0^1(0,\cdot) = U_0^1 \quad \text{in } \Sigma', \tag{3.13}$$

$$u_0^2(0,\cdot) = U_0^2 \quad \text{in } \Sigma', \tag{3.14}$$

and the boundary conditions

$$\partial_\nu u_j^0 = 0 \quad \text{on } I \times \partial\Omega/\Sigma, \tag{3.15}$$

$$\partial_\nu u_j^1 = 0 \quad \text{on } I \times \partial\Sigma', \tag{3.16}$$

$$\partial_\nu u_j^2 = 0 \quad \text{on } I \times \partial\Sigma', \tag{3.17}$$

The solution u_0 is unique.

The proof Theorem 3.1 is presented in Appendix A.4.

We assume that the considered reaction-diffusion equations in the model satisfy the required scaling properties on each compartment, such that we can treat the plasma membrane and the cytosol as a two dimensional sheet. The proof can be extended easily for more complex domains of the form $\Omega \times (0, H)$, where $\Omega \subset \mathbb{R}^{n-1}$ is a convex Lipschitz-domain. For the next section, we assume that the approximation still remains valid if $\Omega(t) \subset \mathbb{R}^2$ is time-dependent.

3.3 The cell geometry described as a moving boundary problem

One feature of the model cell is the ability to transform the shape in response to actomyosin activity. Both, the position of the cell relative to the substrate, and the cell shape itself may change. Thus, the domain that describes the geometry in the x_1-x_2-plane may change its shape in the course of time. To indicate this, we denote at time $t \in \mathbb{R}_+$ the cell area by an open domain $\Omega_t \subset \mathbb{R}^2$, and the circumferential cell boundary by $\Gamma_t := \partial\Omega_t$. For the initial time $t = 0$, we suppose a spherical resting cell area Ω_0 with radius R_0:

$$\Omega_0 := \left\{ x = (x_1, x_2) \in \mathbb{R}^2 : \|x\|_2 < R_0 \right\}.$$

The AMC is connected to the substrate via adhesion sites. We assume that local displacement of the actomyosin cytoskeleton induces the colocated local displacement of the cell relative to the substrate. Thus, the model cell is convected and deformed by the velocity field v, which describes the material flux of F-actin. More precisely, we assume that the boundary of Γ_t is convected by v along the outward normal unit vector $n = n(t, x)$ of Γ_t. From this, we obtain the *Stefan condition*:

$$V_n = v \cdot n, \quad \text{on } \Gamma_t, \tag{3.18}$$

where V_n denotes the a priori unknown normal velocity of the boundary. Hence, the a priori unknown shape of the model cell Ω_t at time t is defined as the enclosure of Γ_t.
In a polarized cell, the F-actin concentration in the lamellipodium is higher than in the cell body. We identify the lamellipodium as the subdomain of Ω_t, where the F-actin concentration $a(t, x)$ exceeds a threshold a_{thr}:

$$\Omega_t^L := \Omega_t \cap \left(\overline{\{x \mid a(t, x) > a_{\text{thr}}\}} \right)^\circ.$$

The boundary segment of the lamellipodium is denoted by $\Gamma_t^L := \partial\Omega_t^L$. The cell body is the remaining subdomain $\Omega_t^B := \Omega_t \backslash \Omega_t^L$ and the corresponding boundary segment is $\Gamma_t^B := \Gamma_t \backslash \Gamma_t^L$.
The corresponding time-space cylinder for the evolution of the domain Ω_t is denoted as

$$\Omega(t) := \bigcup_{t \in I} \left(\{t\} \times \Omega_t \right).$$

The time-space cylinder with respect to the boundaries is

$$\Gamma(t) := \bigcup_{t \in I} \left(\{t\} \times \Gamma_t \right).$$

The subdomains $\Omega^B(t)$, $\Omega^L(t)$ and $\Gamma^B(t)$, $\Gamma^L(t)$ are defined analog.

3.4 Chemical signalling

We model the biochemical processes of Rho-GTPase activation and actin polymerization by reaction-diffusion equations. If we describe reaction-diffusion equations on the moving domain $\Omega(t)$ in Eulerian coordinates, the equations receive an additional advection-dilution term [79]:
Let U denote the concentration of a considered substance, let $f(U)$ be a reaction function and let $J(U) = -D\nabla U$ be the occurring diffusive flux. Let $v = v(t, x(t, x_0)) \in \mathbb{R}^2$ denote the flow by which the material point $x_0 \in \Omega_0$ is in Ω_t convected. Let $V_t \subset \Omega_t$, $t > 0$, be a sequence of open, regular subdomains, such that $x(t, x_0) \in V_t$ iff $x'(t) = v(t)$, $t > 0$ and $x(t) = x_0 \in V_0 \subset \Omega_0$.
The conservation equation in integral form is given by

$$\frac{d}{dt}\int_{V_t} U(t, x(t, x_0))\ dx = \int_{V_t} \operatorname{div}(D\nabla U) + f(U)\ dx.$$

Application of Reynolds' transport theorem on the left-hand side yields:

$$\frac{d}{dt}\int_{V_t} U(t, x(t, x_0))\ dx = \int_{V_t} [\partial_t U + \operatorname{div}(Uv)]\, dx,$$

Since $V_t \subset \Omega_t$ is arbitrary, the equation above is equivalent to

$$\partial_t U - \operatorname{div}(D\nabla U) + \operatorname{div}(Uv) = f(U) \quad \text{on } \Omega(t). \tag{3.19}$$

If U is conserved in the cell, we obtain zero-flux boundary conditions:

$$(-D\nabla U + Uv) \cdot n = 0 \quad \text{on } \Gamma(t), \tag{3.20}$$

where $n = n(x(t))$ denotes the outward unit vector at the boundary Γ_t of the cell-domain.

3.4.1 Rho GTPase dynamics

Although other proteins and lipids are involved in the polarization of neutrophils [34] and several mutual crosstalk circuits have been identified [35], we act on the assumption that only the GTPases Rac and RhoA are decisive for triggering downstream effectors that regulate AMC activity. Based on the derivation of the former section, we restrict ourselves to the investigations of processes in plasma membrane only. We formulate a

system of PDEs for the following unknowns:

$$\begin{aligned}
u_1 : \Omega(t) \to \mathbb{R} &\quad \text{concentration of Rac-GTP,}\\
u_2 : \Omega(t) \to \mathbb{R} &\quad \text{concentration of Rac-GDP,}\\
w_1 : \Omega(t) \to \mathbb{R} &\quad \text{concentration of RhoA-GTP,}\\
w_2 : \Omega(t) \to \mathbb{R} &\quad \text{concentration of RhoA-GDP,}\\
z_1 : \Omega(t) \to \mathbb{R} &\quad \text{concentration of GEF-GTP-Rho complexes,}\\
z_2 : \Omega(t) \to \mathbb{R} &\quad \text{concentration of GEF,}\\
a : \Omega(t) \to \mathbb{R} &\quad \text{concentration of F-actin,}\\
b : \Omega(t) \to \mathbb{R} &\quad \text{concentration of G-actin,}\\
m_F : \Omega(t) \to \mathbb{R} &\quad \text{concentration of myosin-II-F-actin-complexes.}
\end{aligned}$$

Physical units are given by

$$[u_i] = [w_i] = [z_i] = [a] = [b] = [m_F] = \frac{\text{mol}}{\text{dm}^2}, \quad i = 1, 2.$$

Much more extended sets of variables could be considered here. In particular we do not explicitly take into account the cascade of downstream effectors and GAP concentrations. The inactivation process will be described implicitly and the concentrations of GDP-bound Rho will be approximated by a constant amount.

Reaction kinetics

We assume simple mass action kinetics or a Hill type law for catalyzed reactions. With respect to the scheme presented in Figure 2.5, for the change of concentration of the above variables due to reactions we prescribe the following equations. Our choices for the biochemical interactions are similar to the models in [8, 36]. Based on findings of Houk et al. [11], we additionally suggest that membrane tension inhibits Rac activation, and in accordance to [35] we incorporate an inhibitory feedback from Rac on RhoA. Moreover, we hypothesize that increasing membrane tension promotes RhoA activation. The concentration of GTP-Rho is increased by the activation process, which is catalyzed by GEF. Additionally, slow Rho activation also occurs in the absence of GEF (in the following modelled by the rate $\overline{k}_1$). For the corresponding rates we assume that they are proportional to the GTP-Rho concentration and the concentrations of the catalysts. Vice versa GTP-Rho is produced by the inactivation of GDP-Rho. Since we have not taken the GAP concentration into account, we here assume a rate δ_1 for GAP mediated Rho inactivation which is constant with respect to the GEF concentration. The change of u_1 due to Rac activation we therefore describe by

$$[\partial_t u_1]_{\text{reaction}} = \overline{k}_1 u_2 + k_3 z_2 u_2 - \delta_1 u_1.$$

Each GEF has two Rho-specific binding sides and a cooperative binding of active Rho to GEF complex formation has been experimentally verified [80]. Then complex formation and dissociation lead to the following laws for the concentration of the complex and GEF

$$[\partial_t z_2]_{\text{reaction}} = k_4 z_1 u_1^2 - k_5 z_2,$$
$$[\partial_t z_1]_{\text{reaction}} = -k_4 z_1 u_1^2 + k_5 z_2,$$

We assume that the complex formation is fast compared to the whole activation process. Thus, we use a quasi-steady state approximation for the complex formation. If we proceed as in [81], this approximation yields

$$z_2 = \frac{\gamma_1 u_1^2}{K_1^2 + u_1^2}, \tag{3.21}$$

where γ_1 is the concentration of $z_1 + z_2$ at steady state and $K_1 = k_5/k_4$. From this we obtain the simplified kinetics for Rac activation:

$$[\partial_t u_1]_{\text{reaction}} = \overline{k}_1 u_2 + k_3 \frac{\gamma_1 u_1^2}{K_1^2 + u_1^2} u_2 - \delta_1 u_1.$$

Since Rho activation cycling is conserved through the subclasses Rac and RhoA, RhoA activation via GEF catalyzation and GAP mediated RhoA inactivation are similar to the kinetics discussed above. If we assume first oder kinetics and also use a quasi-steady state approximation for GEF-RhoA complex formation, we obtain for RhoA activation the same kinetics as for Rac (apart from the specific values of the rates). Moreover, GTP-Rac is an inhibitor for RhoA activation. The choice of the particular inhibitory function is to a large extend arbitrary. We here assume a Hill function of second order with respect to u_1 as a pre-factor for the GAP mediated inactivation kinetics. The change of w_1 due to activation is described by

$$[\partial_t w_1]_{\text{reaction}} = \overline{k}_2 w_2 + k_6 \frac{\gamma_2 w_1^2}{K_2^2 + w_1^2} w_2 - \frac{\delta_2 u_1^2}{K_3^2 + u_1^2} w_1,$$

where $\overline{k}_2$ is the activation rate for RhoA that is not catalyzed by GEF, the factor of w_2 in the second term models the GEF-catalyzed activation of RhoA, and the factor of w_1 in the third term combines the GAP-mediated RhoA inactivation and the GTP-RhoA suppression due to GTP-Rac.

We model the inhibition of Rac activation due to increasing membrane tension by the assumption that the activation rates $\overline{k}_1$ and k_3 depend on the amount of tension τ, such that $\overline{k_1}$ and k_3 monotonously decrease if the tension increases. To capture this feature,

we suggest that these rates can be written as

$$\begin{aligned}\overline{k}_1(\tau) &:= h_1(\tau)k_1,\\ k_3(\tau) &:= h_1(\tau),\end{aligned}$$

where $h_1(\tau)$ is a monotonously decreasing function with respect to τ and k_1 is a proportionality factor. $h_1(\tau)$ will be specified in Section 3.5.4. In the model, tension generation primary dues to the recruitment of downstream effectors of active Rac. Moreover, active Rac is inhibitory for RhoA activation even at long ranges [82]. However, Rac mediated long-range inhibitors for RhoA are currently unknown. We hypothesize that active Rac constrains RhoA activation implicitly via tension by setting

$$\begin{aligned}\overline{k}_2(\tau) &:= h_2(\tau)k_2,\\ k_6(\tau) &:= h_2(\tau),\end{aligned}$$

where $h_2(\tau)$ is a monotonously increasing function with respect to τ and k_2 is a proportionality factor. $h_2(\tau)$ will be specified in Section 3.5.4.
Finally, we assume that both, GDP-Rac and GDP-RhoA, are homogeneously distributed and are present in the plasma membrane in sufficiently high concentrations such that we may approximate u_2 and w_2 in the reactions by constants. We set w.l.o.g. $u_2 = w_2 = 1$ and consider the actual values of u_2 and w_2 implicitly in the fitting of the respective rates. Based on these assumptions, we obtain the simplified reaction functions for Rac and RhoA activation:

$$\begin{aligned}[\partial_t u_1]_{\text{reaction}} &= h_1(\tau)\left(k_1 + \frac{\gamma_1 u_1^2}{K_1 + u_1^2}\right) - \delta_1 u_1 := f_1(\tau, u_1),\\ [\partial_t w_1]_{\text{reaction}} &= h_2(\tau)\left(k_2 + \frac{\gamma_2 w_1^2}{K_2 + w_1^2}\right) - \frac{\delta_2 u_1^2}{K_3 + u_1^2} w_1 := f_2(\tau, u_1, w_1).\end{aligned} \tag{3.22}$$

Remark 3.2. In the further course we simply write u instead of u_1 and w instead of w_1.

Properties of the reaction functions

To a large extend the particular choices of the kinetic functions used in our model are arbitrary. However, the reaction functions need to exhibit certain characteristics to achieve the wave-based patterning mechanism we aim at. In this section we briefly render the basic requirements, such that we can define initial values for model cell at rest. We refer to Chapter 5 for a more detailed discussion of the requirements on the reaction functions.
A necessary feature is that the kinetic function f_1 of Rac activation has a biologically reasonable parameter regime in which *bistability* with respect to the variable u occurs. More precisely, it is required that the dynamical system $\mathrm{d}_t u = f_1(\tau, u)$ is bistable for fixed τ in a parameter range $\tau_{\min} < \tau < \tau_{\max}$, i.e for fixed $\tau \in (\tau_{\min}, \tau_{\max})$ the reaction

$f_1(\tau, u) = 0$ has three roots

$$u_- < u_m < u_+$$

and

$$\partial_u f(\tau, u_-(\tau)) < 0, \quad \partial_u f(\tau, u_m(\tau)) > 0, \quad \partial_u f(\tau, u_+(\tau)) < 0$$

holds. The initial tension $\tau = \tau_0$ has to be contained in $(\tau_{\min}, \tau_{\max})$. The stable points are $u_-(\tau), u_+(\tau)$. The unstable point is $u_c(\tau)$. It holds $u_-(\tau) < u_c(\tau) < u_+(\tau)$.
A requirement for the function f_2 of RhoA activation with respect to the initial values is that

$$f_2(\tau, u, w) = 0$$

has for fixed $\tau \in (\tau_-, \tau_+)$ and $u(\tau) = u_-(\tau)$, a unique homogenous solution $w_-(\tau)$.
The suggested reaction functions in (3.22) posses a parameter space in which bistability occurs and the uniqueness of a homogenous solution $w_-(\tau)$ is granted, respectively. The specific parameters setting is listed in Section 4.2.

Model equations for Rho

Taking reaction, diffusion, and displacement of the domain Ω_t into account and assume that active Rho is conserved in the domain, we obtain from Section 3.4 the set of equations

$$\begin{aligned} \partial_t u - D_u \Delta u + \operatorname{div}(uv) &= f_1(\tau, u), && \text{on } \Omega(t), \\ \partial_t w - D_w \Delta w + \operatorname{div}(wv) &= f_2(\tau, u, w), && \text{on } \Omega(t), \end{aligned} \tag{3.23}$$

where D_u and D_w are the apparent diffusion coefficients of active Rac and active Rho, respectively. The boundary conditions are given by

$$\begin{aligned} (\nabla D_u u + uv) \cdot n &= 0 \quad \text{on } \Gamma(t), \\ (\nabla D_w w + wv) \cdot n &= 0 \quad \text{on } \Gamma(t). \end{aligned} \tag{3.24}$$

Let $\tau_0 \in (\tau_-, \tau_+)$ be the amount of membrane tension of the model cel at rest. The initial conditions model the resting state in which the Rho proteins are at homogenous steady state. We use the denotations introduced in the former section. The initial values are given by

$$u(0, x) = u_-(\tau_0) := u_0, \quad w(0, x) = w_-(\tau_0) := w_0 \quad \text{on } \Omega_0. \tag{3.25}$$

3.4.2 Actin dynamics

The model distinguishes between two types of actin, G-actin and F-actin, which are assumed to interconvert into each other. Polymerization and depolimerization are modelled by a first oder kinetics: Let a and b be the concentration of F-actin and G-actin,

respectively. We denote the rate of polymerization by k_{ba} and the rate of depolymerization by k_{ab}. Finally, we assume that neither F-actin nor G-actin is synthesized on the timescale we are investigating. The contributing kinetics of F-actin polymerization is given by

$$g(a, b, u) = k_{ba}(u)b - k_{ab}(u)a. \tag{3.26}$$

Experimental evidence shows that the rate of actin polymerization is affected by Rac via downstream effectors [83]. We act on the simplifying assumption that the activation of downstream effectors occurs proportional to the activation of Rac without delay. According to this, we propose the specific rates

$$k_{ba}(u) = k_3 + \frac{\gamma_3 u}{K_4 + u}, \quad k_{ab}(u) = k_4.$$

The rate constants k_3 and k_4 indicate a constant turnover between G-actin and F-actin, while the Hill-term models the promoted F-actin polymerization in response an increase of active Rac. Assuming that the mass of actin is conserved in Ω_t throughout the timespan of interest, we obtain the reaction-diffusion equations

$$\begin{aligned} \partial_t a - D_a \Delta a + \operatorname{div}(av) &= g(a, b, u), \\ \partial_t b - D_b \Delta b + \operatorname{div}(bv) &= -g(a, b, u), \end{aligned} \tag{3.27}$$

on $\Omega(t)$ and the boundary conditions

$$\begin{aligned} (\nabla D_a a + av) \cdot n &= 0 \quad \text{on } \Gamma(t), \\ (\nabla D_b b + bv) \cdot n &= 0 \quad \text{on } \Gamma(t). \end{aligned} \tag{3.28}$$

3.4.3 Myosin dynamics

We assume that myosin is present in high concentrations in the whole cell. Furthermore, we neglect possible occurring fluxes. We model myosin-actin-filament binding by first order kinetics:

$$\partial_t m_F = k_5 a \; m_G - k_6 m_F,$$

where m_F and m_G is the concentration of myosin II bound and unbound to F-actin, respectively. k_5 and k_6 denote the binding and the detachment rate, respectively. Let m_0 be the total initial concentration of myosin. If myosin is not resynthesized during the timespan of observation, m_G can be written as $m_0 - m_F$. We assume that myosin binding to F-actin is fast compared to the other kinetics in our model. A *quasi-steady-state assumption* yields that the concentration of myosin bound to F-actin simplifies

to

$$m_F = \frac{m_0 k_5 a}{k_5 a + k_6}.$$

RhoA activity mediates myosin-II-F-actin complex formation [84]. We neglect the signal transduction via downstream effectors by assuming that active RhoA mediates the binding affinity of myosin to F-actin directly. This yields that $w \mapsto k_5(w)$ is increasing and $w \mapsto k_6(w)$ is non-increasing. Setting

$$k_5(w) := \tilde{k}_5 w, \quad k_6(w) := \tilde{k}_6,$$

where $\tilde{k}_5$ and $\tilde{k}_6$ are constants satisfies this requirement. Dropping the tildes, we obtain for the concentration of myosin II bound to F-actin

$$m_F = m_F(wa) = \frac{m_0 k_5 wa}{k_5 wa + k_6}. \tag{3.29}$$

For small perturbations of the steady state concentrations a_0 and w_0, we may replace (3.29) by its linearization with respect to wa in $w_0 a_0$:

$$m_F(wa) \approx K_5(wa - w_0 a_0) + m_F(w_0 a_0), \tag{3.30}$$

where

$$K_5 := \frac{m_0 k_5}{k_5 w_0 a_0 + k_6} \left(1 - \frac{k_5 w_0 a_0}{k_5 w_0 a_0 + k_6}\right).$$

Obviously, K_5 is a positive parameter since $k_6 > 0$. The concrete parameter values for the model are presented in Section 4.2. We assume that the concentration m_F can be described adequately by approximation (3.30).

3.5 Cytoskeletal mechanics

We model the AMC as an active gel. A brief survey of active gel theory and its application in Cytoskeletal mechanics is given in Appendix B.
We briefly summarize the main statements: Active gel theory is a mechanical theory that considers the AMC as a *viscoelastic medium with the ability to generate stresses actively* due to F-actin treadmilling and myosin mediated contraction. Neglecting possible additional stresses that arise from torque (i.e. neglecting $\sigma^{\mathrm{pol}}_{\alpha\beta}$ in (B.3)), the occurring stress tensor $\sigma^{\mathrm{tot}}_{\alpha\beta}$ is composed of both, a passive and an active element, denoted by $\sigma^{\mathrm{pas}}_{\alpha\beta}$ and $\sigma^{\mathrm{act}}_{\alpha\beta}$, respectively:

$$\sigma^{\mathrm{tot}}_{\alpha\beta} = \sigma^{\mathrm{pas}}_{\alpha\beta} + \sigma^{\mathrm{act}}_{\alpha\beta}. \tag{3.31}$$

The passive stress is determined by the viscoelasticity of the material. The active part depends in general on various factors like ATP-provided energy, F-actin density as well as the myosin II density. The total stress $\sigma^{\mathrm{tot}}_{\alpha\beta}$ is completed by the following components:

1) a constitutive equation,

2) a force-balance equation,

3) an equation of state and

4) a polarity field.

1) The AMC is a highly viscous medium with a complex rheology. In general, its viscosity may depend on the temperature T and on the densities $a(t,x)$ and $m_F(t,x)$. Due to the effects of permeation the viscosity may also depend on $b(t,x)$, $u(t,x)$, and $w(t,x)$. However, since the AMC is a continuously dense network of cross-linked polymeres that rather resist shear stresses due to its architecture than to its density, we hypothesize that its viscosity is not affected drastically by minor fluctuations of $a(t,x)$, $m_F(t,x)$ $b(t,x)$, $u(t,x)$, and $w(t,x)$, such that the viscosity may be modelled approximatively by a constant η.
We describe the viscoelastic properties of the AMC by the *Maxwell model*. If we use Einstein's notation, the Maxwell model reads as

$$\dot{\varepsilon} = \frac{\dot{\sigma}^{\mathrm{pas}}_{\alpha\beta}}{E} + \frac{\sigma^{\mathrm{pas}}_{\alpha\beta}}{\eta}, \tag{3.32}$$

where E denotes Young's modulus of the gel and $\dot{\varepsilon}$ denotes the the strain-rate tensor. Let v be the velocity of the material flow, then is $\dot{\varepsilon}$ given by

$$\dot{\varepsilon} = \frac{1}{2}(\partial_\alpha v_\beta + \partial_\beta v_\alpha).$$

2) Let $\delta_{\alpha\beta}$ be the Kronecker delta. Neglecting inertial forces, typically valid on a cellular scale, we write the force-balance equation as

$$\partial_\alpha \left(\sigma^{\text{tot}}_{\alpha\beta} - \Pi \delta_{\alpha\beta} \right) + F^{\text{ext}}_\beta = 0, \tag{3.33}$$

where Π and F^{ext} denote the internal pressure and an external force contribution, respectively.
3) The pressure Π is defined by an equation of state and will be modelled in the next section.
4) Since F-actin treadmilling is directional, the actin gel is in a natural way endowed with a polarity. The corresponding polarity field is a vector field consisting of unit vectors. We denote the polarity field by p. The polarity field points in the direction in which F-actin assembles.

3.5.1 The polarity field

Polymers such as actin gels are naturally endowed with a polarity field, i.e. a field of unit vectors, running locally parallel to the averaged direction of polymer alignment [85]. Neglecting possible organizational mechanisms that induce polar actin alignment, we phenomenologically assume that 1) F-actin treadmilling occurs in the lamellipodium perpendicular to the boundary, 2) in a moving cell, the polarity field remains static in Ω^L_t with respect to the substrate, and 3) stable F-actin aligns in periphery of the cell body parallel to the boundary while it is unpolar in interior of Ω^B_t.
1) Perpendicular F-actin treadmilling endows the AMC with a polarity field $p = (p_x, p_y) : \overline{\Omega(t)} \to \mathbb{R}^2$ which is initiated at the boundary of the lamellipodium. We write

$$p = n \quad \text{on } \Gamma^L(t). \tag{3.34}$$

2) The leading front is pushed forward due to polymerization of new F-actin at the very front, whereas the orientation of old F-actin remains stationary with respect to the substrate. Thus, we assume that the polarity field is conserved in the bulk if $\Gamma^L(t)$ extends. Then, if $x \in \Omega^L_t$ has been a former boundary point, the polarity at $x \in \Omega^L_t$ is given by the outward normal unit vector of this former boundary point.
More precisely, we consider for $(t, x) \in \Omega^L(t)$ the set $P(t, x)$ of all previous times, where x has been a boundary point:

$$P(t, x) := \{ t' \in \mathbb{R}_+ | t' < t,\ x \in \Gamma^L_{t'} \}.$$

If $P(t,x)$ is not empty, we set $\tilde{t} := \sup P(t,x)$ and denote by $n(\tilde{t},x)$ the outward unit vector in $x \in \Gamma^L_{\tilde{t}}$. For the polarity field in $\Omega^L(t)$ we take

$$p(t,x) = \begin{cases} n(\tilde{t},x), & \text{if } P(t,x) \neq \emptyset, \\ 0, & \text{if } P(t,x) = \emptyset. \end{cases} \tag{3.35}$$

For the following course, we assume that the evolution of $[t \mapsto \Gamma^L_t]$ is sufficiently regular, such that we may assume $p \in L^\infty(\Omega^L(t), \mathbb{R}^2)$.
3) We suppose that the polarity of F-actin is randomly distributed in Ω^B_t. Thus, directional forces exerted on adhesion sites due to myosin contraction cancel each other out. This is equivalent to setting $p = (0,0)$ on $\Omega^B(t)$. Non-treadmilling stable F-actin aligns parallel to the boundary Γ^B_t [47]. We indicate this by setting

$$p = n^\perp \quad \text{on } \Gamma^B(t). \tag{3.36}$$

3.5.2 Constitutive equations and force balance

In this section we consider the combination of both, the constitutive equation (3.32) and the force balance equation (3.33). We will adapt these equations in our framework and reduce the viscoelastic part to a purely viscous material.

Reduction F-actin is convected by the the material flux "av", where v is the velocity field that has to be obtained from the components 1)-4) listed in Section 3.5. Since the stress itself is generated by F-actin activity, it is also affected by the convection of F-actin. Application of Reynold's transport theorem states that we have to exchange the time derivative "∂_t" in constitutive equation (3.32) with the convective time derivative "$\frac{D}{Dt} := \partial_t \cdot + \nabla \cdot (v \cdot)$". Then, (3.32) transforms to

$$\frac{1}{t^*}\left(\partial_t \sigma^{\text{pas}}_{\alpha\beta} + \nabla v \sigma^{\text{pas}}_{\alpha\beta}\right) + \sigma^{\text{pas}}_{\alpha\beta} = \frac{\eta}{2}(\partial_\alpha v_\beta + \partial_\beta v_\alpha), \tag{3.37}$$

where $t^* := \eta/E$ is the *relaxation time* of the viscoelastic medium. t^* indicates the time at which the viscosity of the material starts to dominate the elastic response and at which the material starts to flow. Experimental observations suggest that E is of order 10^3-10^5 Pa [86–88], while η is of order 10^2-10^3 Pa s [89], implying that t^* is in the timescale of seconds. For times $t >> t^*$, we may neglect the elastic response in (3.37) and obtain a purely viscous gel, satisfying the constitutive equation

$$\sigma^{\text{pas}}_{\alpha\beta} = \frac{\eta}{2}(\partial_\alpha v_\beta + \partial_\beta v_\alpha). \tag{3.38}$$

Chemical polarization of Rho GTP occurs in most motile cells on a timescale of about $10 - 100s$. Thus, we consider the AMC within these time-spans as a purely viscous material.

Force balance The constitutive equation (3.38) has to be complemented by a force balance equation. Recall from (3.31) that the composition of the total stress is $\sigma^{\text{tot}}_{\alpha\beta} = \sigma^{\text{pas}}_{\alpha\beta} + \sigma^{\text{act}}_{\alpha\beta}$. Let F^{ext} be a body force. The force balance reads as

$$\partial_\alpha \left(\frac{\eta}{2}(\partial_\alpha v_\beta + \partial_\beta v_\alpha) - \Pi\delta_{\alpha\beta} + \sigma^{\text{act}}_{\alpha\beta} \right) = -F^{\text{ext}}_\beta.$$

If we write $\Delta v := (\Delta v_1, \Delta v_2)^T$ and $\nabla^\perp v := (-\partial_{x_2} v_1, \partial_{x_1} v_2)^T$ and set

$$F^{\text{act}} := (\partial_{x_1}\sigma_{x_1,x_1} + \partial_{x_2}\sigma_{x_2,x_1}, \partial_{x_1}\sigma_{x_1,x_2} + \partial_{x_2}\sigma_{x_2,x_2})^T,$$

the force balance equation in two space dimensions can be written as

$$\eta\Delta v + \frac{\eta}{2}\nabla^\perp \text{rot}(v) - \nabla\Pi = -F^{\text{ext}} - F^{\text{act}}. \tag{3.39}$$

Equation of state for the pressure Actomyosin gels are relatively resistant to compression. If the shear deformations are large compared to the compression, a gel is classified as *weakly compressible* [46]. In particular, this holds for an elastic body having a small ratio between shear and compression modulus. A perfectly incompressible gel has a Poisson ratio ν of exactly $\nu = 0.5$. Shear field measurements by using magnetic tweezers have shown, that the Poisson ratio of actin gels ranges from $\nu = 0.4$ to $\nu = 0.5$ [90], categorizing actin gels as weakly compressible. The relation of pressure and density of weakly compressible media can be modelled by Taint's equation. If we neglect the effect of permeation of the solvent through the gel and use Taint's equation, the pressure Π with respect to the F-actin density is given by

$$\Pi(a) = \frac{K_6}{\theta}\left(\left(\frac{a}{a_0} \right)^\theta - 1 \right) + \Pi_0,$$

where θ denotes the adiabatic index of the gel, K_6 is the compression modulus, and Π_0 (resp. a_0) is the pressure (resp. F-actin concentration) in the resting cell.

External Force The cell exerts force to the substrate via adhesion sites which link the actin filament to the substrate. We assume that F-actin is bounded to the adhesion sites and that the filament slides with an approximately constant velocity v relative to the substrate. Then frictional force is exerted to the substrate. Hence, we take friction as external force responsible for cell movement and set

$$F^{ext} = -\xi v, \tag{3.40}$$

where ξ denotes the friction coefficient. In general, the friction coefficient may depend on the sliding velocity v. We assume that $|v|$ is small compared to L/τ_b, where L stands for the typical length of a focal adhesion molecule and τ_b stands for the binding rate of focal adhesions to F-actin. Then we may treat ξ as a constant, see [46].

Active Force F^{act} denotes the actively generated force due to AMC dynamics. The active force is thought to be generated by two components. F-actin treadmilling at the leading front generates a protrusive force F^{tread} and myosin mediated contractions of the AMC generate a trailing force F^{cont} of the posterior:

$$F^{\text{act}} = F^{\text{tread}} + F^{\text{cont}}.$$

F-actin treadmilling occurs in the lamellipodium Ω_t^L. Based on the observation that F-actin treadmilling propels the cell front forward with constant speed [39, 91–93], we assume that the generated force due to F-actin treadmilling is constant and points towards the leading front:

$$F^{\text{tread}} := -\zeta_F \mathbb{1}_{\{a \geq a_{\text{thr}}\}} p, \tag{3.41}$$

where ζ_F is a positive constant. The mapping $[(t,x) \mapsto \mathbb{1}_{\{a \geq a_{\text{thr}}\}}(t,x)]$ is the indicator function of the subdomain $\Omega^L(t)$ on $\Omega(t)$ defined by

$$\mathbb{1}_{\{a \geq a_{\text{thr}}\}}(t,x) = \begin{cases} 1, & \text{if } a(t,x) \geq a_{\text{thr}} \\ 0 & \text{otherwise.} \end{cases} \tag{3.42}$$

The retraction of the cell body Ω_t^B is mediated by AMC contractions due to myosin motors [46, 85, 94]. Myosin motors crosslink neighbouring F-actin and exert contractile force on the network due to conformational changes [23]. We assume that the contractile force acts perpendicular to the direction of F-actin polarity. Since the polarity field in Ω_t^B is zero, F_{cont} vanishes in Ω_t^B:

$$F^{\text{cont}} := 0 \quad \text{on } \Omega^B(t).$$

3.5.3 Boundary values

F^{cont} is zero in the cell body. On the boundary Γ_t^B, however, follows from (3.36) that perpendicular contractile force points in the direction of the inward normal vector. If the density of myosin motors bound to F-actin is high, we expect a high directional force. Moreover, we assume that the contractile force is zero if the cell is at rest. The simplest ansatz satisfying these requirements is to set F_{cont} proportional to $m_F(wa) - m_F(w_0 a_0)$. From (3.30) follows

$$F^{\text{cont}} := -\zeta_B \mathbb{1}_{\{a < a_{\text{thr}}\}} K_5(wa - w_0 a_0) n \quad \text{on } \Gamma(t) \tag{3.43}$$

where ζ_B is a positive constant and $[(t,x) \mapsto \mathbb{1}_{\{a < a_{\text{thr}}\}}]$ is the indicator function of $\Gamma^B(t)$ on $\Gamma(t)$ defined analogously to (3.42).

We assume that the membrane confines the AMC at the boundary. Hence, two additionally forces are thought to be dominant on Γ_t: A curvature induced force H_{el} due

to bending rigidity of the membrane and an elasticity-related force S due to membrane tension. Force balance on the boundary formally leads to

$$\eta \left(\nabla v + (\nabla v)^T \right) \cdot n - (\Pi - \Pi_0) n = F^{\text{cont}} + H_{\text{el}} + S \quad \text{on} \quad \Gamma(t), \tag{3.44}$$

where Π_0 denotes the atmospheric pressure outside of Ω_t. We define the curvature induced force H_{el} by

$$H_{\text{el}} := \gamma_1^m (\kappa_m - \kappa_0) n.$$

The parameter γ_1^m is a material constant and $\kappa_m(t, x)$ represents the mean curvature in $x \in \Gamma_t$. Since the membrane is a lipid bilayer, we assume that it possesses a spontaneous curvature κ_0. Thus, the curvature induced force is zero if Γ_t has the curvature κ_0 [95]. It seems biologically reasonable that for a resting cell holds $\kappa_m = \kappa_0$. Hence, we take for κ_0 the curvature of the initial boundary Γ_0, i.e. $\kappa_0 = 1/R_0$.

Remark 3.3. In a two-dimensional spatial setting the mean curvature reduces simply to curvature. Let $(X_t(s), Y_t(s))$, $s \in [0, 1)$, be a parametrization of the boundary Γ_t in cartesian coordinates, then the curvature $\kappa_m(x)$ in $x = (X_t(s), Y_t(s))$ can be written as

$$\kappa_m(x) = \frac{d_s X_t(s) d_s^2 Y_t(s) - d_s^2 X_t(s) d_s Y_t(s)}{(X_t(s)^2 + Y_t(s)^2)^{\frac{3}{2}}}.$$

We hypothesize that the elastic stress acts in the normal direction of the cell boundary Γ_t and is spatially homogenous in Γ_t. We set

$$S = -\gamma_2^m |\Gamma_t| n = -\gamma_2^m \int_{\Gamma_t} 1 \, ds \; n.$$

We assume that the resting cell corresponds to the equilibrium of the mechanical system. Thus, we obtain $-\gamma_2^m = \frac{\Pi(a_0)}{|\Gamma_0|}$. The term S contributes to the stretching resistance due to wrinkles in the outer boundary of the membrane. Mathematically it presents a simple means to prevent the model cell from unrestricted swelling. In a more comprehensive model unrestricted swelling may be limited by more factors as e.g. volume conservation. In summary, we obtain for the velocity field the boundary condition

$$\begin{aligned} \eta \left(\nabla v + (\nabla v)^T \right) \cdot n = -\zeta_B \mathbb{1}_{\{a < a_{\text{thr}}\}} K_5 (wa - w_0 a_0) n + \gamma_1^m (\kappa_m - \kappa_0) n \\ -\gamma_2^m \left(\int_{\Gamma_t} 1 \, ds \right) n + (\Pi - \Pi_0) n. \end{aligned} \tag{3.45}$$

3.5.4 Membrane tension

As in [14, 15] we suppose the membrane to be an isotropic medium with linear elasticity and define the membrane tension τ to be proportional to the deviation of the cell surface area from its value at rest. We denote by $|\Omega_t|$ the surface area of Ω_t. Then, for membrane

tension holds

$$\tau \propto \frac{|\Omega_t|}{|\Omega_0|} = \frac{1}{\pi R_0^2} \int_{\Omega_t} 1 \, dx,$$

where R_0 is the radius of the cell at rest. In the model we consider a normalized version of membrane tension:

$$\tau := \frac{1}{\pi R_0^2} |\Omega_t|.$$

An increase in membrane tension is supposed to lower the Rac activation rate. On the other hand, we supposed that an increase in tension promotes RhoA activation. In the simplest conceivable case these requirements are satisfied by

$$h_1(\tau) := -\alpha_1(\tau - 1) + h_0, \quad h_2(\tau) := \alpha_2(\tau - 1) + h_0,$$

where α_1, α_2, $h_0 \geq 0$ are positive constants.

3.6 Model equations

We summarize the model equations.
The model is a spatially two dimensional projection of the cell to the flat substrate from a top view. For fixed $R_0 \in \mathbb{R}_+$ the initial domain describing the shape of this domain at time $t = 0$ is given by

$$\Omega_0 = \left\{ x \in \mathbb{R}^2 : \|x\|_2 < R_0 \right\}.$$

The domain can be convected by a velocity field v which is induced by an actin flow. At time $t > 0$ the domain Ω_t is defined as the inner of the boundary Γ_t, where Γ_t has to be determined from the Stefan condition

$$V_n = v \cdot n, \quad \text{on } \Gamma_t.$$

The model can be subdivided into two units, whose equations will be consecutively displayed:

1) Reaction-diffusion equations (modelled in Section 3.4),

2) Cytoskeletal mechanics (modelled in Section 3.5).

Let $I \subset \mathbb{R}_+$ be an open time interval starting at $t = 0$. Let $n = n_t$ be the outward oriented unit vector on Γ_t. Symbols that are not explicitly mentioned in the following are fixed parameters and are listed in Section 4.2.

1) Reaction-diffusion equations. Let u, w, a, b be the concentration of active Rac, active RhoA, F-actin, G-actin, respectively. The spatiotemporal dynamics are given by the equations

$$\begin{aligned}
\partial_t u - D_u \Delta u - \operatorname{div}(uv) &= f_1(\tau, u) && \text{on } \Omega(t),\\
\partial_t w - D_w \Delta w - \operatorname{div}(wv) &= f_2(\tau, u, w) && \text{on } \Omega(t),\\
\partial_t a - D_a \Delta a - \operatorname{div}(av) &= g(a, b, u) && \text{on } \Omega(t),\\
\partial_t b - D_b \Delta b - \operatorname{div}(bv) &= -g(a, b, u) && \text{on } \Omega(t),
\end{aligned} \tag{3.46}$$

where the reaction functions on the right hand side are

$$\begin{aligned}
f_1(\tau, u) &= h_1(\tau) \left(k_1 + \frac{\gamma_1 u^2}{K_1 + u^2} \right) - \delta_1 u,\\
f_2(\tau, u, w) &= h_2(\tau) \left(k_2 + \frac{\gamma_2 w^2}{K_2 + w^2} \right) - \frac{\delta_2 u^2}{K_3 + u^2} w,\\
g(a, b, u) &= \left(k_3 + \frac{\gamma_3 u}{K_4 + u} \right) b - k_4 a.
\end{aligned} \tag{3.47}$$

The impact of tension in the activation functions is

$$h_1(\tau) = -\alpha_1(\tau - 1) + h_0, \quad h_2(\tau) = \alpha_2(\tau - 1) + h_0,$$

where α_1, α_2, $h_0 \geq 0$ are positive constants. The boundary conditions are

$$\begin{aligned} (D_u \nabla u + uv) \cdot n &= 0 \quad \text{on } \Gamma(t), \\ (D_w \nabla w + wv) \cdot n &= 0 \quad \text{on } \Gamma(t), \\ (D_a \nabla a + av) \cdot n &= 0 \quad \text{on } \Gamma(t), \\ (D_b \nabla b + bv) \cdot n &= 0 \quad \text{on } \Gamma(t). \end{aligned} \tag{3.48}$$

The initial conditions are determined by the homogenous steady state of (3.46) on $\Omega(0) = \{0\} \times \Omega_0$. The initial conditions are denoted by

$$u_0, \quad w_0, \quad a_0, \quad b_0.$$

Recall that $f_1(\tau_0, u) = 0$ has three homogenous solutions for $u_-(\tau_0) < u_m(\tau_0) < u_+(\tau_0)$. As initial condition, we take $u_0 := u_-(\tau_0)$. The conditions on the remaining reaction functions then imply that w_0, a_0, b_0 are unique.

2) Cytoskeletal mechanics. Let $v(t, x) : \Omega(t) \to \mathbb{R}^2$ be the velocity field. In the bulk, the velocity field has to be determined by

$$\eta \Delta v + \frac{\eta}{2} \nabla^{\perp} \mathrm{rot}(v) - \xi v = \nabla \Pi + \zeta_F \mathbb{1}_{\{a \geq a_{\mathrm{thr}}\}} p, \quad \text{on } \Omega(t), \tag{3.49}$$

where

$$\Pi = \Pi(a) = \frac{K_6}{\theta} \left(\left(\frac{a}{a_0} \right)^{\theta} - 1 \right) + \Pi_0. \tag{3.50}$$

The polarity field p has the values

$$p = \begin{cases} n & \text{on } \Gamma^L(t), \\ -n & \text{on } \Gamma^B(t), \\ 0 & \text{on } \Omega^B(t), \end{cases}$$

and on $\Omega^L(t)$ the polarity field p is defined by

$$p(t, x) = \begin{cases} n(\tilde{t}, x), & \text{if } P(t, x) \neq \emptyset, \\ 0, & \text{if } P(t, x) = \emptyset, \end{cases}$$

where $P(t, x) := \{t' \in \mathbb{R}_+ | t' < t, \ x \in \Gamma^L_{t'}\}$, $\tilde{t} := \sup P(t, x)$, and $n(\tilde{t}, x)$ denotes the outward unit vector in $x \in \Gamma^L_{\tilde{t}}$.

On the boundary $\Gamma(t)$, the velocity field has to satisfy

$$\begin{aligned}\eta\left(\nabla v + (\nabla v)^T\right)\cdot n = &-\zeta_B \mathbb{1}_{\{a<a_{\text{thr}}\}} K_5(wa - w_0 a_0)n + \gamma_1^m(\kappa_m - \kappa_0)n \\ &-\gamma_2^m\left(\int_{\Gamma_t} 1\ ds\right)n + (\Pi - \Pi_0)n.\end{aligned} \tag{3.51}$$

Membrane tension is given by

$$\tau := \frac{1}{\pi R_0^2}|\Omega_t|.$$

In particular, the initial membrane tension is $\tau_0 = 1$.

3.7 Discussion

We derived a simple model for mechanochemical cell polarization that considers Rho GTPase activation as a mediation process for directional F-actin polymerization and myosin-II-F-actin complex formation. The model contains a mechanical description of the AMC-layer which induces morphological changes and directional movement if F-actin polymerization and myosin-II-F-actin complex formation is triggered. In the model morphological changes affect membrane tension. The activation kinetics for the considered Rho GTPases are assumed to be dependent on membrane tension.
In Chapter 5 a heuristic explanation for the patterning mechanism of the model is given. In Chapter 4 the simulation results of the model in response to spatiotemporal perturbations are presented. Here, we briefly discuss the model assumptions with respect to their biological relevance.

Layer approximation The model geometry Ω_t describes the contact surface between the cell body and the substrate. The contact surface is considered as an effectively two dimensional sheet consisting of the plasma membrane at the basement. In the model, shape changes and movement of Ω_t are induced by the Rho GTP mediated material flux of F-actin. The layer approximation presented in Section 3.2 is adequate if, compared to the thickness of the layers, the normally directed diffusion in each layer is very small. In Section 3.2.1 we argued that normally directed diffusion in the layers is highly restrained due to the structure of the AMC and the plasma membrane. We suppose that plasma membrane located diffusion in the tangential direction is unaffected by the thickness of the membrane since membrane based Rho proteins are bound to receptor proteins that are anchored in the membrane. Variations in the thickness of the membrane may not affect lateral diffusion of the anchored protein complexes. Considering the diffusion properties in the AMC with vanishing thickness is more complicated. Although it is conceivable that the horizontal alignment of the polymers in the network has a less restraining effect for tangentially directed diffusion than for normally directed diffusion,

it is likely that also diffusion in the tangential diffusion is restrained due to the effects of densification. In the extreme case, where tangential diffusion is degraded by the same order as normal diffusion, we expect for the limit $\varepsilon \to 0$ of the layer-approximation that also the tangential diffusion component vanishes. Thus, the modelled spatiotemporal reaction dynamics in the AMC (which are the actin dynamics) are characterized by convection-reaction equations. This, however, is not a limitation for the patterning process. In the next chapter we will describe the patterning process in the case, where actin concentrations are controlled directly by spatiotemporal changes of active Rho, and in particular where the diffusion of actin is set to zero. Therefore, we expect that the model would lead to similar characteristics if the tangentially directed diffusion in the AMC is drastically reduced.

GTPase assumptions The reaction functions for Rac and RhoA base the observation that Rho GTP cycles between an inactive and active state [13]. Based on the known GEF complex formation in the Rho-activation pathway we derived, similarly as in [8, 25], an autocatalytic activation term for Rac and RhoA. According to experimental findings [35], we include that active Rac is inhibitory for RhoA activation by suggesting that Rac activity affects the deactivation rate of RhoA. Furthermore, we assumed that tension inhibits Rac- and promotes RhoA activation. The first assumption is supported by experimental findings [11]. The second assumption is hypothetical. However, due to the structural similarity within the family of small GTPases, it is conceivable that changes in tension also may affect RhoA. Moreover, it has been shown that microinjection of active Rac in Swiss 3T3 fibroblasts leads to immediate changes in lamellipodial dynamics and then, after a delay, to RhoA-dependent induction of F-actin-myosin-II complex formation [84]. Due to the hypothesized tension impact on RhoA, our model captures this motif via mechanical signal transduction: RhoA activity lowers membrane tension by promoting the contraction of the cell. A decrease in tension, in turn, promotes Rac activation.
Although we only model a very limited set of variables responsible for Rho activation, we consider the modelled characteristics mentioned above as biologically reasonable. However, a crucial simplification is the treatment of the concentrations u_2 and w_2 of inactive Rac and inactive RhoA as constants. This model assumption has primary numerical reasons. Necessary for the patterning mechanism is the existence of a domain $D \subset \mathbb{R}^2$ such that the dynamical system

$$\frac{du_1}{dt} = f_1(\tau, u_1, u_2)$$

is bistable for any $(\tau, u_2) \in D$. The determination of D and the required parameters for the model is numerically very expensive. By setting u_2 to a constant, the fitting of the system is tremendously simplified. We conjecture that the model is able to expose similar characteristics if u_2 is modelled explicitly. However, in this thesis, we confine ourselves to the cases in which u_2 is kept fixed.

Actin polymerization assumptions The actin kinetics are subjected to rough simplifications. The model only considers two types of actin, G-actin and F-actin that can interconvert into each other. Intermediate conversion steps as nucleation, elongation, and cofilin mediated dissoziation were neglected. Furthermore, we neglected the whole cascade of downstream effectors of Rho GTPases for the actin machinery, containing the Scar/WAVE complex and Arp2/3. This traces back to two reasons: First, the course of events starting from Rho signalling and ending by actin polymerization are very complex and not completely understood yet, cf. [48]. An in-depth-modelling of the contained cascades and subprocesses would go beyond our scope. Second, the model gives an account how mechanical and chemical signalling units need to interplay in order to achieve robust polarity. An heuristic model approach of F-actin dynamics avoids the danger of making predictions that are based on wrong conditions. Our appraoch provides a general framework that can be extended to more complex models. The patterning mechanism requires an increase of membrane tension due to changes of the cell morphology. How these changes are achieved in the mechanical modelling of the AMC is subordinate.
It should be stressed that the particular choice of the kinetics for both, Rho activation and actin filamentation, is to a wide extent arbitrary. More complex kinetics could be implemented easily as long as they do not contradict the conditions listed in Section 5.4.

Assumption for cell mechanics Our model of cytoskeletal mechanics is phenomenologically and bases loosely on active gel theory [85]. Therein G-actin monomers are treated as a sol and the cross-linked network of actin filaments is characterized by a viscoelastic material. The active gel approach captures certain experimentally observed features of actin networks: On short time-scales, the mechanical response after a perturbation of the network is elastic with a shear modulus E in the range of $10^3 - 10^5$ Pa [88]. On longer timescales, the actin network flows with a finite viscosity η of the order 100 Pa s [89].
The rheologic model which is used to describe the mechanical properties of the AMC bases on the *Maxwell model*. Our model contains a very basic and simplistic description of the AMC's rheology, were features as ATP consumption, the observed retrograde actin flow [46], filament stiffness and filament alignment induced polarity are neglected. A major simplification is that our model neglects the elastic response at short time scales. Since the mechanism only relies on a protrusion-retraction based generation of membrane tension, the mechanism may still work if a more complex representation of ACM mechanics is included in the model. However, a viscoelastic material might endow the model to exhibit additional biologically relevant features. We will reconsider this point in the summary given in Chapter 6.
The implementation of the boundary force terms play, apart from its biological motivation, a supporting role for the patterning mechanism: Curvature force acts for the polarized cell as a restoring force that drags the cell back into its spherical resting state,

if the Rho activity pattern erase. This induces a reset of the model cell and gives the cell the ability to remain re-excitable. This will be numerically verified in Chapter 4.

Chapter 4

Simulation

In this chapter the simulation results for the model listed in Section 3.6 are presented. The model at steady state is perturbed by a local stimulus that mimics an external signal.

4.1 Stimuli repertoire

An external stimulus increases activation of proteins such as Rho GTPases by up-regulating the GEFs that promote Rho GTP activation. To model the external stimulus, we superimpose an additional activation function f_S perturbing Rac dynamics (by adding to the first equation in system (3.46)). We suggest that stimulus induced activation recruits inactive Rho up to a certain level u_{act} as long as $(u_{\text{act}} - u) > 0$ and becomes inefficient as soon as this concentration is exceeded:

$$f_{\text{stim}}(t, x, u) = k_{\text{stim}}(t, x)(u_{\text{act}} - u),$$

where $k_{\text{stim}}(t, x)$ is the increased rate of Rac activation due to an external signal. The threshold u_{act} is set to the value that u adopts at the wave front, provided the system is excited.
Depending on the nature of the stimulus, the rate $k_{\text{stim}}(t, x)$ may be space- and time-dependent. In the simulations $k_{\text{stim}} = k_t^{\text{l}}$, $k_{\text{stim}} = k_t^{\text{r}}$, and $k_{\text{stim}} = k_t^{\text{t}}$ are used. Each stimulus affects approximately 10% of the cell for a duration of t seconds. The superscripts l, r, t indicate that the stimulus targets the cell at the left, right, and top of the cell, respectively.

Input stimuli The threshold u_{act} is set to the value that u adopts at the wave front, provided the system is excited. Under the default parameters listed in Table 4.1 this

value is $u_{\text{act}} = 1$. We define

$$s_T(t) = \begin{cases} \frac{1}{4} + \frac{1}{8}(1 + \cos(\pi t/T)) & \text{if } 0 \le t \le T, \\ 0 & \text{otherwise.} \end{cases}$$

We set for any $t \in I$

$$\begin{aligned} x_{\text{l}} &:= \min\{x_1 \in \mathbb{R} : (x_1, x_2) \in \Omega_t\}, \\ x_{\text{r}} &:= \max\{x_1 \in \mathbb{R} : (x_1, x_2) \in \Omega_t\}, \\ y_{\text{t}} &:= \max\{x_2 \in \mathbb{R} : (x_1, x_2) \in \Omega_t\}, \end{aligned}$$

and $L(t) := \operatorname{diam}(\Omega_t)$. We define

$$k_T^{\text{t}}(t, x) := s_T(t) \left(1 + \cos\left(\frac{x_2 - y_{\text{t}}}{L(t)}\right)\right) \mathbb{1}_{D^{\text{t}}}(x_1, y_2),$$

and for $j = \text{l}, \text{r}$

$$k_T^j(t, x) := s_T(t) \left(1 + \cos\left(\frac{x_1 - x_j}{L(t)}\right)\right) \mathbb{1}_{D^j}(x_1, x_2),$$

where

$$\begin{aligned} D^{\text{t}} &:= \{(x_1, x_2) \in \Omega_t : 0 \le y_{\text{t}} - y_{\text{l}} \le L(t)/5\}, \\ D^{\text{l}} &:= \{(x_1, x_2) \in \Omega_t : 0 \le x_1 - x_l \le L(t)/5\}, \\ D^{\text{r}} &:= \{(x_1, x_2) \in \Omega_t : 0 \le x_{\text{r}} - x_1 \le L(t)/5\}. \end{aligned}$$

The stimuli k_t^{lt} and k_t^{ld} whose impact will be discussed in the text below are defined as follows. For any $t \in I$ we set

$$m = 1/2(\min\{x_1 \in \mathbb{R} \mid (x_1, x_2) \in \Omega_t\} + \max\{x_1 \in \mathbb{R} \mid (x_1, x_2) \in \Omega_t\})$$

and define subsections

$$D^{\text{lt}} := \{(x_1, x_2) \in \Omega_t : x_2 >= y_{lt}(x_1)\}, \quad D^{\text{ld}} := \{(x_1, x_2) \in \Omega_t : x_2 <= y_{ld}(x_1))\},$$

where

$$y_{lt} := x_1 - (m - \sqrt{2}R_0 - 1), \quad y_{lu} := x_1 - (m - \sqrt{2}R_0 - 1).$$

The respective stimuli are given by

$$k_T^j(t, x) := s_T(t) \mathbb{1}_{D^j}(x_1, x_2), \quad j = lt, ld.$$

4.2 Parameter setting

Macroscopic parameters: Neutrophil granulocytes have an average diameter of $12-15\mu$m in peripheral blood smears. When analyzing neutrophils in suspension, neutrophils have an average diameter of 8.85μm [96]. As a compromise, we take the radius of the resting cell Ω_0 to be $R_0 = 5\mu$m.

Rho GTP related parameters: Following [97] the diffusion coefficients of the active Rho GTPs are set to $D_i = 0.1\mu\text{m}^2/\text{s}$ $(i = u, w)$. Similar values have been measured for membrane bound Cdc42 in *saccharomyces cerevisiae* [98].

The remaining parameter considering Rho dyniamics are fitted to the model: GEF hydrolysis is responsible for Rho inactivation. Thus, we take for the inactivation rate $\delta_i = 1\text{s}^{-1}$ $(i = 1, 2)$. As in [8], we assume that GAP hydrolysis matches in magnitude GEF activation by setting $\gamma_1 = 1\text{s}^{-1}$, $\gamma_2 = 2\text{s}^{-1}$. Again, following [8] , we take the baseline activity of GEF to be $k_i = 6.7 \cdot 10^{-2}\text{s}^{-1}$, $i = 1, 2$. The dissociation constant K_i $(i = 1, 2, 3)$ has the same unit of measurement as u, w, the concentration of active Rho. Here are the occurring concentrations normalized, such that $K_i = 1\mu\text{mol/dm}^2$ $(i = 1, 2)$, and $K_3 = 0.25\mu\text{mol/dm}^2$. Then, the homogenous steady state concentration of active Rho GTP is $u_0 = w_0 = 0.25\mu\text{mol/dm}^2$.

Actin related biochemical parameter: The diffusion coefficient of G-actin is set to $D_b = 10\mu\text{m}^2\text{s}^{-1}$. This value is a compromise with respect to reported values for G-actin in the cytoplasm, ranging from 3 to $30\mu\text{m}^2\text{s}^{-1}$ [99–101]. The diffusivity of F-actin is a model assumption for numerical reasons. We assume the diffusion coefficient of F-actin to be significantly smaller than D_b by taking $D_a = 0.01\mu\text{m}^2\text{s}^{-1}$. We deal with a normalized version of the F-actin dynamics and set $K_4 = 1\mu\text{mol/dm}^2$.

Mechanical parameter: We modelled the AMC as a purely viscous material. From a more realistic point of view, however, the AMC can be characterized as a viscoelastic material. The actin gel is a very soft material, and its elastic modulus is in the range of $E \approx 10^3$-10^4 Pa [102]. At longer time scales, actin flows and has a finite viscosity η. In in vitro experiments on actin, the characteristic viscoelastic relaxation time t^* where actin starts to flow is on the order of 10^2-10^3s [102]. In the simplest viscoelastic model proposed by Maxwell, the viscosity is related to the elastic modulus and the viscoelastic relaxation time by the so-called Maxwell relation $\eta = Et^*$[103]. Although we neglected the elastic character of the AMC we take these findings into account and set the dynamic viscosity to $\eta = 10^7\text{Pa} \cdot \text{s}$.

The friction coefficient strongly depends on the surface the cell adheres to. Micropipette experiments show that the frictional force of an actin gel on a 2μm diameter polystyrene bead coated with an activator of actin polymerization is on the order of 10nN [104]. We assumed the frictional force per unit area to be proportional to the migration velocity. Thus, by taking the mean migration speed $v = 0.4\mu\text{m/s}$ of neutrophils [39] we obtain that the friction coefficient is of the magnitude 10^7 Pa s/m. The reported friction coefficient of an actin gel on a latex bead is of the magnitude 10^{10} Pa s/m [105]. As a compromise we set the friction coefficient to $\xi = 3 \cdot 10^8\text{Pa} \cdot \text{s}/m$. Π_0 is set to the normal pressure

Quality	Value	Source	Quality	Value	Source
R_0	5 μm	[96]	k_1, k_2	$6.7 \cdot 10^{-2}$ s^{-1}	[8]
D_u, D_w	10^{-1} μm^2/s	[97, 98]	k_3, k_4	6.3 s^{-1}	$\star$
D_a	10^{-2} μm^2/s	$\star$	K_1, K_2, K_4	1 μmol/dm^2	[8]
D_b	10 μm^2/s	[99–101]	K_3	0.25 μmol/dm^2	$\star$
δ_1, δ_2, γ_1	1 s^{-1}	[8]	K_5	0.566	$\star$
γ_1^m	75	$\star$	K_6	$9 \cdot 10^4$ Pa	$\star$
γ_2	2 s^{-1}	[8]	h_0	1.987	$\star$
γ_3	4.3 s^{-1}	$\star$	α_1	2.1	$\star$
α_2	11.92	$\star$	ξ	$3 \cdot 10^8$ Pa $\cdot$ s/m	[104, 105]
ζ_F, ζ_b	$-2.1 \cdot 10^8$ Pa	$\star$	a_{thr}	0.938 μmol/dm^2	$\star$
θ	3	$\star$	Π_0	10^5 Pa	[106]
η	10^7 Pa $\cdot$ s	[102, 103]			

TABLE 4.1: Parameter values considered in the model simulations. $\star$ = fitted model parameter.

$\Pi_0 = 10^5$Pa [106].
The remaining parameters displayed in Table 4.1 are fitted model parameters.

4.3 Simulation results

Polarization characteristics

At first, we demonstrate that the model cell adopts a pinned wave front in u and w in response to a suitable stimulus and captures the features *maintenance* and *amplification* mentioned in Section 1.2.1. Therefore, we consider an initially unpolarized cell. In the model the cell is unpolarized if the mathematical system is at steady state. Then, the cell is geometrically represented by the spherical domain Ω_0, whose center is the origin of the x_1-x_2 plane. Figure 4.1 **a** displays a sequence of the evolution of the Rac distribution and of the cell shape in response to a local, transient stimulus applied at the left-hand side. The stimulus is modelled by k_{10}^l. The computational results show that the model cell responds to the stimulus by an increase in u at the front from the initial concentration $u_0 = 0.25$ up to $u_{\max} = 1.2$ within the first 10 seconds. After 10 seconds the stimulus expires and u at the front settles down to $u \approx 1$ within 40 seconds. This characteristic is maintained during the simulated time of 200 seconds. At the rear of the cell u remains throughout the simulated time close to its steady state value. Increased Rac activity induces an increase in membrane tension and locally suppresses RhoA activation. Conversely, membrane tension promotes RhoA activation. Figure 4.1 **b** displays a sequence of the induced evolution of active RhoA. Therein, the concentration of active RhoA, w, at the rear increases from the initial concentration $w_0 = 0.25$ up to $w_{\max} = 1.5$ while w at the front decreases to $w_{\min} = 0.02$ in the first 10 seconds and stabilizes at $w = 0.15$ after the stimulus is removed.
Figure 4.1 **c** displays the concentration profile of u along the central axis $\{x_2 = 0\}$ at different times. The horizontal axis indicates the percentage distance from the leading

front in relation to the cell length at each time t. The local rise in u is spatially amplified by a sharp wavefront. The graph at $t = 0$ displays the concentration profile of u induced by the stimulus k_{10}^l. A comparison of the profiles reveals that the initial profile is amplified up to the threefold on longer timespans. We performed test simulations up to $t = 2000$ seconds. Despite of slight shifts in the concentration and broadness of the wavefront, the profile in u adopts a constant wave-shape over the simulated time. The dotted line at $x = 27\%$ represents the mean horizontal axis of the inflection points of the waves.
In Section 5.5 we conjectured that the wave-speed oscillates relative to the moving domain. The oscillation of the wave-plateau displayed in Figure 4.1 **c** supports this hypothesis.

Actin dynamics

Figure 4.3 **a** and **b** display the evolution of the F-actin distribution $a(t, x)$ and the G-actin distribution $b(t, x)$ in response to stimulus k_{10}^l, respectively. A comparison with Figure 4.1 **a** shows that the spatial increase of $a(t, x)$ co-locates with the increase of $u(t, x)$. The delay between the half-value time of $u(t, x)$ and $a(t, x)$ at the front is approximately 6s. While the stimulus is active, the F-actin concentration $a(t, x)$ increases at the front, starting from its initial value $a_0 = 0.93$ up to the maximal value $a(t, x) = 1$. Afterwards, the concentration at the front settles at $a(t, x) = 0.96$ and remains stable from $t = 150$s on. At the back of the cell $a(t, x)$ remains approximately constant.
Changes in $a(t, x)$ cause changes in $b(t, x)$ due to mass conservation and a slow diffusion. At the homogenous steady state the G-actin concentration is $b(0, x) = 0.93$. Since $a(t, x)$ increases at the front, $b(t, x)$ decreases to 0.85 at the front within 50s while $b(t, x)$ in the cell body remains approximately constant. The profile is maintained, but the concentration at the front slightly increases to $b(t, x) = 0.86$ within $t = 150$.

Shape generation

The increased Rac activity locally promotes actin filamentation segmenting Ω_t in Ω_t^L and Ω_t^B (see Figure 4.3 **a**). The actively generated force F_{tread} acts outward and perpendicular to Γ_t^L, which leads to an even swelling of Ω_t^L. In Ω_t^B, however, the increased concentration of RhoA generates an inwardly directed force on Γ_t^B (see Figure 4.2 **c**). The inwardly directed force tapers the back of the cell. In combination, the joint forces effectuate a morphological change of the whole cell: The spherical resting shape transforms in response to a stimulus to a cone. In the simulation, a morphological steady state is adopted within 150s as displayed in the third panel of Figure 4.1 **a**.
The evolution of the shape undergoes three subsequent phases, an elongation phase (0-80s), a broadening phase (80-160s), and a stable phase ($>$ 160s) (see Figure 4.5 **a**).

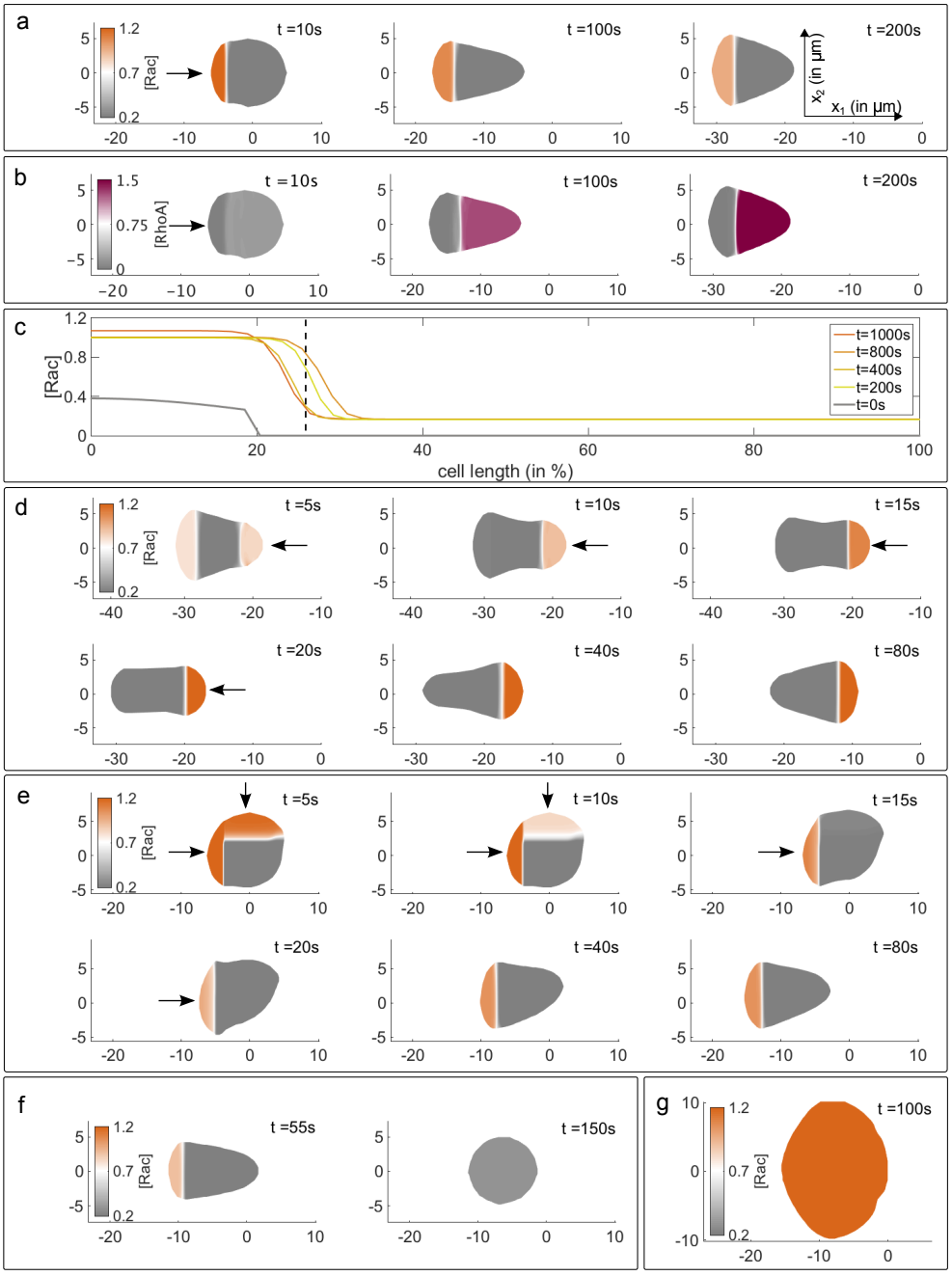

FIGURE 4.1: Polarization plots. The scale is in μm. The arrows indicate the regions of the applied stimuli. **a**, **b**: Polarization behavior and morphological change of the cell in response to k_{10}^{l}. Panel **a** (**b**) displays the distribution of active Rac (active RhoA). **c**: Distribution of u in relation to the cell length at different times. The graph at $t = 0$ shows the concentration profile of u induced by the stimulus k_{10}^{l}. **d**: Redistribution of u and morphological changes in response to repolarization. **e**: Two different located stimuli initiate competing fronts. The front created by the longer lasting stimulus is maintaned. **f**: Shape change and Rac erasure in response to an external increase in tension. **g**: Cell swelling due to decoupling of tension mediated Rac inhibition.

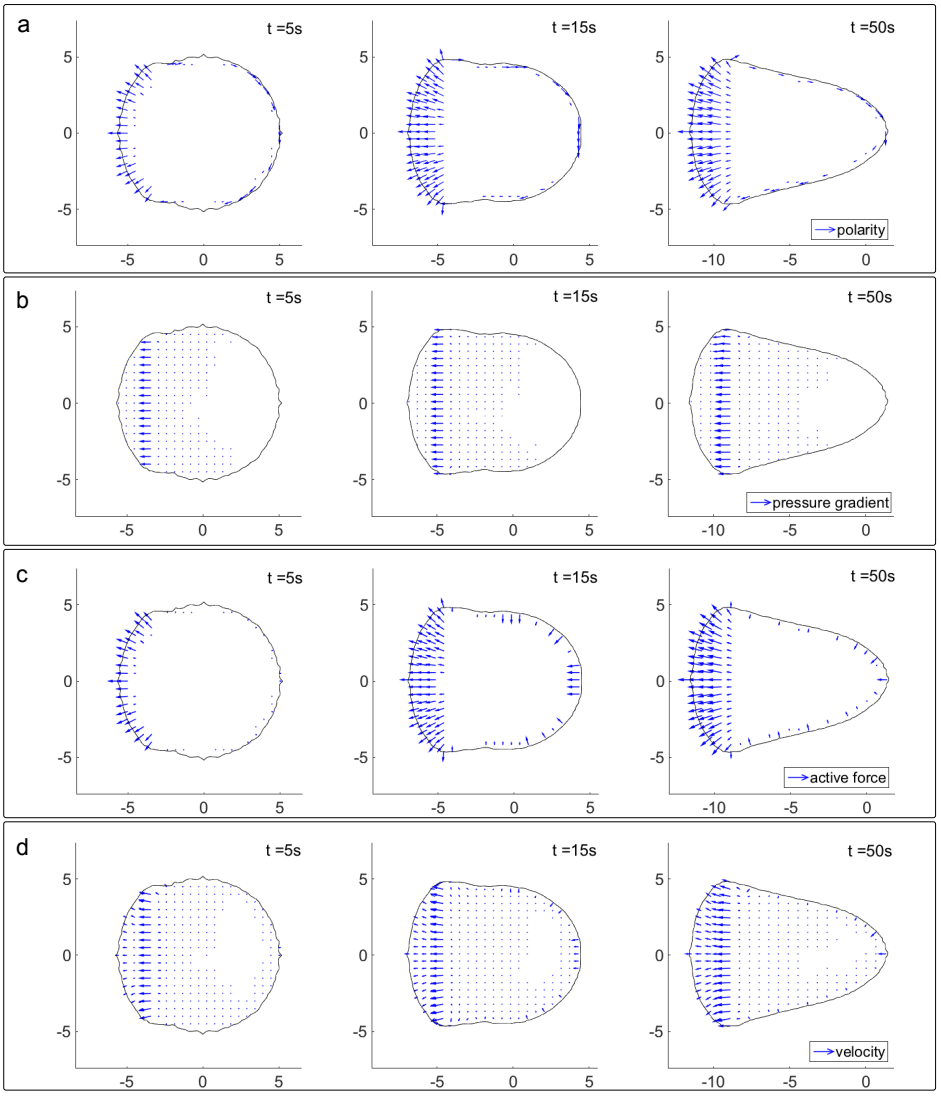

FIGURE 4.2: Vector field plots. The scale size is in μm. Panel **a** displays the generation and alignment of the polarity field p. Panel **b** (resp. **c**) displays the evolution of the pressure gradient $\nabla\Pi$ (resp. active force F_{act}). Panel **d** displays the evolution of the velocity field v.

In the first phase, the cell elongates by 35% due to a rapid increase of F_{tread} pointing towards the cell front. The elongation increases the surface area by $\sim 10\%$ and thus increases membrane tension. In the broadening phase the distribution of F_{tread} is almost constant, while the cell contracts due to an increase of F_{cont}. This results in an increase of the width of the front by 18% and a decrease of the length by 12%. In the last phase, the system stabilizes and length and width settle at $\sim 12\mu$m and $\sim 10\mu$m, respectively. Throughout the broadening and the stable phase the surface area remains approximately constant (see Figure 4.3 **e**).

After $t = 80$ the cell adopts a constant migration speed of about $v^* = 0.19\mu$m/s that is maintained throughout the duration of the simulation.

Repolarization characteristics

We tested if the already polarized model cell has the ability to become reexcited, i.e. to respond to new incoming stimuli with reorientation. This refers to feature 3) listed in Section 1.2.1. We prepolarized the model cell by stimulus k_{10}^{l}. At time $t = 150$s a new stimulus k_{40}^{r} at the opposite site of the cell is applied for 40s. In Figure 4.1 **d** a sequence of the simulation results is displayed. The stimulus triggers a new wave front in u on the right hand side. Consequently, the two opposing fronts generate an increase in membrane tension due to the triggered opposed F-actin treadmilling (see Figure 4.3 **e**). The increasing membrane tension erases the wavefront located on the left side within 15s after the new stimulation of the cell. The new wavefront on the right persists, since there the stimulus is still maintained. The erasure of the old front in u leads to a local increase in w, since u suppresses w. This induces an increased force pointing to the inward normal at the old front, which reduces membrane tension. In the simulations membrane tension approaches a steady state within 40s after the new stimulus was applied. The cell adopts an intermediate dumbbell-like shape. Afterwords the cell readopts a "V"-shape at $t = 80s$. The model cell remains in this shape and u and its downstream maintain their newly gained wavefronts.

Resolving conflicts

Referring to feature 4) in Section 1.2.1, we tested whether the model cell is capable of the resolution of neighboring fronts. Two competing stimuli, k_{30}^{l} and k_{10}^{t}, were applied perpendicular to each other to the model cell. Both stimuli individually have the ability to polarize the model cell. However, the left-handed stimulus k_{30}^{l} lasts 20s longer than the stimulus k_{10}^{t} at the top. Figure 4.1 **e** displays the behavior of the model cell if both stimuli were applied. The arrows indicate the targeted locations of each stimulus, k_{30}^{l} on the left and k_{10}^{t} at the top. The stimuli trigger two local fronts in u. Thus, in turn, membrane tension increases by a factor of 1.3 within 15s (see Figure 4.3 **e**). The increase globally lowers the active Rac concentration u. This leads to an expiration of the wave front generated by the shorter lasting stimulus as soon as k_{10}^{t} ends. Simultaneously, membrane tension settles down at $\tau \approx 1.1$. Hence, the wavefront generated by the longer lasting stimulus is maintained. The maintained wavefront causes the model cell to migrate along the negative x_1-direction. The formerly crooked shape of Ω_t settles back to the normal "V"-shape beginning at $t = 20$s and approaches a morphological steady state at $t = 150$s.
We also tested whether the model cell is capable of the resolution of opposing fronts. If one stimulus lasts longer than the other, the result is similar to the described behavior above: The wavefront induced by longer lasting stimulus is maintained and the other wavefront erases (see Figure 4.3 c). Moreover, we tested the behavior of the cell in response to two qualitatively identical stimuli applied at different locations (see Figure

4.3 s). In this case, even for closely located stimuli, the competing wavefronts erase each other due to the generation of membrane tension and the cell readopts the homogenous steady state.

Membrane tension confines active Rac to the leading front.

During the simulated time, the plateau of increased u remains confined to the leading front of the model cell. We claimed membrane tension τ to be responsible for the confinement. To exclude other possible subliminal factors that might be responsible for the confinement, we performed simulations in which $h_i(\tau(t))$ $(i = 1, 2)$ were replaced by $h_i(\tau_0)$, where $\tau_0 = 1$ denotes the initial membrane tension of the resting cell. The simulated cell shape and active Rac distribution after 100 seconds is displayed in Figure 4.1 **g**. The plot reveals that the Rac activity wave is not stalled and continued to traverse the model cell from front to back. This is accompanied by a swelling of the cell: Since u is homogeneously increased after 100 seconds, the F-actin concentration exceeds the threshold a_{thr} in the whole cell. The swelling is generated by the pushing force due to treadmilling which acts in this scenario on the whole boundary of the whole cell.
Furthermore, we tested whether a sufficient increase in membrane tension is capable to erase the Rac activity front in a polarized cell. In response to the stimulus k_{10}^l, tension τ peaks at $\tau_{\max} = 1.18$ at time $t = 13.75$s. (See Figure 4.3 **e**). To test the behavior of the cell when the tension exceeds this value due to external effects, we stimulate the cell by k_s and artificially set $\tau = 1.25$ at $t = 50$ for 10s. Figure 4.1 **f** displays the response of u and of Ω_t. The numerical experiment shows that the increased front of u erases. Thus, the downstream w, a, and b also approach a spatially homogenous state while the mechanical system tends to an equilibrium. The shape at equilibrium is Ω_0, which the cell adopts at $t = 150$s.

Competing wavefronts

Figure 4.3 **c** displays the evolution of the cell shape and the redistribution of Rac in response to the oppositely applied stimuli k_{30}^l and k_{10}^r. The behavior is similar to the case described in 4.1 **e**. Each stimulus triggers a wavefront of active Rac. The cell starts to expand due to oppositely directed F-actin treadmilling which increases membrane tension. The increase leads to an expiration of the wavefront created by k_{10}^r, the shorter lasting stimulus, within 15s and the increase of contractile force reduces the cell surface. Thus, membrane tension lowers. Due to the decreased membrane tension, the front created by k_{30}^l is maintained. The cell adopts a steady "V"-shape within 80s.
Figure 4.3 **d** displays the evolution of the cell shape and the redistribution of Rac in response to the stimuli k_{10}^{lt} and k_{10}^{ld}. As in Figure 4.1 **e** the stimuli are perpendicular to each other, but in this case both stimuli have the same time course. The generated wavefronts broaden the cell and induce a crescent shape. The broadening increases

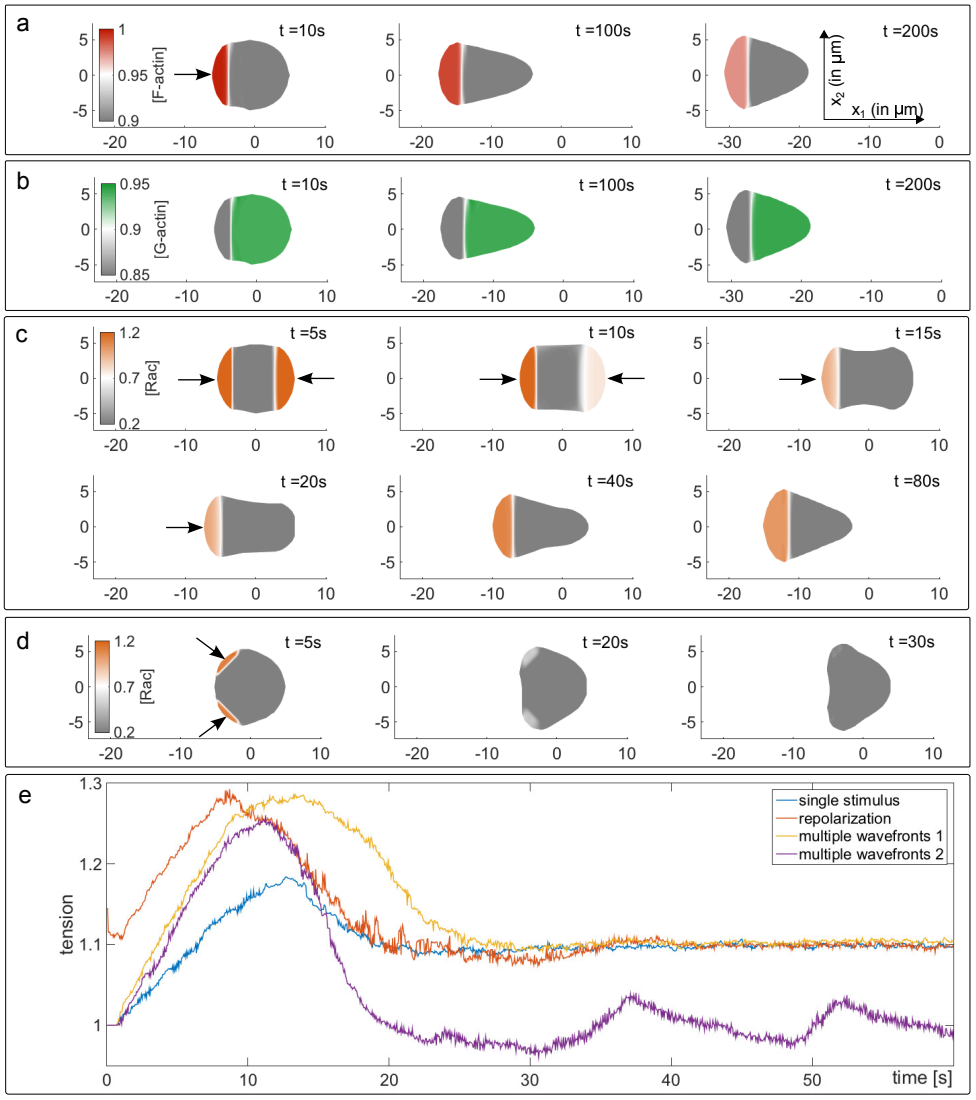

FIGURE 4.3: **a** – **d**. Polarization characteristics and morphological change in response to different stimuli. The scale is in μm. The arrows indicate the regions of the applied stimuli.Evolution of the distribution of F-actin (**a**) and G-actin (**b**). **c**. Two different stimuli initiate competing fronts. The front created by the shorter lasting stimulus expires. **d**. Two equally long lasting stimuli create competing fronts. Both fronts erase due to an increase in tension. **e**. Time-versus-tension plot of the model in the four different scenarios. Evolution of tension if the cell is polarized by the transient single stimulus k_{10}^{l} (blue profile), two oppositely applied stimuli k_{30}^{l} and k_{10}^{t} (yellow profile), two neighboring stimuli k_{10}^{ld} and k_{10}^{lt} (purple profile). The red profile displays the evolution of the tension if an already to the left polarized cell is exposed to the new stimulus k_{40}^{t}.

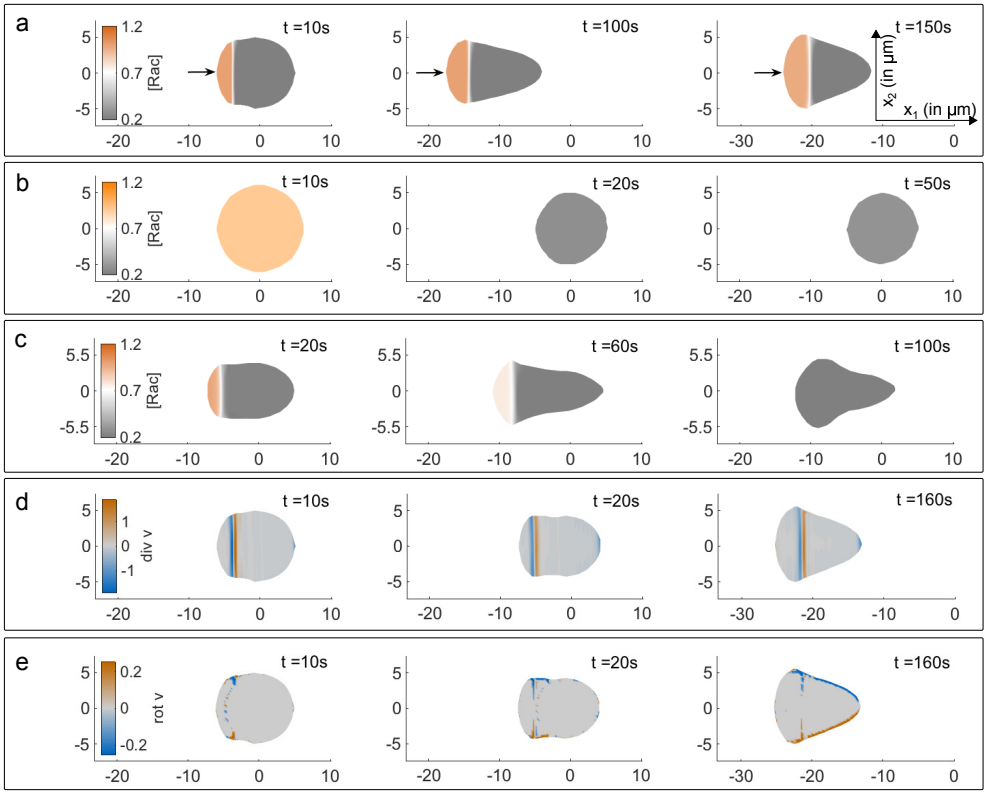

FIGURE 4.4: **a**. Polarization characteristics in response to the temporal maintained stimulus k^l_∞. **b**. Polarization characteristics in response to a $10s$ lasting spatially uniform stimulus. The concentration of Rac increases uniformly and uniformly generated active force induces swelling. The cell reapproaches its resting state if the stimulus is removed. **c**. Cell response to the stimulus k^l_{10} when the cell back locally fixed. The cell elongates due the triggered protruding front. Increasing membrane tension induces the Rac front to expire. **d**–**e**. Plots of the divergence $\mathrm{div}(v)$ and the rotation $\mathrm{rot}(v)$ in the unit s^{-1}, respectively.

membrane tension within the first 10s up to $\tau = 1.25$, cf. panel **e**. This induces an expiration of both wave fronts as soon as the stimuli are removed. The cell tightens and tends back to its spherical steady state accompanied by a decrease of membrane tension.

Polarity in response to maintained stimuli

The model also generates polarity fronts in response to permanent stimuli. The behavior of the cell shape and the distribution of active Rho in response to the permanent stimulus $k^l_\infty = \lim_{T\to\infty} k^l_T$ and in response to the transient stimulus k^l_{10} are very similar. The simulation result is presented in Figure 4.4 **a**. In response to two simultaneously beginning stimuli, k^l_∞ and k^r_{10} (resp. k^t_{10}), the cell forms a unique axis of polarity pointing towards k^l_∞. The front originated by k^r_{10} (resp. k^t_{10}) expires. (Data not shown). The model, however, is not capable of resolving conflicts and fails to produce interpretable results if both of the simultaneously beginning stimuli are permanent.

Cell swelling in response to spatially uniform stimuli

Some cell types exhibit adaptation in a uniform stimulus, that is, the cells generate a persistent response to a gradient of chemoattractant, but transient response to a temporal change in a uniform stimulus [7]. To a certain extent the model captures this feature. In response to the spatially uniform stimulus

$$f_{\text{stim}}(t, x, u) = (u_{\text{act}} - u),$$

active Rac increases homogeneously and the model cell swells until the stimulus is removed at $t = 10$s. Afterwards the cell returns to its resting state. The simulation results are displayed in Figure 4.4 **b**.

Expiration of polarity in response to mechanical manipulation.

Suction experiments provide evidence that neutrophils with a polarized front depolarize if the cell body is fixated to the substrate [11]. The protrusion of the front induces an elongation of the cell which increases membrane tension. The increased tension regarded to be responsible for the expiration of the Rac activity front.
We tested whether our model captures this feature. We virtually fixated the cell back by setting the velocity $v(t, x)$ to zero for $x_1 > 4$ and stimulated the opposite side of the cell by k_{10}^l. Figure 4.4 **c** displays the morphological response and the evolution of the Rac pattern at selected times. The cell expands in the horizontal axis by a magnitude of 1.5 within 60s. Simultaneously, the tension τ increases up to $\tau = 1.22$. This induces an expiration of the Rac activity front within 100s.

Behavior of the velocity field

The model cell migrates in the direction of an applied stimulus. At the generated cell front Ω_t^{L} the velocity field aligns almost parallel to the direction of the stimulus while myosin mediated contractions in the back generate a velocity field perpendicular to the boundary Γ_t^{B}, see Figure 4.2 **d**. The flow is compressible. Thus, the divergence of the velocity field is non-zero. In Figure 4.4 **d** the divergence of v with respect to the cell domain is displayed at selected times. Since at the front holds $a(t, x) > a_{\text{thr}}$, the actively generated force $F_{\text{act}}(a)$ at the front is constant. Moreover, the slope of $a(t, x)$ is flat at the front, which implies that there the pressure gradient $\nabla\Pi(a)$ is small. The simulation results show that there the divergence of v is close to zero. At the back of the cell the active force vanishes apart from the boundaries and, due to the flatness of $a(t, x)$ the pressure gradient $\nabla\Pi(a)$ is small. According to the simulation results, the divergence of v is also close to zero in this regions. Close to the transition zone, where $a(t, x) - a_{\text{thr}}$ changes its sign, the divergence adopts positive values if $a(t, x) < a_{\text{thr}}$ and negative

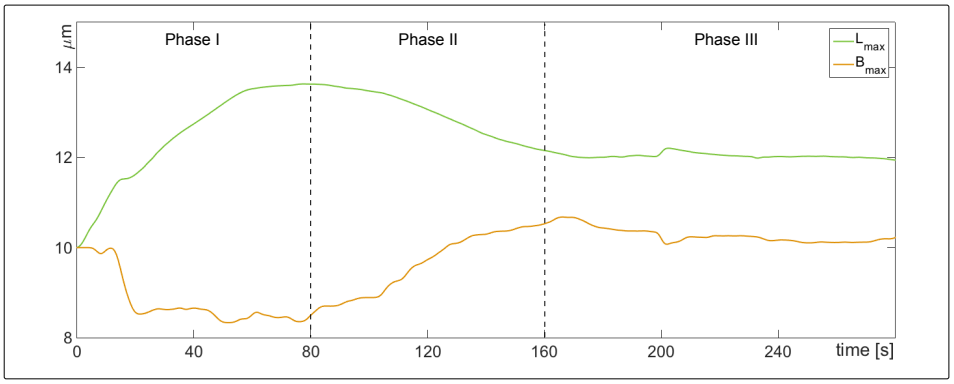

FIGURE 4.5: Evolution of cell length, L_{max}, and cell width, B_{max} if the cell is stimulated by k_{10}^{l}. The evolution can be divided into three subsequent phases: a phase in which L_{max} increases and B_{max} decreases (Phase I), a phase in which L_{max} decreases and B_{max} increases (Phase II), and a phase in which the deflections settle down (Phase III).

values if $a(t,x) > a_{\text{thr}}$. The absolute value of the divergence peaks at $t = 6$s, where $|\text{div}(u)| = 1.21\text{s}^{-1}$.

We investigated the vorticity of the flow, see Figure 4.4 **e**. As to be expected for a slow creeping flow [107], the rotation of the vector field $\text{rot}(v)$ is with a magnitude of about 10^{-1}s^{-1} very low. Vortices predominantly occur in the transition zone, where $a(t,x)$ is close to a_{thr} and in the periphery of Ω_t^{B}. In the positive half space $\{x_2 > 0\}$ the vortices are mainly clockwise, $\text{rot}(v) < 0$. In the negative half space $\{x_2 < 0\}$ the vortices are mainly counterclockwise, $\text{rot}(v) > 0$.

The terms

$$\nabla^{\perp}\text{rot}(v)$$

in (3.39) and

$$(\nabla v)^T$$

in (3.44) are predominantly constitutive for the generation of vortices. We tested whether we can neglect these terms by taking the equations

$$\eta\Delta v - \xi v - \nabla\Pi = -F^{\text{act}} \quad \text{on } \Omega(t),$$

and

$$\begin{aligned}\eta\nabla v \cdot n = &-\zeta_B \mathbb{1}_{\{a<a_{\text{thr}}\}} K_5(w - w_0)n + \gamma_1^m(\kappa_m - \kappa_0)n \\ &-\gamma_2^m\left(\int_{\Gamma_t} 1\ ds\right)n + (\Pi - \Pi_0)n \quad \text{on } \Gamma(t),\end{aligned}$$

for the velocity field. The qualitative behavior of this system with respect to shape and pattern generation remains the same. The quantitative differences in comparison to the original model are minor. The simulation results for the case in which the operators $\nabla^{\perp}\text{rot}(v)$ and $(\nabla v)^T$ are neglected will be presented more in detail in [108].

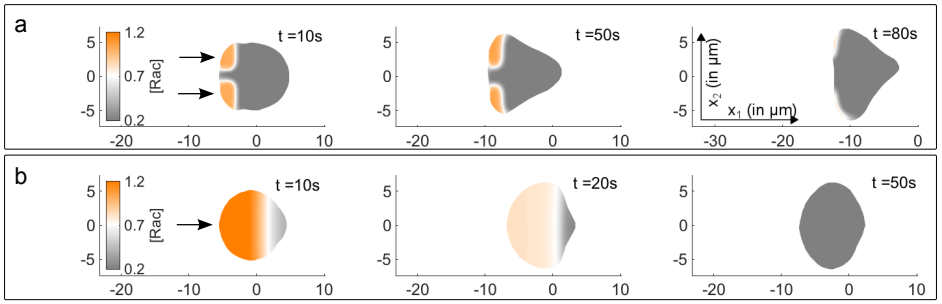

FIGURE 4.6: Rac distribution and morphological changes in response to different stimuli. The arrows indicate the location of the applied stimuli. Panel **a**: Behavior of the cell in response to the double stimulus defined by (4.1). Panel **b**:Behavior of the cell in response to the linearly graded stimulus defined by (4.2) with $(T, \alpha) = (6, 0.5)$.

4.4 Limitations

The model exhibits several shortcomings. Many of them may be resolved due to additional assumptions, others are model specific. We briefly discuss three model specific limitations.

There is evidence that spontaneous polarization in mammalian neutrophils is triggered by fluctuations of RhoA [109]. However, due to its deterministic nature a limitation of the model is that it does not cover stochastic effects like spontaneous polarization in response to noise. An adaptation of the model to noise sensitivity would require a coupling with a stochastic system as an upstream that *translates* stochastic inputs into well-regulated signals. Another limitation is that the model is very likely not capable of fusing neighboring wavefronts into one single front. We performed simulations in which the cell is stimulated in two adjacent regions by taking

$$k_{\text{stim}}(t,x) := \begin{cases} k_{10}^{l}(t,x), & \text{if } |x_2| < 2/3, \\ 0, & \text{otherwise.} \end{cases} \tag{4.1}$$

Figure 4.6 **a** displays a sequence of the evolution of the cell shape and of the Rac distribution. Therein two neighboring wavefronts are generated, but do not coalesce. On the contrary, the activity fronts tear the cell in different directions until the increased membrane tension induces an expiration of the front. We hypothesized that neighboring wavefronts do not coalesce due to the very slow diffusion of active Rac and tested whether a fusion occurs for increased values of D_u. We took the values $D_u \in \{0.5, 0.75, 1, 2.5, 5, 10\}$. For $D_u = 0.5$ the simulation result is similar to the formerly described case: The wavefronts do not coalesce, but expire within 80s. For $D_u \geq 0.75$ both wavefronts extinguish significantly earlier. We conjecture that this dues to a failure of the patterning mechanism, since the mechanism requires a sufficiently slow diffusion of active Rac. A biologically reasonable modification that potentially endows the model with the ability to fuse neighboring fronts aims at the explicit inclusion of inactive Rac. Inactive Rac might diffuse faster than active Rac [97]. While active Rac is locally pinned, inactive Rac might be

free to diffuse on a medium range and become activated at the periphery of the pinned wave patterns. This would locally smoothen the patterns and may induce a fusion of closely neighboring wavefronts.
In some experimental settings the lamellipodium of neutrophils often tends to remain intact and cell migration follows a semicircular path ("U" turn) in response to a spatially change of the stimulus [110, 111]. For this purpose we performed test simulations with a spatially changing stimulus over time. However, we model was not capable to reproduce this feature with an realistic account.
Finally, a limitation is that the cell requires for a stable polarization a stimulus which spatially decreases superlinearly: We tested wether the model cell responds to linearly graded stimuli. The linearly graded stimuli were defined by setting in f_{stim}

$$k_{\text{stim}}(t,x) := s_T(t)\alpha\left(\frac{x_1 - x_b}{L_t}\right), \quad (t,x) \in \Omega(t), \tag{4.2}$$

for fixed $T > 0,\ \alpha > 0$. For the values (T, α)= $(10, 0.5)$, $(10, 0.3)$, $(8, 0.8)$, $(6, 1)$, $(6, 0.5)$, $(3, 0.4)$, the cell only develops transient polarity patterns. Figure 4.6 **b** shows that the cell area in response to a linearly graded stimulus is highly increased. This leads to an expiration of active Rac. However, the transduction from a external gradient to an interior signal via integrins is not well understood yet. It may well be that the transmission from external linear gradients to interior signals acting on Rho GTP bears nonlinear transformations. On a multicellular level, e.g., it has been shown that cells can amplify shallow gradients by transforming them into steep local gradients [112]. We conjecture that this also applies to a certain extent on a singular cell level.

4.5 Parameter dependance

The model equations can be subdivided into a mechanical and a biochemical part. The mechanical part consists of equations (3.49) and (3.51). The biochemical part consists of equations (3.46) and (3.48).
A qualitative requirement of the mechanical system is that the default resting state has to be an equilibrium point. This assures the cells ability to readopt the default resting state in the event of expired polarity.
Qualitatively, parameter variations in the mechanical system primary effect the shape determination of the model cell. The plots **b**-**e** in Figure 4.7 display the horizontal and vertical extension of the cell after $t = 80$s for parameter variations including viscosity, pressure, treadmilling force, and contractile force, respectively. Viscosity: In the parameter regime $\log(v^*) \in [-2, 1]$ the expansion of the cell along the horizontal axis and the shrinkage in the vertical direction is almost linearly correlated to $\log(v^*)$. For $\log(v^*) > 1$ the cell shape transforms from the "V"-shape to an elliptic shape. We could not achieve robust polarity patterns if $\log(v^*) > 1.5$. Pressure: Changes in the pressure coefficient in the regime $\log(\Pi^*) \in [-1, 2]$ have a minor influence on the cell shape. The

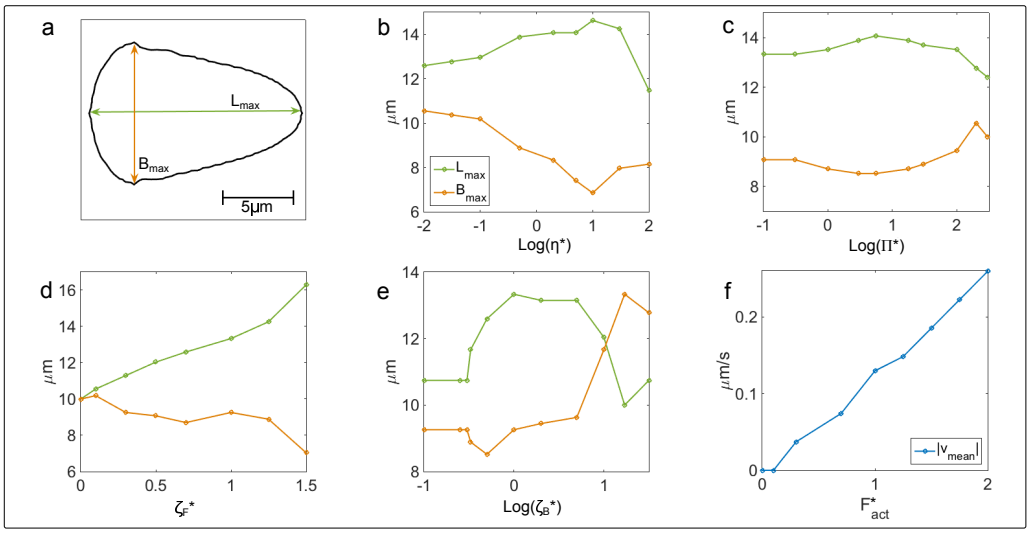

FIGURE 4.7: Shape and motility dependance on parameter variation. Panel **a**: A spherical model cell with parameters listed in Table 4.1 was stimulated by k_{10}^l. The contour displays the shape of the cell at $t = 80$s. The green line denotes $L_{\max}$, the horizontal extension of the cell. The orange line denotes $B_{\max}$, the horizontal extension of the cell. Panels **b-e** display the effect on $L_{\max}$ and $B_{\max}$ at $t = 80$s for variations of a parameter $p \in \mathbb{R}$, respectively. The symbols η, K_6, ζ_F, ζ_B denote the parameters as listed in table 4.1. Panel **b** shows the effect of variations if p is the viscosity coefficient. η^* is defined as $\eta^* := p/\eta$. Panel **c** shows the effect of variations if the pressure factor K_6 is replaced by p. Π^* is defined as $\Pi^* := p/K_6$. Panels **d** and **e** display the effect of variations if ζ_F and ζ_B are replaced by p, respectively. ζ_i^* is defined as $\zeta_i^* = p/\zeta_i$ for $i = F, B$. Panel **f** displays the correlation between the movement velocity of the cell at $t = 80$s and the intensity of active force if F_{tread} in (3.41) and F_{cont} in (3.45) are replaced by $F_{\text{act}}^* F_{\text{tread}}$ and $F_{\text{act}}^* F_{\text{cont}}$.

cell adopts a biologically unrealistic, bulky shape if $\log(\Pi^*) > 2$. Treadmilling force: The system is sensitive to changes in ζ_F^*. If $\zeta_F^* \leq 0.25$, the cell remains almost static with a spherical shape. The Rac activity front expires within $t = 100$s. In the parameter regime $\zeta_F^* \in [0.3, 1.25]$ ζ_F^* correlates almost linearly with $L_{\max}^*$ while having a minor influence on $B_{\max}^*$. If $\zeta_F^* \geq 1.5$, the model cell adopts a biologically unrealistic cylindrical shape. The polarity pattern, however, is still maintained for $\zeta_F^* = 1.5$. Contractile force: For small parameters $\log(\zeta_B) < -0.5$ extinguishes the polarity within $t = 100$s. The cell remains static and adopts a transient elliptic shape. If $\log(\zeta_B^*) \in [-0.5, 0.7]$, $L_{\max}$ is increasing until it adopts a plateau at $\log(\zeta_B^*) \geq 0$. $B_{\max}$ slightly decreases for $\log(\zeta_B^*) \in [-0.5, -0.25]$ and recovers for values $\log(\zeta_B^*) \in [-0.25, 0.7]$. For values $\log(\zeta_B^*) > 0.7$, the cell adopts an elliptic shape and fails to maintain polarity.

Figure 4.7 panel **f** shows the migration velocity of the cell in dependance of the intensity of active force. If $F_{\text{act}}^* < 0.1$, the cell remains motionless. If $F_{\text{act}}^* > 0.1$, there is an almost linear relation between v_{mean} and F_{act}^*.

While in the mechanical subsystem slight parameter deviations from the original calibration primarily induce shape changes without influencing the polarization characteristics, parameter variations in the biochemical subsystem may have a switch-like effect

on the maintenance of the patterning mechanism. Although the particular choice of the rate functions f_1, f_2, g is to a large extent arbitrary, a necessary qualitative feature of $f_1(\tau, u)$ is its bistability with respect to u. More precisely, it is required that $[u \mapsto f_1(\tau, u)] : \mathbb{R} \to \mathbb{R}$ has a non-empty parameter regime $[\tau_-, \tau_+]$ in which the dynamical system $u' = f_1(\tau, u)$ is bistable. While in the mechanical subsystem slight parameter deviations from the original calibration primarily induce shape changes without influencing the polarization characteristics, parameter variations in the biochemical subsystem may have a switch-like effect on the maintenance of the patterning mechanism. Although the particular choice of the rate functions f_1, f_2, g is to a large extent arbitrary, a necessary qualitative feature of $f_1(\tau, u)$ is its bistability with respect to u. More precisely, it is required that $[u \mapsto f_1(\tau, u)] : \mathbb{R} \to \mathbb{R}$ has a non-empty parameter regime $[\tau_-, \tau_+]$ in which the dynamical system $u' = f_1(\tau, u)$ is bistable.
An explanation and the contributing necessary conditions for patterning mechanism are presented in Chapter 5.

4.6 Discussion

In this section we compare the simulation results to biological data.
In the Simulation part we demonstrated that the model cell adopts a pinned wave-front in response to suitable stimuli and that polarization exhibits the demanded qualitative features of maintenance and amplification, as presented in Section 1.2.1. We demonstrated that in response to a single external stimulus an emerging wave-pattern of active Rac predefines the cell front and that the concentration of RhoA is increased in the back of the cell. F-actin is locally increased at spots of high Rac activity. Regions, where the F-actin concentration exceeds a certain threshold where interpreted as the lamellipodium. These simulation results coincide with experimental observations on the polarization characteristics of mammalian neutrophils [113].
In the simulations the cell morphology changes due to the generation of the Lamellipodium, characterized by a broad front and a tapered rear of the cell. We demonstrated that simultaneously to the generation of the Lamellipodium directional cell movement occurs. The movement approaches a constant speed within the first 80 seconds of about $v^* = 0.19\mu$m/s that is maintained throughout the duration of the simulation. In vitro experiments suggest, that leukocytes in response to fMLP adopt a morphological steady state within 2 to 3 minutes [110], which fits the time required by the model in very good agreement. Moreover the mean migration speed obtained by the model is in a good agreement with experimental measurements. The in vitro measured mean migration speed for neutrophils in focal chemoattractant chambers is of the order $10^{-1} - 10^{0} \mu m/s$ [39].
We demonstrated that the model cell is sensitive to new incoming stimuli such that the cell realigns towards new incoming stimuli. If the stimuli are applied at opposite ends, the cell transiently develops a dumbell-like shape. The model cell repolarizes due to the

dissolving of the lamellipodium at the former front and the lamellipodium reassembles at the new, triggered Rac front. This coincides with experimental observations of prepolarized and fMLP-reexcited neutrophils in cell chamber assays [114]. In other experimental settings the lamellipodium of neutrophils often tends to remain intact and cell migration follows a semicircular path ("U" turn) in response to a spatially change of the stimulus [110, 111]. For this purpose we performed test simulations with a spatially changing stimulus over time. However, the simulations revealed that our model cell lacks of this feature. Thus, the model captures feature 2) presented in Section 1.2.1 to a certain extent: Reversal repolarization is captured well, but only for special stimuli, while a 'U" turn response to certain spatially variable stimuli is not achieved by the model.

To a certain extend the model cell is capable to resolve multiple-front conflicts by the resolution of these multiple fronts into a single axis of polarity. However, we demonstrated that the characteristic crucially depends on the design of the stimuli. If stimuli of the same duration and intensity are applied at opposite ends of the cell, a depolarization of the cell may occur. In this event the cell readopts its predefined spherical resting state.

In the simulations we validated that the Rac activity front is confined by membrane tension. An artificial reduction of membrane tension induces spreading of active Rac across the whole cell domain. On the other hand, we demonstrated that mechanical manipulations affect the polarization process. If one end of the model cell is kept fixed and the other end is polarized, the cell elongates until membrane tension exceeds a critical level which induces depolarization. This characteristic coincides with experimental observations in which polarized neutrophils depolarize if the cell body is highly elongated by external mechanical manipulations [11]

We demonstrated that the model cell responds to a spatially uniform increased stimulus by swelling. The cell readopts the spherical resting state if the stimulus is removed. Cell swelling in response to a homogenous chemoattractant has been observed in cells like budding yeast [7] and is not directly related to neutrophil polarization characteristics.

We addressed certain limitations of the model. The model does not exhibit noise sensitiveness. The model does either not respond to noisy initial conditions at all or it develops unrealistic polarity patterns. A further limitation is that the model is not capable of fusing neighboring wave-fronts into one single front, which we consider as a restriction for the demanded feature 4) in Section 1.2.1.

Finally, we demonstrated that the cell requires for a stable polarization a stimulus which spatially decreases superlinearly. To obtain robust polarization in response to a linearly decreasing stimulus, the stimulus has to be transferred into a superlinearly decreasing signal. It is conceivable that the signal conduction from external linear gradients to interior signals acting on Rho GTP yields a nonlinear transformation of the gradient. On a multicellular level, e.g., it has been shown that cells can amplify shallow gradients by transforming them into steep local gradients [112]. We conjecture that this also applies to a certain extent on a singular cell level.

Taking the main aspects into consideration and reconsider the demanded features presented in Section 1.2.1, we conclude that the model captures the features 1) and 2) quite well. Feature 3) is captured for certain types of stimuli, but the model does not exhibit reorientation in response to spatially variable stimuli. The model renders feature 4) quite accurately but is limited to the case in which competing stimuli are sufficiently far apart from each other. Feature 5) is not supported by the model. We have validated that the model exhibits feature 6), 7) and 8). Finally, we demonstrated feature 9), the demanded ability to depolarize and to readopt a spherical resting state if membrane tension is artificially increased.

Chapter 5

Mechanism of Mechanochemical Wave-Pinning

In this chapter we present a simplified, spatially one dimensional version of the model in which the ability to exhibit mechanochemical wave-pinning is retained. This chapter can be read without knowledge about the subsequent chapters. In contrast to the original model, we neglect the boundary forces and the internal pressure. Furthermore, we assume that the polarity field is implicitly given by $p = 1$, and that the transition of the active force from front to back is smooth.

The simplified model again consists of three interconnected units: biochemical signalling of Rho GTPases, cytoskeletal mechanics, and membrane tension. The simplified model considers the concentration profile of the Rho GTPases Rac and RhoA along a cell diameter transect, front to back, approximated as a one-dimensional segment: Active Rac and active RhoA are assumed to affect the mechanics of the cytoskeleton in two different ways. Active Rac induces a protrusive force which leads to an extension of the cell front and active RhoA induces a contractile force which leads to a shrinkage of the posterior. Again, we assume that membrane tension is proportional to the diameter of the cell and that it promotes RhoA activation and inhibits Rac activation.
To model Rho activation, we take a very simple reaction-diffusion approach. The active Rho proteins are assumed to be slowly diffusing with respect to the size of the cell and the time-scale in which polarization occurs, while the distribution of inactive Rho is treated as a constant for simplicity. The activation functions for Rac and RhoA depend on membrane tension. To preserve a general approach of the patterning mechanism, we omit the explicit modelling of the Rho-related reaction functions. Instead, we list qualitative features which the reaction functions need to satisfy. In order to describe actomyosin mechanics as simple as possible, we resort to an extension of former models [37, 38] describing the actomyosin as a mechanochemical gel: Filamentous actin (F-actin) is treated as an active material with viscous properties. We assume that both, F-actin

and myosin is always present in sufficiently high amounts and that they are distributed homogeneously, such that we may tread them as constants. F-actin treadmilling and myosin contractions take place at different locations of the cell. Usually treadmilling occurs in the lamellipodium at the front of the cell, where the concentration of active Rac is high. Myosin contractions, on the other hand, take place at the rear of the cell, where the concentration of active Rac is low [58]. In the model, we artificially distinguish between the lamellipodium and the cell body by subdividing the cell domain with respect to the profile of active Rac: We identify the lamellipodium as the set of points, where the active Rac concentration exceeds a predefined value and identify the complement with the cell body. We assume that the force due to treadmilling in the lamellipodium is directed towards the outward pointing boundary normal and that the force exerted by myosin contractions is oriented inwardly with respect to the boundary at the dorsal cell.

In response to a local perturbation of the chemical subsystem at steady-state, a travelling wave of active Rac is triggered which moves inside the cell domain and locally defines the lamellipodium. Simultaneously the generated force in the lamellipodium extends the cell domain, which increases membrane tension. Membrane tension is assumed to be an upstream for RhoA and Rac: On the one hand increased membrane tension inhibits Rac activation, on the other hand increased membrane tension promotes RhoA activation. An increase of active RhoA, in turn, induces a shortening of the cell domain by affecting myosin contractions. The mutual inhibitory feedback-loop between Rac and membrane tension may induce the wave to stall and to obtain a persistent wave front of active Rac.

In this chapter, we formulate the model and list necessary conditions on the parameters and reaction functions such that the model may exhibit mechanochemical wave-pinning as depicted above. By the application of matched asymptotic analysis, we give a phenomenological explanation of this phenomenon.

Thereby we assume that a perturbation of the system at steady-state initiates a transition layer between two stable points of the system. We demonstrate how the transition layer generates a travelling-wave-like solution which is stalled and then is maintained due to the dynamical organization of membrane tension. We argue that the stalled wave-profile may approach a standing shock-wave on longer time scales. In the biological context, this result represents a persisting pattern of high Rac concentration at the front and a low Rac concentration at the back of the cell.

5.1 Model equations

We consider a one dimensional strip of the cell from top view, see Figure 5.1 (a). We assume that the strip contains a fraction of the plasma membrane, where active Rho is located, and a fraction of the AMC. We assume that appreciable chemical gradients do not develop in the height direction of the cell and thus consider a single coordinate

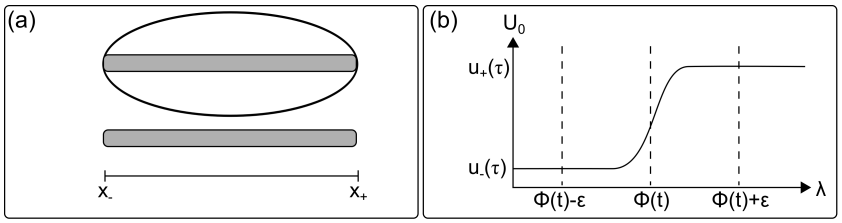

FIGURE 5.1: (a) Our model represents a 1-D strip across the cell diameter with endpoints x_- and x_+, shown top-down and sideview. (b) Possible choice of the position ϕ in the transition layer.

x. We assume that the height of the plasma membrane and of the AMC is negligible, respectively. Thus, we approximate both the plasma membrane and the AMC as residing in the same 1-D domain. The edges of the strip may be convected due to the active mechanical behavior of the cytoskeleton. For the initial resting state, we assume a cell diameter of $L = 10\,\mu$m. At time $t \in \mathbb{R}$, the cell strip is denoted by

$$\Omega_t = (x_-(t), x_+(t)),$$

where the boundary points

$$\begin{aligned} x_+(t) &= \max\left\{x(t) \mid x'(t) = v(t, x(t)),\ x(0) \in (0, 10)\right\}, \\ x_-(t) &= \min\left\{x(t) \mid x'(t) = v(t, x(t)),\ x(0) \in (0, 10)\right\} \end{aligned}$$

depend on the displacement by the velocity of the actomyosin flow; see Figure 5.1 (a). We define the space-time cylinder

$$\Omega(t) := \bigcup_{t \in I} \left(\{t\} \times (x_-(t), x_+(t))\right).$$

as the spatio-temporal domain on which the model equations will be defined. The active forms of Rac and RhoA on $\Omega(t)$ are modelled by a reaction-diffusion approach:

$$\begin{aligned} \partial_t u - D_u \Delta u + \operatorname{div}(uv) &= f_1(\tau, u), \\ \partial_t w - D_w \Delta w + \operatorname{div}(wv) &= f_2(\tau, u, w). \end{aligned} \tag{5.1}$$

Here, u denotes the concentration of active Rac, w denotes the concentration of active RhoA in mol/μm^2, respectively. The variable τ is a dimensionless measure of membrane tension and will be defined in the following. D_u and D_a are the diffusion coefficients of membrane based Rac and Rho in μm^2/s. Rac and RhoA activation are modelled by the kinetic functions f_1 and f_2, which will be specified in Section 5.4. For simplicity, we do not model the dynamics of the inactive forms explicitly.

Since Ω_t may be convected by the velocity field v, the reaction-diffusion system for Rac and RhoA transform on $\Omega(t)$ in Euler coordinates to a reaction-diffusion-convection system with the convection term $\operatorname{div}(uv)$ and $\operatorname{div}(wv)$, respectively [79]. The variable τ is a measure for membrane tension, normalized such that the initial tension is $\tau^0 = 1$

and defined by

$$\tau = 0.1(x_+(t) - x_-(t)).$$

y The velocity field describes the material flow of actomyosin. The constitutive equation of the active material is here given by

$$\sigma = \eta \partial_x v + \sigma^{\text{act}}.$$

The total stress σ consists of viscous stress $\eta \partial_x v$, where η is the viscosity, and an actively generated stress σ^{act} that is assumed to be dependent on the active Rac and Rho concentrations u and w. Neglecting inertial forces, typically valid on a cellular scale, we write the force balance as

$$\partial_x \sigma = \xi v,$$

where we have introduced a friction coefficient ξ to account for relative motion against the substrate. Locally, the actively generated force $-g := \partial_x \sigma^{\text{act}}$ is subdivided into two regions. In the lamellipodium F-actin treadmilling is assumed to exert a constant force ζ_F pointing to the outer boundary. For the cell body, we assume that exerted force due to myosin contractions is proportional to the deviation of the active RhoA concentration w from its steady state concentration w_0. The generation and localization of the lamellipodium is controlled by active Rac: We identify the lamellipodium as the set of points in Ω_t for which u exceeds a threshold value u_{thr}. Thus, we set for a small $\delta > 0$

$$g(y, w) = \zeta_F, \text{ wherever } y \geq u_{\text{thr}}, \tag{5.2}$$

and

$$g(y, w) = \zeta_B K_5 (w - w^0), \text{ wherever } y < u_{\text{thr}} - \delta. \tag{5.3}$$

Since we presuppose the existence of analytic solutions, the transmission $y \mapsto g(y, w)$ on $[u_{\text{thr}} - \delta, u_{\text{thr}}]$ is assumed to be smooth. Thus we model the active force by a smooth function $g(y, w)$, monotonous in y, that satisfies (5.2) and (5.3). Taken together actomyosin mechanics in $\Omega(t)$ are modelled by the equation

$$\eta \partial_x^2 v - \xi v = g(u, w). \tag{5.4}$$

For the reaction-diffusion equations (5.1), we assume that the total mass is conserved within Ω_t if Rho activation is inhibited, i.e. if $f_1 = f_2 = 0$. This assumption leads to

zero-flux boundary conditions:

$$\partial_x u(x_-) + v(x_-)u(x_-) = \partial_x u(x_+) + v(x_+)u(x_+) = 0,$$
$$\partial_x w(x_-) + v(x_-)w(x_-) = \partial_x w(x_+) + v(x_+)w(x_+) = 0.$$

Moreover, we assume that no force on the boundaries of Ω_t is applied, which yields

$$\partial_x v(x_-) = \partial_x v(x_+) = 0.$$

The initial conditions of subsystem (5.1) are chosen such that the system is at homogenous steady state. This will be specified in Section 5.4.

5.2 Nondimensionalization

5.2.1 Scaling parameters

Let v^* be a typical velocity. Let m be a typical concentration for u and w. Let ξ_1, ξ_2 be typical rates of the reaction functions f_1 and f_2, respectively. The initial domain length of the cell strip is denoted by L. We introduce the dimensionless variables $\overline{u}$, $\overline{w}$, $\overline{v}$, $\overline{v_m}$, $\overline{x}$, $\overline{t}$ by writing

$$u = m\overline{u}, \quad w = m\overline{w} \quad v = v^*\overline{v}, \quad v_m = v^*\overline{v_m}, \quad x = L\overline{x}, \quad t = L(\xi_1 D_u)^{-1}\overline{t}.$$

We introduce the dimensionless reaction functions $\overline{f}_1$ and $\overline{f}_2$ defined by

$$\overline{f}_1(\tau, \overline{u}) := \frac{1}{m\xi_1} f_1(\tau, u), \quad \overline{f}_2(\tau, \overline{u}, \overline{w}) := \frac{1}{m\xi_2} f_2(\tau, u, w),$$

where ξ_1 and ξ_2 are parameters of the dimension $1\mathrm{s}^{-1}$. ξ_1 and ξ_2 stand for the typical reaction speeds of the respective functions. The rescaled active force function $\overline{g}$ takes the form

$$\overline{g}(\overline{u}, \overline{w}) := \frac{1}{\zeta_F} g(u, w).$$

In particular in the upper and lower bounds $\overline{g}$ adopts the values

$$\overline{g}(\overline{u}, \overline{w}) := \begin{cases} 1 & \text{if } \overline{u} \geq \overline{u}_{\mathrm{thr}} \\ \zeta(\overline{w} - \overline{w}^0) & \text{if } \overline{u} < \overline{u}_{\mathrm{thr}} - \overline{\delta}, \end{cases}$$

where $\overline{w}^0 = m^{-1}w$, $\overline{u}_{\text{thr}} = m^{-1}u_{\text{thr}}$, and $\overline{\delta} = m^{-1}\delta$.
We set

$$\varepsilon_1 = \left(\frac{D_u}{\xi_1 L^2}\right)^{1/2}, \quad \varepsilon_2 = \frac{v^*}{\xi_1 L}, \quad \varepsilon_3 = \frac{\xi_2}{\xi_1},$$
$$\varepsilon_4 = \left(-\frac{\eta v^*}{\zeta_F L^2}\right)^{1/3}, \quad \overline{\xi} = -\frac{\xi v^*}{\zeta_F}, \quad \overline{\zeta} = -\frac{\zeta_B m}{\zeta_F}.$$

5.2.2 Parameter values

We take for L the length of the cell strip at rest: $L = 10\mu$m. Active Rho proteins are attached to the plasma membrane. For typical normal conditions, the diffusion coefficient of membrane-based Rho protein is of the order $0.1\,\mu\text{m}^2\text{s}^{-1}$ [98]. Hence, we take $D_u = D_v = 0.1\,\mu\text{m}^2\text{s}^{-1}$. We premise that the reaction functions f_1 and f_2 act on timescales of 1 s and 10^2 s, respectively. This will be expressed by taking the corresponding rates $\xi_1 = 1\text{s}^{-1}$ and $\xi_2 = 10^{-2}\text{s}^{-1}$. For v^* we take the mean migration speed of the 2D-model, calculated in Chapter 4: $v^* = 0.19\mu$m/s. The concentration m is set to $m = 1\mu\text{mol/dm}^2$. For the viscosity coefficient we assume $\eta = 10^7$Pa s and the factors contributing to the actively generated forces are set to $\zeta_F = \zeta_B = -2.1 \cdot 10^8$Pa.
The used parameters are the same as for the original 2D-model, see Table 4.1.
A comparison between the rescaled parameters reveals that ε_1, ε_2, ε_3, ε_4 are of the same magnitude of about 10^{-2}. Thus, we take

$$\varepsilon := \varepsilon_1 = \varepsilon_2 = \varepsilon_3 = \varepsilon_4$$

as an approximation.

5.2.3 The dimensionless system

Substituting these expressions in system (5.1), (5.4) and dropping the bars on the dimensionless variables and parameters, and using the same symbol f_i $(i = 1, 2)$, g for the dimensionless right-hand sides, we obtain the non-dimensional system

$$\varepsilon\partial_t u - \varepsilon^2\Delta u + \varepsilon v_m \nabla u = f_1(\tau, u), \tag{5.5}$$
$$\varepsilon\partial_t w - \varepsilon^2\Delta w + \varepsilon\text{div}(wv) = \varepsilon f_2(\tau, u, w), \tag{5.6}$$
$$-\varepsilon^3\Delta v + \xi v = g(u, w), \tag{5.7}$$
$$\tau = x_+(t) - x_-(t), \tag{5.8}$$

with the boundary conditions

$$\begin{aligned} \varepsilon\partial_x u(x_-) + \varepsilon v u(x_-) = \varepsilon\partial_x u(x_+) + \varepsilon v u(x_+) = 0, \\ \varepsilon\partial_x w(x_-) + \varepsilon v w(x_-) = \varepsilon\partial_x w(x_+) + \varepsilon v w(x_+) = 0, \\ \partial_x v(x_-) = \partial_x v(x_+) = 0. \end{aligned} \tag{5.9}$$

The system is defined on the rescaled space-time cylinder

$$\Omega(t) = \bigcup_{t\in I} \left(\{t\} \times (x_-(t), x_+(t))\right),$$

where

$$\begin{aligned} x_+(t) &= \max\left\{x(t) \mid x'(t) = v(t, x(t)),\ x(0) = X \in (0,1)\right\}, \\ x_-(t) &= \min\left\{x(t) \mid x'(t) = v(t, x(t)),\ x(0) = X \in (0,1)\right\}. \end{aligned}$$

Assumptions on Ω_t

Ω_t is assumed to remain simply connected, which requires that if $X_1 < X_2$, then $x(t, X_1) < x(t, X_2)$ for all t. This implies that the mapping

$$X \mapsto x(\cdot, X)$$

is injective. Consequently, if the mapping is differentiable follows that the *metric tensor* $\partial_X x(t, X)$ does not vanish for any (t, X). By construction the mapping $[X \mapsto x(\cdot, X)]$ is surjective. Therefore the inverse $\Lambda(t, x)$ of $[X \mapsto x(\cdot, X)]$ exists, which gives the initial location of a position x at time t.
By assuming that Ω_t is simply connected, the boundary values can be written as solutions of the ODEs

$$\begin{aligned} x'_+(t) &= v(t, x_+(t)),\ x_+(0) = 1, \\ x'_-(t) &= v(t, x_-(t)),\ x_-(0) = 0. \end{aligned}$$

5.3 Analysis outline

We are interested in *wave-like* solutions of the variable u if the parameter ε is very small ($0 < \varepsilon << 1$). In general, wave-solutions of parabolic equations are only defined on unbounded domains. In order to attribute to wave-like solutions on bounded domains, we introduce the notion *asymptotic wave-front solution* for a parabolic equation that is defined on a bounded domain. Therein a suitable expansion of the solution is rescaled to an *inner domain* depending on ε which formally approaches an unbounded interval if ε tends to zero. In the inner domain we seek travelling wave-front solutions for the

leading order term of the expansion. Afterwards the travelling wave-front solution has to match the boundary conditions of the original system. This approach is based on matching asymptotic expansions (cf. [115]) and will be specified for our needs in the following.
As a starting point, consider the reaction-diffusion equation

$$\varepsilon\partial_t z - \varepsilon^2\partial_x^2 z = f(z) \quad \text{on } (0,T)\times(a,b), \tag{5.10}$$

where $f:\mathbb{R}\to\mathbb{R}$ is a smooth function, $T>0$ is a given time, and $-\infty \le a < b \le \infty$ refer to the bounds of the domain.

Definition 5.1. Let $a=-\infty$, $b=\infty$. Equation (5.10) possesses a *wave-front solution*

$$Z(\lambda) := z(t,x), \quad \lambda := x - ct,$$

with wave-speed $c\in\mathbb{R}$ if (Z,c) is a solution of equation (5.10) satisfying

$$\lim_{\lambda\to-\infty} Z(\lambda) \neq \lim_{\lambda\to\infty} Z(\lambda).$$

Now consider the case in which (a,b) is finite and equation (5.10) is complemented with the boundary conditions

$$\partial_x z(t,a) = \partial_x z(t,b) = 0 \quad \text{for } 0<t<T. \tag{5.11}$$

We are interested in wave-like solutions of the bounded system.

Definition 5.2. Assume that for every $t\in(0,T)$ there is an element $\phi(t)\in(a,b)$ and a segmentation

$$\mathcal{U}(t) = \{(a,\phi(t)-\varepsilon),(\phi(t)-\varepsilon,\phi(t)+\varepsilon),(\phi(t)+\varepsilon,b)\}$$

of (a,b), such that equation (5.10) possess a solution u, analytic with respect to ε, on each element of $\mathcal{U}(t)$. We refer to this solution as an *asymptotic wave-front solution to the leading order* of the boundary-value problem (5.10)–(5.11) if for the expansion

$$u = u_0 + u_1\varepsilon + u_2\varepsilon^2 + ... \tag{5.12}$$

the following statements hold:

(1) *Outer solution.* The leading-order term $u_0(t,x)$ of expansion (5.12) is constant on $(a,\phi(t)-\varepsilon)$ and $(\phi(t)+\varepsilon,b)$, respectively, with

$$u_0^- \neq u_0^+,$$

where $u_0^- := u_0(t,\cdot)|(a,\phi(t)-\varepsilon)$ and $u_0^+ := u_0(t,\cdot)|(\phi(t)+\varepsilon,b)$.

(2) *Inner solution.* Let $x \in (\phi(t) - \varepsilon, \phi(t) + \varepsilon)$. The leading-order term $u_0(t, \lambda)$ of expansion (5.12) possesses a wave solution $U_0(\lambda)$ in the sense of Definition 5.1 (with respect to the stretched coordinate $\lambda = \frac{x-\phi(t)}{\varepsilon}$).

(3) *Matching inner and outer solution.* The inner and outer solutions satisfy

$$\lim_{\lambda \to \pm\infty} U(\lambda) = u_0^{\pm}.$$

It should be stressed that this approach serves only as an approximation of the original solution. Nevertheless, it provides an insight into the structure of the patterning mechanism.

5.4 Patterning mechanism

The patterning mechanism is based on the following characteristics: The scaling-parameter ε is thought to be very small ($\varepsilon << 1$), and the right-hand sides satisfy the following properties:

(*i*) *Bistability.* The dynamical system $\mathrm{d}_t u = f_1(\tau, u)$ is bistable for fixed τ in a parameter range $\tau_{\min} \leq \tau \leq \tau_{\max}$. The initial tension $\tau^0 = 1$ is contained in $[\tau_{\min}, \tau_{\max}]$. The stable points are $u_-(\tau), u_+(\tau)$. The unstable point is $u_c(\tau)$. It holds $u_-(\tau) < u_c(\tau) < u_+(\tau)$.

(*ii*) *Mechanical response.* The threshold u_{thr} satisfies $u_c(\tau) < u_{\mathrm{thr}} < u_+(\tau)$ for $\tau_{\min} \leq \tau \leq \tau_{\max}$.

(*iii*) *Velocity-sign condition.* The integral mapping

$$I(\tau) = \int_{u_-(\tau)}^{u_+(\tau)} f_1(\tau, u)\ du$$

is continuous and vanishes for a unique $\tau_c \in [\tau_{\min}, \tau_{\max}]$.

(*iv*) *Intermediate wave-control 1.* We write $f_+(\tau, y) := f_2(\tau, u_+(\tau), y)$. For any $\tau \in [\tau_{\min}, \tau_{\max}]$ the ODE

$$d_t y = f_+(\tau, y), \quad y(0) > 0,$$

has a unique, non-negative solution.

(*v*) *Intermediate wave-control 2.* We write $f_-(\tau, y) := f_2(\tau, u_-(\tau), y)$. For any $\tau \in [\tau_{\min}, \tau_{\max}]$ a solution $w_-(\tau)$ of the ODE

$$d_t y = f_-(\tau, y), \quad y(0) = w^0,$$

satisfies

$$0 \leq w_-(\tau) - w^0 \begin{cases} < \zeta^{-1} & \text{if } \tau < \tau_c, \\ = \zeta^{-1} & \text{if } \tau = \tau_c, \\ > \zeta^{-1} & \text{if } \tau > \tau_c. \end{cases}$$

In particular, we assume that $f_-(\tau, w^0) = 0$ if $\tau = \tau^0$. Moreover, for any parameter $y > w^0$ and $\tau \in (\tau^0, \tau_{\max}]$ holds

$$f_-(\tau, y) \begin{cases} < 0 & \text{if } \tau < \tau_c, \\ = 0 & \text{if } \tau = \tau_c, \\ > 0 & \text{if } \tau > \tau_c. \end{cases}$$

The dynamics of system (5.5)–(5.9) take place on three time scales, short-time (of the order $t \in \mathcal{O}(\varepsilon)$), intermediate time (of the order $t \in \mathcal{O}(1)$), and long-time (of the order $t \in \mathcal{O}(1/\varepsilon)$). On the intermediate time-scale the wave is pinned. We will briefly explain how a wave-like solution in $u(t, x)$ is initiated on the short time scale and is pinned on the intermediate time scale by using matched asymptotics with respect to the parameter ε.

5.4.1 Perturbation of the initial values at short times

We consider system (5.5)–(5.9) to be initially at homogenous steady state. In particular, we take for u the lower homogenous steady state, i.e. $u = u^0 = u_-(\tau^0)$. Assume now that the initial value of the first equation in (5.5) is perturbed by the addition of a monotonous function $f_{\text{stim}}(x)$ with the property

$$f_{\text{stim}}(x_-(0)) = u_-(\tau^0), \quad f_{\text{stim}}(x_+(0)) = u_+(\tau^0).$$

Since $[u \mapsto f(\tau, u)]$ is bistable, we assume that this perturbation initiates a transition layer: There is a $x_s \in L(0)$ such that $u(t, x)$ for $x \geq x_s \in L(0)$ tends to $u_+(\tau^0)$ and that $u_0(t_s, x)$ for $x < x_s \in L(0)$ tends to $u_-(\tau^0)$.

5.4.2 Behavior at intermediate times

The assumed profile for u obtained in the short time scale provides the initial condition for u on the intermediate time scale $t \in \mathcal{O}(1)$. We use the technique of matched asymptotic expansions to show that to the leading order a travelling wavefront evolves which is pinned within the intermediate time scale. At first we discuss the outer solution and afterwards we discuss the inner solution. Let $\phi(t)$ be the position of the transition zone where u transfers from $u_-(\tau)$ to $u_+(\tau)$. We refer to $\phi(t)$ as the location of the wave-front; see Figure 5.1 (b).

Outer solution We analyze system (5.5) – (5.9) in the vicinity of the boundary. Therefore it is convenient to describe the system in Lagrangian coordinates, see e.g. [116]. By construction, in Lagrangian coordinates the advection terms in equations (5.5), (5.6) drop out, and system (5.5)–(5.8) takes on $(t, X) \in I \times (0, 1)$ the form

$$\begin{aligned}
\varepsilon \partial_t u_X - \varepsilon^2 \partial_X \left(\frac{1}{M} \partial_X u_X \right) &= f_1(\tau, u_X), \\
\varepsilon \partial_t w_X - \varepsilon^2 \partial_X \left(\frac{1}{M} \partial_X w_X \right) &= \varepsilon f_2(\tau, u_X, w_X), \\
-\varepsilon^3 \partial_X \left(\frac{1}{M} \partial_X v_X \right) + \xi v_X &= \mathbb{1}_{\{u_X \geq u_{\text{thr}}\}} + \zeta \mathbb{1}_{\{u_X < u_{\text{thr}}\}} (w_X - w^0), \\
\tau &= x_+(t) - x_-(t).
\end{aligned}$$

The boundary condition transform to

$$\begin{aligned}
\varepsilon \frac{1}{M} \partial_X u_X(0) = \varepsilon \frac{1}{M} \partial_X u_X(1) = 0, \\
\varepsilon \frac{1}{M} \partial_X w_X(0) = \varepsilon \frac{1}{M} \partial_X w_X(1) = 0, \\
\partial_x v(0) = \partial_x v(1) = 0.
\end{aligned}$$

Here

$$u_X(t, X) = u(t, x(t, X)), \quad w_X(t, X) = w(t, x(t, X)), \quad v_X(t, X) = v(t, x(t, X))$$

are the trajectories of the concentrations u, w with the initial position X at time $t = 0$ and the advection-velocity of the initial position X, respectively. M is induced by the metric tensor and given by

$$M(X) = |\partial_X x(t, X)|.$$

The boundary locations at time t, in particular, read as $x_-(t) = x(t, X = 0)$ and $x_+(t) = x(t, X = 1)$.
Let now $x \in (x_-(t), \phi(t) - \mathcal{O}(\varepsilon))$ or $x \in (\phi(t) + \mathcal{O}(\varepsilon), x_+(t))$. Since Ω_t is simply connected, this is equivalent to $X \in (0, \Lambda(t, \phi(t) - \mathcal{O}(\varepsilon))$ or $X \in (\Lambda(t, \phi(t) + \mathcal{O}(\varepsilon), 1)$. Expanding

$$u_X(t, X) = u_{X0}(t, X) + u_{X1}(t, X)\varepsilon + ...$$

and likewise for w_X, v_X, substituting the expansions into System (5.5) – (5.8), and retaining the leading order terms yield the outer solution:

$$f_1(\tau, u_{X0}) = 0, \tag{5.13}$$

$$\partial_t w_{X0} = f_2(\tau, u_{X0}, w_{X0}), \tag{5.14}$$

$$v_{X0} = g(u_{X0}, w_{X0}), \tag{5.15}$$

$$\tau = x_+(t) - x_-(t). \tag{5.16}$$

For the boundary conditions (5.9) we obtain to the zeroth-order homogenous Neumann-conditions :

$$\partial_X u_{X0}(t,0) = \partial_X u_{X0}(t,1) = 0,$$
$$\partial_X w_{X0}(t,0) = \partial_X w_{X0}(t,1) = 0,$$

We obtain from (5.13) and its homogenous Neumann-boundary conditions the outer solution of u_0:

$$u_{X0}(t,X) = \begin{cases} u_+(\tau), & 0 \le X < \Lambda(t, \phi(t) - \mathcal{O}(\varepsilon)), \\ u_-(\tau), & \Lambda(t, \phi(t) + \mathcal{O}(\varepsilon)) < X \le 1, \end{cases} \tag{5.17}$$

which is equivalent to

$$u_0(t,x_\pm) = \begin{cases} u_+(\tau), & x_-(t) \le x < \phi(t) - \mathcal{O}(\varepsilon), \\ u_-(\tau), & \phi(t) + \mathcal{O}(\varepsilon) < x \le x_+(t). \end{cases} \tag{5.18}$$

Apart from the outer solution of u_0 we obtain qualitative data of τ. Since τ is an integral expression over the whole domain, τ is affected by changes in the size of the domain. This will be shown now.
Substitution of (5.17) in (5.14) yields for $X \to 0$ and $X \to 1$ the expressions

$$d_t w_{X0}(t,0) = f_-(\tau, w_{X0}(t,0)), \quad d_t w_{X0}(t,1) = f_+(\tau, w_{X0}(t,1)). \tag{5.19}$$

due to the homogenous Neumann conditions in x_-, x_+. Substitution of (5.17) in (5.15) yields for $X \to 0$ and $X \to 1$

$$v_0(t,x_-) = \frac{\zeta}{\xi}(w_0(t,x_-) - w^0), \quad v_0(t,x_+) = \frac{1}{\xi}. \tag{5.20}$$

Equation (5.19) and equation (5.16) imply

$$d_t \tau = \frac{1}{\xi}\left(1 - \zeta(w_0(t,x_-) - w^0)\right) \tag{5.21}$$

From condition (v) and equation (5.20) we obtain

$$d_t \tau \begin{cases} < 0 & \text{if } \tau > \tau_c, \\ = 0 & \text{if } \tau = \tau_c, \\ > 0 & \text{if } \tau < \tau_c. \end{cases} \tag{5.22}$$

Consequently, τ is increasing in the beginning of the intermediate time-scale. Furthermore, differentiation of (5.21) with respect to t yields for $\tau > \tau^0$

$$d_t^2\tau \begin{cases} < 0 & \text{if } \tau > \tau_c, \\ = 0 & \text{if } \tau = \tau_c, \\ > 0 & \text{if } \tau < \tau_c. \end{cases} \tag{5.23}$$

τ is a spatially global variable and the qualitative behavior of u depends on changes of τ. In the next paragraph will be shown how τ locally affects the inner solution of (5.5).

Inner solution We will show now that to the leading order the inner solution has a wave-like solution. For the treatment of the inner solution, we reconsider the system in Eulerian coordinates. Close to the front $\phi(t)$, a stretched coordinate $\lambda = (x - \phi(t))/\varepsilon$ is introduced. The inner solutions of u and v are denoted by U and V, respectively, where

$$U(t, \lambda) = u(t, (x - \phi(t))/\varepsilon), \tag{5.24}$$

$$V(t, \lambda) = v(t, (x - \phi(t))/\varepsilon) \tag{5.25}$$

Note that (5.24) is not a wave-front solution in the strict sense, since the wave-speed $d\phi/dt$ is not constant. We consider the expansions

$$\begin{aligned} U(t, \lambda) =& U_0(t, \lambda) + U_1(t, \lambda)\varepsilon + ..., \\ V(t, \lambda) =& V_0(t, \lambda) + V_1(t, \lambda)\varepsilon + ..., \\ \phi(t) =& \phi_0(t) + \phi_1(t)\varepsilon + ... \ . \end{aligned}$$

Substitution of these expansions into (5.5) and writing $f_1(\tau, U)$ as a Taylor series with respect to ε yields

$$\begin{aligned} \varepsilon\partial_t U_0(t, \lambda) - \varepsilon\partial_\lambda U_0(t, \lambda)\frac{1}{\varepsilon}d_t\phi_0(t) - \varepsilon^2\partial_\lambda^2 U_0(t, \lambda)\frac{1}{\varepsilon^2} + \varepsilon V_0\partial_\lambda U_0(t, \lambda)\frac{1}{\varepsilon} \\ = f_1(\tau, U_0) - \varepsilon U_0\partial_\lambda V_0(t, \lambda)\frac{1}{\varepsilon} + \text{higher order terms in } \varepsilon. \end{aligned} \tag{5.26}$$

In order to simplify this equation, it would be desirable to get rid of the dilution term $\partial_\lambda V_0(t, \lambda)$ on the right hand side. The numerical simulations in the Chapter 4 indeed reveal that after some spatial fluctuations V_0 settles to an almost spatially constant value at intermediate times. The reason behind this is that after some time both, the active force at the front and the active force at the back, are approximately equal, which induces $|\nabla g(u, v)| \approx 0$. At this point this cannot be shown from our asymptotic approach. Therefore, to keep the analysis simple, we assume henceforth that the expansion of V on the intermediate time scale takes the form

$$V(t, \lambda) = V_0(t) + V_1(t, \lambda)\varepsilon + \text{higher order terms in } \varepsilon.$$

(This is, for example, the case if the gradient $\nabla g : \mathbb{R}^2 \to \mathbb{R}^2$ is of the order of ε, i.e.

$$|\nabla g(y_1, y_2)| \leq \varepsilon \text{ for all } (y_1, y_2) \in \mathbb{R}^2.)$$

Under this assumption, the dilution term $U_0 \partial_\lambda V_0(t, \lambda)$ on the right hand side of (5.26) vanishes. If we neglect in (5.26) higher order terms, we obtain to the leading order the equation

$$\partial_\lambda^2 U_0 - (d_t \phi_0 - V_0)\partial_\lambda U_0 + f_1(\tau, U_0) = 0., \tag{5.27}$$

where V_0 only depends on t. Inner and outer solution of u_0 match if the solution of (5.27) adopts the limits

$$\lim_{\lambda \to -\infty} U_0(t, \lambda) = u_-(\tau), \quad \lim_{\lambda \to \infty} U_0(t, \lambda) = u_+(\tau). \tag{5.28}$$

Due to the scaling of (5.5) we may neglect the term $\varepsilon \partial_t U_0(t, \lambda)$ in which the time derivative of U_0 appeared. The advantage is that we can consider now equation (5.27), due to the bistability of $f_1(\tau, U_0)$, as a classical wave-equation at each time $t > 0$.
The following statement holds:

Theorem 5.3. *For each $(t, \tau) \in \mathbb{R}_+ \times [\tau_{\min}, \tau_{\max}]$ exists a smooth solution $U_0^\phi(t, \lambda, \tau)$ of equation (5.27) satisfying (5.28). The solution is unique up to translation, i.e.: If $\overline{U}_0^\phi(t, \lambda, \tau)$ is also a solution, a suitable $h \in \mathbb{R}$ exists such that*

$$U_0^\phi(t, \lambda + h, \tau) = \overline{U}_0^\phi(t, \lambda, \tau).$$

Moreover, there is a constant $M > 0$ such that

$$\left(\int_{-\infty}^{\infty} (\partial_\lambda U_0^\phi(t, \lambda, \tau))^2 \, d\lambda \right) < M \quad \text{for all } t \in \mathbb{R}. \tag{5.29}$$

The velocity of the wavefront relative to the moving cell is

$$c(t, \tau) := d_t \phi_0 - V_0 = \left(\int_{-\infty}^{\infty} (\partial_\lambda U_0^\phi(t, \lambda, \tau))^2 \, d\lambda \right)^{-1} \int_{u_-(\tau)}^{u_+(\tau)} f(\tau, s) \, ds. \tag{5.30}$$

Proof. A proof of the existence and uniqueness up to translation can be found in [117]. Corollary 1.3.5 in [117] implies due to the continuity of $I(\tau)$

$$\int_{-\infty}^{\infty} (\partial_\lambda U_0^\phi(t, \lambda, \tau))^2 \, d\lambda \leq |I(\tau)| \leq \max_{\tau \in [\tau_{\min}, \tau_{\max}]} |I(\tau)| =: M.$$

Multiplying (5.27) by $\partial U_0^\phi / \partial \lambda$ and subsequent integration from $\lambda = -\infty$ to $\lambda = +\infty$ yield equation (5.30). □

Wave-pinning We demonstrate now how the wave-speed of a wave-front solution of (5.27), (5.28) is affected by the system. Theorem 5.3 states that the wave-speed is controlled by the generation of tension τ. Two considerable cases may occur: $\tau > \tau_c$ and $\tau < \tau_c$. We will show that in both cases the system approaches τ_c.
It is easy to see that the mapping $[t \mapsto c(t, \tau(t))]$ is continuous on $\mathbb{R}$. Consider the case where $\tau > \tau^0$ and $c(t, \tau(t)) < 0$. Then, the right hand side of (5.30) is negative and condition (iii) implies $\tau(t) \in (\tau^0, \tau_c)$. From relation (5.22) and relation (5.23) we obtain $d_t\tau(t) > 0$ and $d_t^2\tau(t) > 0$ as long $\tau(t) < \tau_c$. This implies that a time $t_c^- \in \mathbb{R}$ exists such that

$$\tau \to \tau_c \quad \text{for } t \to t_c^-.$$

From condition (iii) and (5.30) follows

$$c(t, \tau(t)) \left(\int_{-\infty}^{\infty} (\partial_\lambda U_0^\phi(t, \lambda, \tau))^2 \, d\lambda \right) \to 0 \quad \text{for } t \to t_c^-.$$

The mapping $[\lambda \mapsto U_0^\phi(t, \lambda, \tau)]$ is smooth and (5.28) implies that the mapping is non-constant for any $(t, \tau) \in \mathbb{R}_+ \times (\tau^0, \tau_{\max}]$. This implies $\|U_0^\phi(t, \cdot, \tau)\|_{C(\mathbb{R})} > 0$. Hence, we obtain

$$c(t, \tau(t)) \to 0 \quad \text{for } t \to t_c^-.$$

Assume $c(\tau) < 0$. Similar as above can be shown that a time t_c^+ exists such that

$$c(\tau) \to 0 \quad \text{for } t \to t_c^+.$$

We obtain that in both cases the velocity approaches pointwise to zero in finite time. Figuratively, this means that the wave-speed oscillates around zero at times $t \in \mathcal{O}(1)$.

5.4.3 Behavior at long times

We investigate the behavior of zeroth-order solution on the long time scale $t_l = \frac{1}{\varepsilon}t$, whereby we assume that the initial conditions for u on the long time-scale are given by an asymptotic wave-solution as presented in the former section.

Lemma 5.4. *Let $t_l = \frac{1}{\varepsilon}t$. Then v has the scaling property*

$$v\left(\frac{t}{\varepsilon}\right) = \frac{1}{\varepsilon} v(t_l).$$

Proof. Let X be the initial value of the trajectory $x(t) = x(t, X)$ generated by the field $v(t, x)$. We obtain

$$v(t, x(t)) = \partial_t x\left(\frac{t}{\varepsilon}\right) = \frac{1}{\varepsilon}\partial_{t_l} x(t_l) = v(t_l, x(t_l)).$$

□

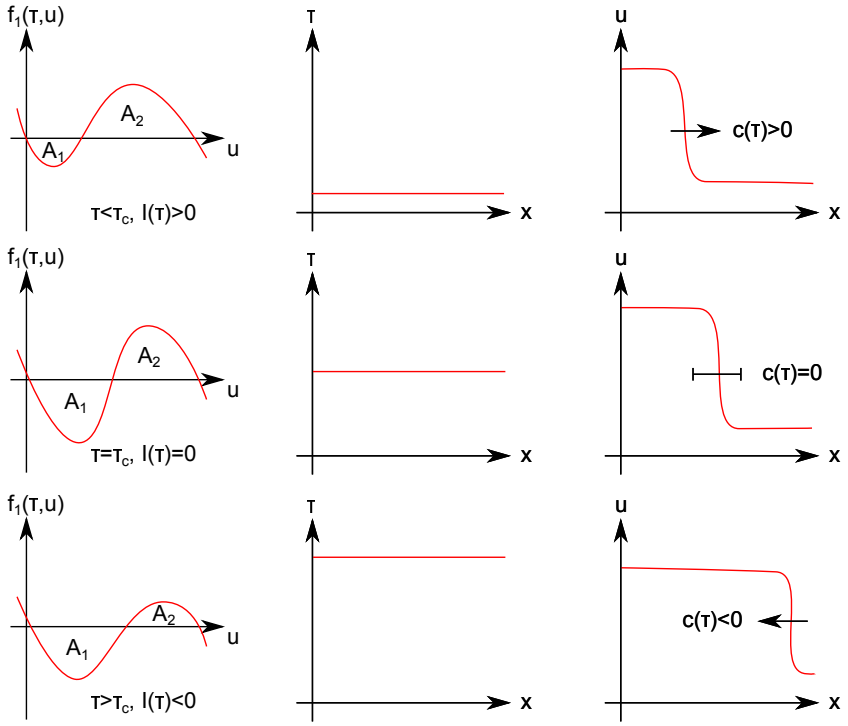

FIGURE 5.2: Intuitive illustration of mechano-chemical wave-pinning based on the velocity-sign condition (*iii*). The left column shows the reaction rate $f_1(\tau, u)$ in dependency of u for fixed τ. The column in the middle shows the response of τ due to increasing membrane tension induced by the elevation of u. The right column displays the related spatial distribution u. The arrow denotes the current velocity $c(\tau)$ of the travelling wave-front. A_1 (resp. A_2) is the enclosed area between the negative (resp. positive) part o $f(\tau, u)$ and the abscissa. If $A_1 < A_2$ (resp. $A_1 > A_2$) follows $I(\tau) > 0$ (resp. $I(\tau) < 0$). If $A_1 = A_2$ is $I(\tau) = 0$ and the wave is stalled.

Once again we consider system (5.5)–(5.8), but now on the time-scale $t_l = t/\varepsilon$. Writing u, w, v as expansions

$$\begin{aligned} u &= u_0 + u_1\varepsilon + ..., \\ w &= w_0 + w_1\varepsilon + ..., \\ v &= v_0 + v_1\varepsilon + ..., \end{aligned}$$

and substitution into (5.5)–(5.6) yields up to zeroth order on the time scale t_l

$$\partial_{t_l} u_0 + \partial_x(v_0 u_0) = f_1(\tau, u_0), \tag{5.31}$$

$$\partial_{t_l} w_0 + \partial_x(v_0 w_0) = 0, \tag{5.32}$$

where we used Lemma 5.4. Moreover, if we assume that u_0 possesses a wave-like solution as constructed in the former section, we obtain from (5.8) for values close to the boundaries

$$\begin{aligned} \xi v_0 &= 1, \quad \text{if } x \text{ is close to } x_+(t), \\ \xi v_0 &= \zeta(w_0 - w_0^0) \quad \text{if } x \text{ is close to } x_-(t). \end{aligned} \tag{5.33}$$

The boundary conditions imply that close to the boundaries w_0 is constant. In the intermediate timescale holds that τ is close to τ_c. Thus, we obtain from condition (v) that $w - w^0 \approx \zeta^{-1}$ at intermediate times. If we assume that close to the boundary $w_l^0 := \zeta^{-1} - w^0$ is the initial value for w on the long time scale, we can deduce from (5.33) that the boundaries x_- and x_+ are convected with the same speed, as long as the wave-like solution in u_0 persists. In this case, the interval does not change in size at longer time scales. It follows $\tau(t_l) = \tau_c$ and $v_0 = const.$

Now we consider the behaviour of the solution u_0 at long times and assume that the solutions on this scale are analytical in ε. (If we considerd (5.5) with respect to the stretched coordinate $\lambda = (x - \phi(t_l))/\varepsilon$ once again, and matched the equations, we would obtain the same result.) Consider the moving coordinate $\lambda = x - x_-(t_l)$ and set $\lambda_l = 0$, $\lambda_r = x_+(t_l = 0) - x_+(t_l = 0)$. With respect to this coordinate, equation (5.31) transforms to

$$\partial_{t_l} u_0(t_l, \lambda) = f_1(\tau_c, u_0) \quad \text{on } I \times (\lambda_l, \lambda_r), \tag{5.34}$$

since $v_0(x_+(t)) = v_0(x_-(t))$. The boundary conditions transform to

$$\partial_\lambda u_0(t_l, \lambda_l) = \partial_\lambda u_0(t_l, \lambda_r) = 0.$$

We assume that the initial value u_0^0 for u_0 at long times is given by the constructed wave-solution of u_0 that is generated at intermediate times. Moreover, since $\tau(t_l) = \tau_c$, we may deduce that the initial value u_0^0 has the wave-speed $c(\tau_c) = 0$, which means that the wave moves with the same speed as the reference frame $[x_-(t_l), x_+(t_l)]$. Then we can express u_0^0 in dependency of λ and obtain that $u_0^0(\lambda)$ is sigmoidal and satisfies the boundary conditions

$$u_0^0(\lambda_l) = u_-(\tau_c), \quad u_0^0(\lambda_r) = u_+(\tau_c), \quad d_\lambda u_0^0(\lambda_l) = d_\lambda u_0^0(\lambda_r) = 0.$$

Since $[y \mapsto f(\tau_c, y)]$ is bistable, it is well known that the dynamical system (5.34) under these initial values approaches to

$$u_0(t_l, \lambda) \to \begin{cases} u_+(\tau_c), & \text{if } u_0^0(\lambda) > u_c(\tau_c), \\ u_-(\tau_c), & \text{if } u_0^0(\lambda) < u_c(\tau_c), \end{cases} \qquad \text{for } t_l \to \infty.$$

Since $u_0^0(\lambda)$ is sigmoidal, we can deduce that $\lim_{t_l \to \infty} u_0(t_l, \lambda)$ has the shape of a shock wave: There a $\lambda_c \in (\lambda_l, \lambda_r)$ exists such that

$$\lim_{t_l \to \infty} u_0(t_l, \lambda) = \begin{cases} u_+(\tau_c), & \text{if } \lambda > \lambda_c, \\ u_-(\tau_c), & \text{if } \lambda < \lambda_c. \end{cases}$$

Consequently, if the assumptions hold, the stalled wave persists at longer times spans, but looses regularity and transforms into a shock wave.

5.5 Discussion

We presented a simple, spatially one-dimensional model of tension-mediated Rho GTPase polarization. We rescaled the system to a non-dimensional system where the reactions and diffusions take place on different powers of a small scaling parameter ε. Based on matched asymptotic analysis we have argued heuristically how a wave solution in the zeroth order approximation u_0 of u evolves and is stalled with respect to the moving reference interval. We argued that at longer time scales the stalled wave-solution may transform into a shock wave that moves with the same speed as the reference interval. These characteristics can be interpreted as a pattern mechanism that enables a cell to generate a persistent front and a persistent back. Bistability of the activation function for Rac in a certain parameter regime is a necessary condition for our mechanism to work. In a biological context bistability may arise from positive feedback due to GEF-Rho complex formation which catalyzes Rho activation [63].
The novelty of the presented pattern mechanism is that it depends on the coupling between a system of reaction-diffusion equations (for u, w) that are weakly coupled with an integral equation (for τ), which globally affects the reaction functions. The presented explanation of the generation of wave patterns is purely phenomenological and must not be regarded as a rigorous proof. A major simplification is that we only investigated terms of zeroth order. To this order the scaling of the system allowed us to ignore the time derivative $\varepsilon\partial_t U_0$ such that we could find travelling wave-solutions. For higher order terms the time derivative cannot be neglected and the analysis becomes far more complex. Since then we cannot find wave solutions in a classical sense for these terms, we have to consider if the higher order solutions approach to a wave (or, in the most trivial scenario, approach to zero). However, if the higher order solutions in fact do approach to a wave, it can be shown that the wave-speed must be different from zero, cf. Theorem 5.2.2.1 in [117]. On the other hand, a non-zero wave-speed may perturb the amount of membrane tension τ, which in turn slows the wave-speed. This interaction may lead to an oscillatory behavior where one part of the system tries to approach to a state which is unstable for the other part.
Analytically this behavior seems to be hard to verify for multiple reasons. Firstly, a stability analysis requires knowledge about the spectrum of the linearized system. However, the spatial differential operators are defined on unbounded domains. There, the spectrum of the Laplace operator includes not only discrete eigenvalues, but also a continuous spectrum. Moreover, it can be shown that the linerarized equations for the higher-order system have a zero eigenvalue. In order to cope with these characteristics, a different notion of stability is required which is called *stability with shift* and classical asymptotic stability results cannot be applied. (We refer to [117] for a deeper treatment of stability properties of travelling wave solutions.) Secondly, we cannot treat perturbations of τ near τ_c as a classical bifurcation problem, where we could seek for conditions of a Hopf-related bifurcation since τ affects the quality of the solution at finite time in a way that prevents to solution to approach a steady state.

In numerical simulations of a related model, however, oscillations in the wave-speed are observable [108]. Since the oscillations seem to be partly independent of the choice of the time iteration size and of the mesh size which represents the domain Ω_t, it is likely that the oscillations emerge form the approach of higher order solutions to waves with non-zero speed and the repelling impact of tension τ.

Nevertheless, the asymptotic explanation presented in this chapter provides an insight of the qualitative behavior of the solution. The necessary conditions for mechanochemical wave-pinning listed in Section 5.4 give an account of the coupling between cell mechanics and biochemical signalling in order to achieve robust polarity patterns. In this context, we consider our model as a minimal model with the ability to exhibit mechanochemical wave-pinning, which may serve as an guideline for more detailed mechanochemical polarization models.

Thereby the model provides possible biological implications. We hypothesized that membrane tension inhibits Rac- and promotes RhoA-activation. Although the molecular mechanisms by which cells sense and respond to mechanical signals are not fully understood, there are several known mechanisms by which a cell could translate membrane tension into chemical signals [43]. It is known that Rac activation is catalyzed by GEF-complex formation while RhoA inactivation is facilitated by GAP interaction [63]. A possible implication of our model is that membrane tension may mechanically promote the recruitment of Rac specific GEF and RhoA specific GAP.

The small parameter ε exploited in our analysis depends on several biological parameters, including the diffusion coefficients, the reaction rates and the domain size. Our fundamental assumption $0 < \varepsilon_1 << 1$ is satisfied by virtue of the ratio between the slow diffusion of membrane based Rho-proteins and the relatively large size of the domain. Assuming a typical cell diameter of $10\,\mu$m, a reaction time scale for Rac activation $\zeta_1 = 1\text{s}^{-1}$, and diffusion coefficients $D_u = D_w = 0.1\,\mu\text{m}^2\text{s}^{-1}$, the non-dimensional factor of the diffusion of Rho proteins is $\varepsilon_1 \approx 0.03$. We consider ε_1 to be sufficiently small to use an matched asymptotic approach. However, if the diffusion coefficient is increased by a magnitude, the activation speed η_1 is increased to $\xi_1 > 10\ \text{s}^{-1}$, or the cell length is decreased to $L \leq 0.1\ \mu$m, the scaling parameter ε_1 is of the order 0.1. For this order matched asymptotic analysis is not suited anymore to justify the phenomenon of wave-pinning. On the contrary, based on findings for a comparable model [33], we conjecture that in this setting wave-based pattern formation fails. (Similar considerations apply to the assumption $0 < \varepsilon_2 << 1$.)

Such predictions are partially experimentally testable. Cell fragments whose ability to polarize is retained [53] could be made successively smaller to test the effect of the domain size. In the model the activation rate of Rac can be varied by changes in membrane tension. If membrane tension is drastically increased, we expect that Rac activity patterns extinguish. Aspiration experiments in neutrophils show that increased membrane tension can result in dissipation of polarity [11], which supports this thesis.

A further requirement of the model is $\varepsilon_3 << 1$, which means that RhoA activation has to be slower than Rac activation. Since the model neglects possible delays due to

downstream effectors targeting at actin treadmilling and AMC contractions, we cannot conclude directly that this characteristic has to be mirrored by experimental investigations. However, if we also take the mechanical response into consideration, from a biological viewpoint the requirement suggests that Rac mediated front protrusions occur at shorter time scales (of seconds) than RhoA mediated contractions of the rear (within minutes), which may be experimentally testable by the manipulation of the amounts of Rac and RhoA in a cell [118].

The parameter ε_4 represents the rescaled viscosity of the actin gel. Assuming the values $\eta = 10^7$ Pa s, $\zeta_F = -2.1 \cdot 10^8$ Pa, and v^*, L as listed above, the non-dimensional factor is $\varepsilon_4 \approx 0.04$. In the model equations ε_4 occurs with a cubic power. We consider mild parameter variations in ε_4 as unproblematic. The analysis of the model is unaffected if ε_4 is increased to the order 10^{-1}. (Then ε_4 has a quadratic power in the model equations.) If ε_4 is drastically increased, we expect that contractile and protrusive forces globally interfere with each other such that the cell looses its ablilty to move. In consequence the cell is not able to generate membrane tension which prevents the establishment of a persistent front of active Rac. This expectation could be tested experimentally in the case in which the protrusive force is highly attenuated. This may be obtained when the already polarized cell hits an obstacle which resists the protrusive force.

Chapter 6

Discussion

6.1 Model summary

We proposed a mechanochemical model to explain cell polarization in neutrophils. Experimental investigations have shown both, biochemical and mechanical signal transmission to be necessary for a persistent polarization in neutrophils [11]. Membrane tension is regarded as a suppressor of Rac activation. Our model includes this role of membrane tension and provides an account how biochemical and mechanical signalling could interplay to generate locally confined activity patterns of the Rho distribution in response to external gradients. We computationally demonstrated that the mechanism captures certain key features of polarity in neutrophils and generates a cone-like cell morphology with a broad cell front and a tapered rear. The model contains a strongly simplified circuit consisting of the functional units Rho GTPase signalling, actin polymerization, and force exertion due F-actin treadmilling and myosin contractions. In response to an external stimulus, Rac is locally activated. Active Rac promotes actin polymerization and directional F-actin treadmilling and suppresses RhoA activation. Subdomains whose F-actin concentration exceed a certain threshold were identified with the lamellipodium. The pushing force generated by F-actin treadmilling propels the lamellipodium forward. This induces an increase of membrane tension due to the spatial extension of the cell domain. The increase of tension prevents active Rac to spread across the cell and confines it to the leading edge. If tension would increase without restriction, also the remaining Rac activity front would expire. In the model, however, membrane tension is downregulated by RhoA: Increasing tension promotes RhoA activation. Since Rac is thought to inhibit RhoA, active RhoA is predominantly generated at the rear of the model cell. The emerging contractile force due to increased RhoA activity leads to a retraction of the rear, which lowers membrane tension. Consequently, membrane tension in a polarized cell is increased by a pushing force and constrained by a retracting force. The increased tension suppresses Rac activation globally. In the lamellipodium, where the

Rac concentration is already high, however, autocatalysis of Rac counteracts tension mediated Rac inhibition and prevents the activity front from expiration. Thus, the model combines two essential suggestions, the confinement of Rac signals to the leading edge [11] and the maintenance of cell protrusion due to F-actin-myosin-balancing generation in tension [53].

6.2 Model features and limitations

The polarization process of neutrophils exhibits certain qualitative features, see Section 1.2.1. A significant mathematical model for neutrophil polarization should reproduce these features. In Section 4.6 we assessed the simulation results displayed in Section 4.3 with respect to biological data.
We demonstrated that in our model membrane tension confines active Rac patterns to the leading edge, which has been observed in neutrophils [11]. We come to the conclusion that the proposed model exhibits a number of biologically essential properties of cellular polarization:

- The model cell responds to various stimuli, graded and localized, by spatially amplifying the stimulus, and attaining a polarized state.
- The polarization is maintained even after the signal is removed.
- The model cell remains sensitive to new incoming stimuli, and reverses its polarity in response to a new sufficiently chosen stimulus at the back of the cell.
- The model cell has the ability to resolve conflicting fronts by forming a single front of activity.

The model produces macroscopic data which are compared to experimental findings, see Section 4.3. The model cell develops an approximately constant shape within the first $150s$ after the stimulation. Biologically, we interpret this time span as the required time for the cell to *fully polarize*, i.e. to develop a lamellipodium which enables the cell to move across the substrate due to a persistently generated Rac front. In this sense, in vitro experiments suggest, that upon stimulation with fMLP polymorphonuclear leukocytes fully polarize within 2 to 3 minutes [110], which matches the required time in the model. With respect to a fully polarized cell, our model generates an average migration speed of the cell of about $0.19\mu m/s$. The in vitro measured migration speed of neutrophils is of the order 10^{-1}–$10^{0}\mu m/s$ [39]. The migration speed can be fitted more precisely by varying the magnitude of the active force term F_{act}, (see Figure 4.7). There is evidence that the migration velocity crucially depends on the compound of the substrate [119]. Thus, a more realistic fitting would also include a specific calibration of the adhesion parameter ξ. Unfortunately, broad experimental data for this parameter is not yet accessible. The default state of a resting neutrophil adhering to a flat surface

is approximately spherical. In response to Rac activation triggered by graded external signals, a broad flat front, i.e. the lamellipodium, and a tapered posterior is generated [120]. Our model exhibits this behavior. We conclude:

- The model cell develops a front of increased Rac activity which is directed to the stimulus. Initiated movement of the model cell approaches a constant migration speed.
- The model cell develops a "V"-shape with a broad front and a tapered rear.
- The model cell adopts a dumbell-like shape if two spatially opposite stimuli are applied.
- The model cell approaches a spherical resting state if active Rac is erased.

From a mathematical point of view, we explained in Chapter 5 how the propagation of a wave-like solution of a reaction-diffusion system on a moving domain is pinned through the coupling with an integral operator. We used a matched asymptotic analysis approach for a related model that is spatially one-dimensional and explained how under certain assumptions a travelling wave-front like solution for the zeroth-order terms of a suitable expansion of the system is achieved and how the wave-pattern is finally stalled. It should be stressed that the presented explanation does not provide a rigorous proof for the existence of pinned waves. However, the explanation provides at least an insight of the generation of pinned wave-patterns and gives necessary conditions.

The model possesses certain limitations, some originate in the mathematical modelling, some are exposed by the simulation results.
In Section 3.7 we highlighted the model assumptions that we regard as crucial. While we consider the thin layer approximation and the simplistic submodel of actin-binding dynamics as relatively unproblematic, the assumption that inactive Rho can be treated as a constant and the oversimplified description of the AMC are shortages of the model. In particular, the assumption that AMC mechanics can be described by a purely viscous material with a constant viscosity η may be not adequate. Since the active process of actin filamentation affects AMC mechanics, we expect that η also depends on the actin concentration. However, the rheology of actin gels is highly complex and not well understood yet, such that reliable assumptions on η cannot be provided. A model of the AMC described by a viscoelastic material would be more biologically reasonable. Moreover, a viscoelastic description might exhibit different polarization characteristics. In a viscoelastic medium the global mechanical response to local perturbations is quasi instantaneous compared to the global response of viscous media. This property may equip the mechanochemical polarisation processes with a higher sensitiveness to local signals that only occur for short times.
Further limitations are obtained by the simulations. In Section 4.3 we concluded that the model does not exhibit sensitiveness to noise. We did not intend the model to exhibit

this feature and we do not consider the lack of this feature as critical, since multiple redundant pathways for the achievement of cell polarization have been identified and it is not yet clear which one accounts to noise sensitiveness [34].
A graver limitation is that the model is very likely not capable of fusing neighboring wavefronts into one single front. We conjecture that this dues the patterning mechanism, since it requires a sufficiently slow diffusion of active Rac to work. Thus, an increased diffusion coefficient for Rac is not well suited to fuse the wave-front. A biologically reasonable modification that potentially endows the model with the ability to fuse neighboring fronts aims at the explicit inclusion of inactive Rac. Inactive Rac might diffuse faster than active Rac [97]. While active Rac is locally pinned, inactive Rac might be free to diffuse on a medium range and become activated at the periphery of the pinned wave patterns. This might locally smoothen the patterns and induce a fusion of closely neighboring wavefronts.
Finally, a limitation is that the cell requires for a stable polarization a stimulus which spatially decreases superlinearly. However, it is conceivable that external linear chemical gradients are processed in a nonlinear way, such that the input signal for Rac activation is superlinearly decreasing. On a multicellular level, e.g., it has been shown that cells can amplify shallow gradients by transforming them into steep local gradients [112]. We conjecture that this also may occur on a singular cell level.

6.3 Contributions of the model

The major contribution of the model is the proposal of a mechanochemical mechanism that gives an account how active Rac patterns may remain confined to the cell front due to the generation of membrane tension. There is a growing demand for models accounting to mechanochemical patterning in general [22, 41] and for models accounting to GTPase-tension interactions in cell polarization in particular [11]. Purely mechanical [14, 15, 121, 122] as well as purely chemical mechanisms [7] have been proposed to give an account for cell polarization. The diversity of these models exhibit a wide range of abilities to generate patterns which have been qualitatively characterized over the last decades. Mechanochemical patterning with respect to cell polarization, however, represents a new, not yet well understood class [22, 41].
We provided a reaction-diffusion based wave-propagation processes, whose propagation is pinned due to a mechanical response. The disclosure of the necessary qualitative properties for the reaction terms and the AMC mechanics may be of importance for future studies. In each modelling step, the necessary conditions for the patterning mechanism are highlighted. We summarized the conditions in Chapter 5. Consequently, the mechanism is not restricted to particular choices of the functions we suggested in this thesis, but rather consists of basic units whose modelling requires certain qualitative characteristics. Thus, our approach may provide a suitable framework for more complex and more biologically relevant models aiming at mechanochemical cell polarization.

6.4 Model design and model comparison

The mechanical unit in our model adopts ideas from [14, 37] by introducing competition between polymerization and protrusion at different sites in the cell via membrane tension, and the treatment of the ACM as an active viscous gel, respectively. Actin gels are commonly endowed with a with a polarity field [85]. Our very simple version of the polarity field segregates the cell into regions of protrusive and contractile forces. Since active Rac orchestrates the segregation, regions of propelling fronts and increased Rac activity geometrically coincide. In response to a single stimulus the model cell generates a cone-like morphology where active Rac is predominantly located at the front while active RhoA is located in the tapered back.
The biochemical unit of the model is related to the patterning mechanism presented by Mori et al. [8]. Therein, a reaction-diffusion system is described in which a triggered travelling wave of slow diffusing active Rho is locally pinned by a fast diffusing inactive Rho. Experimental investigations on neutrophils, however, have shown that the required diffusion coefficient is unrealistically high [11]. Unlike Mori's and other generic models for cell polarization containing Rho GTPase related chemical signalling which require fast diffusing quantities to serve as a long-range signal conductor [1–3, 24–28, 118], the presented model transmits long-range signals mechanically via changes in membrane tension. Therefore, our proposed model avoids the issue to rely on unrealistically high diffusion coefficients.

6.5 Outlook

The model suggests a number of experimental tests that could be used to check its validity. For example, the model predicts that multiple fronts of polarity can be resolved by the expiration of all fronts except for one. In the model the maintained front is determined by the actual choice of the stimulus: The front created in response to the longest stimulus dominates. Currently, it is not known if a neutrophil *decides* in accordance to this prediction.
Another example refers to the model prediction by which changes in membrane tension affect the activation rate of Rho. In reality, Rho activation is not mediated via a simple reaction scheme as used in the model, but by a whole process in which Rho GDP is dephosphorylated to Rho GTP via GEF. The Hill terms in the *on*-rates of the reaction functions $f_{1,2}$ model the autocatalysis which may be mediated by GEF. Hence, we hypothesize that membrane tension suppresses GEF mediated activation.
The presented minimal model provides the necessary features for more complex and more biologically relevant models. We propose a mechanism that explains how changes in membrane tension qualitatively affect Rho GTPase activity in order to generate polarity pattern, but does not give an account which molecular links translate mechanical

into chemical signals. However, there are several aspirants that may provide a mechanism capable of translating plasma membrane tension into chemical signals. A possible mechanism of tension sensation in neutrophils relying on the properties of the actin nucleation machinery has been suggested by [11]: Actin is a down- as well as an upstream effector for SCAR/WAVE. The complex stimulates actin assembly, and, on the other hand, the presence of F-actin is required to remove the complex from the membrane. It has been shown that this characteristic results in multiple propagating waves of the SCAR/WAVE complex, that appear to organize actin filamentation at the leading edge. Furthermore, it has been shown that the waves extinguish if mechanical barriers prevent them from propagation [123]. Houk et al. [11] hypothesize that increased membrane tension could similarly extinguish waves by antagonizing propagation. Moreover, in neutrophils is SCAR/WAVE is also feeds back on Rac activation. Since our model is bases on a wave-process, an adaption of the model including SCAR/WAVE dynamics seems to be well suited and could give a model based prediction about possible mechanosensitive linkages containing Rho GTPases, SCAR/WAVE, and cell mechanics.

The model considers the AMC as a viscous material. From a more realistic point of view, the AMC can be characterized as a viscoelastic active material [103]. While the purely viscous behavior of the AMC affects the generation of membrane tension with a delay, an elastic response at short time scales would influence membrane tension instantaneous. An adaption of the model with respect to a viscoelastic could improve some model features like the required time to repolarize in response to new incoming stimuli.

Appendix A

Proof of Theorem 3.1

A.1 A priori estimates

We require suitable energy estimates that state the uniformly boundedness of u_ε with respect to $\varepsilon > 0$. The boundedness will be required later to apply certain compactness properties.

Lemma A.1. *Let u_ε be a solution of (3.5)–(3.6). Then constants $M > 0$, $C > 0$, independent of $\varepsilon > 0$, exist such that for $0 < \varepsilon < M$ the following estimates hold:*

$$\|\partial_t u_\varepsilon\|_{L^\infty(I,L^2(\Omega^0,\mathbb{R}^m))} + \|u_\varepsilon\|_{L^\infty(I,H^1(\Omega^0,\mathbb{R}^m))} \leq C, \tag{A.1}$$

$$\frac{1}{\sqrt{\varepsilon}}\|\chi_{\Omega_\varepsilon^i}\partial_t u_\varepsilon\|_{L^\infty(I,L^2(\Omega_\varepsilon^i,\mathbb{R}^m))} + \frac{1}{\sqrt{\varepsilon}}\|\chi_{\Omega_\varepsilon^i} u_\varepsilon\|_{L^\infty(I,L^2(\Omega_\varepsilon^i,\mathbb{R}^m))} \leq C \quad (i = 1, 2), \tag{A.2}$$

$$\frac{1}{\sqrt{\varepsilon}}\|\chi_{\Omega_\varepsilon^i}\nabla_{x'} u_\varepsilon\|_{L^\infty(I,L^2(\Omega_\varepsilon^i,\mathbb{R}^m))} + \frac{\varepsilon^{1+l}}{\sqrt{\varepsilon}}\|\chi_{\Omega_\varepsilon^i}\nabla_y u_\varepsilon\|_{L^\infty(I,L^2(\Omega_\varepsilon^i,\mathbb{R}^m))} \leq C, \quad (i = 1, 2), \tag{A.3}$$

Moreover, the growth conditions on f_j^i imply the pointwise bounds

$$0 \leq u_\varepsilon \leq C\exp(-mT) \quad \text{for a.e. } (t, x) \in I \times \Omega. \tag{A.4}$$

Proof. We test (3.5) with $(u^0_{j\varepsilon}, u^1_{j\varepsilon}, u^2_{j\varepsilon})$ and obtain

$$\begin{aligned}
&\int_{\Omega^0_\varepsilon} \partial_t u^0_{j\varepsilon} u^0_{j\varepsilon} dx + D^0_j \int_{\Omega^0_\varepsilon} \nabla u^0_{j\varepsilon} \nabla u^0_{j\varepsilon} dx \\
&+ \sum_{i=1,2} \left\{ \frac{1}{\varepsilon} \int_{\Omega^i_\varepsilon} \partial_t u^i_{j\varepsilon} u^i_{j\varepsilon} dx + \frac{1}{\varepsilon} \int_{\Omega^i_\varepsilon} D^i_j \nabla_{x'} u^i_{j\varepsilon} \nabla_{x'} u^i_{j\varepsilon} dx + \varepsilon^{1+2l} \int_{\Omega^i_\varepsilon} \overline{D}^i_j \nabla_y u^i_{j\varepsilon} \nabla_y u^i_{j\varepsilon} dx \right\} \\
&= \int_{\Omega^0_\varepsilon} f^0_j(u^0_\varepsilon) u^0_{j\varepsilon} dx + \sum_{i=1,2} \left\{ \frac{1}{\varepsilon} \int_{\Omega^i_\varepsilon} f^i_j \left(u^i_\varepsilon \right) u^i_{j\varepsilon} dx \right\} \\
&\leq \int_{\Omega^0_\varepsilon} (1 + |u^0_\varepsilon|) u^0_{j\varepsilon} dx + \sum_{i=1,2} \left\{ \frac{1}{\varepsilon} \int_{\Omega^i_\varepsilon} (1 + |u^i_\varepsilon|) u^i_{j\varepsilon} dx \right\}
\end{aligned}$$

for a.e. $t \in I$. The inequality holds since $z \mapsto f(z)$ is Lipschitz-continuous. Therefore, there exists a constant $C > 0$ such that

$$|f(z)| \leq C(1 + |z|) \quad \forall z \in \mathbb{R}^n.$$

Adding up the estimates for $j = 1, ..., m$ and subsequently integration with respect to $t \in I$ yields

$$\begin{aligned}
&\frac{1}{2} \|u^0_\varepsilon(t)\|^2_{L^2(\Omega^0_\varepsilon)} + \|\nabla u^0_\varepsilon\|^2_{L^2(I, L^2(\Omega^0_\varepsilon))} \\
&+ \sum_{i=1,2} \left\{ \frac{1}{2\varepsilon} \|u^i_\varepsilon(t)\|^2_{L^2(\Omega^i_\varepsilon)} + \frac{1}{\varepsilon} \|\nabla_{x'} u^i_\varepsilon\|^2_{L^2(I, L^2(\Omega^i_\varepsilon))} + \varepsilon^{1+2l} \|\nabla_y u^i_\varepsilon\|^2_{L^2(I, L^2(\Omega^i_\varepsilon))} \right\} \\
&\leq C \int_I \left(1 + \|u^0_\varepsilon(t)\|^2_{L^2(I, L^2(\Omega^0_\varepsilon))} \right) dx + C \sum_{i=1,2} \frac{1}{\varepsilon} \int_I \left(1 + \|u^i_\varepsilon(t)\|^2_{L^2(I, L^2(\Omega^i_\varepsilon))} \right) dx
\end{aligned} \tag{A.5}$$

for a.e. $t \in I$, where we used that $\|D^0_j\|_{L^\infty(\Omega^0_\varepsilon)}$, $\|D^i_j\|_{L^\infty(\Omega^i_\varepsilon)}$, $\|\overline{D}^i_j\|_{L^\infty(\Omega^i_\varepsilon)} \geq c$ $(i = 1, 2)$. Grönwall's inequality implies that for a suitable $M > 0$ and $\varepsilon \leq M$ the time dependent functions on the right hand side can be estimated by

$$\|u^0_\varepsilon\|^2_{L^\infty(I, L^2(\Omega^0_\varepsilon))} - \|U^0_\varepsilon\|^2_{L^2(\Omega^0_\varepsilon)} + \frac{1}{\varepsilon} \sum_{i=1,2} \left\{ \|u^i_\varepsilon\|^2_{L^\infty(I, L^2(\Omega^i_\varepsilon))} - \|U^i_\varepsilon\|^2_{L^2(\Omega^0_\varepsilon)} \right\} \leq C.$$

From condition (3.7) we can deduce

$$\|u^0_\varepsilon\|^2_{L^\infty(I, L^2(\Omega^0_\varepsilon))} + \frac{1}{\varepsilon} \sum_{i=1,2} \|u^i_\varepsilon\|^2_{L^\infty(I, L^2(\Omega^i_\varepsilon))} \leq C.$$

Application of this estimate in the right-hand side of (A.5) yields

$$\|\nabla u^0_\varepsilon\|^2_{L^2(I, L^2(\Omega^0_\varepsilon))} + \frac{1}{\varepsilon} \sum_{i=1,2} \|\nabla_{x'} u^i_\varepsilon\|^2_{L^2(I, L^2(\Omega^i_\varepsilon))} + \varepsilon^{1+2l} \sum_{i=1,2} \|\nabla_y u^i_\varepsilon\|^2_{L^2(I, L^2(\Omega^i_\varepsilon))} \leq C.$$

Now, in the same way as in the proof of Lemma 3.1 in [124], we obtain

$$\|\partial_t u_\varepsilon^0\|^2_{L^\infty(I,L^2(\Omega_\varepsilon^0))} + \frac{1}{\varepsilon}\sum_{i=1,2}\|\partial_t u_\varepsilon^i\|^2_{L^\infty(I,L^2(\Omega_\varepsilon^i))} + \|\nabla u_\varepsilon^0\|^2_{L^\infty(I,L^2(\Omega_\varepsilon^0))}$$
$$+\frac{1}{\varepsilon}\sum_{i=1,2}\|\nabla_{x'} u_\varepsilon^i\|^2_{L^\infty(I,L^2(\Omega_\varepsilon^i))} + \varepsilon^{1+2l}\sum_{i=1,2}\|\nabla_y u_\varepsilon^i\|^2_{L^\infty(I,L^2(\Omega_\varepsilon^i))} \leq C$$

as well as the pointwise bounds (A.4). □

A.2 Auxiliaries

In this section we will present the required tools that enable us to consider the limit case of system (3.1)–(3.6).
From a more general point of view, we are interested in the behavior of the solution u_ε if the thickness of the layers approaches zero. This will be done by the investigation of the asymptotic behavior of the sequence u_ε for $\varepsilon \to 0$. In this case the domains Ω_ε^1 and Ω_ε^2 approach to interface Σ and the bulk domain Ω_ε^0 approaches

$$\Omega := (0,1)^{n-1} \times (0,H).$$

In order to introduce a suitable notion of convergence, we investigate the behavior of u_ε with respect to a reference domain on which test-functions will be defined. This is the roughly idea behind the concept of two-scale convergence.

A.3 Two-scale convergence

For different $\varepsilon > 0$ the respective solutions u_ε are defined on different domains. Thus, we cannot apply classical compactness arguments that are required to obtain the existence of the limit case $\lim_{\varepsilon\to\infty} u_\varepsilon$.
The concept of convergence in the two-scale sense allows lower dimensional approximation and provides suitable compactness theorems to consider the limit case.
Let $G_\varepsilon := \Sigma' \times (0,\varepsilon)$ for a bounded, convex Lipschitz-domain $\Sigma' \subset \mathbb{R}^{n-1}$. To investigate the equations in the limit $G_\varepsilon \to \Sigma := \Sigma' \times \{0\}$, we introduce the reference layer $\Sigma' \times Z$, where $Z := (0,1)$.

Definition A.2 (Weak two-scale convergence)**.** A sequence $(u_\varepsilon)_{\{\varepsilon>0\}}$ with elements $u_\varepsilon \in L^2(I, L^2(G_\varepsilon))$ converges *weakly in the two-scale sense* to $u_0(t,x',y) \in L^2(I, L^2(\Sigma' \times Z))$ if

$$\lim_{\varepsilon\to 0}\frac{1}{\varepsilon}\int_I\int_{G_\varepsilon} u_\varepsilon(t,x)\varphi\left(t,x',\frac{y}{\varepsilon}\right)\,dx\,dt = \int_I\int_{\Sigma'}\int_Z u_0(t,x',y)\varphi(t,x',y)\,dy\,dx'\,dt$$

for every test function $\varphi \in C(I \times \Sigma' \times Z)$

Definition A.3 (Strong two-scale convergence)**.** A sequence $(u_\varepsilon)_{\{\varepsilon>0\}}$ with elements $u_\varepsilon \in L^2(I, L^2(G_\varepsilon))$ which converges weakly in the two-scale sense to $u_0 \in L^2(I, L^2(\Sigma' \times Z))$ is said to *converge strongly in the two-scale sense* if

$$\lim_{\varepsilon\to 0} \|u_\varepsilon\|_{L^2(I,L^2(G_\varepsilon))} = \|u_0\|_{L^2(I,L^2(\Sigma'\times Z))}.$$

A simple consequence is formulated in the following

Remark A.4. If u_0 does not depend on $y \in Z$, it can be verified easily that the weakly convergent sequence $u_\varepsilon \to u^0(t, x')$ in the two-scale sense converges strongly in the two-scale sense if and only if

$$\lim_{\varepsilon\to 0} \frac{1}{\sqrt{\varepsilon}} \|u_\varepsilon - u_0\|_{L^2(I,L^2(G_\varepsilon))} = 0.$$

The compactness properties of sequences in the two-scale sense are achieved by certain boundedness criteria. For weakly convergent sequences in the two-scale sense the following holds:

Proposition A.5. *Let u_ε be a sequence in $L^2(I \times G_\varepsilon)$, such that*

$$\frac{1}{\sqrt{\varepsilon}} \|u_\varepsilon\|_{L^2(I\times G_\varepsilon)} \le C,$$

with a constant $C > 0$, independent of ε. Then there exists a subsequence, again denoted by u_ε, and a limit function $u^0 \in L^2(I, L^2(\Sigma \times Z))$ such that

$$u_\varepsilon \to u^0 \text{ weakly in the two-scale sense.}$$

Proof. The proof is a time-dependent version of the proof of Theorem 1 in [125]. □

A simple, but yet remarkable observation is that the weak two-scale convergence of u_ε and $\nabla_{x'} u_\varepsilon$ induce the weak two-scale convergence of $\varepsilon\nabla_y u_\varepsilon$. This is directly obtained through the application of the divergence theorem, which will be shown now.

Lemma A.6. *Let u_ε be a sequence in $L^2(I, H^1(G_\varepsilon))$ and C a constant independent of ε, such that*

$$\frac{1}{\sqrt{\varepsilon}} \|u_\varepsilon\|_{L^2(I\times G_\varepsilon)} + \frac{1}{\sqrt{\varepsilon}} \|\nabla_{x'} u_\varepsilon\|_{L^2(I\times G_\varepsilon)} \le C.$$

Then there exists a function $u_0 \in L^2(I, L^2(\Sigma' \times Z))$ and a subsequence, again denoted by u_ε, such that

$$\begin{aligned} u_\varepsilon &\to u_0(t, x', y) \text{ weakly in the two-scale sense,} \\ \nabla_{x'} u_\varepsilon &\to \nabla_{x'} u_0(t, x', y) \text{ weakly in the two-scale sense,} \\ \varepsilon\nabla_y u_\varepsilon &\to \nabla_y u_0(t, x', y) \text{ weakly in the two-scale sense.} \end{aligned}$$

Proof. Let $u_\varepsilon \in L^2(I \times H^1(G_\varepsilon))$ satisfy the estimate. Proposition A.4 allows us to extract a subsequence, again denoted by u_ε, such that

$$u_\varepsilon \to u_0 \text{ and } \nabla_{x'} u_\varepsilon \to \nabla_{x'} u_0 \text{ weakly in the two-scale sense.}$$

We show now that $\varepsilon \nabla_y u_1(t, x', y)$ weakly converges to $\nabla_y u_0(t, x', y)$ in the two-scale sense. The divergence theorem implies

$$\begin{aligned} &\int_I \int_{G_\varepsilon} u_\varepsilon \mathrm{div}_{x'} \varphi \left(x', \frac{x_n}{\varepsilon}\right) dx_n \; dx' \; dt + \frac{1}{\varepsilon} \int_I \int_{G_\varepsilon} u_\varepsilon \mathrm{div}_y \varphi \left(x', \frac{x_n}{\varepsilon}\right) dx_n \; dx' \; dt \\ &= -\int_I \int_{G_\varepsilon} \nabla_{x'} u_\varepsilon \varphi_{x'} \left(x', \frac{x_n}{\varepsilon}\right) dx_n \; dx' \; dt - \int_I \int_{G_\varepsilon} \nabla_y u_\varepsilon \varphi_y \left(x', \frac{x_n}{\varepsilon}\right) dx_n \; dx' \; dt, \end{aligned} \tag{A.6}$$

for test functions $\varphi \in C_0^\infty(I \times \Sigma' \times Z)^n$, where we used the notation $\mathrm{div}_{x'} \varphi := \mathrm{div}\,(\varphi_{x'})$, $\mathrm{div}_y \varphi := \mathrm{div}\,(\varphi_y)$ for $\varphi = (\varphi_{x'}, \varphi_y)$. This is equivalent to

$$\begin{aligned} &\varepsilon \frac{1}{\varepsilon} \int_I \int_{G_\varepsilon} u_\varepsilon \mathrm{div}_{x'} \varphi \left(x', \frac{x_n}{\varepsilon}\right) dx_n \; dx' \; dt + \frac{1}{\varepsilon} \int_I \int_{G_\varepsilon} u_\varepsilon \mathrm{div}_y \varphi \left(x', \frac{x_n}{\varepsilon}\right) dx_n \; dx' \; dt \\ &= -\varepsilon \frac{1}{\varepsilon} \int_I \int_{G_\varepsilon} \nabla_{x'} u_\varepsilon \varphi_{x'} \left(x', \frac{x_n}{\varepsilon}\right) dx_n \; dx' \; dt - \frac{1}{\varepsilon} \int_I \int_{G_\varepsilon} \varepsilon \nabla_y u_\varepsilon \varphi_y \left(x', \frac{x_n}{\varepsilon}\right) dx_n \; dx' \; dt. \end{aligned}$$

Since u_ε, $\nabla_{x'} u_\varepsilon$ weakly converge in the two-scale sense, the first term on the left hand side and the first term on the right hand side vanish for $\varepsilon \to 0$. Thus, we obtain for $\varepsilon \to 0$

$$-\frac{1}{\varepsilon} \int_I \int_{G_\varepsilon} \varepsilon \nabla_y u_\varepsilon \varphi_y \left(x', \frac{x_n}{\varepsilon}\right) dx_n \; dx' \; dt \to \int_I \int_{\Sigma'} \int_Z u_0 \; \mathrm{div}_y \varphi \; dy dx' dt \tag{A.7}$$

which is equivalent to $\varepsilon \nabla_y u_1(t, x', y) \to \nabla_y u_0(t, x', y)$ in the two-scale sense. □

The limit system presented in Theorem 3.1 has no transmission conditions and the equations are formulated independently of the reference layer. A necessary condition therefore is that the weak two-scale limit of u_ε is constant in $y \in Z$. In this case Lemma A.6 is equivalent to

Corollary A.7. *Let u_ε be a sequence in $L^2(I, H^1(G_\varepsilon))$ and $u_0 \in L^2(I, H^1(\Sigma' \times Z))$ constant with respect to $y \in Z$, such that*

$$u_\varepsilon \to u_0(t, x'), \quad \nabla_{x'} u_\varepsilon \to \nabla_{x'} u_0(t, x'),$$

converge weakly in the two-scale sense, respectively.
Then

$$\varepsilon \nabla_y u_\varepsilon \to 0 \quad \textit{converges weakly in the two-scale sense.}$$

Proof. The assertion follows directly from equation (A.7) and the application of the divergence theorem with respect to the variable y on the right hand side. □

In order to obtain convergency of the right hand sides of (3.1) to the right hand sides of (3.9)–(3.11), strong convergence in the two-scale sense is required. In general, it is not trivial to establish the strong convergence of sequences in the two-scale sense for transmission problems since suitable extensions are required to apply classical compactness theorems. Fortunately, the case covered in Corollary A.7 endows the sequence with a "natural" scaling function such that we can map the sequence into the reference space $L^2(I, H^1(\Sigma' \times Z))$ easily.

Proposition A.8. *Let $u_\varepsilon \in L^2(I, H^1(G_\varepsilon))$ be a sequence, such that $\partial_t u_\varepsilon \in L^2(I, L^2(G_\varepsilon))$, and let $u_0 \in L^2(I, H^1(\Sigma' \times Z))$ be constant with respect to $y \in Z$, such that*

$$u_\varepsilon \to u_0(t, x'), \quad \partial_t u_\varepsilon \to \partial_t u_0(t, x'), \quad \nabla_{x'} u_\varepsilon \to \nabla_{x'} u_0(t, x'), \quad \varepsilon \nabla_y u_\varepsilon \to 0$$

converge weakly in the two-scale sense, respectively. Then converges

$$u_\varepsilon \to u_0(t, x')$$

strongly in the two-scale sense.

Proof. We define the scaled function

$$\overline{u}_\varepsilon(t, x', y) := u_\varepsilon\left(t, x', \varepsilon y\right) \text{ for } (t, x', y) \in I \times \Sigma' \times Z.$$

Then

$$\frac{1}{\varepsilon} \int_I \int_{G_\varepsilon} |u_\varepsilon(t, x)|^2 dx dt = \int_I \int_{\Sigma'} \int_Z |\overline{u}_\varepsilon(t, x', y)|^2 dy dx' dt. \tag{A.8}$$

Moreover, it can be seen easily that $\overline{u}_\varepsilon$, $\nabla \overline{u}_\varepsilon$, and $\partial_t \overline{u}_\varepsilon$ are elements of $L^2(I, L^2(\Sigma' \times Z)$ which weakly converge to u_0, $\nabla'_x u_0$, and $\partial_t u_0$, respectively. The Lemma of Aubin-Lions implies that the embedding

$$L^2(I, L^2(\Sigma' \times Z)) \hookrightarrow \{u \in L^2(I, H^1(\Sigma' \times Z)) : \partial_t u \in L^2(I, L^2(\Sigma' \times Z))\}$$

is compact. Thus, there exists a subsequence, again denoted by $\overline{u}_\varepsilon$, such that

$$\overline{u}_\varepsilon \to u_0 \text{ in } L^2(I, L^2(\Sigma' \times Z))$$

for $\varepsilon \to 0$. From A.8 we can deduce

$$\lim_{\varepsilon \to 0} \frac{1}{\sqrt{\varepsilon}} \|u_\varepsilon\|_{L^2(I \times G_\varepsilon)} = \lim_{\varepsilon \to 0} \|\overline{u}_\varepsilon\|_{L^2(I \times \Sigma' \times Z)} = \|u_0\|_{L^2(I \times \Sigma' \times Z)}$$

□

Finally, for the proof of Theorem 3.1 we need control of the traces on ∂G_ε. The required statement gives the following lemma.

Lemma A.9. *Let the conditions of Lemma A.6 hold. For all testfunctions* $\varphi \in C^\infty(I \times \overline{\Sigma}')$ *converge*

$$\int_I \int_{\Sigma' \times \{\varepsilon\}} \varepsilon \nabla_y u_\varepsilon(t, x', \varepsilon)\varphi(t, x')dx'dt \to \int_I \int_\Sigma \nabla_y u_0(t, x', 0)\varphi(t, x')dx'dt,$$
$$\int_I \int_{\Sigma' \times \{0\}} \varepsilon \nabla_y u_\varepsilon(t, x', 0)\varphi(t, x')dx'dt \to \int_I \int_\Sigma \nabla_y u_0(t, x', 0)\varphi(t, x')dx'dt,$$

for $\varepsilon \to 0$.

Proof. This is a special case of Proposition 5 in [125] since $\varepsilon \nabla_y u_\varepsilon$ converges weakly in the two-scale sense to $\nabla_y u_0$. □

Remark A.10. The definition of G_ε is equivalent to Ω_ε^2 if $\Sigma' = (0,1)^{n-1}$. To investigate two-scale convergence for functions defined on Ω_ε^1, we replace G_ε by

$$G_\varepsilon := \Sigma' \times (\varepsilon, 2\varepsilon).$$

It is easy to see that all results still remain valid if for this particular G_ε two-scale convergence is defined as in Definition A.2.

A.4 Proof of the main theorem

We proof Theorem 3.1. The proof is split in multiple parts. At first we present several preliminary results which will be used in the main part of the proof. Then we consider the convergence of system defined in the bulk. In the third part the convergence of the system defined in the layers is considered. Thereafter we will show that in the limit-case the transmission conditions reduce to homogenous Neumann-conditions. The existence of solutions for the limit-system is well known. In the last step the uniqueness of the solutions of the limit system is proofed.

Proposition A.11 (Convergence in the bulk region)**.** *There exists a subsequence* u_ε *of weak solutions of (3.1)–(3.4) and a limit function* $u_0 \in L^2(I, H^1(\Omega, \mathbb{R}^m))$*, with* $\partial_t u_0 \in L^2(I, L^2(\Omega, \mathbb{R}^m))$*, such that*

1) $u_{j\varepsilon} \to u_0$ *strongly in* $L^2(I, L^2(\Omega))$*;*

2) $\nabla u_{j\varepsilon} \to \nabla u_0$ *weakly in* $L^2(I, L^2(\Omega))$*;*

3) $\partial_t u_{j\varepsilon} \to \partial_t u_0$ *weakly in* $L^2(I, L^2(\Omega))$.

Proof. Considering the energy estimates given in Section A.1 the proof is almost identical to the proof of Proposition 2.1 in [124]. □

Proposition A.12 (Weak convergence of the fluxes)**.** *Let $\varphi \in C^\infty(I \times \overline{\Sigma' \times H})$ and set $\varphi^\varepsilon(t,x) = \varphi\left(t, x', \frac{H-2\varepsilon}{H} y + 2\varepsilon\right)$. There exists a subsequence u_ε of weak solutions of (3.1)–(3.4), such that*

$$\int_I \int_{S_\varepsilon^1} \nabla_y u_{j\varepsilon}^0 \varphi^\varepsilon dx' dt \to \int_I \int_\Sigma \nabla_y u_{j0}^0 \varphi dx' dt$$

for all $\varphi \in C^\infty(I \times \overline{\Sigma' \times H})$.

Proof. A similar assertion is proofed in [124], Section 5.2. An adaptation of the proof ist left to the reader. □

Proposition A.13 (Weak two-scale convergence in the layers)**.** *There exists a subsequence u_ε of weak solutions of (3.1)–(3.4), and a limit function $u_{j0}^i \in L^2(I, H^1(\Sigma' \times Z))$, with $\partial_t u_{j0}^i \in L^2(I, L^2(\Sigma' \times Z))$ (i=1,2), such that*

$$\begin{gathered} u_{j\varepsilon}^i \to u_{j0}^i(t,x'), \quad \nabla_{x'} u_{j\varepsilon}^i \to \nabla_{x'} u_{j0}^i, \quad \varepsilon \nabla_y u_{j\varepsilon}^i \to \nabla_y u_{j0}^i, \\ \partial_t u_{j\varepsilon}^i \to \partial_t u_{j0}^i, \end{gathered} \tag{A.9}$$

converge weakly in the two-scale sense, respectively.

Proof. We directly obtain the statements of the first two rows from Lemma A.1, Proposition A.4, and Lemma A.6. We also obtain from Lemma A.1 and Proposition A.4 that $\partial_t u_{j\varepsilon}^i$ converges weakly in the two-scale sense to a function $\overline{u}_j^i(t,x',y)$. Thus, we obtain by partial integration with respect to t

$$\int_I \int_{\Sigma'} \int_Z \overline{u}_j^i(t,x',y)\varphi \, dy dx' dt = \lim_{\varepsilon \to 0} \frac{1}{\varepsilon} \int_I \int_{\Omega_\varepsilon^i} \partial_t u_{j\varepsilon}^i \varphi\left(t, x', \frac{x_n}{\varepsilon}\right)$$

$$= \lim_{\varepsilon \to 0} \frac{1}{\varepsilon} \left\{ \int_{\Omega_\varepsilon^i} U_{j\varepsilon}^i(x', x_n) \varphi\left(0, x', \frac{x_n}{\varepsilon}\right) dx + \int_I \int_{\Omega_\varepsilon^i} u_{j\varepsilon}^i \partial_t \varphi\left(t, x', \frac{x_n}{\varepsilon}\right) dx dt \right\}$$

for all test functions $\varphi \in C^\infty(I \times \Sigma' \times Z)$. From (3.7) and Lemma A.6 we deduce that $U_{j\varepsilon}^i(x', x_n)$ converges weakly in the two-scale sense to an element of $L^2(I, L^2(\Sigma' \times Z))$. For a suitable subsequence of u_ε, we obtain $\overline{u}_j^i(t,x',y) = \partial_t u_{j0}(t,x',y)$. □

Convergence of the system in the bulk region

Proof. Consider test functions $\varphi \in C_0^\infty(I \times \overline{\Omega}, \mathbb{R}^m)$ with $\mathrm{supp}(\varphi) \subset I \times \overline{\Omega}/\Sigma$. For fixed ε_0 satisfying

$$\mathrm{dist}\{\Sigma, \mathrm{supp}(\varphi)\} \geq 2\varepsilon_0$$

holds fo every $\varepsilon < \varepsilon_0$

$$\mathrm{supp}(\varphi) \cap \left(\Omega_\varepsilon^1 \cup \Omega_\varepsilon^2\right) = \emptyset.$$

Let $\varepsilon < \varepsilon_0$. Testing (3.5) with φ as defined above yields

$$\int_I \int_{\Omega_\varepsilon^0} \partial_t u_{j\varepsilon}^0 \varphi \, dx \, dt + \int_I \int_{\Omega_\varepsilon^0} D_j^0 \nabla u_{j\varepsilon}^0 \nabla \varphi \, dx \, dt$$
$$+ D_j^0 \int_I \int_{\partial\Omega_\varepsilon^0/\Sigma} \partial_\nu u_{j\varepsilon}^0 \varphi \, dS \, dt = \int_I \int_{\Omega_\varepsilon^0} f_j(u_\varepsilon^0)\varphi \, dx \, dt.$$

Due to Proposition A.11 and Proposition A.12, we can proceed as in [124], Section 6.1, and obtain a subsequence, such that for $\varepsilon \to 0$

$$\int_I \int_\Omega \partial_t u_{j0}^0 \varphi \, dx \, dt + \int_I \int_\Omega D_j^0 \nabla u_{j0}^0 \nabla \varphi \, dx \, dt$$
$$= \int_I \int_\Omega f_j(u_0^0)\varphi \, dx \, dt,$$
$$\int_I \int_{\partial\Omega_\varepsilon^0/\Sigma} D_j^0 \partial_\nu u_{j\varepsilon}^0 \varphi \, dS \, dt = 0$$

and

$$u_j^0(0,x) = U_{j0}^0(x), \quad \text{for a.e. } x \in \Omega.$$

Thus, (3.9), (3.12), and (3.15) hold. □

Convergence of the system in the layers Here we derive the set of the equations on the limit-layer Σ'. The main idea is to show the convergency to a limit-system in which the derivatives in the y-direction vanish. The obtained system does not depend explicitly on $y \in Z$ anymore. Under assumption (3.7) for the initial conditions will be shown that the whole solution is indeed independent of $y \in Z$. Then, we can apply the compactness properties presented in Section A.2.

Proof. 1) We start with the weak formulation (3.5) and consider the test functions

$$\varphi_j^\varepsilon(t,x) = \varphi_j\left(t, x', \frac{2y}{\varepsilon} - 1\right), \tag{A.10}$$

where $\varphi_j \in C^\infty(I \times \overline{\Sigma' \times Z})$. Let $\Gamma_\varepsilon^1 := \Omega_\varepsilon^1/(S_\varepsilon^1 \cup S_\varepsilon^2)$. Testing of (3.5) with $\varphi_j^\varepsilon(t,x)$ yields

$$\begin{aligned}
&\frac{1}{\varepsilon}\int_I \int_{\Omega_\varepsilon^1} \partial_t u_{j\varepsilon}^1 \varphi_j^\varepsilon(t,x)dx \, dt + \frac{1}{\varepsilon}\int_I \int_{\Omega_\varepsilon^1} D_j^1 \nabla_{x'} u_{j\varepsilon}^1 \nabla_{x'} \varphi_j^\varepsilon(t,x) \\
&+2\varepsilon^{2l}\overline{D}_j^1 \nabla_y u_{j\varepsilon}^1 \nabla_y \varphi_j\left(t, x', \frac{2y}{\varepsilon} - 1\right) dx \, dt + \frac{1}{\varepsilon}\int_I \int_{\Gamma_\varepsilon^1} D_j^1 \partial_\nu u_{j\varepsilon}^1 \varphi_j^\varepsilon(t,x) dS \, dt \\
&= \frac{1}{\varepsilon}\int_I \int_{\Omega_\varepsilon^1} f_j^1\left(u_\varepsilon^1\right)\varphi_j^\varepsilon(t,x)dxdt - \int_I \int_{S_\varepsilon^1 \cup S_\varepsilon^2} \varepsilon^{1+2l}\overline{D}_j^1 \nabla_y u_{j\varepsilon}^1 \cdot \nu \varphi_j\left(t, x', \frac{2y}{\varepsilon} - 1\right) dx'dt
\end{aligned} \tag{A.11}$$

where we used the identity $\nabla_{x_n}\varphi^\varepsilon = \frac{2}{\varepsilon}\nabla_y \varphi_j\left(t, x', \frac{2y}{\varepsilon} - 1\right)$. Since $l > 1/2$, we obtain from Proposition A.13 and the imposed homogenous Neumann-conditions of u_ε^1 on Γ_ε^1

that in the limit for $\varepsilon \to 0$ the left hand side is

$$\int_I \int_{\Sigma'} \int_Z \partial_t u^1_{j0}(t,x',y)\varphi_j(t,x',y) + D^1_j \nabla_{x'} u^1_{j0}(t,x',y)\nabla_{x'}\varphi_j(t,x',y) dy dx' dt$$

Lemma A.9 states that the trace term on the right hand side tends to zero for $\varepsilon \to 0$:

$$\begin{aligned}&\int_I \int_{S^1_\varepsilon \cup S^2_\varepsilon} \varepsilon^{1+2l} \overline{D}^1_j \nabla_y u^1_{j\varepsilon} \cdot \nu \varphi_j \left(t, x', \frac{2y}{\varepsilon} - 1\right) dx' dt \\ &= \varepsilon^{2l} \int_I \int_{S^1_\varepsilon \cup S^2_\varepsilon} \overline{D}^1_j \varepsilon \nabla_y u^1_{j\varepsilon} \cdot \nu \varphi_j \left(t, x', \frac{2y}{\varepsilon} - 1\right) dx' dt \to 0.\end{aligned}$$

Since f^1_j is Lipschitz-continous and $\|u^1_\varepsilon\|_{L^2(I,L^2(\Sigma'\times Z))} \leq C\sqrt{\varepsilon}$, the estimate

$$\|f^1_j(u^i_\varepsilon)\|_{L^2(I,L^2(\Sigma'\times Z))} \leq C_0(\varepsilon + \|u^1_\varepsilon\|_{L^2(I,L^2(\Sigma'\times Z))}) \leq C_1\sqrt{\varepsilon}$$

holds. Thus, we can deduce from Proposition that $f^1_j(u^i_\varepsilon)$ converges weakly in the two-scale sense to an element $f^1_{j0} \in L^2(I, L^2(\Sigma' \times Z))$. Consequentely we obtain from (A.11) for $\varepsilon \to 0$

$$\begin{aligned}\int_I \int_{\Sigma'} \int_Z \partial_t u^1_{j0}(t,x',y)\varphi_j(t,x',y) + D^1_j \nabla_{x'} u^1_{j0}(t,x',y)\nabla_{x'}\varphi_j(t,x',y) dy dx' dt \\ = \int_I \int_{\Sigma'} \int_Z f^1_{j0}\varphi_j(t,x',y) dy dx' dt.\end{aligned} \tag{A.12}$$

Since we tested with functions that do not vanish on the boundary of $I \times \Sigma' \times Z$, we obtain in particular weak homogenous Neumann conditions for u_{j0} on $I \times \Sigma' \times Z$.
2) We show now that $u(t,x',y) = u(t,x')$ for a.e. $(t,x',y) \in I \times \Sigma' \times Z$ and that the initial conditions (3.13) hold.
The initial conditions are obtained by testing (3.5) with test functions

$$\psi\left(t, \overline{x}, \frac{x}{\varepsilon}\right) = \xi(t)\varphi\left(x', \frac{2y}{\varepsilon} - 1\right),$$

where $\varphi \in C^\infty_0(\Sigma' \times Z)$ and $\xi \in C^\infty(I)$ such that $\xi(T) = 0$. Passing $\varepsilon \to 0$ yields for the time derivative

$$\begin{aligned}\int_I \int_{\Sigma'} \int_Z \partial_t u^1_{j0}\xi(t)\varphi\left(x',y\right) \; dydxdt = -\int_{\Sigma'} \int_Z U^1_{j0}\xi(0)\varphi\left(x',y\right) \; dydxdt \\ - \int_I \int_{\Sigma'} \int_Z u^1_{j0}\partial_t\xi(t)\varphi\left(x',y\right) \; dydxdt,\end{aligned}$$

which is equivalent the initial conditions (3.13) if $f^1_{j0} = f^1_j(u^1_0)$ (which will be shown in the next steps). If φ is constant with respect to $x' \in \Sigma'$, we obtain

$$\int_I \int_{\Sigma'} \int_Z -f^1_{j0}\varphi(y)\xi(t) + u^1_{j0}\partial_t\xi(t)\varphi(y) \; dydxdt = -\int_{\Sigma'} \int_Z U^1_{j0}\xi(0)\varphi(y) \; dydx$$

Moreover, we can deduce from estimate (3.7) and Theorem 1 in [125] that U^1_{j0} is constant in $y \in Z$. Thus

$$\left(\int_Z \varphi(y)\ dy\right)^{-1} \int_I \int_{\Sigma'} \int_Z -f^1_{j0}\varphi(y)\xi(t) + u^1_{j0}\partial_t\xi(t)\varphi(y)\ dydxdt = -\int_{\Sigma'} U^1_{j0}\xi(0)dx.$$

The right hand side does not depend on $y \in Z$. Therefore the left hand side does not depend on $y \in Z$, which implies

$$\partial_t u^1_{j0}(t,x',y) + f^1_{j0}(t,x',y) = \partial_t u^1_{j0}(t,x') + f^1_{j0}(t,x') \quad \text{for a.e. } (t,x',y) \in (I \times \Sigma' \times Z).$$

From (A.12) we can deduce now that

$$u^1_{j0}(t,x',y) = u^1_{j0}(t,x') \quad \text{for a.e. } (t,x',y) \in (I \times \Sigma' \times Z).$$

3) We show that $f^1_{j0} = f^1_j(u^1_0)$. Part 2) of the proof implies that $u^1_{j0}(t,x')$, $\partial_t u^1_{j0}(t,x')$ and $\nabla_{x'} u^1_{j0}(t,x')$ are almost everywhere independent of $y \in Z$. According to Proposition A.8 there exists a subsequence, again denoted by $u^1_\varepsilon(t,x',y)$, such that

$$u^1_\varepsilon(t,x',y) \to u^1_0(t,x') \quad \text{strongly in the two-scale sense.}$$

Since $f^1_j(\cdot)$ is Lipschitz-continuous, follows from Proposition 3 in [125] for $\varepsilon \to 0$

$$f^1_j(u^1_\varepsilon(t,x',y)) \to f^1_j(u^1_0(t,x')) \quad \text{weakly in the two-scale sense.}$$

4) Part 2) and 3) of this proof imply that a solution of

$$\begin{aligned} &\int_I \int_{\Sigma'} \partial_t u^1_{j0}(t,x')\varphi_j(t,x')dx'dt \\ &+ \int_I \int_{\Sigma'} D^1_j \nabla_{x'} u^1_{j0}(t,x')\nabla_{x'}\varphi_j(t,x')dx'dt = \int_I \int_{\Sigma'} f^1_j(u^1_0(t,x'))\varphi_j(t,x')dx'dt. \end{aligned} \tag{A.13}$$

is a solution of (A.12).
Thus (3.10), (3.13), and (3.16) hold in the weak sense.
5) If we replace $\varphi^\varepsilon_j(t,x)$ in (A.10) by

$$\varphi^\varepsilon_j(t,x) = \varphi_j\left(t,x',\frac{y}{\varepsilon}\right)$$

and repeat the arguments from the first part of the proof, we obtain

$$\begin{aligned} &\int_I \int_{\Sigma'} \int_Z \partial_t u^2_{j0}(t,x')\varphi_j(t,x',y)dydx'dt \\ &+ \int_I \int_{\Sigma'} \int_Z D^2_j \nabla_{x'} u^2_{j0}(t,x')\nabla_{x'}\varphi_j(t,x',y)dydx'dt = \int_I \int_{\Sigma'} \int_Z f^2_j(u^2_{j0})\varphi_j(t,x',y)dydx'dt. \end{aligned}$$

Thus, (3.11) and (3.17) hold in the weak sense. The initial conditions (3.14) are obtained similarly as in part 5) of this proof. □

Convergence of the transmission conditions Here we derive the the limit of the transmission conditions for the macroscopic model.

Proof. Let $\varphi \in C^\infty(I \times \overline{\Sigma' \times H})$. Testing (3.5) with $\varphi^\varepsilon(t,x) = \varphi\left(t, x, \frac{H-2\varepsilon}{H}y + 2\varepsilon\right)$ yields

$$\int_{S_\varepsilon^1} D_j^0 \nabla_y u_{j\varepsilon}^0 \varphi^\varepsilon dx' = \varepsilon \int_{S_\varepsilon^1} D_j^0 \varepsilon \nabla_y u_{j\varepsilon}^1 \varphi^\varepsilon dx'.$$

Integration over $t \in I$ and sending $\varepsilon \to 0$ yields, considering Lemma A.9, that the right hand side vanishes. On the other hand states Proposition A.12 that

$$\int_I \int_{S_\varepsilon^1} D_j^0 \nabla_y u_{j\varepsilon}^0 \varphi^\varepsilon dx' dt \to \int_\Sigma D_j^0 \nabla_y u_{j0}^0 \varphi dx' dt$$

converges for $\varepsilon \to 0$. Thus

$$\int_I \int_\Sigma D_j^0 \nabla_y u_{j0}^0 \varphi^\varepsilon dx' dt = 0,$$

which is the weak formulation of (3.16). □

Uniqueness of the limit-solution The uniqueness of solutions for solutions of (3.1)–(3.4) is a well known fact. Nevertheless, we will present the proof for the sake of completion.

Proof. Let u and $\overline{u}$ be solutions of the limit-system given in Theorem 3.1 with the same initial data. If we subtract the weak formulations of both solution from another and test the result with $\tilde{u}_j := u_j - \overline{u}_j$, we obtain for $j = 1, ..., m$

$$\begin{aligned}
&\frac{1}{2}\frac{d}{dt}\|\tilde{u}_j^0(t)\|^2_{L^2(I,L^2(\Omega))} + c\|\nabla \tilde{u}_j^0(t)\|^2_{L^2(I,L^2(\Omega))} \le \int_\Omega (f_j^0(u^0) - f_j^0(\overline{u}^0))\tilde{u}_j^0 dx,\\
&\frac{1}{2}\frac{d}{dt}\|\tilde{u}_j^i(t)\|^2_{L^2(I,L^2(\Sigma))} + c\|\nabla \tilde{u}_j^i(t)\|^2_{L^2(I,L^2(\Sigma))} \le \int_\Sigma (f_j^i(u^i) - f_j^i(\overline{u}^i))\tilde{u}_j^i dx, \quad i = 1,2,
\end{aligned}$$

where we used the condition $\|D_j^0\|_{L^\infty(\Omega_\varepsilon^0)}$, $\|D_j^i\|_{L^\infty(\Omega_\varepsilon^i)} \ge c$. Adding up the equations with respect to the indices j and usage of the Lipschitz-continuity of the right-hand sides yields for a.e. $t \in I$

$$\begin{aligned}
&\frac{d}{dt}\|\tilde{u}^0(t)\|^2_{L^2(I,L^2(\Omega))} \le C\|\tilde{u}^0(t)\|^2_{L^2(I,L^2(\Omega))},\\
&\frac{d}{dt}\|\tilde{u}^i(t)\|^2_{L^2(I,L^2(\Omega))} \le C\|\tilde{u}^i(t)\|^2_{L^2(I,L^2(\Omega))}, \quad i = 1,2.
\end{aligned}$$

Application of Grönwall's inequality on the inequalities yields $\overline{u}^0(t,x) = u^0(t,x)$ for a.e. $(t,x) \in I \times \Omega$ and $\overline{u}^i(t,x) = u^i(t,x)$ for a.e. $(t,x) \in I \times \Sigma'$ $(i = 1,2)$. □

Appendix B

Active Gel Theory

We briefly describe a basic version of the active gel theory for actin-networks. In common, there are two strategies to model the characteristics of the actomyosin complex of a cell, the *build from the bottom* approach and the *phenomenological* approach.
The build from the bottom approach takes the molecular composition of the cytoskeleton under consideration and pieces their functional units in a way that the end result fits the qualitative behavior of the actomyosin complex on the macroscopic level. This model approach has the big advantage, that it ensures clarity about the interplay of the functional units observed in the experiment. However, on a scale of a typical cell size, this approach is computationally too expensive to realize. Furthermore, if, as in this thesis, rather a description of the qualitative behavior of the whole actin-myosin cytoskeleton, than a deeper knowledge of its functional units is required, a build from the bottom approach would distract from the essentials due to its complexity.
Another approach to model cytoskeletal dynamics is phenomenologically and bases on the observation, that the actin-myosin cytoskeleton behaves fluid-like on longer timescales and on a macroscopic level. This observation dates back to the late seventies when micrograph experiments became more elaborated and has been more and more refined over the years [54, 126]: While unbounded G-actin monomers merely have the characteristic of a sol, a cross-linked network of actin filaments forms a viscoelastic gel with a mesh size of a few tens of nanometre. At short time-scales, the mechanical response after a perturbation of the gel is elastic with a shear modulus E in the range of $10^3 - 10^5$ Pa [88]. On longer timescales, the actin gel flows with a finite viscosity η of the order 100 Pa s [89]. After an elastic response, the gel starts to flow after a timespan $[0, t^*]$. t^* is called relaxation time. From a polymer physics point of view the actin network does have a similar rheology as liquid crystals over long time scales. This observation inspired theoretical scientists to interpret actomyosin as a physical gel, for which a proper equilibrium temperature can be defined and well-established theoretical methods exist.
The rheologic model which is commonly used to describe the mechanical properties of

the actomyosin network is the *Maxwell model*. To a linear order this model consist of a combination of a Hooke element, describing the elastic part as a linear spring, and a Newton element, describing the viscous part as a linear damper. In the Maxwell model Hooke and Newton elements are connected in series. Due to the damper the deformation is unlimited and irreversible. If the strain rate changes, the purely viscous behavior is overlain with a immediate elastic response due to the Hooke element. The elastic response prevails the viscous response as long as the material needs to counterbalance the spring force by the viscous force. In the Maxwell model the relaxation time thus is given by $Et^* = \eta$, and the series connection implies the stress-stain relation

$$\dot{\varepsilon} = \frac{\dot{\sigma}^{\text{pas}}_{\alpha\beta}}{E} + \frac{\sigma^{\text{pas}}_{\alpha\beta}}{\eta}, \tag{B.1}$$

where $\sigma^{\text{pas}}_{\alpha\beta}$ denotes the stress tensor due to the passive mechanics of the gel and the strain-rate tensor $\dot{\varepsilon}$ is in the terms of the local velocity-field v_α given by

$$\dot{\varepsilon} = \frac{1}{2}(\partial_\alpha v_\beta + \partial_\beta v_\alpha),$$

where we used Einstein's notation, which will be used unmentioned from now on.
In addition to constitutive equation (B.1), the law of momentum conservation in also important. However, since in viscoelastic gels on scales of micrometers inertial forces are negligible, momentum conservation is commonly replaced by a force balance condition. Let $\sigma^{\text{tot}}_{\alpha\beta}$ be the total stress tensor (i.e. the sum of all stresses to be considered). Then force-balance is given by

$$\partial_\alpha(\sigma^{\text{tot}}_{\alpha\beta} - \Pi\delta_{\alpha\beta}) + F^{\text{ext}}_\beta = 0, \tag{B.2}$$

where F^{ext}_β is an external force, and Π is the pressure [85].
Equations (B.1), (B.2) need to be exerted to describe the mechanics of the F-actin network properly, since the network is also endowed with a polarity, due to its averaged directional alignment. Thus, in addition to the material- and the force-balance equation, a polarity field has to be defined. This is typically done in analogy to studies of the directional alignment of liquid crystals [103]. On average, F-actin networks align parallel to each actin filament and the (+)- and (−)-ends are pointing in the same direction, respectively. This naturally induces the existence of a polarity field $\mathbf{p} = (p_\alpha)_\alpha$, consisting of unit vectors, which locally run parallel to the F-actin alignment. This has the following impact on the stress tensor: A fully parallel polarized F-actin network is stiff in the sense, that if the orientation on the molecules is changed due to an external perturbation the polarization field becomes nonhomogeneous and torque arises, which causes the molecules to remigrate to the parallel position. This torque is associated with an orientational field $\mathbf{h} = (h_\alpha)_\alpha$ proportional to the second spatial derivative of the

polarity field $\mathbf{p}$, which yields

$$\mathbf{h} = K\nabla^2\mathbf{p},$$

where K denotes the Franck constant [103]. Taking the polarity under consideration, the total stress tensor comprises a stress $\sigma^{\mathrm{pol}}_{\alpha\beta}$ due to torque generation, which reads in the linear hydrodynamic theory as

$$\sigma^{\mathrm{pol}}_{\alpha\beta} = v_\alpha h_\beta. \tag{B.3}$$

and has to be added to $\sigma^{\mathrm{tot}}_{\alpha\beta}$ in the force-balance equation (B.2) [85].
The system (B.1)-(B.3) is suitable to describe the mechanics of a passive network consisting only of F-actin. However, the treatment of F-actin networks as a passive and purely viscoelastic material holds only in the abscence of myosin II and ATP. In a more recent and prominent *in vitro* experiment performed in the group of Schmidt [127], Myosin II is added to a permanently crosslinked probe of actin filaments and in order to measure the rheology of this complex a so-called micro-rheology approach, where the motion of beads interspersed in the the gel is studied, is done. In the absence of ATP, the beads remain, apart from minimal fluctuations, at their original position, since the myosin motors are inactive. As in physical gels, the actomyosin complex behaves as a classical thermal equilibrium system. The scenario changes, when ATP is added to the probe. Due to the activation of the treadmilling process and myosin motor activity through hydrolysis, the beads are moved across the gel. In this case, the gel is permanent out of equilibrium, thus a proper equilibrium-temperature cannot be defined and methods from physical or chemical gel theory are not applicable, since an active force is continuously generated. In fact, the actomyosin gel can be characterized as an active gel, where the actively generated stress is fuelled by ATP consumption, leading the statement and the total stress hast to be composed of an internal active and a passive part. Taking the polarity induced from equation (B.3) also under consideration, the total stress is given by

$$\sigma^{\mathrm{tot}}_{\alpha\beta} = \sigma^{\mathrm{pas}}_{\alpha\beta} + \sigma^{\mathrm{pol}}_{\alpha\beta} + \sigma^{\mathrm{act}}_{\alpha\beta}.$$

The actively generated force related to the stress tensor $\sigma^{\mathrm{act}}_{\alpha\beta}$ then must depend on the chemical potential difference $\Delta\mu$ of ATP and its hydrolysis products ADP and inorganic phosphate Pi:

$$\Delta\mu = \mu_{\mathrm{ADP}} - \mu_{\mathrm{ADP}} - \mu_{\mathrm{Pi}}.$$

If $\Delta\mu = 0$, the chemical reaction is at equilibrium and no energy is produced and in the case where $\Delta\mu > 0$, the free energy $\Delta\mu$ is consumed per hydrolyzed ATP molecule. To

linear order the active internal stress has the form

$$\sigma_{\alpha\beta}^{\mathrm{act}} = \zeta \Delta\mu p_{\beta}, \tag{B.4}$$

where the stress is exerted along the field p_β, because myosin motors slide along F-actin. The activity coefficient ζ is a material property of the cytoskeleton that describes both, the activity of myosin II motors and ATP consumption in the tread- milling process. In general, ζ is a phenomenological parameter, which has to be estimated from experiments [128], [129].

Appendix C

Methods

C.1 Numerical implementation

The code used for the simulations is implemented in MATLAB v.8.6 (R2015b). In parts, three preexistent codes were modified and included:

1) The convection of the domain Ω_t is computed by a code of Sumengen [130] which bases on a level set method as described in [131].

2) The triangulation of the domain was computed at each time step with aid of a pre-implemented Delaunay algorithm provided by MATLAB [132].

3) The solution of the boundary operator for the mechanical system, including curvature force, is obtained by the finite-element technique presented provided by the MATLAB PDE toolbox.

All other components of the code contributed to the author.
To avoid technical, but yet simple extensions for our modelled system case, we illustrate how the code processes the reduced toy model

$$\partial_t u - \operatorname{div}(\nabla u - uv) = f_u(t, x, \tau, u) \quad \text{on } \Omega(t) \tag{C.1}$$

$$(\Delta v + \nabla(\nabla \cdot v)) - v = f_v(u, \nabla u) \quad \text{on } \Omega(t). \tag{C.2}$$

It can be seen easily that the operator $\Delta v + \nabla(\nabla \cdot v)$ is apart from a positive constant equivalent to the original operator $\Delta v + \nabla^{\perp}(\mathrm{rot} v)$. The advantage of this representation is that the ellipticity of the operator $-\Delta v - \nabla(\nabla \cdot v)$ can be verified more easily. The right hand side $f(t, x, \tau, u)$ is a smooth scalar-valued function, for which we assume that it models the actin and Rho kinetics and the stimulus. The function

$$f_v(u, \nabla u) := \nabla \Pi(u) + \overline{F}^{\mathrm{act}}(u)$$

is supposed to mimic the active force and the pressure term. More precisely Π denotes term (3.50) where a, a_0 are replaced by u, u_0. For the convergence of the spatial iteration process described in the following, we require continuous and uniformly bounded right hand sides. Therefore we replace F^{act} as defined in (3.41), where a are replaced by u, by a mollified version. We introduce the mollifier

$$j(x) := \begin{cases} c \exp\left(-\frac{1}{1-\frac{x^2}{4}}\right), & \text{if } |x| < 1, \\ 0, & \text{else.} \end{cases}$$

The constant $c > 0$ is chosen such that $\|j\|_{L^1} = 1$. We consider

$$\overline{F}^{\text{act}}(u) := \zeta_F \mathbb{1}_{\{u \geq u_{\text{thr}}\}} p * j(u),$$

where '$*$' denotes the convolution operator, and u_{thr} is a constant that is an element of the image of u.

The polarity field p, F^{act} are chosen as in the original model, but spatially mollified by a convolution with suitable Dirac delta functions. The boundary conditions are

$$(D_u \nabla u + uv) \cdot n = 0 \quad \text{on } \Gamma(t)$$

and the boundary conditions for v are given by (3.51), where we set $a = a_0 = 1$ to keep the description simple. The initial conditions are u_0, Ω_0, where u_0 is a homogenous steady state of (C.1) at time $t = 0$, and Ω_0 is a circle with radius $R > 0$.
In the following, we sketch how the code works. We will point out the important steps and skip some details by referring to literature. The presentation of the code will mostly informally and, for the sake of universality, not code specific.

C.1.1 Preliminaries

In order to increase the accuracy of the numerical computation, a priori estimates are required. More precisely, we require Lipschitz continuity on the right hand sides of (C.1) and (C.2). To enforce Lipschitz continuity, we replace the right hand sides of the original system by specific cutoff function: For a function $f : \mathbb{R}^n \to \mathbb{R}^m$ we define the cutoff function $(f(x))_\beta^\alpha$ of f with upper bound $\alpha \in \mathbb{R}^m$ and lower bound $\beta \in \mathbb{R}^m$ component wise by

$$(f_i(x))_\beta^\alpha = \begin{cases} \alpha_i & \text{if } f_i(x) \geq \alpha_i, \\ f_i(x) & \text{if } \beta_i < f_i(x) < \alpha_i, \\ \beta_i & \text{if } \beta_i \leq f_i(x), \end{cases} \quad i = 1, ..., m.$$

The advantage of replacing the original non-linearities by cut versions is that the induced uniformly boundedness implies Lipschitz continuity, since the original non-linearities are

smooth. We choose constants α_w, β_w, $L > 0$ such that the right-hand sides f_w $(w = u, v)$ in (C.1), (C.2) satisfy

$$|(f_w(t,x,y))_\beta^\alpha - (f_w(t,x,z))_\beta^\alpha|_m \leq L|y-z|_n \quad \forall y,z \in \mathbb{R}^n,\ i = 1,...,m,$$

where $|\cdot|_{n,m}$ denotes the 1-norm in $\mathbb{R}^{n,m}$ and $m, n = 1, 2$, depending on the considered function.
To assure that the cutoffs coincide with the original functions, test simulations were performed, in which the bounds α_w, β_w were fitted such that the components $w = u, v$ of the solution satisfy

$$(f_w(t,x,w(t,x)))_{\beta_w}^{\alpha_w} = f_w(t,x,w(t,x)).$$

To keep the notation simple, we will write in the following f_w instead of $(f_w)_{\beta_w}^{\alpha_w}$, and keep in mind that the considered a priori estimates always refer to the cutoff functions.

C.1.2 Evolution of the level set

In the level set method, the boundary of the cell is described by the zero level contour of a *signed distance function* ϕ. In this setting is $\overline{\Omega}_t \subset \mathbb{R}^2$ represented by the set of points $x \in \mathbb{R}^2$ for which $\phi(t,x)$ is non-positive. The boundary $\partial\Omega_t$ corresponds to the set of points satisfying $\phi(t,x) = 0$.
We explain briefly how the evolution of the level set function progresses. For a discussion of the details, we refer to [131], Chapter 6.
The level set function $\phi(t,x)$ satisfies

$$\phi(t,x) = \begin{cases} -d, & \text{if } x \in \Omega_t, \\ +d, & \text{if } x \in \mathbb{R}^2/\Omega_t, \end{cases}$$

where d represents the Euclidian distance between x and the boundary $\partial\Omega_t$. This characteristic is realized by the evolution of the initial conditions

$$\phi(0,x) = \begin{cases} -d, & \text{if } x \in \Omega_0, \\ +d, & \text{if } x \in \mathbb{R}^2/\Omega_0, \end{cases}$$

under the transport equation

$$\partial_t\phi + v \cdot \nabla\phi = 0 \quad \text{on } I \times \mathbb{R}^2, \tag{C.3}$$

where $v = v(t,x)$ represents the velocity field at each time step, governed by the active-gel-equation (C.2).

C.1.3 Numerical implementation

For the numerical computation of the evolution of ϕ we used an algorithm which bases on the Stencil local Lax-Friedrichs method (SLLF) (cf. [131], section 6.4) and was originally published by [130].
In the algorithm is $\mathbb{R}^2$ in (C.3) replaced by a rectangular grid $G \times G$, where

$$G := \{x \in \mathbb{R} : x = nr,\ n \in \mathbb{N}\}$$

for a fixed $r > 0$. Equation (C.3) is completed by periodic boundary conditions and discretized on $G \times G$. The domain $\overline{\Omega}_t$ is approximated by the subset of points $x \in G \times G$ on which the function $\phi(t, x)$ is negative.

The initial domain, defined by the level-set, is successively convected in time and space by the application of the SLLF-method on equation (C.3). In particular, equation (C.3) is solved in time by an implicit Euler method. Starting at time $t = 0$ SLLF generates successively (not necessarily equidistant) time iteration steps dt_1, dt_2, ..., and the corresponding timespan $t = 0$, $t_1 = dt_1$, $t_2 = t_1 + dt_2$,... . After each iteration the level set function ϕ is spatially convected. In the SLLF-method provided by [130] the convection at time t_n has to be determined by the velocity field $v(t_n, x)$. Since the field $v(t_n, x)$ is a priori unknown, we modified the preexisting code by taking $v(t_{n-1}, x)$ instead of $v(t_n, x)$.
If there is no likelihood of confusion, we denote by $\partial\Omega_{t_n} = \{\phi(t_n, x) = 0 : x \in G \times G\}$ the boundary of the discretized domain at time t_n, obtained by the level-set method. The interior of the domain at time t_n is $\Omega_{t_n} = \{\phi(t_n, x) < 0 : x \in G \times G\}$.
We briefly sketch the framework of the complete code and comment on it afterwards more in detail: Let $T > 0$ be an upper bound for the simulated time and let $0 \leq t_n < T$ be a time date attained by the Euler method.
The evolution of the level set and the subsequent time $t_n + dt$, starting at $t_0 = 0$, and the computations of the equations in the bulk are determined by a while-loop. Thereby the code processes the following scheme:

While $t_n \leq T$

1) allocation of $\partial\Omega_{t_n} = \{\phi(t_n, x) = 0 : x \in G \times G\}$;

2) main body of the code:

   2.1) implementation of a triangular mesh on Ω_{t_n};

   2.2) spatial solution of the equations (C.1), (C.2) on Ω_{t_n} at time t_n;

   2.3) extrapolation of the velocity field $v(t_n, x)$ defined on Ω_{t_n} to $\overline{v}(t_n, x)$ defined on the whole grid $G \times G$;

3) computation of the time step dt by the SLLF-method;

4) iteration step size control; the algorithm checks if $dt < b$, where $b > 0$ is a bound defined later; otherwise a new step size

$$dt < b$$

   is chosen;

5) computation of the boundary $\partial\Omega_{t_n+dt}$ by the level set method, where the solution $\phi(t_n+dt, x)$ is determined by (C.3) with the velocity field $v = \overline{v}(t_n, x)$;

6) reinitialisation of ϕ as a signed distance function;

7) time-step transferation $t_{n+1} := t_n + dt$;

end.

The iteration steps 1), 3), 5) and 6) are executed by the level set method provided by [130].

Item 2.1) is devoted to the mesh implementation. The implementation is described in Section C.1.4. Item 2.2) consists of an algorithm, in which both, the kinetic and the mechanical equations are discretized in time and then solved numerically due to a semi-linear approach. This approach consists of a compound of two schemes. First an explicit Euler method is applied to discretize the PDE system in time and subsequently a finite elements method is applied for the spatial discretization. The discretization scheme is presented in Section C.1.5.

The approach may produce unstable solutions that oscillate and grow unconstrained if dt is chosen too large. In order to avoid this effect, the code constrains the step size in 4) the bound b, which prevents the numerical solution of (C.1) and (C.2) from oscillating. The construction of b is presented in Section C.1.5.

In step 5) dt is used to compute the evolution of the level set. In the temporal iteration of this scheme the values of the level set function tend to smear off and ϕ may loose the characteristic to be a signed distance function. To avoid this, the code reinitializes ϕ in step 6) as a signed distance function. This is done as described in [133]. Subsequently

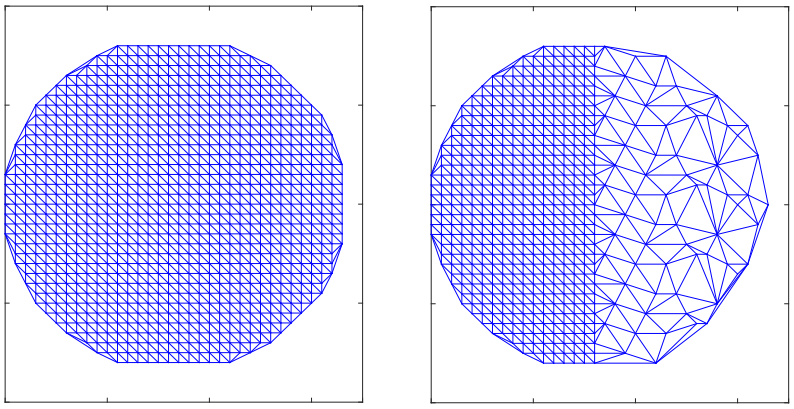

FIGURE C.1: Illustration of the triangulation after thinning. The left plane shows the original grid. The right panel shows the thinned out grid for the case $\rho = (-1, 0)$. Used parameters: $G = \{1, 2, ..., 40\}$, $\partial\Omega_t = \{x \in G \times G : \|x - (20, 20)\|_2 \leq 17\}$, $n = 7$.

the code passes the new gained time t_{n+1} and continues the procession starting again at step 1). The code continues to execute until t_n exceeds the predefined bound T.

C.1.4 Mesh generation

This section refers to item 2.1). The numerical treatment of the equations requires the generation of a mesh approximating the points contained in Ω_t.
The common approach is to take at each time t the predefined points of the grid $(x, y) \in G \times G$, that satisfy $\varphi(t, x, y) \leq 0$ and to construct an equidistant triangularization between these points. However, the issue of this approach is that the mesh size of the resulting mesh accords one-to-one with the size of the grid $G \times G$. In our particular case are the concentration fluctuations of the chemical ingredients at the front highly dynamic, which requires a high mesh resolution at the front. On the other hand the concentrations at the back of the cell remain almost constant. An equidistant mesh induced by $G \times G$ has to be fine gained to capture the dynamics at the front. This is numerically very costly, since both, the computation of the evolution of the level set requires all points defined in $G \times G$ and the spatial discretisation of the PDE contained in Ω_t takes even triangles in consideration on which values hardly differ.
In order to speed up the calculations, the code generates an inhomogeneous, adaptive mesh at any considered time $t > 0$. At $t = 0$ an initial mesh is generated as follows:

1) Find all points $p \in G \times G$, such that $\phi(0, p) \leq 0$, and set $\Omega_0 = \{p\}$;

2) generate a Delaunay triangularization and obtain the triangles $\{tr(p)\}$ with respect to these points;

3) find all edges of $\{tr(p)\}$ whose start- and endpoints coincidence with $\partial\Omega_0$ and label them as boundary edges $\{e(p)\}$.

With respect to the the initial mesh $\{p, tr, e\}$ the equations (C.1), (C.2) are solved numerically as described in the next section.
For times $t > 0$ the mesh is generated such that it is densely grained at the front an coarse grained at the back. This is realized in two steps. If $t > 0$, the mesh representing the domain Ω_t is created at first again as in item 1), i.e. it is defined as the set of all points p such that $\phi(t, p) \leq 0$. Subsequently the domain is segregated in a front and a back. To differ between front and back, we introduce a measure ρ for the mean orientation of the cell:

$$\rho(t) := \frac{1}{|\Omega_t|} \int_{\Omega_t} \nabla u \, dx.$$

The code determines (a discrete approximation of) the line

$$g = \{m + sR : s \in \mathbb{R}\},$$

where m is the centre of mass of Ω_t and R is a vector satisfying $R \perp \rho(t_-)$ and where t_- denotes the former time step of t. The front Ω_t^F and the back Ω_t^B are then defined by

$$\Omega_t^F := \{x \in \Omega_t : x = s\rho + y, \ y \in g, \ s > 0\},$$
$$\Omega_t^B := \{x \in \Omega_t : x = s\rho + y, \ y \in g, \ s \leq 0\}.$$

In the second step is Ω_t^B thinned with respect to a predefined coarseness $n \in \mathbb{N}$. All points $a_{jk} \in G \times G$ can be relabelled by the index $i = |G|(k-1) + j$. With respect to this index the code removes $p \in \Omega_t^B$ from Ω_t^B iff $p = a_{jk}$ satisfies

$$\text{mod } (i, n) = 0.$$

After this step Ω_t^F and Ω_t^B are merged by redefining Ω_t as

$$\Omega_t := \Omega_t^F \cup \Omega_t^B,$$

and a Delaunay triangulation for the set of points that are contained in Ω_t is generated. This provides the triangles $\{tr(p)\}$ and the boundary edges $\{e(p)\}$. An example of the thinned mesh is shown in Figure C.1.

Remark C.1. The thinning of Ω_t^B can only be applied if the cell is stimulized by a single, locally confined stimulus since only in this case a single wave front is generated. For simulations of the repolarization behavior and the response to multiple stimuli the regular mesh, constructed as in the items 1)-3), has to be used.

C.1.5 Numerical solution of the PDE system on Ω_t for a fixed time t

This section refers to item 2.2) in the main body of the code in which the equations (C.1), (C.2) are solved at time t numerically. This is realized in three subsequent steps:

1) the equations are discretized in time,

2) the equations are discretized in space,

3) the discretized equations are solved.

1) Forward Euler method method is applied in order to discretize the equations (C.1), (C.2) in time. Let t_- a time yield by the algorithm as described in the *while loop* and let dt be the corresponding time step. We consider the scheme at time $t = t_- + dt$. The time derivative is approximated by

$$\partial_t u \approx \frac{1}{dt}(u(t) - u(t_-)).$$

The temporal approximation of (C.1), (C.2) then is

$$\begin{aligned} dt(-\Delta u(t,x) + \operatorname{div}(u(t,x)v(t,x)) + u(t,x) &= dt f_u(t,x,u(t,x)) + u(t_-,x), \\ (\Delta v(t,x) + \nabla(\nabla \cdot v(t,x))) - v(t,x) &= f_v(u(t,x), \nabla u(t,x)). \end{aligned} \tag{C.4}$$

2) The difficulty in (C.4) is that at time t both, the velocity $v(t,x)$ in the divergence part of the first equation and the values of the reaction rate $f_u(t,x,u(t,x))$ are unknown. In order to apply FE-methods for linear elliptic equations, the code recursively approximates (C.4) by the following scheme:

Set

$$\begin{aligned} \overline{f}_u(t,x,u) &:= f_u(t,x,u(t,x)) - \frac{1}{|\Omega_t|}\int_{\Omega_t} f_u(t,x,u(t,x))\ dx \\ \overline{u}(t_-,x) &:= u(t_-,x) - \frac{1}{|\Omega_t|}\int_{\Omega_t} u(t_-,x)\ dx \end{aligned} \tag{C.5}$$

and seek approximated solutions of the system

$$\begin{aligned} dt(-\Delta u(t,x) + \operatorname{div}(u(t,x)v(t,x)) + u(t,x) = dt\overline{f}_u(t,x,u(t,x)) + \overline{u}(t_-,x), \\ (\Delta v(t,x) + \nabla(\nabla\cdot v(t,x))) - v(t,x) = f_v(u(t,x),\nabla u(t,x)), \end{aligned} \tag{C.6}$$

on Ω_t with zero-flux boundary conditions with respect to u_n and

$$\begin{aligned} \left(\nabla v + (\nabla v)^T\right)\cdot n = -\zeta_B \mathbb{1}_{\{u<u_{\text{thr}}\}} K_5(u_- - u_0)n + \gamma_1^m(\kappa_m - \kappa_0)n \\ -\gamma_2^m\left(\int_{\Gamma_t} 1\ ds\right)n + (\Pi(u_-) - \Pi_0)n, \end{aligned}$$

on Γ_t.
Let $u_1(x) = u(t,x)$, $v_1(x) = v(t,x)$. Recall that t, t_-, dt, $u(t_-,x)$, $v(t_-,x)$ are known from the former temporal iteration step. Initially, the active gel equation

$$(\Delta v_1(x) + \nabla(\nabla\cdot v_1(x))) - v_1(x) = f_v(u(t_-,x),\nabla u(t_-,x)) \tag{C.7}$$

is numerically solved for v_0 such that the boundary condition above are satisfied. Then the diffusion reaction equation

$$dt(-\Delta u_1(x) + \operatorname{div}(u_1(x)v_1(x))) + u_1(x) = dt\overline{f}_u(t,x,u(t_-,x)) + \overline{u}(t_-,x) \tag{C.8}$$

is solved numerically for u_1. The code iterates n-times the following rule:

Let u_{n-1}, v_{n-1} be the solutions obtained from the $(n-1)$-th iteration step. Solve

$$(\Delta v_n(x) + \nabla(\nabla\cdot v_n(x))) - v_n(x) = f_v(u_{n-1},\nabla u_{n-1}) \tag{C.9}$$

on Ω_t and

$$\begin{aligned} \left(\nabla v_n + (\nabla v_n)^T\right)\cdot n = -\zeta_B \mathbb{1}_{\{u_{n-1}<u_{\text{thr}}\}} K_5(u_{n-1} - u_0)n + \gamma_1^m(\kappa_m - \kappa_0)n \\ -\gamma_2^m\left(\int_{\Gamma_t} 1\ ds\right)n + (\Pi(u_{n-1}) - \Pi_0)n, \end{aligned} \tag{C.10}$$

on Γ_t. Then solve

$$dt(-\Delta u_n(x) + \operatorname{div}(u_n(x)v_n(x))) + u_n(x) = dt\overline{f}_u(t,x,u_{n-1}(x)) + \overline{u}(t_-,x) \quad \text{on } \Omega_t \tag{C.11}$$

and

$$(\nabla u_n - u_n v_n)n = 0$$

on Γ_t.

If we neglect the boundary-force impact on v, i.e. if we replace equation (C.10) by

$$v_{x_1} n = v_{x_2} n = 0 \quad \text{on } \partial\Omega_t,$$

the following statement holds under certain assumptions on the domain Ω_t:

Theorem C.2. *Let $\Omega_t \subset \mathbb{R}^2$ be an open, bounded, Lipschitz-domain that is dense in $\mathbb{R}^2$. Assume that v_n converges weakly to $v \in L^2(\Omega_t, \mathbb{R}^2)$ for $n \to \infty$.*
There is a constant $b > 0$ such that the iteration scheme defines sequences

$$(u_n)_{n\in\mathbb{N}} \subset L^2(\Omega_t) \quad \textit{and} \quad (\nabla u_n)_{n\in\mathbb{N}} \subset L^2(\Omega_t, \mathbb{R}^2),$$

such that the L^2-limit $u(x) := \lim_{n\to\infty} u_n(x)$ and the weak limit ∇u, where $\nabla u_n \rightharpoonup \nabla u$ in $L^2(\Omega, \mathbb{R}^2)$, is a solution of (C.6) if the time iteration step satisfies $dt < b$.

Proof. The proof is presented in Appendix C.2. □

The upper bound b depends on t, Ω_t, the parameters of the PDE system, and the cutting bounds α, β. The derivation of b can be obtained if the occurring constants in Appendix C.2 are calculated explicitly. We skip the explicit representation of b, since its calculation is long-winded, but yet straight forward. The only constant which does not directly follow from the used estimates in Appendix C.2 is the required Poincare constant C_p. Fortunately Friedrich's inequality states that

$$C_p \leq d,$$

where d is the diameter of Ω_t (cf. [134]).

Remark C.3. If higher regularity results are applied, it can be shown for a sufficiently small b that $\nabla u_n \to \nabla u$ in $L^2(\Omega_t)$. In this case, the assumption on the weakly convergence of v_n can be omitted since this implies $v_n \to v$ in $L^2(\Omega_t)$ due to the Lipschitz-continuity of the right hand sides. However, the determination of the bound b such that the convergency of ∇u_n is guaranteed is very complex. We had to choose an open cover of the domain Ω_t on which localized energy estimates for a difference scheme had to be obtained (cf. [135], theorem 6.3.1). This is computationally very costly, because the domain changes after each temporal iteration step. Therefore we decided to validate experimentally wether dt is chosen small enough to prevent $\|v_n\|_{L^2(\Omega_t,\mathbb{R}^2)}$ from unrealistically oscillations. Fortunately this is the case if b is chosen as demanded in the proof of Theorem C.2. For this choice of b the sequences u_n and v_n seem to converge to a limit even if the force boundary-conditions (C.10) on v_n are considered:
In the simulations we chose the iteration length $n = 10$. This choice yields regular results, which hardly differ from the results obtained if $n > 10$ is chosen. Figure C.2 displays a convergence plot. The error $\|\overline{u}_n(x) - \overline{u}_{n-1}(x)\|_{L^\infty(\Omega_t)}$ decreases almost linearly and the error $\|\overline{v}_n(x) - \overline{v}_{n-1}(x)\|_{L^\infty(\Omega_t,\mathbb{R}^2)}$ is almost constant, approaching zero.

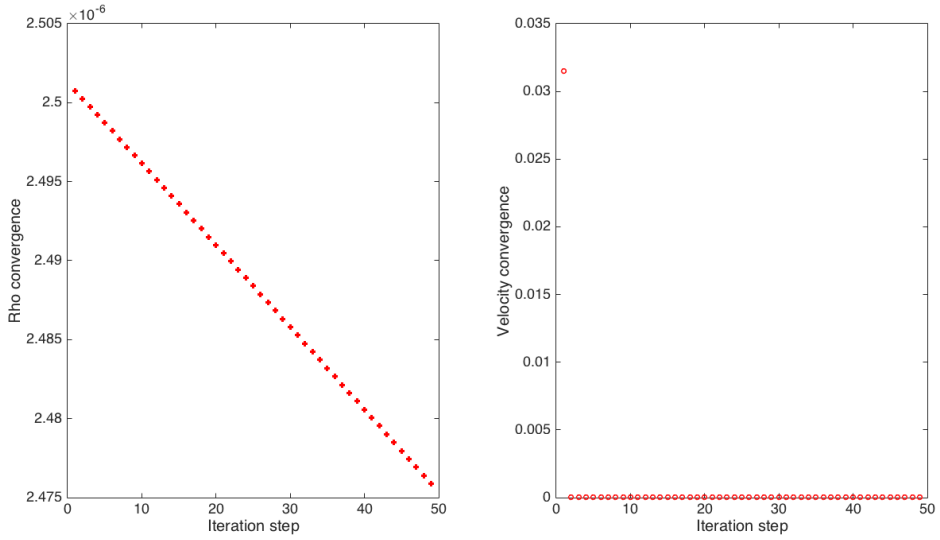

FIGURE C.2: Left panel: A posteriori error of the Rho concentration profile for the cell model after $t = 30s$ and $dt = 0.001$ with parameters taken from Table 4.1. The x-axis denotes the iteration steps ($n = 1, ..., 50$). The y-axis denotes the error $\|\overline{u}_n(x) - \overline{u}_{n-1}(x)\|_{L^\infty(\Omega_{30})}$. Right panel: A posteriori error of the velocity profile.The x-axis is the same as in the left panel. The y-axis represents the error $\|\overline{v}_n(x) - \overline{v}_{n-1}(x)\|_{L^\infty(\Omega_{30},\mathbb{R}^2)}$.

In addition, a bound for the temporal stepsize with respect to the mesh is required. We did not perform a stability analysis for the numerical scheme. For the control of the temporal stepsize we simply took the bound $dt \leq ch^2$, where $c = D_u/4$ and h is the diameter of the smallest triangle of the triangularization. The choice of this bound is numerically very costly. However, the code seems to remain stable with this setting.

3) We discuss the spatial discretization of the system. For the finite elements scheme, we approximate $u_n(t,x)$ and $v_n(t,x)$ by a finite Fourier series. More precisely, we seek approximated solutions which are spatially constant on each triangle $q \in \{tr\}$. The approximated solution $\overline{u}_n$ (resp. $\overline{v}_n$) of u_n (resp. v_n) has the form

$$\overline{u}_n(t,x) = \sum_{q\in\{tr\}} u_n^q(t)\phi_{|q}(x),$$
$$\overline{v}_n(t,x) = \sum_{q\in\{tr\}} v_n^q(t)\phi|q(x),$$

where $\phi|q \in \{\omega : \Omega_t \to \mathbb{R}|\omega_{|q} \in P_1(q), \text{continuous in edge points}\}$, $P_1(q)$ is polynomial of order 1, defined on q, is the node basis function of the triangle q. Moreover, the righthand side $dt\overline{f}_u(t,x,\overline{u}_{n-1})+u(t_-,x)$ of (C.27) is also approximated by a finite Fourier sequence:

$$\overline{f}_n(x) = \sum_{q\in\{tr\}} dt(f_n^q(t) + u^q(t_-))\phi_{|q}(x). \tag{C.12}$$

The right hand side of (C.9) is also approximated by a finite Fourier series, similar

to (C.12). We denote each Fourier coefficient by $F_n^q = (F_{1,n}^q, F_{2,n}^q)$ and approximate $F_n(t,x) := -f_v(\overline{u}_{n-1}(t,x), \nabla\overline{u}_{n-1}(t,x))$ by

$$F_n(x) := \sum_{q\in\{tr\}} F_n^q(t)\phi_{|q}(x).$$

The task is to determine the coefficients $u_n^q(t)$, $v_n^q(t)$, such that the weak formulations of equations (C.6)–(C.10) are satisfied for any test function $\omega \in \{\omega : \Omega_t \to \mathbb{R} | \omega_{|q} \in P_1(q), \text{continuous in edge points}\}$. The FE-scheme provided by the MATLAB PDE toolbox was used to determine the coefficients.
4) $u(t,x)$ and $v(t,x)$ for $x \in \Omega_t$ are computed successively done at each time $t > 0$ obtained from the level set scheme.

C.1.6 Transmission of the variables to $G \times G$

$v(t,x)$ is defined on $\Omega_t \subsetneq (G \times G)$. The level set method, however, requires for a velocity field that is defined on whole mesh $G \times G$. To avoid irregularities in the evolution of (C.3), the code extrapolates (resp. interpolates) $v|\Omega_t$ to $v|G\times G$ by the nearest-neighbour method:
If $x \in G \times G$ is a point outside of the boundary $\partial\Omega_t$, the closest point $y \in \partial\Omega_t$ to x is computed and $v(t,x) := v(t,y)$ is set. If $x \in (G \times G)\backslash\Omega_t$ is a point in the inner of $\partial\Omega_t$, then $v(t,x)$ is defined as the mean value of the three nearest points contained in Ω_t.
After the expansion of $v(t,x)$ on $G \times G$, the evolution of (C.3) is computed by the SLLF-method, which yields a new temporal iteration step dt_+ and a new time date $t_+ := t + dt_+$ (cf. section C.1.2). The zero-level set of $\varphi(t_+, x)$ represents the boundary of the domain Ω_{t_+}. Subsequently a new mesh on Ω_{t_+} as described in section C.1.4 is generated by the code.
Finally the whole area of Ω_{t_+} and consequently the membrane tension τ is computed. The code now proceeds as explained in the former paragraphs.

C.2 L^2–Convergence of the iteration scheme.

Throughout this Appendix we write for convenience $\Omega := \Omega_t$. Moreover, we denote by $\|\cdot\|$ both the L^2-norm $\|\cdot\|_{L^2(\Omega)}$, as well as the L^2-norm $\|\cdot\|_{L^2(\Omega,\mathbb{R}^2)}$.
Under the assumption that v_n weakly converges to v, we show that $(u_n)_{n\in\mathbb{N}}$, $(v_n)_{n\in\mathbb{N}}$ as defined by the recursion rule (C.7)-(C.11) are sequences in $L^2(\Omega_t)$, $L^2(\Omega_t,\mathbb{R}^2)$, respectively, whose limits are a fixed point of equation (C.6) if the time iteration step size $dt > 0$ is sufficiently small. Throughout this appendix we assume that f_u, f_v are smooth and bounded. Since a smooth, bounded function is Lipschitz continuous, there is a constant $L > 0$ such that for all $y_1, y_2, z_1, z_2 \in \mathbb{R}$

$$\begin{aligned}|f_u(\cdot,\cdot,y_1) - f_u(\cdot,\cdot,y_2)| \leq& L|y_1 - y_2|,\\ |f_v(\cdot,\cdot,y_1,z_1) - f_v(\cdot,\cdot,y_2,z_2)| \leq& L\left(|y_1 - y_2| + |z_1 - z_2|\right).\end{aligned}$$

Moreover, it is easily verified that $[u \mapsto \overline{f}_u(\cdot,\cdot,u)]$ as defined in (C.5) maps elements of $L^2(\Omega)$ Lipschitz-continuously onto $L^2(\Omega)$. Thus, a constant $L > 0$ exists, such that for all $u_1, u_2 \in L^2(\Omega)$

$$\|\overline{f}_u(\cdot,\cdot,u_1) - \overline{f}_u(\cdot,\cdot,u_2)\| \leq L\|\|u_1 - u_2\|\|.$$

In the following the originally defined function f_u is not used. In order to keep the notation as simple as possible, we drop the line from $\overline{f}_u$ and simply write f_u. For the same reason we will write $u(t_-, x)$ instead of $\overline{u}(t_-, x)$.

C.2.1 A priori estimates

Lemma C.4. *There is a constant $c > 0$ independent of u, such that for every $u \in W^{1,2}(\Omega)$ a solution $v \in W^{2,2}(\Omega,\mathbb{R}^2)$ of*

$$\Delta v + \nabla(\nabla\cdot v) - v = f_v(u, \nabla u) \tag{C.13}$$

with zero-flux boundary conditions satisfies

$$\|v\|_{W^{2,2}(\Omega,\mathbb{R}^2)} \leq c. \tag{C.14}$$

Proof. With aid of the Lax-Milgram lemma can be shown easily, that the mapping

$$[v \mapsto -\Delta v - \nabla(\nabla\cdot v) + v] \in \mathcal{L}(H^2_2(\Omega,\mathbb{R}^2), L^2(\Omega,\mathbb{R}^2)), \quad \delta \in [0,1)$$

is an isomorphism. Moreover is $f_v(u,\nabla u) \in L^2(\Omega,\mathbb{R}^2)$, which implies $v \in H^2_2(\Omega,\mathbb{R}^2) = W^{2,2}(\Omega,\mathbb{R}^2)$, and

$$c_0\|v\|_{W^{2,2}(\Omega,\mathbb{R}^2)} \leq \|f_v(u,\nabla u)\|$$

for an appropriate constant $c_0 > 0$. Since $f_v(\cdot, \nabla\cdot)$ is bounded, we obtain

$$c_0 \|v\|_{W^{2,2}(\Omega,\mathbb{R}^2)} \leq c_1$$

for an appropriate constant $c_1 > 0$. □

Due to standard arguments provided by L^p-regularity theory and the embedding $W^{2,2}(\Omega) \hookrightarrow C(\overline{\Omega})$ we obtain

Corollary C.5. *Let v be a solution of (C.13). It holds $v \in W^{2,2}(\Omega, \mathbb{R}^2)$ and it exists a constant $c > 0$ independent of u such that*

$$\|v\|_{C(\overline{\Omega},\mathbb{R}^2)} \leq c.$$

Identical to the proof of Lemma C.4 can be shown

Corollary C.6. *Let $g, h \in W^{1,2}(\Omega)$. Let $v \in W^{2,2}(\Omega)$ be a solution of*

$$\Delta v + \nabla(\nabla \cdot v) - v = f_v(g, \nabla g) - f_v(h, \nabla h).$$

on Ω with zero-flux boundary conditions. Then a constant $c > 0$ exists such that

$$\|v\|_{W^{2,2}(\Omega,\mathbb{R}^2)} \leq c \|f_v(g, \nabla g) - f_v(h, \nabla h)\|. \tag{C.15}$$

Lemma C.7. *Let $v \in C^0(\overline{\Omega}, \mathbb{R}^2)$ and $g \in L^2(\Omega)$. The equation*

$$dt(-\Delta u + \operatorname{div}(uv)) + u = g \tag{C.16}$$

on Ω with zero-flux boundary conditions satisfies has a unique solution $u \in W^{2,2}(\Omega)$. Moreover it exists a constant $c > 0$, such that

$$\left(1 - dt\left(\frac{1}{2}\|v\|_{C^0(\overline{\Omega},\mathbb{R}^2)}\right)^2\right)\|u\|_{L^2(\Omega)} \leq \|g\|_{L^2(\Omega)}. \tag{C.17}$$

Proof. Since the right hand side is an element of $L^\infty(\Omega)$, follows the assertion about the existence and uniquness directly from the theory of elliptic PDE (cf. e.g. [138]).
For convenience, we set $\|\cdot\|_C := \|\cdot\|_{C(\overline{\Omega})}$. In order to verify (C.17), we take the weak formulation of the considered PDE and test it with u. Since we have zero-flux boundary conditions, this yields the estimate

$$dt\|\nabla u\|^2 + \|u\|^2 \leq \|g\|\|u\| + dt\|v\|_C \int_\Omega |u\nabla u| \, dx \tag{C.18}$$

Application of Young's inequality for $p = q = 2$ and $\varepsilon = \|v\|_C^{-1}$ leads to

$$dt\|v\|_C \int_\Omega |u\nabla u| \, dx \leq dt\|\nabla u\|^2 + dt\frac{1}{4}\|v\|_C^2\|u\|^2.$$

Thus, from (C.18) follows the estimate

$$\begin{aligned} \|u\|^2 &\leq \|g\|\|u\| + dt\frac{1}{4}\|v\|_C^2\|u\|^2 \\ \Leftrightarrow \left(1 - dt\frac{1}{4}\|v\|_C^2\right)\|u\|^2 &\leq \|g\|\|u\|. \end{aligned}$$

This proves (C.17). □

Lemma C.8. *Let conditions as formulated in lemma C.7 with* $g := dtf_u(t,x,\overline{u}) + \overline{u}$ *hold. The mean value of a solution* u *of (C.16) is zero:*

$$\frac{1}{|\Omega|}\int_\Omega u\ dx = 0.$$

Proof. Take the weak solution of (C.16) and test it with the constant test function $\varphi = 1$. This yields

$$\frac{1}{|\Omega|}\int_\Omega u\ dx = \frac{1}{|\Omega|}\int_\Omega dtf_u(t,x,\overline{u}) + \overline{u}\ dx.$$

Recall, that $dtf_u(t,x,\overline{u}) + \overline{u}$ is constructed such that

$$\int_\Omega dtf_u(t,x,\overline{u}) + \overline{u}\ dx = 0$$

holds. □

C.2.2 Proof of convergence

Proof. (1) Let (u_n, v_n) be solutions obtained by (C.7)-(C.11) after the n-th iteration step, and let (u,v) be a solution of (C.4). Subtracting the weak formulation of (C.11) substituted with u_n, v_n from the weak formulation of (C.4) yields if we set $w_n := u - u_n$

$$\begin{aligned} dt\int_\Omega \nabla w_n \nabla\phi dx + dt\int_\Omega v_n u_n \nabla\phi - vu\nabla\phi dx + \int_\Omega w_n\phi dx \\ = dt\int_\Omega (f_u(t,x,u) - f_u(t,x,u_{n-1}))\phi dx \end{aligned} \tag{C.19}$$

for all $\phi \in H^1(\Omega)$. Testing the weak equation with the test function $w_n := u - u_n$ implies the estimate

$$\begin{aligned} dt\|\nabla w_n\|^2 + \|w_n\|^2 \leq& dt\|f_u(t,x,u) - f_u(t,x,u_{n-1})\|\|w_n\| \\ &+ dt\int_\Omega |v_n u_n \nabla w_n - vu\nabla w_n|\, dx \end{aligned} \tag{C.20}$$

The Lipschitz-continuity of f_u and the iteration rule imply

$$\|f_u(t,x,u) - f_u(t,x,u_{n-1})\|\|w_n\| \leq L\|w_{n-1}\|\|w_n\|,$$

and the second summand of the right hand side can be estimated by standard inequalities as follows

$$\begin{aligned}\int_\Omega |vu\nabla w_n - v_n u_n \nabla w_n|\,dx &\le \int_\Omega |(v-v_n)u + v_n w_n||\nabla w_n|\,dx \\ &\le \|u\|\|v-v_n\|_{C^0(\overline{\Omega})}\|\nabla w_n\| + \|v_n\|_{C^0(\overline{\Omega})}\|w_n\|\|\nabla w_n\|.\end{aligned} \tag{C.21}$$

From corollary C.5 follows $\|v_n\|_{C^0(\overline{\Omega})}, \|v\|_{C^0(\overline{\Omega})} < c_1$ for a suitable constant $c_1 > 0$. Consequently, we obtain from Lemma C.7 and the boundedness of f_v and $u(t_-, x)$ that for appropriate constants $c_2, c_3 > 0$ holds

$$\|u\| \le \frac{c_2}{c_3 - dt}.$$

We choose $dt < 1/2c_3$. Then we have $\|u\| \le c_4$, where $c_4 := 2c_2/c_3$. From $C(\Omega) \hookrightarrow W^{1,2}(\Omega)$, estimate (C.15), and the Lipschitz-continouty of f_v follows the existence of a constant $c_5 > 0$, such that

$$\|v - v_n\|_{C^0(\overline{\Omega})} \le c_5\|f_v(u,\nabla u) - f_v(u_{n-1},\nabla u_{n-1})\| \le c_5 L\left(\|w_{n-1}\| + \|\nabla w_{n-1}\|\right).$$

Observe, that in the second estimate the iteration rule was used. Application of these estimates in (C.20) yields

$$\begin{aligned}dt\|\nabla w_n\|^2 + \|w_n\|^2 \le\ & dt\ cL(\|w_n\|\|w_{n-1}\| + \|w_{n-1}\|\|\nabla w_n\|) \\ & + dt\ cL\|\nabla w_n\|\|\nabla w_{n-1}\| + dt\|w_n\|\|\nabla w_n\|\end{aligned} \tag{C.22}$$

for an appropriate constant $c > 0$.
(2) We apply Young's inequality on each summand of the right hand side which contains the term $\|w_n\|$. Thus, we obtain

$$\begin{aligned}\|w_{n-1}\|\|w_n\| &\le \frac{cL\ dt}{2}\|w_{n-1}\|^2 + \frac{1}{2cL\ dt}\|w_n\|^2, \\ \|w_n\|\|\nabla w_n\| &\le \frac{dt}{2}\|\nabla w_n\|^2 + \frac{1}{2\ dt}\|w_n\|^2.\end{aligned}$$

Application of these inequalities on the right hand side of (C.22) leads to the estimate

$$\begin{aligned}\|\nabla w_n\|^2 \le\ & dt\frac{(cL)^2}{2}\|w_{n-1}\|^2 + cL\|w_{n-1}\|\|\nabla w_n\| \\ & + cL\|\nabla w_n\|\|\nabla w_{n-1}\| + \frac{dt}{2}\|\nabla w_n\|^2\end{aligned}$$

We choose $dt < 1$. Thus we can write

$$\|\nabla w_n\|^2 \le dt\ (cL)^2\|w_{n-1}\|^2 + 2cL\left(\|w_{n-1}\|\|\nabla w_n\| + \|\nabla w_n\|\|\nabla w_{n-1}\|\right).$$

On the right hand side of this inequality appears $\|\nabla w_n\|$ exclusively with a power of first oder. It is now easy to verify, that there exists a constant $c > 0$ (independent of dt,

since we already chose $dt < 1$), such that

$$\|\nabla w_n\| \leq c(\|w_{n-1}\| + \|\nabla w_{n-1}\|).$$

Thanks to Lemma C.8 we know, that the mean value of w_{n-1} is zero. We obtain by application of Poincare's inequality $\|w_{n-1}\| \leq C_p\|\nabla w_{n-1}\|$, where C_p is the Poincare constant. Thus, there exists a constant $c_1 > 0$, such that

$$\|\nabla w_n\| \leq c_1\|\nabla w_{n-1}\|. \tag{C.23}$$

(3) We apply Young's inequality on each summand on the right hand side of (C.22) which contains the term $\|\nabla w_n\|$. This yields

$$\begin{aligned}
\|w_{n-1}\|\|\nabla w_n\| \leq& \frac{3cL}{4}\|w_{n-1}\|^2 + \frac{1}{3cL}\|\nabla w_n\|^2,\\
\|\nabla w_n\|\|\nabla w_{n-1}\| \leq& \frac{3cL}{4}\|\nabla w_{n-1}\|^2 + \frac{1}{3cL}\|\nabla w_n\|^2,\\
\|w_n\|\|\nabla w_n\| \leq& \frac{3}{4}\|w_n\|^2 + \frac{1}{3}\|\nabla w_n\|^2,
\end{aligned}$$

and from (C.22) we obtain in a similar way as in (2) the estimate

$$\|w_n\|^2 \leq dt\ c(\|w_n\|\|w_{n-1}\| + \|w_{n-1}\|^2 + \|\nabla w_{n-1}\|^2 + \|w_n\|^2)$$

for a constant $c > 0$ (independent of dt). Subtraction of $dt\|w_n\|^2$ from both sides and subsequent application of Young's inequality in the term $\|w_n\|\|w_{n-1}\|$ gives us

$$\|w_n\|^2 \leq dt\ c_2(\|w_{n-1}\|^2 + \|\nabla w_{n-1}\|^2) \tag{C.24}$$

for a suitable constant $c_2 > 0$.
(4) By induction we obtain from (C.23) and (C.24)

$$\|w_n\|^2 \leq (dt\ c)^n(\|w_0\|^2 + \|\nabla w_0\|^2)$$

for a suitable constant $c > 0$. If we choose $dt < 1/c$, follows $\|w_n\| \to 0$ if $n \to \infty$. Therefore $u_n \to u$ converges in $L^2(\Omega)$.
Form the weak formulation (C.19) we can deduce that for $n \to \infty$

$$\nabla w_n + u(v_n - v) \to 0 \quad \text{weakly in } L^2(\Omega).$$

Since we assumed that v_n converges weakly to $v \in L^2(\Omega, \mathbb{R}^2)$ for $n \to \infty$, follows

$$\nabla u_n - \nabla u \to 0 \quad \text{weakly in } L^2(\Omega).$$

□

Remark C.9. The subtraction of the mean value of $f_u - u(t_-, x)$ is essential for the convergence of the iteration scheme. If we performed the iteration as described above without subtracting the mean value, we would obtain the convergence estimate

$$\|\nabla(u - u_n)\|_{L^2(\Omega_t)} \leq c \left(\|(u - u_{n-1})\|_{L^2(\Omega_t)} + \|\nabla(u - u_{n-1})\|_{L^2(\Omega_t)} \right). \tag{C.25}$$

This estimate is sharp and from it follows that the scheme does not converge for any dt. However, if the iteration is performed with the subtraction of the mean value of $f_u - u(t_-, x)$, we yield the same estimate (C.25), but we also can estimate with aid of Poincare's inequality

$$\|(u - u_{n-1})\|_{L^2(\Omega_t)} \leq c\|\nabla(u - u_{n-1})\|_{L^2(\Omega_t)},$$

which implies for a suitable constant $c > 0$

$$\|\nabla(u - u_n)\|_{L^2(\Omega_t)} \leq c\|\nabla(u - u_{n-1})\|_{L^2(\Omega_t)}.$$

This estimate is suitable to enforce the convergence of the scheme. See appendix C.2 for details.

2.2) Let now n be the final iteration step. The code computes

$$g := \frac{1}{|\Omega|} \int_\Omega dt \; f_u(t, x, u_{n-1}) + u(t_-, x) \; dx \tag{C.26}$$

and solves

$$\begin{aligned} dt(-\Delta u_n + \operatorname{div}(u_n v_n(t, x)) + u_n = dt\overline{f}_u(t, x, u_{n-1}) + \overline{u}(t_-, x) + g \\ (\Delta v_n + \nabla(\nabla \cdot v_n) - v(t, x) = f_v(u_{n-1}, \nabla u_{n-1}), \end{aligned} \tag{C.27}$$

numerically for u_n, v_n. (Recall that $dt \; f_u + u(t_-, x) = dt \; \overline{f}_u + \overline{u}(t_-, x) + g$.) These solutions were taken as approximated solutions of system (C.4).

Appendix D

Existence of the one-dimensional system for short times

We heuristically argued that the one-dimensional system (5.5)–(5.8) is has the ability of generating patterns. This gives rise to the question whether the system possesses a solution at all. Due to its description as a moving boundary problem, it is not evident that the system is well defined. In this appendix we will show that at least for sufficient short times a solution for a comparable system exists.
A proof of the original system of the 2-dimensional setting is in preparation.

We assume that at short times, the impact of τ on the system is negligible. Moreover, we neglect the RhoA dynamics characterized by the variable w. We consider the normalized PDE-system

$$\begin{aligned} \partial_t u - \Delta u + \nabla(uv) &= f(u) \quad \text{on} \quad \Omega(t), \\ -\Delta v + v &= g(u) \quad \text{on} \quad \Omega(t), \end{aligned} \tag{D.1}$$

with zero-flux boundary conditions and given initial value u_0 for u in (D.1). The assumptions for the initial conditions and the right-hand sides will be declared in the next section. As before, the moving domain Ω_t is convected by the velocity field V along the normal direction of the boundary:

$$V = v \quad \text{on } \partial\Omega_t = \{x | x'(t, x_0) = v(t, x_0), x_0 \in \partial\Omega_0\}, \tag{D.2}$$

where

$$\Omega_0 := (0, 1) \tag{D.3}$$

is the initial domain of the 1D problem.
We act on the following assumptions: Let $f, g : \mathbb{R} \to \mathbb{R}$ be Lipschitz-continuous, and let u_0 be sufficiently smooth.

We will show that on suitable Banach spaces equation (D.1) possesses a solution at sufficiently short times t. This is mathematically precisely formulated in Theorem D.21, which is the main result of this appendix.

D.0.1 Outline of the poof

The proof can be broadly separated in three steps: reformulation, reduction, and proving existence. In the first step, we will reformulate the original moving boundary system on a fixed reference frame by the introduction of a *boundary location function* ϕ. The reformulation is constructed in section D.0.3 and leads to a parabolic-elliptic system that is coupled to a "displacement" ODE. In the next step this system will be reduced to a degenerated parabolic system by solving the elliptic part of the system a priory in dependency of the unknown variables. This is done in section D.0.4. The last step is presented in section D.0.5, where the short time existence for the reduced system on suitable Banach-spaces is proven.
In the proof we consult techniques and results from the theory of analytic semigroups as presented in [139] and [140]. The disadvantage of this approach is that it does not deliver a numerical scheme which theoretically corroborates the convergence assumption of the implemented scheme, used in numerical simulation in Chapter 4. The advantage, however, is that analytic semigroup theory provides a very abstract tool for the treatment of evolution equations, which presents a prospect of a possible generalization of the presented proof to a 2-dimensional spatial setting.

D.0.2 Preliminaries

Definition D.1 (Spaces of continuous functions and generalized Sobolev spaces)**.** Let X,Y be real Banach spaces and $\alpha \in \mathbb{R}_+$. We denote by

$$C^\alpha(X,Y) \quad (\text{resp.} \quad \mathrm{BUC}^\alpha(X,Y)\ )$$

the space of $[\alpha]$-fold differentiable functions (resp. the space of $[\alpha]$-fold differentiable uniformly bounded functions) from X to Y, whose $[\alpha]$-th derivative is Hölder continuous with Hölder exponent $\alpha - [\alpha]$. For the sake of a simple notation, we will, unless stated otherwise, write

$$\|u\| := \|u\|_{\mathrm{BUC}^0(X,Y)}.$$

The space of all locally Lipschitz continuous functions from X to Y is denoted by

$$C^{1-}(X,Y).$$

Let $\Omega \subset \mathbb{R}^N$ be smoothly bounded. We denote by

$$W_p^s := W_p^s(\Omega), \quad 1 \leq p < \infty$$

either the usual Sobolev space, if $s \in \mathbb{N}$, or the Slobodeckij space, if $s \in \mathbb{R}_+ \backslash \mathbb{N}$. In the particular case $s \in \mathbb{R}_+ \backslash \mathbb{N}$ consists the Slobodeckij space of functions $u \in W_p^{[s]}$ such that

$$[\partial_\alpha u]_p^{(s-[s])p} := \int_{\Omega\times\Omega} \frac{|\partial_\alpha u(x) - \partial_\alpha u(y)|^p}{|x-y|^{(s-[s])p+N}}\, dx\, dy < \infty, \quad |\alpha| = [s].$$

The Slobodeckij-space, endowed with the norm

$$\|u\|_{W_p^s} := \left(\|u\|_{W_p^{[s]}}^p + \sum_{|\alpha|=[s]} [\partial_\alpha u]_p^{(s-[s])p} \right)^{1/p}$$

is a Banach space. Let $\mathbb{K} = \mathbb{R}, \mathbb{C}$. We denote by $\mathcal{F}$ the Fourier transform on $\mathcal{S}'(\mathbb{R}^N, \mathbb{K})$, the Schwarz space of tempered $\mathbb{K}$-valued distributions. Lastly, we put

$$\|u\|_{H_p^s} := \|(1-\Delta)^{s/2} u\|_p,$$

where $(1-\Delta)^{s/2} := \mathcal{F}^{-1}(1+\xi^2)^{s/2}\mathcal{F}$. Then the Bessel potential spaces, $H_p^s(\mathbb{R}^N, \mathbb{K})$, are defined as

$$H_p^s(\mathbb{R}^N, \mathbb{C}) := (\{u \in \mathcal{S}'(\mathbb{R}^N, \mathbb{K}) \mid \|u\|_{H_p^s} < \infty\}, \|\cdot\|_{H_p^s}), \quad 1 < p < \infty,\ s \in \mathbb{R}.$$

We denote by $\mathcal{D}$ and by $\mathcal{D}'$ the space of $\mathcal{K}$-valued test functions and distributions on Ω, respectively, and by

$$r_\Omega \in \mathcal{L}(\mathcal{S}'(\mathbb{R}^N, \mathbb{K}), \mathcal{D}')$$

the 'restriction operator', given by

$$\langle r_\Omega u, \varphi \rangle := \langle u, \varphi \rangle, \quad u \in \mathcal{S}'(\mathbb{R}^N, \mathbb{K})\ \varphi \in \mathcal{D}.$$

Then the Bessel potential spaces over Ω are defined by restriction, i.e.

$$H_p^s := H_p^s(\Omega, \mathbb{K}) = r_\Omega H_p^s(\mathbb{R}^N, \mathbb{K}).$$

Definition D.2 (Multiplier-spaces of uniformly elliptic Operators)**.** In the following

$$\mathcal{A}u = -\partial_x(\alpha\partial_x u + \beta u) + \gamma\partial_x u + \delta u,$$

denotes an uniformly elliptic operator with boundary operator

$$\mathcal{B}u := T(\alpha\partial_x u + \beta u) + \epsilon T u,$$

where T denotes the trace operator. The pair $(\mathcal{A}, \mathcal{B})$ is called a linear, uniformly elliptic

boundary-value operator. The set of all these operators is denoted by $\mathcal{E} = \mathcal{E}(\Omega)$. We topologize the set of these boundary-value problems by identifying them with subsets of the Banach spaces

$$\mathbb{E}^0 := \left[\mathrm{BUC}^0(\Omega)\right]^3 \times L_\infty(\Omega) \times C^0(\partial\Omega), \text{ resp.}$$

by means of the identification

$$(\mathcal{A}, \mathcal{B}) \leftrightarrow (\alpha, \beta, \gamma, \delta, \epsilon)$$

and set

$$\mathcal{E}^0 := \mathcal{E} \cap \mathbb{E}^0.$$

It can be shown that $\mathcal{E}^0 \subset \mathbb{E}^0$ is open; see [139], Chapter 4.1, Remark 8.6.

Definition D.3 (Analytic semigroup)**.** Let E and F be Banach spaces over $\mathbb{K}$ such that $E \hookrightarrow F$. We write

$$A : \mathrm{dom}(A) \subset E \to F$$

if A is a linear operator with domain $\mathrm{dom}(A)$ in E and $\mathrm{im}(A)$ in F. We denote $D(A)$ by the domain of A endowed with its graph norm. Then $D(A) \hookrightarrow E$, $A \in \mathcal{L}(D(A), F)$, and $D(A)$ is a Banach space iff A is closed; see [139], Section 3.
Let E_0, E_1 be Banach spaces with $E_1 \hookrightarrow E_0$. We denote by

$$\mathcal{H}(E_1, E_0)$$

the set of all $A \in \mathcal{L}(E_1, E_0)$, such that A, considered as a linear operator in E_0 with domain E_1, is the negative infinitesimal generator of an analytic semigroup $\{e^{-tA} : t \geq 0\}$ on E_0, that is in $\mathcal{L}(E_0)$

We refer to [140], for the general theory of analytic semigroups and assume that the reader has a working knowledge of that theory.

Definition D.4 (Boundary problem spaces)**.** Suppose $(\mathcal{A}, \mathcal{B}) \in \mathbb{E}$ and $S_p^s \in \{W_p^s, H_p^s \ : \ 1 \leq p < \infty\}$. We define

$$S_{p,\mathcal{B}}^s := \begin{cases} \{u \in S_p^s \ : \ \mathcal{B} = 0\}, & \text{if } 1 + 1/p < s \leq 2, \\ S_p^s, & \text{if } 0 \leq s < 1 + 1/p. \end{cases}$$

Moreover, we define the set of *singular positive values* by

$$\Sigma_p^+ := \{1 + 1/p\}.$$

Definition D.5 (Interpolation spaces)**.** Let $X \hookrightarrow Y$ be real Banach spaces such that X is dense in Y with respect to the norm of Y. We denote by

$$[X, Y]_\theta, \quad 0 < \theta < 1$$

the complex interpolation space, and by

$$(X, Y)_{\theta,q}, \quad 0 < \theta < 1,\ 1 \leq q \leq \infty$$

the real interpolation space of the couple (X, Y).

We refer to [141] for the general theory of interpolation spaces and only list the particular properties of interpolation spaces that are required for the proof:

Lemma D.6 ([139], Theorem 7.2)**.** *Suppose that* $1 < p < \infty$ *and*

$$-2 + 1/p < s_0 < s_1 < 1 + 1/p.$$

Moreover, suppose that $0 < \theta < 1$ *and* $s_0, s_1, s_\theta := (1-\theta)s_0 + \theta s_1 \notin \Sigma_p^+$*. Then*

$$\begin{aligned}
[H^{s_0}_{p,\mathcal{B}}, H^{s_1}_{p,\mathcal{B}}]_\theta &= H^{s_\theta}_{p,\mathcal{B}}, \\
(H^{s_0}_{p,\mathcal{B}}, H^{s_1}_{p,\mathcal{B}})_{\theta,p} &= W^{s_\theta}_{p,\mathcal{B}}, \quad s_\theta \notin \mathbb{N}, \\
[W^{s_0}_{p,\mathcal{B}}, W^{s_1}_{p,\mathcal{B}}]_\theta &= W^{s_\theta}_{p,\mathcal{B}}, \quad s_\theta \notin \mathbb{N}, \\
(W^{s_0}_{p,\mathcal{B}}, W^{s_1}_{p,\mathcal{B}})_{\theta,p} &= W^{s_\theta}_{p,\mathcal{B}}, \quad s_\theta \notin \mathbb{N}.
\end{aligned}$$

D.0.3 Abstract formulation

The aim of this section is to introduce suitable Banach spaces and to reformulate the moving boundary problem (D.1)-(D.3) as an abstract evolution equation on a fixed reference frame Ω_0.

Definition D.7 (Pull-back & push-forward)**.** For fixed $t > 0$ we denote the set of all C^1-diffeomorphisms, mapping from Ω_0 onto Ω_t by $\mathrm{Diff}^1(\Omega_0, \Omega(t))$. For $\Phi \in \mathrm{Diff}^1(\Omega_0, \Omega(t))$, we define the *pull-back operator* Φ^* and the *push-forward operator* Φ_* by

$$\Phi^* a := a \circ \Phi, \quad \text{for } a \in C^0(\Omega(t), \mathbb{R}), \tag{D.4}$$

$$\Phi_* b := b \circ \Phi^{-1}, \quad \text{for } b \in C^0(\Omega_0, \mathbb{R}), \tag{D.5}$$

respectively.
In the following we will consider time depending pull-backs and push-forwards induced by a mapping $\phi \in C([0, t], \Omega_0)$. Therefore we denote formally by ϕ^{-1} the spatial inverse of ϕ at time t, i.e.

$$\phi^{-1}(t, \phi(t, x_0)) = x_0.$$

Definition D.8. Let $\Phi \in \mathrm{Diff}^1(\Omega_0, \Omega(t)) \cap \mathrm{BUC}(\Omega_0)$. For sufficiently regular functions $w, r : \Omega_0 \to \mathbb{R}$ we define the operators

$$\begin{aligned} \mathcal{A}_{11}(\Phi, r)w &:= -\,\Phi^* \left(\mathrm{div}\left(\nabla\Phi_* w - \Phi_* w\ \Phi_* r\right)\right), \\ C(\Phi)r &:= -\,\Phi^* \left(\mathrm{div}\left(\nabla\Phi_* r\right)\right) + r, \end{aligned}$$

and the corresponding boundary operators by

$$\begin{aligned} \mathcal{B}_{11}(\Phi, r)w &:= -\,\Phi^* \left(\nabla\Phi_* w - \Phi_* w\ \Phi_* r\right) && \text{on } \partial\Omega_0, \\ b(\Phi)r &:= -\,\Phi^* \left(\nabla\Phi_* r\right) && \text{on } \partial\Omega_0. \end{aligned}$$

Furthermore we define the right-hand side nonlinearities

$$F_1(\phi, w) := f(w) - \phi_* \nabla\phi^* w, \quad G(w) := g(w).$$

Taking these definitions under consideration, the equations (D.1)–(D.2) of the original system transform to

The abstract system I We consider the PDE system

$$\begin{aligned} \partial_t w + \mathcal{A}_{11}(\phi, r)w &= F_1(w) \text{ on } I \times \Omega_0, \\ C(\phi)r &= G(w) \text{ on } I \times \Omega_0, \\ \partial_t \phi &= r \text{ on } I \times \Omega_0, \end{aligned} \tag{D.6}$$

with the boundary conditions

$$\begin{aligned} \mathcal{B}_{11}(\phi, r)w &= 0 \text{ on } I \times \partial\Omega_0, \\ b(\phi)r &:= 0 \text{ on } I \times \partial\Omega_0, \end{aligned} \tag{D.7}$$

and the initial values

$$\begin{aligned} w(0) &= w_0 \text{ on } \Omega_0, \\ \phi(0) &:= x \text{ on } \Omega_0. \end{aligned} \tag{D.8}$$

Definition D.9 (Classical solution of the abstract system)**.** For a given initial value $w_0 \in C^1(\overline{\Omega_0})$ we call the triple (w, r, ϕ) a classical (lokal-in-time) solution of the abstract system, if a $t_+ = t_+(w_0) > 0$ exists, such that

$$\begin{aligned} w &\in C^2((0, t_+) \times \Omega_0), \\ r(t, \cdot) &\in C^2((0, t_+) \times \Omega_0) \quad \text{for } t \in (0, t_+), \\ \phi &\in C^2((0, t_+), \mathrm{Diff}^2(\Omega_0)) \end{aligned}$$

satisfies (D.6)-(D.8) in the classical sense.

Definition D.10 (Classical solution of the moving boundary system)**.** For a given initial value $u_0 \in C^1(\overline{\Omega_0})$ we call (u, v, Ω_t) a classical (lokal-in-time) solution of the free boundary system, if a $t_+ = t_+(u_0) > 0$ exists, such that

$$\begin{aligned} u &\in C^2((0,t_+), C^2(\Omega_t)), \\ (u(t,\cdot), v(t,\cdot)) &\in C^2(\Omega_t) \times C^2(\Omega_t) \quad \text{for } t \in (0,t_+), \end{aligned} \tag{D.9}$$

satisfies (D.1)-(D.3) point-wise on $\bigcup_{t\in(0,t_+)}(\{t\} \times \Omega_t)$.

Lemma D.11. *Let $w_0 = \phi_0^* u_0 := u_0(\phi(0, x_0))$ be sufficiently smooth. Let (w, r, ϕ) be a classical (lokal-in-time) solution in the sense of definition D.9. Then (u, v), where*

$$u := \phi_* w, \quad v := \phi_* r,$$

is a classical (lokal-in-time) solution in the sense of definition D.10 with initial value u_0.

Proof. Symbolically we distinct between $x \in \Omega_t$ and $x_0 \in \Omega_0$. The mapping $\phi(t, \cdot)$ maps at each time $t \in [0, t_+)$ a point $x_0 \in \Omega_0$ bijectively onto

$$x \in \Omega_t := \mathrm{Im}\left(\phi(t, \cdot)\right).$$

Hence, the normal velocity V of $\partial\Omega_t = \{x | x = \phi(t, x_0) \wedge x_0 = 0, 1\}$ satisfies the Stefan-condition (D.2):

$$V(x)|_{\partial\Omega_t} = \partial_t \phi(t, x_0)|_{x_0=0,1} = r(t, x_0)_{x_0=0,1} = v(t, x)|_{\partial\Omega_t}.$$

Apparently (u, v) satisfies condition (D.9). Moreover we obtain for open subsets $I \subset (0, t_+)$, $U \subset \bigcap_{t\in I} \Omega_t$ and $(t, x) \in I \times U$ the transformated time derivative

$$\begin{aligned} \partial_t u(t,x) &= \partial_t \phi_*(t, w(t,x)) = \partial_t w(t, \phi^{-1}(t, \phi(t, x_0))) \\ &= \partial_t w(t,\zeta)|_{\zeta=\phi^{-1}(t,\phi(t,x_0))} + \partial_\zeta w(t,\zeta)|_{\zeta=\phi^{-1}(t,\phi(t,x_0))} \partial_t \phi^{-1}(t, \phi(t, x_0)) \\ &= \phi_* \phi^* \partial_t w(t, x_0) + \phi_* \nabla \phi^* w(t, x_0), \end{aligned}$$

since differentiation of the inverse yields

$$\partial_t \phi^{-1}(t, \phi(t, x_0)) = \partial_t \phi^{-1}(t,\zeta)|_{\zeta=\phi(t,x_0)} \partial_t \phi(t, x_0) = 1.$$

Similarly, we obtain the transformed operators

$$\begin{aligned} \mathrm{div}(\nabla u - uv)(t,x) &= \mathcal{A}_{11}(\phi, r) w(t, x_0), \\ (-\mathrm{div}(\nabla v) + v)(t,x) &= C(\phi) r(t, x_0), \end{aligned}$$

and in the same way we obtain that the transformations of the corresponding boundary conditions. Substitution of these expressions in the abstract system yields the assertion. □

In the further course we will show that the abstract system possesses a *weak* solution at sufficiently short times. As usual, under additional regularity assumptions may be shown that a weak solution of a parabolic-elliptic system is also a solution in the classical sense.

Definition D.12 (Weak solution of the abstract system)**.** Let $I = (0, T)$, $T > 0$. Fix $1 < s < 2$ and choose $w_0 \in W^s_{2,\mathcal{B}_{11}}(\Omega_0)$. We call (w, r, ϕ) a weak solution of the system if

$$(w, \phi) \in C(I, W^s_{2,\mathcal{B}_{11}}(\Omega_0) \times \mathrm{BUC}^1(\Omega_0)) \cap C^s(I, L_p(\Omega_0) \times \mathrm{BUC}^1(\Omega_0)),$$
$$r \in L^\infty(I, W^s_2(\Omega_0)).$$

satisfy (D.6)-(D.8) in the distributive sense.

Finally, we have to define the set of admissible functions describing the boundary deformation:

Definition D.13.

$$\mathrm{Ad} := \left\{ \phi \in \mathrm{BUC}^2(\Omega_0) : \inf_{x \in \Omega_0} |\partial_x \phi| \neq 0 \right\}. \tag{D.10}$$

Remark D.14. It holds $\mathrm{Ad} \subset \mathrm{Diff}^1(\Omega_0) \cap \mathrm{BUC}(\Omega_0)$. Thus, ϕ_* and ϕ^* exist for $\phi \in \mathrm{Ad}$ and the operators in definition D.8 are well defined in the weak L^2-formulation.

D.0.4 The reduced system

In this step the degenerated parabolic-elliptic system (D.6) is reduced to a degenerated parabolic system, by expressing the inverse of the elliptic operator C as a mapping depending on (r, ϕ).

Lemma D.15. *Let $\phi \in Ad$. The Operator*

$$[r \mapsto C(\phi)r] \in \mathcal{L}(H^2_{2,b}, H^0_2)$$

is an isomorphism. Moreover for fixed $r \in H^0_2$ holds

$$[\phi \mapsto C^{-1}(\phi)r] \in C^{1-}(Ad, H^2_{2,b}). \tag{D.11}$$

Proof. 1) We show the first assertion. Let $\phi \in Ad$ be fixed. We set $g := \langle \partial_x \phi | \partial_x \phi \rangle$, where $\langle \cdot | \cdot \rangle$ denotes the Euclidian inner product. Observe that the main part of $C(\phi)$, as defined

in Definition D.8, is the Laplace-Beltrami operator with respect to the Riemannian tensor g. Thus $C(\phi)$ can be written with respect to local coordinates as

$$C(\phi)r = -\frac{1}{\sqrt{|g|}}\partial_x\left(\frac{1}{\sqrt{|g|}}\partial_x r\right) + r \quad \text{on } \Omega_0.$$

and the space $H^2_{2,b}$ transforms to a domain independent of ϕ, simply containing homogenous Neumann boundary conditions:

$$H^2_{2,b} = \left\{ r \in H^2_2 |\ \frac{\partial_x r(0)}{\sqrt{|g|}} = \frac{\partial_x r(1)}{\sqrt{|g|}} = 0 \right\} = \left\{ r \in H^2_2 |\ \partial_x r(0) = \partial_x r(1) = 0 \right\}. \quad \text{(D.12)}$$

We set $\tilde{C}(\phi)r := \sqrt{|g|}C(\phi)r$. Since $\phi \in \mathrm{Ad}$, $\sqrt{|g|} \in \mathrm{BUC}(\Omega_0)$ and $\sqrt{|g|} > 0$ hold. Thus, operator $\tilde{C}(\phi)$ is uniformly elliptic, with sufficient regular coefficients, such that

$$\tilde{C}(\phi) \in \mathcal{L}(H^2_{2,b}, H^0_2)$$

is an isomorphisms. This follows from standard results for elliptic partial differential equations, cf. [138]. Consequently

$$C(\phi) \in \mathcal{L}(H^2_{2,b}, H^0_2)$$

is an isomorphism.

2) We verify assertion (D.11). Let U be a bounded subsection of Ad such that $\partial U \cap \partial\mathrm{Ad} = \emptyset$. Let $\phi_1, \phi_2 \in U$. The first assertion assures that for given $f \in H^0_2$ solutions $u_1, u_2 \in H^2_{2,b}$ of

$$-\mathrm{div}\left(\frac{1}{\sqrt{|g_i|}}\nabla u_i\right) + \sqrt{|g_i|}u_i = \sqrt{|g_i|}f \quad \text{on } \Omega_0 \quad (i = 1, 2) \quad \text{(D.13)}$$

exist, where $g_i = \langle \partial_x\phi_i | \partial_x\phi_i \rangle$. From the standard L_p-theory for elliptic PDE, we obtain the estimate

$$\|u_i\|_{H^2_2} \leq c_1 \|f\|_{H^0_2}, \quad \text{(D.14)}$$

where the constant $c_1 = c_1(\Omega_0, U)$ does not depend on u_i, ϕ_i, f, $i = 1, 2$. Subtracting the first from the second equation in (D.13) and subsequent multiplication of $\omega := (u_1 - u_2)$ on both sides leads after integration to

$$\begin{aligned} \int_{\Omega_0} \nabla\omega \left(\frac{1}{\sqrt{|g_1|}}\nabla u_1 - \frac{1}{\sqrt{|g_2|}}\nabla u_2\right)\, dx + \int_{\Omega_0} \omega\left(\sqrt{|g_1|}u_1 - \sqrt{|g_2|}u_2\right)\, dx \\ \leq \int_{\Omega_0} \left|\omega(\sqrt{|g_1|} - \sqrt{|g_2|})f\right|\, dx, \end{aligned} \quad \text{(D.15)}$$

where we used partial integration and the fact that the integral vanishes on the boundary due to the boundary conditions implied by (D.12). Using standard inequalities, the first

term on the left hand side can be estimated as

$$\int_{\Omega_0} \nabla\omega \left(\frac{1}{\sqrt{|g_1|}} \nabla u_1 - \frac{1}{\sqrt{|g_2|}} \nabla u_2 \right) \, dx \geq \inf |\frac{1}{\sqrt{|g_1|}}| \|\nabla\omega\|_{H_2^0}^2 \\ - \|\nabla\omega\|_{H_2^0} \|\nabla u_2\|_{H_2^0} \|\sqrt{|g_1|} - \sqrt{|g_2|}\|.$$

For the second term on the left hand side we obtain

$$\int_{\Omega_0} \omega \left(\sqrt{|g_1|} u_1 - \sqrt{|g_2|} u_2 \right) \, dx \geq \inf \sqrt{|g_1|} \|\omega\|_{H_2^0}^2 \\ - \|\sqrt{|g_1|} - \sqrt{|g_2|}\| \|\omega\|_{H_2^0} \|u_2\|_{H_2^0},$$

while the right hand side can be estimated by

$$\int_{\Omega_0} \left| \omega (\sqrt{|g_1|} - \sqrt{|g_2|}) f \right| \, dx \leq \|\sqrt{|g_1|} - \sqrt{|g_2|}\| \|f\|_{H_2^0} \|\omega\|_{H_2^0}.$$

In summary we obtain that (D.15) yields the estimate

$$\inf \left(\frac{1}{\sqrt{|g_1|}} \right) \|\nabla\omega\|_{H_2^0}^2 + \inf \left(\sqrt{|g_1|} \right) \|\omega\|_{H_2^0}^2 \leq \kappa(u_1, u_2, f) \|\sqrt{|g_1|} - \sqrt{|g_2|}\|, \tag{D.16}$$

where

$$\kappa(u_1, u_2, f) := \|\nabla\omega\|_{H_2^0} \|\nabla u_2\|_{H_2^0} + \|\omega\|_{H_2^0} \|u_2\|_{H_2^0} + \|f\|_{H_2^0} \|\omega\|_{H_2^0}.$$

Thanks to (D.14) it holds $\kappa(u_1, u_2, f) < K$ for a suitable constant $K > 0$ independent of (u_1, u_2, f). Moreover, since $\phi_1, \phi_2 \in U$, and U is bounded in Ad, it is easy to verify that a constant $c_2 = c_2(U, \Omega_0)$ independent of ϕ_1, ϕ_2 exists, such that

$$\min \left\{ \inf \left(\frac{1}{\sqrt{|g_1|}} \right), \inf \sqrt{|g_1|} \right\} \geq c_2.$$

If $U \subset \mathrm{Ad}$ is chosen sufficiently small, it can be shown that a constant $c_3 = c_3(U, \Omega_0)$ independent of ϕ_1, ϕ_2 exists, such that

$$\left\| \sqrt{|g_1|} - \sqrt{|g_2|} \right\| \leq c_3 \|\phi_1 - \phi_2\| \quad \text{for } \phi_1, \phi_2 \in U.$$

(The details of this proof will be shown in a more general version in the proof of Lemma D.19.) In summary, we obtain from inequality (D.16)

$$[\phi \mapsto C^{-1}(\phi) f] \in C^{1-}(\mathrm{Ad}, H_{2,b}^1). \tag{D.17}$$

We consider once again (D.13). Subtraction of equation (D.13) with respect to $i = 2$ from equation (D.13)with respect to $i = 1$ yields

$$\frac{1}{\sqrt{|g_1|}}\Delta\omega = -\left(\frac{1}{\sqrt{|g_1|}} - \frac{1}{\sqrt{|g_2|}}\right)\Delta u_2 - \nabla\frac{1}{\sqrt{|g_1|}}\nabla\omega - \nabla\left(\frac{1}{\sqrt{|g_1|}} - \frac{1}{\sqrt{|g_2|}}\right)\nabla u_2 \\ +\sqrt{|g_1|}\omega - (\sqrt{|g_1|} - \sqrt{|g_2|})(u_2 - f).$$

Multiplication of $\Delta\omega$ on both sides and integration leads after the application of (D.14), the Minkowski- and the Hölder inequality to the estimate

$$\inf\left(\frac{1}{\sqrt{|g_1|}}\right)\|\Delta\omega\|^2_{H^2_0} \leq \gamma\|\Delta\omega\|_{H^2_0}, \tag{D.18}$$

where for a suitable constant c_4 independent of ϕ_i, u_i, $(i = 1, 2)$

$$\gamma := c_4\left(\left\|\frac{1}{\sqrt{|g_1|}} - \frac{1}{\sqrt{|g_2|}}\right\|_{\mathrm{BUC}^1(\Omega_0)} + \left\|\sqrt{|g_1|} - \sqrt{|g_2|}\right\|_{\mathrm{BUC}(\Omega_0)} + \|\omega\|_{H^1_2}\right)$$

In the proof of Lemma D.19 will be shown that the first two summands on the right hand side can locally estimated by a Lipschitz expression. From (D.17) we know that $\|\omega\|_{H^1_2}$ can locally estimated by a Lipschitz expression. Hence, from (D.18) follows for a constant $L = L(\Omega_0, U)$

$$c_2\|\Delta\omega\|_{H^2_0} \leq L\|\phi_1 - \phi_2\|_{\mathrm{BUC}^1(\Omega_0)},$$

which proofs the assertion. □

Applying standard results from the regularity theory of elliptic partial differential equations, we obtain

Lemma D.16. *Let $\phi \in Ad$. Then for fixed $r \in H^1_2$ is*

$$[\phi \mapsto C^{-1}(\phi)r] \in C^{1-}(Ad, H^3_{2,b}).$$

The two lemmata above imply

Lemma D.17. *The following mapping conditions hold:*

$$[(\phi, r) \mapsto C^{-1}(\phi)r] \in C^{1-}(Ad \times H^0_p, \mathrm{BUC}^1(\Omega_0)),$$
$$[(\phi, r) \mapsto C^{-1}(\phi)r] \in C^{1-}(Ad \times H^1_p, \mathrm{BUC}^2(\Omega_0)).$$

Proof. We only prove the first mapping property. The second assertion follows in an almost identical way.

Let $(\phi_1, r_1), (\phi_2, r_2) \in \mathrm{Ad} \times H^0_p$, and $u_1, u_2 \in H^2_p$ be the solutions of

$$C(\phi_i)u_i = r_i \quad \text{on } \Omega_0$$

with homogenous Neumann boundary conditions. Subtraction of u_2 from u_1 and application of the $H^2_{2,b}$-norm yields

$$\|u_1 - u_2\|_{H^2_{2,b}} \leq \|C^{-1}(\phi_1)r_1 - C^{-1}(\phi_2)r_1\|_{H^2_{2,b}} + \|C^{-1}(\phi_2)r_1 - C^{-1}(\phi_2)r_2\|_{H^2_{2,b}}.$$

Lemma D.15 implies that it only remains to show that the second term on the right hand side can be estimated suitably: From the standard theory for elliptic PDEs (cf. e.g. [138]) follows the energy estimate

$$\|C^{-1}(\phi_2)r_1 - C^{-1}(\phi_2)r_2\|_{H^2_{2,b}} \leq c(\phi_2)\|r_1 - r_2\|_{H^0_2},$$

where $c(\phi_2)$ depends continuously on ϕ. In summary, we obtain that

$$[(\phi, r) \mapsto C^{-1}(\phi)r] \in C^{1-}(\mathrm{Ad} \times H^0_p, H^2_{2,b}).$$

Due to the embedding $H^2_{2,b} \hookrightarrow \mathrm{BUC}^1(\Omega_0)$ follows the assertion. □

Definition D.18 (The reduced system)**.** We set $u = (u_1, u_2) := (w, \phi)$. Moreover for $F(u) := (F_1(u), F_2(u))$ we set $F_2(u) := C^{-1}(u_2)G(u_1)$. We introduce the operators

$$\mathcal{A}(u) := \begin{pmatrix} \mathcal{A}_{11}(u_2, F_2(u)) & 0 \\ 0 & 0 \end{pmatrix} \tag{D.19}$$

and

$$\mathcal{B}(u) := \begin{pmatrix} \mathcal{B}_{11}(u_2, F_2(u)) & 0 \\ 0 & 0 \end{pmatrix}. \tag{D.20}$$

The reduced system formally transforms to the abstract, degenerated evolution equation

$$\partial_t u + \mathcal{A}(u)u = F(u) \quad \text{for } t > 0, \quad u(0) = u_0. \tag{D.21}$$

with values in a set whose elements $u(t)$ satisfy $\mathcal{B}(u)u = 0$.

D.0.5 Well-posedness of the reduced system

Lemma D.19. $[(\phi, r) \mapsto \mathcal{A}_{11}(\phi, r)] \in C^{1-}(Ad \times BUC^1(\Omega_0), \mathcal{E}^0(\Omega_0))$

Proof. Let $g := \langle \partial_x \phi | \partial_x \phi \rangle$. By the same argument as in the proof of lemma D.15 $\mathcal{A}_{11}(\phi, r)$ can be written in local coordinates as

$$\begin{aligned}\mathcal{A}_{11}(\phi, r)w =& -\frac{1}{\sqrt{|g|}}\partial_x\left(\frac{1}{\sqrt{|g|}}\partial_x w\right) + \frac{r}{\sqrt{|g|}}\partial_x w + \frac{\partial_x r}{\sqrt{|g|}}w \\ =& -\partial_x\left(\frac{1}{|g|}\partial_x w\right) + \frac{1}{\sqrt{|g|}}\left(r + \partial_x \frac{1}{\sqrt{|g|}}\right)\partial_x w + \frac{\partial_x r}{\sqrt{|g|}}w,\end{aligned}$$

where the last term is the non-divergence representation of the operator. Hence, it is to show that the mapping

$$\mathrm{Ad} \times \mathrm{BUC}^1(\Omega_0) \ni (\phi, r) \mapsto \left(\frac{1}{|g|}, 0, \frac{1}{\sqrt{|g|}}\left(r + \partial_x \frac{1}{\sqrt{|g|}}\right), \frac{\partial_x r}{\sqrt{|g|}}, 0\right) \in \mathcal{E}^0$$

is locally Lipschitz continuous. Due to the definition of Ad is $g \in BUC^1(\Omega_0)$. Thus, the components of $\mathcal{A}_{11}(\phi, r)$ are elements of $\mathcal{E}^0(\Omega_0)$. Exemplarily, we will show that the first term of the third component

$$\left[(\phi, r) \mapsto \frac{1}{\sqrt{|g|}} r\right] \in C^{1-}(\mathrm{Ad} \times \mathrm{BUC}^1(\Omega_0), \mathrm{BUC}^0(\Omega_0)) \tag{D.22}$$

is locally Lipschitz continuous. The whole assertion for the remaining components follows similarly or even more easily.
Choose $\phi_0 \in \mathrm{Ad}$, $r_0 \in \mathrm{BUC}^1(\Omega_0)$ and keep them fixed. Moreover, since $\inf_{x\in\Omega_0} |\partial_x \phi| > 0$ we can choose a $L > 0$ such that

$$\left\| \frac{1}{(\partial_x \phi_0 - L)^2} \right\| < \infty.$$

Let $\phi, \phi' \in \{\phi : \|\phi - \phi_0\|_{\mathrm{BUC}^2} < L\}$ and $r, r' \in \{r : \|r - r_0\|_{\mathrm{BUC}^1} < L\}$. Recall $\sqrt{|g|} = |\partial_x \phi|$. Usage of standard estimates yields

$$\begin{aligned}&\left\| \frac{r}{|\partial_x \phi|} - \frac{r'}{|\partial_x \phi'|} \right\| \leq \left\| \frac{1}{\partial_x \phi' \partial_x \phi} \right\| \left(\|\partial_x \phi'\| \|r - r'\| + \|r'\| \|\partial_x \phi - \partial_x \phi'\|\right) \\ \leq &\left\| \frac{1}{(\partial_x \phi_0 - L)^2} \right\| \left((\|\partial_x \phi_0\| + L)\|r - r'\| + (\|r_0\| + L)\|\partial_x \phi - \partial_x \phi'\|\right).\end{aligned} \tag{D.23}$$

It follows that

$$\mathrm{Ad} \times C^1 \ni (\phi, r) \mapsto \frac{1}{\sqrt{|g|}} r \in \mathrm{BUC}^0(\Omega_0) \tag{D.24}$$

is locally Lipschitz continuous. □

Lemma D.20. $[(\phi, r) \mapsto \mathcal{A}_{11}(\phi, C^{-1}(\phi)(r))] \in C^{1-}(Ad \times H^0_p, \mathcal{E}^0)$

Proof. The assertion follows from lemma D.17, lemma D.19, and the property that compositions of locally Lipschitz continuous functions in $\mathrm{BUC}^\tau(\Omega_0)$, $\tau > 0$, remain to

be locally Lipschitz continuous. □

We have now provided all auxiliaries to proof the short time existence of the abstract system.

Theorem D.21. *Let $1 < s < 2$. For each $u_{1,0} \in W^s_{2,\mathcal{B}_{11}}(\Omega_0)$ a time $t_+(u_0) > 0$ exists, such that equation (D.21) posses a unique solution*

$$u \in C((0,t_+), W^s_{2,\mathcal{B}_{11}}(\Omega_0) \times \mathrm{BUC}^2(\Omega_0)) \cap C^s((0,t_+), L_p(\Omega_0) \times \mathrm{BUC}^2(\Omega_0)).$$

Proof. 1) Set $\mathbb{E}_j := E_j \times \mathrm{BUC}^2(\Omega_0)$, $j = 0, 1$, where $E_0 := H^0_{2,a}(\Omega_0)$ and $E_1 := H^2_p(\Omega_0)$. Define the set of interpolation spaces $\mathcal{F} := \{(\cdot,\cdot)_\theta : 0 < \theta < 1)\}$ by

$$(\cdot,\cdot)_\theta := \begin{cases} [\cdot,\cdot]_\theta & \text{if } \theta = 1/2, \\ (\cdot,\cdot)_\theta & \text{else.} \end{cases}$$

Then (E_0, E_1) a densely injected Banach space couple and [139], Theorem 7.2, implies

$$E_\theta := (E_0, E_1)_\theta = W^{2\theta}_{2,\mathcal{B}_{11}}(\Omega_0), \quad 0 < \theta < 1, \quad 2\theta \notin \Sigma^+_p.$$

Consequently is $(\mathbb{E}_0, \mathbb{E}_1)$ is a densely injected Banach space couple and

$$\mathbb{E}_\theta := (\mathbb{E}_0, \mathbb{E}_1)_\theta = E_\theta \times \mathrm{BUC}^2(\Omega_0), \quad 0 < \theta < 1, \quad 2\theta \notin \Sigma^+_p.$$

Fix $0 < \tau \le r \le s < 2$ and set

$$\alpha := 1 - (2-s)/2, \quad \beta := 1 - (2-r)/2, \quad \gamma := 1 - (2-\tau)/2.$$

Then

$$0 < \gamma \le \beta < \alpha < 1 \tag{D.25}$$

and

$$E_\alpha = W^s_{2,\mathcal{B}_{11}}(\Omega_0), \quad E_\beta = W^r_{2,\mathcal{B}_{11}}(\Omega_0), \quad E_\gamma = W^\tau_{2,\mathcal{B}_{11}}(\Omega_0).$$

Moreover, it is easy to verify that Ad is an open subset of $\mathrm{BUC}^2(\Omega_0)$. Consequentely

$$X_\beta := E_\beta \times \mathrm{Ad}$$

is open in $\mathbb{E}_\beta$.
2) Since $E_\beta \hookrightarrow H^0_p$, we have $[u \mapsto (\mathcal{A}_{11}, a)(u)] \in C^{1-}(X_\beta, \mathcal{E}^0)$ due to lemma D.20. If we denote by $\overline{A}_{11}$ the E_0-realization of $(\mathcal{A}_{11}, a)$, we obtain

$$\overline{A}_{11} \in C^{1-}(X_\beta, \mathcal{H}(E_0, E_1)),$$

thanks to [139], Theorem 8.5. From [142], Theorem 2.1, we obtain

$$\overline{A} \in C^{1-}(X_\beta, \mathcal{H}(\mathbb{E}_0, \mathbb{E}_1)), \tag{D.26}$$

where $\overline{A}$ denotes the $\mathbb{E}_0$ realization of $\mathcal{A}$.
3) We are going to verify

$$F \in C^{1-}(X_\beta, \mathbb{E}_\gamma), \quad \gamma \leq 1/2. \tag{D.27}$$

Consider the first component $F_1 : W^r_{2,a}(\Omega_0) \to W^\tau_{2,a}(\Omega_0)$. By the choice of $\gamma \leq 1/2$ it necessarily follows $r > 1 > \tau$. Hence, there exists a Hölder exponent $\zeta \in (0,1)$ such that

$$W^r_{2,a}(\Omega_0) \hookrightarrow C^\zeta_a(\Omega_0) \hookrightarrow W^\tau_{2,a}(\Omega_0).$$

Since $F_1 : \mathbb{R} \to \mathbb{R}$ is Lipschitz continuous, it is easy to verify that the mapping

$$F_1 : C^\zeta_a(\Omega_0) \to C^\zeta_a(\Omega_0)$$

is Lipschitz continuous. Thus, the mapping $F_1 : W^r_{2,a}(\Omega_0) \to W^\tau_{2,a}(\Omega_0)$ is Lipschitz continuous.
Consider the second component F_2. Recall

$$F_2(u) = C^{-1}(u_2)u_1.$$

Since $r > 1$, we have $u_1 \in H^1_2$. It follows from Lemma D.17 that (D.27) holds.
4) The assertion follows now from (D.25), (D.26), (D.27) and the the application of [139], Theorem 12.1. □

Bibliography

[1] H Meinhardt and A Gierer. Applications of a theory of biological pattern formation based on lateral inhibition. *J Cell Sci*, 15(2):321–346, Jul 1974. ISSN 0021-9533 (Print); 0021-9533 (Linking).

[2] H Meinhardt. Orientation of chemotactic cells and growth cones: models and mechanisms. *J Cell Sci*, 112 (Pt 17):2867–2874, Sep 1999. ISSN 0021-9533 (Print); 0021-9533 (Linking).

[3] Matthew Onsum and Christopher V Rao. A mathematical model for neutrophil gradient sensing and polarization. *PLoS Comput Biol*, 3(3):e36 EP –, 03 2007. URL http://dx.plos.org/10.1371%2Fjournal.pcbi.0030036.

[4] Herbert Levine, David A Kessler, and Wouter-Jan Rappel. Directional sensing in eukaryotic chemotaxis: A balanced inactivation model. *Proceedings of the National Academy of Sciences of the United States of America*, 103(26):9761–9766, 06 2006. doi: 10.1073/pnas.0601302103. URL http://www.ncbi.nlm.nih.gov/pmc/articles/PMC1502527/.

[5] Andrea Gamba, Antonio de Candia, Stefano Di Talia, Antonio Coniglio, Federico Bussolino, and Guido Serini. Diffusion-limited phase separation in eukaryotic chemotaxis. *Proc Natl Acad Sci U S A*, 102(47):16927–16932, Nov 2005. ISSN 0027-8424 (Print); 0027-8424 (Linking). doi: 10.1073/pnas.0503974102.

[6] Matthew P. Neilson, Douwe M. Veltman, Peter J. M. van Haastert, Steven D. Webb, John A. Mackenzie, and Robert H. Insall. Chemotaxis: A feedback-based computational model robustly predicts multiple aspects of real cell behaviour. *PLoS Biol*, 9(5):e1000618 EP –, 05 2011. URL http://dx.doi.org/10.1371%2Fjournal.pbio.1000618.

[7] Alexandra Jilkine and Leah Edelstein-Keshet. A comparison of mathematical models for polarization of single eukaryotic cells in response to guided cues. *PLoS Comput Biol*, 7(4):e1001121, 04 2011. doi: 10.1371/journal.pcbi.1001121. URL http://dx.doi.org/10.1371%2Fjournal.pcbi.1001121.

[8] Yoichiro Mori, Alexandra Jilkine, and Leah Edelstein-Keshet. Wave-pinning and cell polarity from a bistable reaction-diffusion system. *Biophysical Journal*, 94

(9):3684–3697, 5 2008. doi: http://dx.doi.org/10.1529/biophysj.107.120824. URL http://www.sciencedirect.com/science/article/pii/S0006349508704442.

[9] Kit Wong, Olivier Pertz, Klaus Hahn, and Henry Bourne. Neutrophil polarization: Spatiotemporal dynamics of rhoa activity support a self-organizing mechanism. *Proceedings of the National Academy of Sciences of the United States of America*, 103(10):3639–3644, 03 2006. doi: 10.1073/pnas.0600092103. URL http://www.ncbi.nlm.nih.gov/pmc/articles/PMC1450135/.

[10] Chris Janetopoulos, Lan Ma, Peter N Devreotes, and Pablo A Iglesias. Chemoattractant-induced phosphatidylinositol 3,4,5-trisphosphate accumulation is spatially amplified and adapts, independent of the actin cytoskeleton. *Proc Natl Acad Sci U S A*, 101(24):8951–8956, Jun 2004. ISSN 0027-8424 (Print); 0027-8424 (Linking). doi: 10.1073/pnas.0402152101.

[11] Andrew R. Houk, Alexandra Jilkine, Cecile O. Mejean, Rostislav Boltyanskiy, Eric R. Dufresne, Sigurd B. Angenent, Steven J. Altschuler, Lani F. Wu, and Orion D. Weiner. Membrane tension maintains cell polarity by confining signals to the leading edge during neutrophil migration. *Cell*, 148(1–2):175–188, 1 2012. doi: http://dx.doi.org/10.1016/j.cell.2011.10.050. URL http://www.sciencedirect.com/science/article/pii/S0092867411013638.

[12] Alan R. Kimmel and Carole A. Parent. The signal to move: D. discoideum go orienteering. *Science*, 300(5625):1525–1527, 2003. doi: 10.1126/science.1085439. URL http://www.sciencemag.org/content/300/5625/1525.abstract.

[13] Sandrine Etienne-Manneville and Alan Hall. Rho gtpases in cell biology. *Nature*, 420(6916):629–635, 12 2002. URL http://dx.doi.org/10.1038/nature01148.

[14] Michael M Kozlov and Alex Mogilner. Model of polarization and bistability of cell fragments. *Biophysical Journal*, 93(11):3811–3819, 12 2007. doi: 10.1529/biophysj.107.110411. URL http://www.ncbi.nlm.nih.gov/pmc/articles/PMC2084245/.

[15] Kinneret Keren, Zachary Pincus, Greg M. Allen, Erin L. Barnhart, Gerard Marriott, Alex Mogilner, and Julie A. Theriot. Mechanism of shape determination in motile cells. *Nature*, 453(7194):475–480, 05 2008. URL http://dx.doi.org/10.1038/nature06952.

[16] Mary C Dinauer. Regulation of neutrophil function by rac gtpases. *Curr Opin Hematol*, 10(1):8–15, Jan 2003. ISSN 1065-6251 (Print); 1065-6251 (Linking).

[17] Eric Albrecht and Howard R. Petty. Cellular memory: Neutrophil orientation reverses during temporally decreasing chemoattractant concentrations. *Proceedings of the National Academy of Sciences*, 95(9):5039–5044, 1998. URL http://www.pnas.org/content/95/9/5039.abstract.

[18] Elisabeth M Gardiner, Kersi N Pestonjamasp, Benjamin P Bohl, Chester Chamberlain, Klaus M Hahn, and Gary M Bokoch. Spatial and temporal analysis of rac activation during live neutrophil chemotaxis. *Curr Biol*, 12(23):2029–2034, Dec 2002. ISSN 0960-9822 (Print); 0960-9822 (Linking).

[19] Orion D Weiner, William A Marganski, Lani F Wu, Steven J Altschuler, and Marc W Kirschner. An actin-based wave generator organizes cell motility. *PLoS Biol*, 5(9):e221, 08 2007. doi: 10.1371/journal.pbio.0050221. URL http://dx.doi.org/10.1371%2Fjournal.pbio.0050221.

[20] Thomas D. Pollard. Regulation of actin filament assembly by arp2/3 complex and formins. *Annual Review of Biophysics and Biomolecular Structure*, 36(1): 451–477, 2014/12/15 2007. doi: 10.1146/annurev.biophys.35.040405.101936. URL http://dx.doi.org/10.1146/annurev.biophys.35.040405.101936.

[21] Anne J Ridley. Life at the leading edge. *Cell*, 145(7):1012–1022, Jun 2011. ISSN 1097-4172 (Electronic); 0092-8674 (Linking). doi: 10.1016/j.cell.2011.06.010.

[22] Nathan W. Goehring and Stephan W. Grill. Cell polarity: mechanochemical patterning. *Trends in Cell Biology*, 23(2):72–80, 2013. doi: 10.1016/j.tcb.2012.10.009. URL http://www.cell.com/trends/cell-biology/abstract/S0962-8924(12)00201-2.

[23] Matthew J Tyska and David M Warshaw. The myosin power stroke. *Cell Motil Cytoskeleton*, 51(1):1–15, Jan 2002. ISSN 0886-1544 (Print); 0886-1544 (Linking). doi: 10.1002/cm.10014.

[24] H Meinhardt and A Gierer. Pattern formation by local self-activation and lateral inhibition. *Bioessays*, 22(8):753–760, Aug 2000. ISSN 0265-9247 (Print); 0265-9247 (Linking). doi: 10.1002/1521-1878(200008)22:8<753::AID-BIES9>3.0.CO;2-Z.

[25] Andreas Rätz and Matthias Röger. Turing instabilities in a mathematical model for signaling networks. *Journal of Mathematical Biology*, 65(6):1215–1244, 2012. doi: 10.1007/s00285-011-0495-4. URL http://dx.doi.org/10.1007/s00285-011-0495-4.

[26] Peter Devreotes and Chris Janetopoulos. Eukaryotic chemotaxis: distinctions between directional sensing and polarization. *J Biol Chem*, 278(23):20445–20448, Jun 2003. ISSN 0021-9258 (Print); 0021-9258 (Linking). doi: 10.1074/jbc.R300010200.

[27] Pablo A Iglesias and Andre Levchenko. Modeling the cell's guidance system. *Sci STKE*, 2002(148):re12, Sep 2002. ISSN 1525-8882 (Electronic); 1525-8882 (Linking). doi: 10.1126/stke.2002.148.re12.

[28] Andre Levchenko and Pablo A Iglesias. Models of eukaryotic gradient sensing: application to chemotaxis of amoebae and neutrophils. *Biophys J*, 82(1 Pt 1):

50–63, Jan 2002. ISSN 0006-3495 (Print); 0006-3495 (Linking). doi: 10.1016/S0006-3495(02)75373-3.

[29] Yoichiro Mori, Alexandra Jilkine, and Leah Edelstein-Keshet. Wave-pinning and cell polarity from a bistable reaction-diffusion system. *Biophys J*, 94(9):3684–3697, May 2008. ISSN 1542-0086 (Electronic); 0006-3495 (Linking). doi: 10.1529/biophysj.107.120824.

[30] Mikiya Otsuji, Shuji Ishihara, Carl Co, Kozo Kaibuchi, Atsushi Mochizuki, and Shinya Kuroda. A mass conserved reaction-diffusion system captures properties of cell polarity. *PLoS Comput Biol*, 3(6):e108, Jun 2007. ISSN 1553-7358 (Electronic); 1553-734X (Linking). doi: 10.1371/journal.pcbi.0030108.

[31] Alexandra Jilkine, Athanasius F M Maree, and Leah Edelstein-Keshet. Mathematical model for spatial segregation of the rho-family gtpases based on inhibitory crosstalk. *Bull Math Biol*, 69(6):1943–1978, Aug 2007. ISSN 0092-8240 (Print); 0092-8240 (Linking). doi: 10.1007/s11538-007-9200-6.

[32] Alexandra Jilkine, Sigurd B. Angenent, Lani F. Wu, and Steven J. Altschuler. A density-dependent switch drives stochastic clustering and polarization of signaling molecules. *PLoS Comput Biol*, 7(11):e1002271 EP –, 11 2011. URL http://dx.doi.org/10.1371%2Fjournal.pcbi.1002271.

[33] Yoichiro Mori, Alexandra Jilkine, and Leah Edelstein-Keshet. Asymptotic and bifurcation analysis of wave-pinning in a reaction-diffusion model for cell polarization. *SIAM journal on applied mathematics*, 71(4):1401–1427, 2011. doi: 10.1137/10079118X. URL http://www.ncbi.nlm.nih.gov/pmc/articles/PMC3235655/.

[34] Chanchal Sadhu, Boris Masinovsky, Ken Dick, C Gregory Sowell, and Donald E Staunton. Essential role of phosphoinositide 3-kinase delta in neutrophil directional movement. *J Immunol*, 170(5):2647–2654, Mar 2003. ISSN 0022-1767 (Print); 0022-1767 (Linking).

[35] Edward Giniger. How do rho family gtpases direct axon growth and guidance? a proposal relating signaling pathways to growth cone mechanics. *Differentiation*, 70(8):385–396, Oct 2002. ISSN 0301-4681 (Print); 0301-4681 (Linking). doi: 10.1046/j.1432-0436.2002.700801.x.

[36] Andreas Rätz and Matthias Röger. Turing instabilities in a mathematical model for signaling networks. *Journal of Mathematical Biology*, 65(6-7):1215–1244, 2012. doi: 10.1007/s00285-011-0495-4. URL http://dx.doi.org/10.1007/s00285-011-0495-4.

[37] Wolfgang Alt and Robert T. Tranquillo. Basic morphogenetic system modeling shape changes of migrating cells: How to explain fluctuating lamellipodial dynamics. *Journal of Biological Systems*, 03(04):905–916, 1995. doi: 10.1142/S0218339095000800. URL http://dx.doi.org/10.1142/S0218339095000800.

[38] M. A. Lewis and J. D. Murray. Analysis of stable two-dimensional patterns in contractile cytogel. *Journal of Nonlinear Science*, 1(3):289–311, 1991. doi: 10.1007/BF01238816. URL http://dx.doi.org/10.1007/BF01238816.

[39] Anh N Hoang, Caroline N Jones, Laurie Dimisko, Bashar Hamza, Joseph Martel, Nikola Kojic, and Daniel Irimia. Measuring neutrophil speed and directionality during chemotaxis, directly from a droplet of whole blood. *Technology*, 1(1):49–, 10 2013. doi: 10.1142/S2339547813500040. URL http://www.ncbi.nlm.nih.gov/pmc/articles/PMC4010229/.

[40] M. Yanai, J. P. Butler, T. Suzuki, H. Sasaki, and H. Higuchi. Regional rheological differences in locomoting neutrophils. *American Journal of Physiology - Cell Physiology*, 287(3):C603–C611, 08 2004. URL http://ajpcell.physiology.org/content/287/3/C603.abstract.

[41] Jonathon Howard, Stephan W. Grill, and Justin S. Bois. Turing's next steps: the mechanochemical basis of morphogenesis. *Nat Rev Mol Cell Biol*, 12(6):392–398, 06 2011. URL http://dx.doi.org/10.1038/nrm3120.

[42] Kinneret Keren. Membrane tension leads the way. *Proceedings of the National Academy of Sciences*, 108(35):14379–14380, 08 2011. URL http://www.pnas.org/content/108/35/14379.short.

[43] Alba Diz-Muñoz, Daniel A. Fletcher, and Orion D. Weiner. Use the force: membrane tension as an organizer of cell shape and motility. *Trends in Cell Biology*, 23(2):47–53, 2 2013. doi: http://dx.doi.org/10.1016/j.tcb.2012.09.006. URL http://www.sciencedirect.com/science/article/pii/S0962892412001778.

[44] Klaus Hausmann, Norbert Hülsmann, and Renate Radek. *Protistology*. Schweizerbart'sche, Berlin u.a., 3. edition, 2003.

[45] T. J Mitchison and L. P Cramer. Actin-based cell motility and cell locomotion. *Cell*, 84(3):371–379, 2 1996. doi: http://dx.doi.org/10.1016/S0092-8674(00)81281-7. URL http://www.sciencedirect.com/science/article/pii/S0092867400812817.

[46] K Kruse, J F Joanny, F Julicher, and J Prost. Contractility and retrograde flow in lamellipodium motion. *Phys Biol*, 3(2):130–137, Jun 2006. ISSN 1478-3975 (Electronic); 1478-3967 (Linking). doi: 10.1088/1478-3975/3/2/005.

[47] Qing Deng and Anna Huttenlocher. Leukocyte migration from a fish eye's view. *Journal of Cell Science*, 125(17):3949–3956, 10 2012. URL http://jcs.biologists.org/content/125/17/3949.abstract.

[48] Roberto Dominguez and Kenneth C. Holmes. Actin structure and function. *Annual Review of Biophysics*, 40(1):169–186, 2011. doi: 10.

1146/annurev-biophys-042910-155359. URL http://dx.doi.org/10.1146/annurev-biophys-042910-155359. PMID: 21314430.

[49] F Huber, J Schnauß, S Rönicke, P Rauch, K Müller, C Fütterer, and J Käs. Emergent complexity of the cytoskeleton: from single filaments to tissue. *Advances in Physics*, 62(1):1–112, 01 2013. doi: 10.1080/00018732.2013.771509. URL http://www.ncbi.nlm.nih.gov/pmc/articles/PMC3985726/.

[50] Akihiro Narita, Shuichi Takeda, Atsuko Yamashita, and Yuichiro Maeda. Structural basis of actin filament capping at the barbed-end: a cryo-electron microscopy study. *EMBO J*, 25(23):5626–5633, Nov 2006. ISSN 0261-4189 (Print); 0261-4189 (Linking). doi: 10.1038/sj.emboj.7601395.

[51] S K Akiyama. Integrins in cell adhesion and signaling. *Hum Cell*, 9(3):181–186, Sep 1996. ISSN 0914-7470 (Print); 0914-7470 (Linking).

[52] Revathi Ananthakrishnan and Allen Ehrlicher. The forces behind cell movement. *International Journal of Biological Sciences*, 3(5):303–317, 2007. URL http://www.ncbi.nlm.nih.gov/pmc/articles/PMC1893118/.

[53] Alexander B. Verkhovsky, Tatyana M. Svitkina, and Gary G. Borisy. Self-polarization and directional motility of cytoplasm. *Current Biology*, 9(1):11–S1, 1 1999. doi: http://dx.doi.org/10.1016/S0960-9822(99)80042-6. URL http://www.sciencedirect.com/science/article/pii/S0960982299800426.

[54] Alexander B. Verkhovsky, Tatyana M. Svitkina, and Gary G. Borisy. Self-polarization and directional motility of cytoplasm. *Current Biology*, 9(1):11–S1, 1 1999. doi: http://dx.doi.org/10.1016/S0960-9822(99)80042-6. URL http://www.sciencedirect.com/science/article/pii/S0960982299800426.

[55] Francoise Coussen, Daniel Choquet, Michael P Sheetz, and Harold P Erickson. Trimers of the fibronectin cell adhesion domain localize to actin filament bundles and undergo rearward translocation. *J Cell Sci*, 115(Pt 12):2581–2590, Jun 2002. ISSN 0021-9533 (Print); 0021-9533 (Linking).

[56] Carlos Jurado, John R Haserick, and Juliet Lee. Slipping or gripping? fluorescent speckle microscopy in fish keratocytes reveals two different mechanisms for generating a retrograde flow of actin. *Mol Biol Cell*, 16(2):507–518, Feb 2005. ISSN 1059-1524 (Print); 1059-1524 (Linking). doi: 10.1091/mbc.E04-10-0860.

[57] Alexandra Jilkine. A wave-pinning mechanism for eukaryotic cell polarization based on rho gtpase dynamics. *UNIVERSITY OF BRITISH COLUMBIA*, 2009.

[58] Myrto Raftopoulou and Alan Hall. Cell migration: Rho gtpases lead the way. *Developmental Biology*, 265(1):23–32, 1 2004. doi: http://dx.doi.org/10.1016/j.ydbio.2003.06.003. URL http://www.sciencedirect.com/science/article/pii/S001216060300544X.

[59] Anne J. Ridley. Rho gtpases and cell migration. *Journal of Cell Science*, 114 (15):2713, 08 2001. URL http://jcs.biologists.org/content/114/15/2713.abstract.

[60] A L Bishop and A Hall. Rho gtpases and their effector proteins. *Biochem J*, 348 Pt 2:241–255, Jun 2000. ISSN 0264-6021 (Print); 0264-6021 (Linking).

[61] Orion D Weiner, Paul O Neilsen, Glenn D Prestwich, Marc W Kirschner, Lewis C Cantley, and Henry R Bourne. A ptdlnsp(3)- and rho gtpase-mediated positive feedback loop regulates neutrophil polarity. *Nature cell biology*, 4(7):509–513, 07 2002. doi: 10.1038/ncb811. URL http://www.ncbi.nlm.nih.gov/pmc/articles/PMC2823287/.

[62] Zhong Guo, Mohammad Reza Ahmadian, and Roger S Goody. Guanine nucleotide exchange factors operate by a simple allosteric competitive mechanism. *Biochemistry*, 44(47):15423–15429, Nov 2005. ISSN 0006-2960 (Print); 0006-2960 (Linking). doi: 10.1021/bi0518601.

[63] Johannes L Bos, Holger Rehmann, and Alfred Wittinghofer. Gefs and gaps: critical elements in the control of small g proteins. *Cell*, 129(5):865–877, Jun 2007. ISSN 0092-8674 (Print); 0092-8674 (Linking). doi: 10.1016/j.cell.2007.05.018.

[64] Roland Wedlich-Soldner and Rong Li. Spontaneous cell polarization: undermining determinism. *Nat Cell Biol*, 5(4):267–270, 04 2003. URL http://dx.doi.org/10.1038/ncb0403-267.

[65] Reina E Itoh, Kazuo Kurokawa, Yusuke Ohba, Hisayoshi Yoshizaki, Naoki Mochizuki, and Michiyuki Matsuda. Activation of rac and cdc42 video imaged by fluorescent resonance energy transfer-based single-molecule probes in the membrane of living cells. *Molecular and Cellular Biology*, 22(18):6582–6591, 09 2002. doi: 10.1128/MCB.22.18.6582-6591.2002. URL http://www.ncbi.nlm.nih.gov/pmc/articles/PMC135619/.

[66] Anja Schmidt and Alan Hall. Guanine nucleotide exchange factors for rho gtpases: turning on the switch. *Genes Dev*, 16(13):1587–1609, Jul 2002. ISSN 0890-9369 (Print); 0890-9369 (Linking). doi: 10.1101/gad.1003302.

[67] R S Goody, A Rak, and K Alexandrov. The structural and mechanistic basis for recycling of rab proteins between membrane compartments. *Cell Mol Life Sci*, 62 (15):1657–1670, Aug 2005. ISSN 1420-682X (Print); 1420-682X (Linking). doi: 10.1007/s00018-005-4486-8.

[68] Suzanne Pfeffer. Membrane domains in the secretory and endocytic pathways. *Cell*, 112(4):507–517, February 2003. doi: 10.1016/S0092-8674(03)00118-1. URL http://www.cell.com/cell/abstract/S0092-8674(03)00118-1.

[69] Vadim S. Kraynov, Chester Chamberlain, Gary M. Bokoch, Martin A. Schwartz, Sarah Slabaugh, and Klaus M. Hahn. Localized rac activation dynamics visualized in living cells. *Science*, 290(5490):333–337, 2000. URL http://www.sciencemag.org/content/290/5490/333.abstract.

[70] Perihan Nalbant, Louis Hodgson, Vadim Kraynov, Alexei Toutchkine, and Klaus M. Hahn. Activation of endogenous cdc42 visualized in living cells. *Science*, 305(5690):1615–1619, 2004. URL http://www.sciencemag.org/content/305/5690/1615.abstract.

[71] Alexandra Van Keymeulen, Kit Wong, Zachary A Knight, Cedric Govaerts, Klaus M Hahn, Kevan M Shokat, and Henry R Bourne. To stabilize neutrophil polarity, pip3 and cdc42 augment rhoa activity at the back as well as signals at the front. *J Cell Biol*, 174(3):437–445, Jul 2006. ISSN 0021-9525 (Print); 0021-9525 (Linking). doi: 10.1083/jcb.200604113.

[72] Jingsong Xu, Fei Wang, Alexandra Van Keymeulen, Paul Herzmark, Aaron Straight, Kathleen Kelly, Yoh Takuwa, Naotoshi Sugimoto, Timothy Mitchison, and Henry R Bourne. Divergent signals and cytoskeletal assemblies regulate self-organizing polarity in neutrophils. *Cell*, 114(2):201–214, Jul 2003. ISSN 0092-8674 (Print); 0092-8674 (Linking).

[73] Hongmei Yu, Janna Kay Mouw, and Valerie M Weaver. Forcing form and function: biomechanical regulation of tumor evolution. *Trends Cell Biol*, 21(1):47–56, Jan 2011. ISSN 1879-3088 (Electronic); 0962-8924 (Linking). doi: 10.1016/j.tcb.2010.08.015.

[74] Drazen Raucher and Michael P Sheetz. Cell spreading and lamellipodial extension rate is regulated by membrane tension. *The Journal of Cell Biology*, 148(1):127–136, 01 2000. URL http://www.ncbi.nlm.nih.gov/pmc/articles/PMC2156205/.

[75] S J Singer and G L Nicolson. The fluid mosaic model of the structure of cell membranes. *Science*, 175(4023):720–731, Feb 1972. ISSN 0036-8075 (Print); 0036-8075 (Linking).

[76] Surface forces of the arbacia egg. *Protoplasma*, 17(1):480–480, 1933. doi: 10.1007/BF01604112. URL http://dx.doi.org/10.1007/BF01604112.

[77] D Raucher, T Stauffer, W Chen, K Shen, S Guo, J D York, M P Sheetz, and T Meyer. Phosphatidylinositol 4,5-bisphosphate functions as a second messenger that regulates cytoskeleton-plasma membrane adhesion. *Cell*, 100(2):221–228, Jan 2000. ISSN 0092-8674 (Print); 0092-8674 (Linking).

[78] Peter K Koo, Matthew Weitzman, Chandran R Sabanaygam, Kenneth L van Golen, and Simon G J Mochrie. Extracting diffusive states of rho gtpase in

live cells: Towards in vivo biochemistry. *PLoS Computational Biology*, 11(10): e1004297, 10 2015. doi: 10.1371/journal.pcbi.1004297. URL http://www.ncbi.nlm.nih.gov/pmc/articles/PMC4626024/.

[79] Edmund J. Crampin, Eamonn A. Gaffney, and Philip K. Maini. Reaction and diffusion on growing domains: Scenarios for robust pattern formation. *Bulletin of Mathematical Biology*, 61(6):1093–1120, 1999. doi: 10.1006/bulm.1999.0131. URL http://dx.doi.org/10.1006/bulm.1999.0131.

[80] Kent L. Rossman, Channing J. Der, and John Sondek. Gef means go: turning on rho gtpases with guanine nucleotide-exchange factors. *Nat Rev Mol Cell Biol*, 6 (2):167–180, 02 2005. URL http://dx.doi.org/10.1038/nrm1587.

[81] James D. Murray. *Mathematical Biology II*. Springer, New York ; Berlin ; Heidelberg, 2004. ISBN 978-0-387-95228-4; 0-387-95228-4.

[82] Alexandra Van Keymeulen, Kit Wong, Zachary A. Knight, Cedric Govaerts, Klaus M. Hahn, Kevan M. Shokat, and Henry R. Bourne. To stabilize neutrophil polarity, pip3 and cdc42 augment rhoa activity at the back as well as signals at the front. *The Journal of Cell Biology*, 174(3):437, 07 2006. URL http://jcb.rupress.org/content/174/3/437.abstract.

[83] Soon-Tuck Sit and Ed Manser. Rho gtpases and their role in organizing the actin cytoskeleton. *Journal of Cell Science*, 124(5):679–683, 02 2011. URL http://jcs.biologists.org/content/124/5/679.abstract.

[84] C D Nobes and A Hall. Rho, rac, and cdc42 gtpases regulate the assembly of multimolecular focal complexes associated with actin stress fibers, lamellipodia, and filopodia. *Cell*, 81(1):53–62, Apr 1995. ISSN 0092-8674 (Print); 0092-8674 (Linking).

[85] K. Kruse, J. F. Joanny, F. Jülicher, J. Prost, and K. Sekimoto. Generic theory of active polar gels: a paradigm for cytoskeletal dynamics. *The European Physical Journal E*, 16(1):5–16, 2005. doi: 10.1140/epje/e2005-00002-5. URL http://dx.doi.org/10.1140/epje/e2005-00002-5.

[86] P A Janmey, S Hvidt, J Kas, D Lerche, A Maggs, E Sackmann, M Schliwa, and T P Stossel. The mechanical properties of actin gels. elastic modulus and filament motions. *J Biol Chem*, 269(51):32503–32513, Dec 1994. ISSN 0021-9258 (Print); 0021-9258 (Linking).

[87] M. L. Gardel, J. H. Shin, F. C. MacKintosh, L. Mahadevan, P. Matsudaira, and D. A. Weitz. Elastic behavior of cross-linked and bundled actin networks. *Science*, 304(5675):1301–1305, 05 2004. URL http://science.sciencemag.org/content/304/5675/1301.abstract.

[88] F Gerbal, P Chaikin, Y Rabin, and J Prost. An elastic analysis of listeria monocytogenes propulsion. *Biophys J*, 79(5):2259–2275, Nov 2000. ISSN 0006-3495 (Print); 0006-3495 (Linking). doi: 10.1016/S0006-3495(00)76473-3.

[89] Taeyoon Kim, Margaret L Gardel, and Ed Munro. Determinants of fluid-like behavior and effective viscosity in cross-linked actin networks. *Biophysical Journal*, 106(3):526–534, 02 2014. doi: 10.1016/j.bpj.2013.12.031. URL http://www.ncbi.nlm.nih.gov/pmc/articles/PMC3944977/.

[90] Frank G. Schmidt, Florian Ziemann, and Erich Sackmann. Shear field mapping in actin networks by using magnetic tweezers. *European Biophysics Journal*, 24(5): 348–353, 1996. doi: 10.1007/BF00180376. URL http://dx.doi.org/10.1007/BF00180376.

[91] Fabian Heinemann, Holger Doschke, and Manfred Radmacher. Keratocyte lamellipodial protrusion is characterized by a concave force-velocity relation. *Biophysical Journal*, 100(6):1420–1427, 03 2011. doi: 10.1016/j.bpj.2011.01.063. URL http://www.ncbi.nlm.nih.gov/pmc/articles/PMC3059597/.

[92] Revathi Ananthakrishnan and Allen Ehrlicher. The forces behind cell movement. *International Journal of Biological Sciences*, 3(5):303–317, 2007. URL http://www.ncbi.nlm.nih.gov/pmc/articles/PMC1893118/.

[93] Colin P. McCann, Erin C. Rericha, Chenlu Wang, Wolfgang Losert, and Carole A. Parent. <italic>dictyostelium</italic> cells migrate similarly on surfaces of varying chemical composition. *PLoS ONE*, 9(2):e87981–, 02 2014. URL http://dx.doi.org/10.1371%2Fjournal.pone.0087981.

[94] F. Jülicher, K. Kruse, J. Prost, and J. F. Joanny. Active behavior of the cytoskeleton. *Physics Reports*, 449(1–3):3–28, 9 2007. doi: http://dx.doi.org/10.1016/j.physrep.2007.02.018. URL http://www.sciencedirect.com/science/article/pii/S0370157307001330.

[95] Sascha Martens and Harvey T. McMahon. Mechanisms of membrane fusion: disparate players and common principles. *Nat Rev Mol Cell Biol*, 9(7):543–556, 07 2008. URL http://dx.doi.org/10.1038/nrm2417.

[96] M. J. Niemiec, B. De Samber, J. Garrevoet, E. Vergucht, B. Vekemans, R. De Rycke, E. Bjorn, L. Sandblad, G. Wellenreuther, G. Falkenberg, P. Cloetens, L. Vincze, and C. F. Urban. Trace element landscape of resting and activated human neutrophils on the sub-micrometer level. *Metallomics*, 7:996–1010, 2015. doi: 10.1039/C4MT00346B. URL http://dx.doi.org/10.1039/C4MT00346B.

[97] Marten Postma, Leonard Bosgraaf, Harriet M Loovers, and Peter J M Van Haastert. Chemotaxis: signalling modules join hands at front and tail. *EMBO Rep*, 5(1):35–40, Jan 2004. ISSN 1469-221X (Print); 1469-221X (Linking). doi: 10.1038/sj.embor.7400051.

[98] Eugenio Marco, Roland Wedlich-Soldner, Rong Li, Steven J Altschuler, and Lani F Wu. Endocytosis optimizes the dynamic localization of membrane proteins that regulate cortical polarity. *Cell*, 129(2):411–422, Apr 2007. ISSN 0092-8674 (Print); 0092-8674 (Linking). doi: 10.1016/j.cell.2007.02.043.

[99] J. L. McGrath, Y. Tardy, C. F. Dewey Jr., J. J. Meister, and J. H. Hartwig. Simultaneous measurements of actin filament turnover, filament fraction, and monomer diffusion in endothelial cells. *Biophysical Journal*, 75(4):2070–2078, 10 1998. doi: http://dx.doi.org/10.1016/S0006-3495(98)77649-0. URL http://www.sciencedirect.com/science/article/pii/S0006349598776490.

[100] Daniel Zicha, Ian M. Dobbie, Mark R. Holt, James Monypenny, Daniel Y. H. Soong, Colin Gray, and Graham A. Dunn. Rapid actin transport during cell protrusion. *Science*, 300(5616):142–145, 04 2003. URL http://science.sciencemag.org/content/300/5616/142.abstract.

[101] Christi Andrin Gerda de Vries Darin McDonald, Gustavo Carrero and Michael J. Hendzel. Nucleoplasmic β-actin exists in a dynamic equilibrium between low-mobility polymeric species and rapidly diffusing populations. *J Cell Biol*, 1(172): 541–552 doi:10.1083/jcb.200507101, 2006.

[102] Falk Wottawah, Stefan Schinkinger, Bryan Lincoln, Revathi Ananthakrishnan, Maren Romeyke, Jochen Guck, and Josef Kas. Optical rheology of biological cells. *Phys Rev Lett*, 94(9):098103, Mar 2005. ISSN 0031-9007 (Print); 0031-9007 (Linking). doi: 10.1103/PhysRevLett.94.098103.

[103] Jean-François Joanny and Jacques Prost. Active gels as a description of the actin-myosin cytoskeleton. *HFSP Journal*, 3(2):94–104, 04 2009. doi: 10.2976/1.3054712. URL http://www.ncbi.nlm.nih.gov/pmc/articles/PMC2707794/.

[104] Yann Marcy, Jean-François Joanny, Jacques Prost, and Cécile Sykes. Probing friction in actin-based motility. *New Journal of Physics*, 9(11):431, 2007. URL http://stacks.iop.org/1367-2630/9/i=11/a=431.

[105] Yann Marcy, Jacques Prost, Marie-France Carlier, and Cécile Sykes. Forces generated during actin-based propulsion: A direct measurement by micromanipulation. *Proceedings of the National Academy of Sciences of the United States of America*, 101(16):5992–5997, 04 2004. URL http://www.pnas.org/content/101/16/5992.

[106] A. D. McNaught and A. Wilkinson. *IUPAC. Compendium of Chemical Terminology, 2nd ed.* Blackwell Scientific Publications, Oxford, 2 edition, 1997.

[107] L.D. Landau and E.M. Lifshitz. *Fluid Mechanics*. Number Bd. 6. Elsevier Science, 1960. ISBN 9781483140506. URL https://books.google.de/books?id=CeBbAwAAQBAJ.

[108] Kai Kopfer and Franziska Matthäus. A mechanochemical model for RHO GTPase mediated cell polarization. *In preparation*, 2018.

[109] Adriana T Dawes and Leah Edelstein-Keshet. Phosphoinositides and rho proteins spatially regulate actin polymerization to initiate and maintain directed movement in a one-dimensional model of a motile cell. *Biophysical Journal*, 92(3):744–768, 02 2007. doi: 10.1529/biophysj.106.090514. URL http://www.ncbi.nlm.nih.gov/pmc/articles/PMC1779977/.

[110] Cell polarity: an examination of its behavioral expression and its consequences for polymorphonuclear leukocyte chemotaxis. *The Journal of Cell Biology*, 89(3):585–592, 06 1981. URL http://www.ncbi.nlm.nih.gov/pmc/articles/PMC2111809/.

[111] Jeremie Dalous, Emmanuel Burghardt, Annette Muller-Taubenberger, Franz Bruckert, Gunther Gerisch, and Till Bretschneider. Reversal of cell polarity and actin-myosin cytoskeleton reorganization under mechanical and chemical stimulation. *Biophys J*, 94(3):1063–1074, Feb 2008. ISSN 1542-0086 (Electronic); 0006-3495 (Linking). doi: 10.1529/biophysj.107.114702.

[112] Luke Tweedy, David A. Knecht, Gillian M. Mackay, and Robert H. Insall. Self-generated chemoattractant gradients: Attractant depletion extends the range and robustness of chemotaxis. *PLOS Biology*, 14(3):e1002404–, 03 2016. URL https://doi.org/10.1371/journal.pbio.1002404.

[113] W S Ramsey. Analysis of individual leucocyte behavior during chemotaxis.. *Exp Cell Res*, 70(1):129–139, Jan 1972. ISSN 0014-4827 (Print); 0014-4827 (Linking).

[114] Eric Albrecht and Howard R Petty. Cellular memory: Neutrophil orientation reverses during temporally decreasing chemoattractant concentrations. *Proceedings of the National Academy of Sciences of the United States of America*, 95(9):5039–5044, 04 1998. URL http://www.ncbi.nlm.nih.gov/pmc/articles/PMC20209/.

[115] Wiktor Eckhaus. *Asymptotic analysis of singular perturbations*. North-Holland, Amsterdam, 1979.

[116] Edmund J. Crampin. *Reaction-Diffusion Equations on Growing Domains*. PhD thesis, University of Oxford, 2000.

[117] A.I. Volpert, V.A. Volpert, and V.A. *Traveling Wave Solutions of Parabolic Systems*. American Mathematical Society, 2000. URL https://books.google.de/books?id=1qP--BRsLAwC.

[118] Steven J. Altschuler, Sigurd B. Angenent, Yanqin Wang, and Lani F. Wu. On the spontaneous emergence of cell polarity. *Nature*, 454(7206):886–889, 08 2008. URL http://dx.doi.org/10.1038/nature07119.

[119] Guillaume Charras and Erik Sahai. Physical influences of the extracellular environment on cell migration. *Nat Rev Mol Cell Biol*, 15(12):813–824, 12 2014. URL http://dx.doi.org/10.1038/nrm3897.

[120] Chun Xiang Sun, Gregory P. Downey, Fei Zhu, Adeline L. Y. Koh, Herman Thang, and Michael Glogauer. Rac1 is the small gtpase responsible for regulating the neutrophil chemotaxis compass. *Blood*, 104(12):3758, 11 2004. URL http://www.bloodjournal.org/content/104/12/3758.abstract.

[121] Mark J. Dayel, Orkun Akin, Mark Landeryou, Viviana Risca, Alex Mogilner, and R. Dyche Mullins. In silico reconstitution of actin-based symmetry breaking and motility. *PLOS Biology*, 7(9):e1000201–, 09 2009. URL https://doi.org/10.1371/journal.pbio.1000201.

[122] Anders E. Carlsson. Dendritic actin filament nucleation causes traveling waves and patches. *Physical Review Letters*, 104(22):228102–, 06 2010. URL https://link.aps.org/doi/10.1103/PhysRevLett.104.228102.

[123] Orion D Weiner, William A Marganski, Lani F Wu, Steven J Altschuler, and Marc W Kirschner. An actin-based wave generator organizes cell motility. *PLoS Biol*, 5(9):e221–, 08 2007. URL http://dx.doi.org/10.1371%2Fjournal.pbio.0050221.

[124] M. Neuss-Radu and W. Jäger. Effective transmission conditions for reaction-diffusion processes in domains separated by an interface. *SIAM Journal on Mathematical Analysis*, 39(3):687–720, 2017/11/13 2007. doi: 10.1137/060665452. URL https://doi.org/10.1137/060665452.

[125] S Marusic and Eduard Marusic-Paloka. *Two-scale convergence for thin domains and its applications to some lower-dimensional models in fluid mechanics*, volume 23. IOS Press, 05 2000.

[126] Susan B Hellewell and D Lansing Taylor. The solation-contraction coupling hypothesis of cell movemen. In *University of Tokyo*. Press, 1979.

[127] Daisuke Mizuno, Catherine Tardin, C. F. Schmidt, and F. C. MacKintosh. Nonequilibrium mechanics of active cytoskeletal networks. *Science*, 315(5810):370–373, 01 2007. URL http://science.sciencemag.org/content/315/5810/370.abstract.

[128] K Takiguchi. Heavy meromyosin induces sliding movements between antiparallel actin filaments. *J Biochem*, 109(4):520–527, Apr 1991. ISSN 0021-924X (Print); 0021-924X (Linking).

[129] Yohko Tanaka-Takiguchi, Toshihito Kakei, Akinori Tanimura, Aya Takagi, Makoto Honda, Hirokazu Hotani, and Kingo Takiguchi. The elongation and contraction

of actin bundles are induced by double-headed myosins in a motor concentration-dependent manner. *J Mol Biol*, 341(2):467–476, Aug 2004. ISSN 0022-2836 (Print); 0022-2836 (Linking). doi: 10.1016/j.jmb.2004.06.019.

[130] Baris Sumengen. A matlab toolbox implementing level set methods.

[131] Stanley Osher and Ronald Fedkiw. *Level set methods and dynamic implicit surfaces*. Springer, New York ; Berlin ; Heidelberg, 2003. ISBN 0-387-95482-1; 978-0-387-95482-0.

[132] MATLAB. Delaunay triangulation, 10 2016. URL http://de.mathworks.com/help/matlab/math/delaunay-triangulation.html.

[133] Mark Sussman, Peter Smereka, and Stanley Osher. A level set approach for computing solutions to incompressible two-phase flow. *Journal of Computational Physics*, 114(1):146–159, 1994. doi: http://dx.doi.org/10.1006/jcph.1994.1155. URL http://www.sciencedirect.com/science/article/pii/S0021999184711557.

[134] Kôsaku Yoshida. *Functional analysis*. Springer, Berlin ; Heidelberg [u.a.], 1971. ISBN 3-540-05506-1.

[135] Lawrence C. Evans. *Partial differential equations*. American Mathematical Society, Providence, RI, 2010. ISBN 978-0-8218-4974-3; 0-8218-4974-3.

[136] G. R. Liu and S. S. Quek. *The finite element method : a practical course*. Butterworth-Heinemann, Oxford, U.K., 2013. ISBN 978-0-08-099441-3; 0-08-099441-5; 978-0-08-098356-1.

[137] Keith W. Morton and David F. Mayers. Numerical solution of partial differential equations : an introduction. 1994.

[138] David Gilbarg and Neil S. Trudinger. *Elliptic partial differential equations of second order*. Springer, Berlin ; Heidelberg, 2001. ISBN 3-540-41160-7; 978-3-540-41160-4.

[139] Herbert Amann. *Nonhomogeneous Linear and Quasilinear Elliptic and Parabolic Boundary Value Problems*, pages 9–126. Vieweg+Teubner Verlag, Wiesbaden, 1993. ISBN 978-3-663-11336-2. doi: 10.1007/978-3-663-11336-2{_}1. URL http://dx.doi.org/10.1007/978-3-663-11336-2_1.

[140] Herbert Amann. *Linear and quasilinear parabolic problems*. Birkhäuser, Basel [u.a.], 1995.

[141] Hans Triebel. *Theory of function spaces*. Birkhäuser, Basel [u.a.], 1983. ISBN 3-7643-1381-1; 978-3-7643-1381-4.

[142] Herbert Amann. Highly degenerate quasilinear parabolic systems. *Annali della Scuola Normale Superiore di Pisa*, 18(1):135–166, 1991.